

AD-A058 669

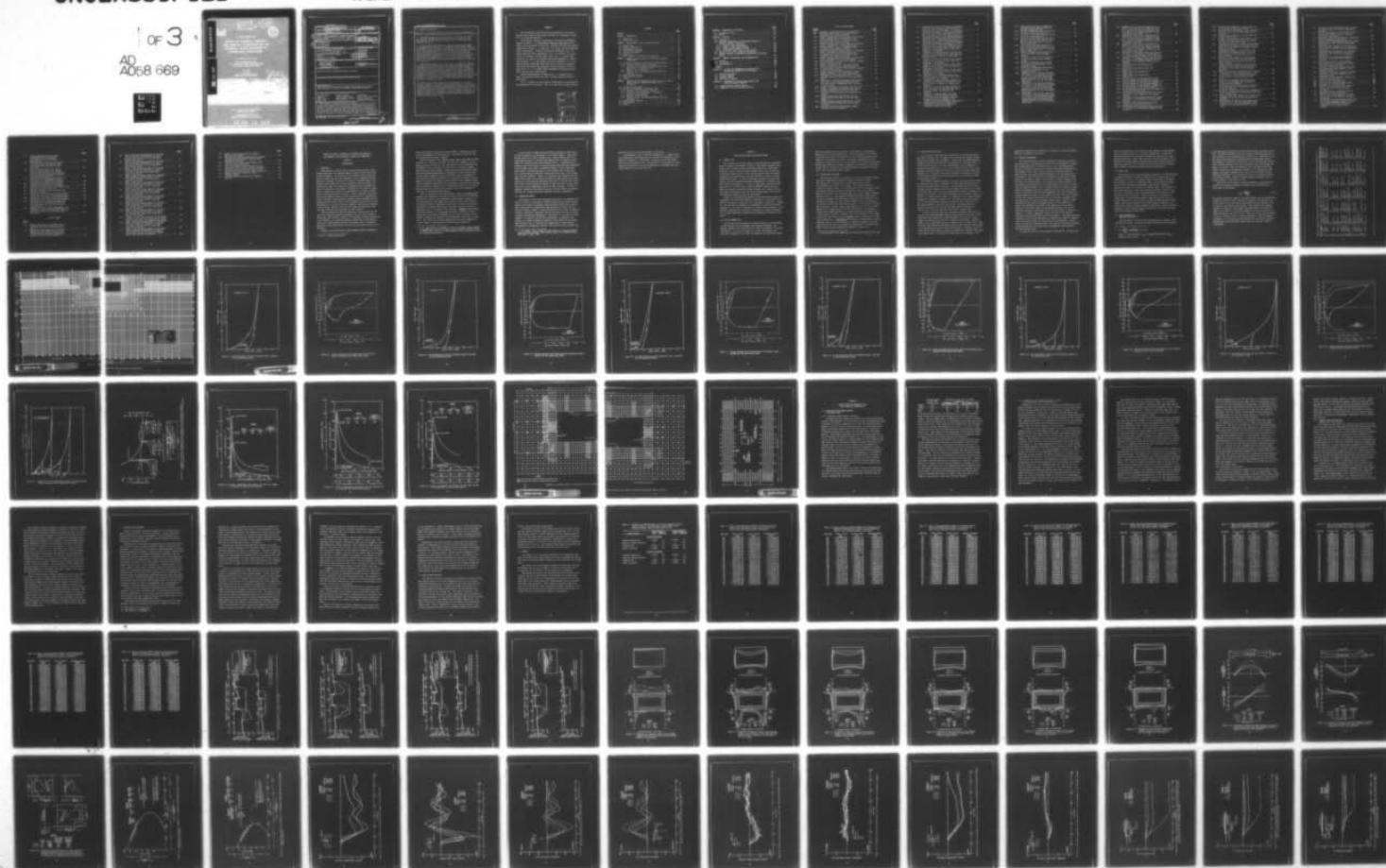
ARMY ENGINEER WATERWAYS EXPERIMENT STATION VICKSBURG MISS F/G 18/3  
EFFECT OF BACKFILL PROPERTY AND AIRBLAST VARIATIONS ON THE EXTE--ETC(U)  
JUN 78 J E WINDHAM, J O CURTIS

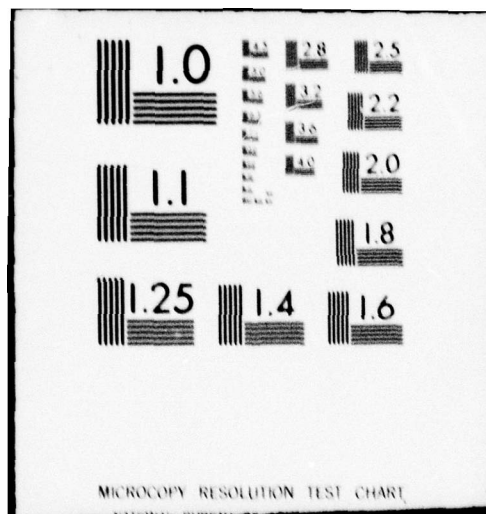
UNCLASSIFIED

WES-TR-S-78-5

NL

OF 3  
AD  
A058 669





AD A058669

DDC FILE COPY

LEVEL

12 B.S.



TECHNICAL REPORT S-78-3

# EFFECT OF BACKFILL PROPERTY AND AIRBLAST VARIATIONS ON THE EXTERNAL LOADS DELIVERED TO BURIED BOX STRUCTURES

by

Jon E. Windham, John O. Curtis

Soils and Pavements Laboratory  
U. S. Army Engineer Waterways Experiment Station  
P. O. Box 631, Vicksburg, Miss. 39180

June 1978  
Final Report

Approved For Public Release; Distribution Unlimited



Prepared for: Director, Defense Nuclear Agency  
Washington, D. C. 20305

Under Subtask SC062, Work Unit 01  
"Influence of Backfill on Structural Response"

78 09 14 047

Unclassified

SECURITY CLASSIFICATION OF THIS PAGE (When Data Entered)

REPORT DOCUMENTATION PAGE		READ INSTRUCTIONS BEFORE COMPLETING FORM
1. REPORT NUMBER Technical Report S-78-5	2. GOVT ACCESSION NO.	3. RECIPIENT'S CATALOG NUMBER
4. TITLE (and subtitle) EFFECT OF BACKFILL PROPERTY AND AIRBLAST VARIATIONS ON THE EXTERNAL LOADS DELIVERED TO BURIED BOX STRUCTURES.	5. DATE OF REPORT & PERIOD COVERED Final Report.	
6. AUTHOR Jon E. Windham John O. Curtis	7. PERFORMING ORG. REPORT NUMBER Oct 75 - Dec 76	
8. PERFORMING ORGANIZATION NAME AND ADDRESS U. S. Army Engineer Waterways Experiment Station Soils and Pavements Laboratory P. O. Box 631, Vicksburg, Miss. 39180	9. PROGRAM ELEMENT, PROJECT, TASK AREA & WORK UNIT NUMBERS Subtask SC062 Work Unit 01	
11. CONTROLLING OFFICE NAME AND ADDRESS Director Defense Nuclear Agency Washington, D. C. 20305	12. REPORT DATE June 1978	
14. MONITORING AGENCY NAME & ADDRESS (if different from Controlling Office) 12 210p.	13. NUMBER OF PAGES 203	
15. SECURITY CLASS. (of this report) Unclassified		15a. DECLASSIFICATION/DOWNGRADING SCHEDULE
16. DISTRIBUTION STATEMENT (of this Report) Approved for public release; distribution unlimited.		
17. DISTRIBUTION STATEMENT (of the abstract entered in Block 20, if different from Report)		
18. SUPPLEMENTARY NOTES This research was sponsored by the Defense Nuclear Agency under Subtask SC062, Work Unit 01, "Influence of Backfill on Structural Response."		
19. KEY WORDS (Continue on reverse side if necessary and identify by block number) Air blast waves      Dynamic response      Overpressure Backfills      Finite element method      Soil-structure interaction Blast effects      HONDO (Computer program)      Surface explosions Blast loads      Loads (Forces)      Underground structures		
20. ABSTRACT (Continue on reverse side if necessary and identify by block number) The results of analytical studies are presented in which (1) the SAP IV elastic finite-element (FE) code was used to perform modal analyses for a rectangular structure in vacuo and embedded in different backfill materials; and (2) a series of dynamic and static two-dimensional (2D), plane-strain, FE, structure-medium interaction (SMI) code calculations were performed using the HONDO code. The HONDO code SMI calculations were made to investigate the effect of variations in (1) surface airblast loadings; and (2) constitutive (Continued)		

DD FORM 1 JAN 73 1473

EDITION OF 1 NOV 65 IS OBSOLETE

Unclassified

SECURITY CLASSIFICATION OF THIS PAGE (When Data Entered)

Q38 100

Cont  
11B

Unclassified

SECURITY CLASSIFICATION OF THIS PAGE(When Data Entered)

20. ABSTRACT (Continued).

CONT → properties of the backfill region around a hypothetical, shallow-buried structure on the transient loading environments experienced by the structure.

The model analyses showed that the natural frequencies increased as the quality of the material surrounding the structure increases. They also indicated that the planned SMI calculations would have sufficient frequency response.)

A first series of four dynamic 2D, SMI calculations were performed on this plane-strain idealization of a simple buried structure. These calculations involved two surface loadings (e.g., nominal 300-psi (20.7-bar) overpressure pulses for 1-MT and 10-KT weapons) over two backfill conditions (i.e., loose and dense backfill cases). A fifth dynamic calculation, essentially identical to the first four calculations with a nominal 1000-psi (68.9-bar) overpressure pulse for a 10-KT weapon over the dense backfill condition was conducted. A final calculation (a "pseudostatic" calculation) was conducted in which the structure surrounded by dense backfill was loaded with a monotonically increasing load from 0 to 300 psi (0 to 20.7 bars).

Comparisons of results of the first series of calculations indicated that the use of both loose backfill rather than dense backfill and higher weapon-yield loading cases increased (1) deflections across backfill sections; (2) loads on, deflections of, and thrusts, shears, and bending moments within the structure; and (3) amplitudes of the shock spectra for points on the inside surface of the structure. The results of the fifth calculation indicated that the stresses and bending moment within and the deflections of the structure for the nominal 1000-psi (68.9-bar) overpressure airblast for a 10-KT weapon over the dense backfill problem were almost identical to those for the 300-psi (20.7-bar) airblast for a 1-MT weapon over the dense backfill problem.

→ There was a noticeable reduction in the frequencies at which the structures responded in the HONDO code calculations due to a decrease in stiffness of the soil backfill. A linear elastic single-degree-of-freedom system model based on the predominant natural mode of the embedded structure simulated the response of the structure to the three different airblast loadings only when a 20 to 40 percent of critical damping was applied. The damping is believed to be necessary to account for energy removed from the elastic structure because of radiation into the surrounding media and the hysteretic nature of this media.

Unclassified

SECURITY CLASSIFICATION OF THIS PAGE(When Data Entered)

## PREFACE

The investigation reported herein was sponsored by the Defense Nuclear Agency under Subtask SC062, Work Unit 01, "Influence of Back-fill on Structural Response."

The study was conducted by personnel of the Soils and Pavements Laboratory (S&PL), U. S. Army Engineer Waterways Experiment Station (WES), during the period October 1975 - December 1976 under the general supervision of Messrs. J. P. Sale and R. G. Ahlvin, Chief and Assistant Chief, respectively. Technical guidance was provided by Dr. P. F. Hadala under the direct supervision of Dr. J. G. Jackson, Jr., Chief of the Soil Dynamics Division (SDD), S&PL. Mr. J. O. Curtis (SDD) conducted the computer calculations and prepared Appendix A. Messrs. Fred Bourgeois, U. S. Army Engineer Division, Huntsville; R. A. Cole, Weapons Effects Laboratory (WEL), WES; and D. W. Walters, Automatic Data Processing Center, WES, assisted in various aspects of the computer work. Dr. J. E. Windham (SDD) performed the analyses and prepared the main text of this report.

Special acknowledgment is made to Drs. J. P. Balsara and S. A. Kiger, Structures Division, WEL, WES, for their technical review of this report.

COL J. L. Cannon, CE, was Director of WES during the investigation and preparation of this report. Mr. F. R. Brown was Technical Director.

ACCESSION for	
NTIS	Wife Section <input checked="" type="checkbox"/>
DDC	B.H. Section <input type="checkbox"/>
UNANNOUNCED	<input type="checkbox"/>
JUSTIFICATION	
BY	
DISTRIBUTION/AVAILABILITY CODES	
Dist.	SPECIAL
A	

# CONTENTS

	<u>Page</u>
PREFACE . . . . .	1
CHAPTER 1 INTRODUCTION . . . . .	13
1.1 Background . . . . .	13
1.2 Purpose and Scope . . . . .	15
CHAPTER 2 DESCRIPTION OF FIRST CALCULATION SERIES . . . . .	17
2.1 Overall Plan . . . . .	17
2.2 Finite Element Grid . . . . .	17
2.3 Hypothetical Structure . . . . .	18
2.4 Constitutive Properties . . . . .	19
2.5 Surface Overpressure . . . . .	20
2.6 Output Data . . . . .	21
2.7 Time Increment and Frequency Transmission . . . . .	21
CHAPTER 3 RESULTS FROM AND ANALYSIS OF THE FIRST SERIES OF COMPUTATIONS . . . . .	48
3.1 Stress and Displacement Patterns at Selected Times . . . . .	48
3.1.1 Deflection Across Backfill Sections . . . . .	48
3.1.2 Stresses on the Exterior Structure Surfaces and Deflections of the Neutral Axis . . . . .	50
3.1.3 Rotation of the Structure . . . . .	52
3.1.4 Thrusts, Shear, and Bending Moments Within the Structure . . . . .	53
3.2 Selected Time Histories . . . . .	55
3.3 Shock Spectra Analyses . . . . .	58
3.4 Summary . . . . .	59
CHAPTER 4 PRESENTATION AND ANALYSES OF RESULTS FOR 10-KT WEAPON YIELD, 1000-PSI OVERPRESSURE DENSE BACKFILL CALCULATION . . . . .	116
4.1 Calculation Description . . . . .	116
4.2 Stress and Displacement at Selected Times . . . . .	116
4.2.1 Deflections Across Backfill Sections . . . . .	116
4.2.2 Stresses on and Deflection of the Exterior Surfaces of the Structure . . . . .	117
4.2.3 Rotation of the Structure . . . . .	117
4.2.4 Thrusts, Shears, and Bending Moments Within the Structure . . . . .	118
4.3 Selected Time Histories . . . . .	119
4.4 Shock Spectra . . . . .	121
4.5 Summary . . . . .	121

	<u>Page</u>
CHAPTER 5 PSEUDOSTATIC CALCULATION . . . . .	137
5.1 Computational Plan . . . . .	137
5.2 Results . . . . .	137
CHAPTER 6 ANALYSIS . . . . .	147
6.1 Introduction . . . . .	147
6.2 Phenomena Responsible for Differences Caused by a Change in Backfill Properties . . . . .	147
6.2.1 Vertical Stress Attenuation . . . . .	148
6.2.2 Lateral at Rest Earth Pressures . . . . .	149
6.2.3 Lateral Passive Earth Pressures . . . . .	149
6.2.4 Stress Wave Reflections off the Concrete . . . . .	151
6.3 Effect of Soil Cover on Natural Frequencies . . . . .	152
6.4 Apparent Damping in Equivalent Single-Degree-of-Freedom System . . . . .	152
CHAPTER 7 SUMMARY, CONCLUSIONS, AND RECOMMENDATIONS . . . . .	168
7.1 Summary . . . . .	168
7.2 Conclusions . . . . .	168
7.3 Recommendations . . . . .	169
REFERENCES . . . . .	170
APPENDIX A IN VACUO AND EMBEDDED MODAL ANALYSES FOR A HYPOTHETICAL STRUCTURE IN PLANE STRAIN . . . . .	172
A.1 Objective and Scope . . . . .	172
A.2 In Vacuo Analyses . . . . .	172
A.3 Embedded Analyses . . . . .	174
A.4 Discussion of Results . . . . .	175
APPENDIX B COMPARISON OF CALCULATIONAL RESULTS WITH RIGID BODY MOTION ANALYSIS . . . . .	190
B.1 Single-Degree-of-Freedom Analyses . . . . .	190
B.2 Comparisons With 2D Calculation Results . . . . .	192

# LIST OF ILLUSTRATIONS

<u>Figure</u>		<u>Page</u>
2.1	Geometry of problem and FE grid representation . . . . .	25
2.2	UX stress-strain curve for free-field layer 1 produced by the constitutive model . . . . .	27
2.3	Failure envelope and UX stress path for free-field layer 1 produced by the constitutive model . . . . .	28
2.4	UX stress-strain curve for free-field layer 2 produced by the constitutive model . . . . .	29
2.5	Failure envelope and UX stress path for free-field layer 2 produced by the constitutive model . . . . .	30
2.6	UX stress-strain curve for free-field layer 3 produced by the constitutive model . . . . .	31
2.7	Failure envelope and UX stress path for free-field layer 3 produced by the constitutive model . . . . .	32
2.8	UX stress-strain curve for free-field layer 4 produced by the constitutive model . . . . .	33
2.9	Failure envelope and UX stress path for free-field layer 4 produced by the constitutive model . . . . .	34
2.10	UX stress-strain curve for loose backfill produced by the constitutive model . . . . .	35
2.11	Failure envelope and UX stress path for loose backfill produced by the constitutive model . . . . .	36
2.12	UX stress-strain curve for dense backfill produced by the constitutive model . . . . .	37
2.13	Failure envelope and UX stress path for dense backfill produced by the constitutive model . . . . .	38
2.14	Comparison of UX stress-strain curves for loose and dense backfills produced by the constitutive model . . . . .	39
2.15	Comparison of surface overpressure time histories for 1-MT and 10-KT weapons producing 300-psi (20.7-bar) surface overpressure over the center of the structure . . . . .	40
2.16	Surface overpressure time history over the left boundary of problem for 1-MT and 10-KT weapons. . . . .	41
2.17	Surface overpressure time history over the centerline of the structure for 1-MT and 10-KT weapons . . . . .	42
2.18	Surface overpressure time history over the right boundary of problem for 1-MT and 10-KT weapons . . . . .	43
2.19	Detailed layout of the FE grid in the vicinity of the structure showing time history output locations . . . . .	45
2.20	Structure sections for which shear, moment, and thrust will be calculated . . . . .	47

	<u>Page</u>
3.1 Instantaneous pattern of vertical displacements along two lines through the backfill at 60 ms after the start of the problem, 1 MT loading. . . . .	70
3.2 Instantaneous pattern of vertical displacements along two lines through the backfill at 100 ms after the start of the 1-MT loading problem . . . . .	71
3.3 Instantaneous pattern of vertical displacements along two lines through the backfill at 60 ms after the start of the 10-KT loading problem. . . . .	72
3.4 Instantaneous pattern of vertical displacements along two lines through the backfill at 100 ms after the start of the 10-KT loading problem. . . . .	73
3.5 Comparison of deflected shape of and stresses normal to the structure at 40 ms after the beginning of the problem . . . . .	74
3.6 Comparison of deflected shape of and stresses normal to the structure at the times that the maximum relative deflection of the center of the roof occurs . . . . .	75
3.7 Comparison of deflected shape of and stresses normal to the structure at 80 ms after the beginning of the problem . . . . .	76
3.8 Comparison of deflected shape of and stresses normal to the structure at 100 ms after the beginning of the problem . . . . .	77
3.9 Comparison of deflected shape of and stresses normal to the structure at 150 ms after the beginning of the problem . . . . .	78
3.10 Comparison of the deflected shape of and stresses normal to structure at 200 ms after the beginning of the problem. . . . .	79
3.11 Comparison of moment and shear diagrams for selected roof sections at the time that the radial stress in element 514 (Figure 2.20) maximizes . . . . .	80
3.12 Comparison of moment and shear diagrams for floor sections at the time that the radial stress in element 515 (Figure 2.20) maximizes . . . . .	81
3.13 Comparison of maximum moment and shear diagrams for selected sidewall sections at the time that the vertical stress in elements 369 and 679 maximize in the blastward and leeward sidewalls, respectively . . . . .	82
3.14 Moment-thrust interaction diagram for a rectangular beam-column and data for selected roof and floor sections . . . . .	83

	<u>Page</u>
3.15 Moment-thrust interaction diagram for a rectangular beam-column and data for selected sidewall sections . . . . .	84
3.16 Vertical displacement time histories for the center of the structure roof . . . . .	85
3.17 Vertical velocity time histories for the center of the structure roof . . . . .	86
3.18 Horizontal stress time histories for a point in the roof three-quarters of the way from the neutral axis to the top fiber (element 511) . . . . .	87
3.19 Horizontal stress time history for a point in the roof three-quarters of the way from the neutral axis to the bottom fiber (element 514) . . . . .	88
3.20 Vertical velocity time histories for a point (node 268) on the blastward sidewall . . . . .	89
3.21 Horizontal velocity time histories for a point (node 268) on the blastward sidewall . . . . .	90
3.22 Vertical displacement time histories for a point at the midheight of the blastward sidewall . . . . .	91
3.23 Horizontal displacement time histories for a point at midheight of the blastward sidewall . . . . .	92
3.24 Comparison of the vertical deflection for a point on the structure at a depth of 5 feet (1.52 m) below the ground surface with that for a point in the adjacent backfill for the 1-MT weapon-yield cases . . . . .	93
3.25 Comparison of the vertical deflection for a point on the structure at a depth of 5 feet (1.52 m) below the ground surface with that for a point in the adjacent backfill for the 10-KT weapon-yield cases . . . . .	94
3.26 Comparison of the vertical deflection for a point on the structure at a depth of 15 feet (4.57 m) below the ground surface with that for a point in the adjacent backfill for the 1-MT weapon-yield cases . . . . .	95

	<u>Page</u>
3.27 Comparison of the vertical deflection for a point on the structure at a depth of 15 feet (4.57 m) below the ground surface with that for a point in the adjacent backfill for the 10-KT weapon-yield cases . . . . .	96
3.28 Comparison of the vertical deflection for a point on the structure at a depth of 30 feet (9.14 m) below the ground surface with that for a point in the adjacent backfill for the 1-MT weapon-yield cases . . . . .	97
3.29 Comparison of the vertical deflection for a point on the structure at a depth of 30 feet (9.14 cm) below the ground surface with that for a point in the adjacent backfill for the 10-KT weapon-yield cases. . . . .	98
3.30 Comparison of horizontal stress time histories at a point in the adjacent backfill near the top of the blastward sidewall of the structure. . . . .	99
3.31 Comparison of horizontal stress time histories at a point in the adjacent backfill near the midheight of the blastward sidewall of the structure . . . . .	100
3.32 Horizontal stress time histories for element 323 . . . . .	101
3.33 Horizontal stress time histories for element 342 . . . . .	102
3.34 Shear stress time histories for element 323 . . . . .	103
3.35 Shear stress time histories for element 342 . . . . .	104
3.36 Vertical stress time histories for el 299 at the midheight of the blastward sidewall. . . . .	105
3.37 Vertical stress time histories for element 369 at the midheight of the blastward sidewall. . . . .	106
3.38 Vertical stress time histories for element 679 at the midheight of the leeward sidewall. . . . .	107
3.39 Horizontal stress time histories for element 515 at the center of the floor. . . . .	108
3.40 Horizontal velocity time histories for a point (node 666) at the midheight of the leeward sidewall . . . . .	109
3.41 Horizontal velocity time histories for a point (node 361) at the midheight of the blastward sidewall . . . . .	110
3.42 Vertical velocity time histories for the centerline of the structure floor . . . . .	111
3.43 Horizontal shock spectra for a point (node 361) on the inside of the blastward sidewall of the structure . . . . .	112

	<u>Page</u>
3.44 Vertical shock spectra for a point (node 513) on the inside of the structure roof . . . . .	113
3.45 Horizontal shock spectra for a point (node 666) on the inside of the leeward sidewall of the structure . . . . .	114
3.46 Vertical shock spectra for a point (node 514) on the structure floor . . . . .	115
4.1 Surface overpressure time histories for 10-KT surface burst producing 1000 psi (68.9 bars) over the center of the structure . . . . .	125
4.2 Instantaneous pattern of vertical displacements along two lines through the backfill at 40 and 100 ms after the start of the 10-KT, 1000-psi (68.9-bar) problem . . . . .	126
4.3 Instantaneous patterns of deflection of and distribution of normal stresses on the ex- terior surfaces of the structure at 40, 70, 150, and 200 ms . . . . .	127
4.4 Moment and shear diagrams for the structure roof and floor at 40 ms (the time that the radial stress at the center of the roof and floor maximized). . . . .	128
4.5 Moment and shear diagrams for the structure sidewalls at 40 ms (the time that the verti- cal stress at the center of the sidewalls maximized) . . . . .	129
4.6 Vertical displacement time histories for points at the center of the structure roof and floor . . . . .	130
4.7 Vertical velocity time histories for points at the center of the structure roof and floor . . . . .	131
4.8 Horizontal displacement time histories for points at the midheight and on the inside of the structure sidewalls . . . . .	132
4.9 Horizontal velocity time histories for points at the midheight and on the inside of the structure sidewalls . . . . .	133
4.10 Horizontal stress time histories for elements 514 and 515 at the center of the structure roof and floor, respectively . . . . .	134
4.11 Vertical stress time histories for points at the midheight and on the inside of the structure sidewalls . . . . .	135
4.12 Shock spectra for points on the inside of the structure floor, roof, and sidewalls (10-KT/ 1000-psi (68.9 bars)/dense backfill calcula- tions). . . . .	136

	<u>Page</u>
5.1 Vertical velocity time histories for a point at the center of the roof from the pseudostatic calculation . . . . .	141
5.2 Vertical displacement of time histories for a point at the center of the roof from the pseudostatic calculation . . . . .	142
5.3 Horizontal stress time histories for element 511 from the pseudostatic calculation . . . . .	143
5.4 Normal stress and deformation pattern for three applied stress levels from the pseudostatic calculation . . . . .	144
5.5 Moment and shear diagrams for the structure roof and floor at 360 ms from the pseudostatic calculation . . . . .	145
5.6 Moment and shear diagrams for the structure sidewalls at 360 ms from the pseudostatic calculation . . . . .	146
6.1 Maximum vertical stress versus depth for a station 3.5 m upstream of the structure, 1-MT case . . . . .	160
6.2 Stress attenuation in linear hysteretic media similar to loose and dense backfills for 20-bar airblast loadings . . . . .	160
6.3 Horizontal stress time histories from 1-MT calculations for points adjacent to the blastward sidewall . . . . .	161
6.4 Horizontal stress time histories from 10-KT calculations for points adjacent to the blastward sidewall . . . . .	162
6.5 Comparison of shear strength envelopes for loose and dense backfills . . . . .	163
6.6 Stress on the roof versus time . . . . .	164
6.7 Side sway and roof-floor bending modes . . . . .	165
6.8 Comparison of roof deflections . . . . .	166
6.9 Relative roof deflection versus time for 300-psi (20-bar)/1-MT/dense backfill calculation . . . . .	167
A.1 Idealized structure and springs added to approximate in vacuo condition . . . . .	181
A.2 Finite element descriptions of structure used for in vacuo and embedded eigenvalue calculations . . . . .	182
A.3 Frequencies and associated mode shapes from the in vacuo eigenvalue analysis for the four-element-thickness structural approximation using constant strain elements . . . . .	183

	<u>Page</u>
A.4 FE grid representations for HONDO structure/backfill interaction calculations and SAP IV embedded modal analyses . . . . .	185
A.5 Frequencies and associated mode shapes of structure from the embedded eigen- value calculation using lower bound properties . . . . .	187
A.6 First 12 natural frequencies and as- sociated mode shapes for the embedded structure and surrounding soil determined from the embedded eigenvalue calculation using lower bound properties . . . . .	188
A.7 Frequencies and associated mode shapes of structure from the embedded eigenvalue calculation using upper bound properties. . . . .	189
B.1 Dimensions and configuration of buried rectangular structure for SDF analyses. . . . .	194
B.2 Vertical free-field stress time history at the structure roof and floor level . . . . .	195
B.3 Resultant vertical free-field stress time history on structure . . . . .	196
B.4 Comparison of the free-field vertical stress at the roof level from 1D and 2D calculations . . . . .	197
B.5 Comparison of the free-field vertical stress at the floor level from 1D and 2D calculations. . . . .	198
B.6 Comparison of the structure velocity time histories from 1D analyses with those for the bottom corners of the structure from 2D calculations . . . . .	199
B.7 Comparison of the structure displacement time histories from the 1D analyses with those for the bottom corners of the structure from 2D calculations . . . . .	200

#### LIST OF TABLES

##### Table

2.1 Material Constants for Cap Model Fits for Free-Field and Backfill Materials (Fig- ure 2.1) . . . . .	23
3.1 Maximum and Final Rotations of the Chord Formed by the Two Bottom Corners of the Structure; 300-psi Nominal Overpressure, Dynamic 1-MT and 10-KT Calculations . . . . .	60

	<u>Page</u>
3.2 Shear, Thrust, and Bending Moment for Selected Sections Through the Structure at a Time of 62.5 ms after the start of the 1-MT Dense Backfill Calculation . . . . .	61
3.3 Shear, Thrust, and Bending Moment for Selected Sections Through the Structure at A time of 67.5 ms after the start of the 1-MT Dense Backfill Calculation . . . . .	62
3.4 Shear, Thrust, and Bending Moment for Selected Sections Through the Structure at a Time of 65 ms after the start of the 1-MT Loose Backfill Calculation . . . . .	63
3.5 Shear, Thrust, and Bending Moment for Selected Sections Through the Structure at a Time of 70 ms after the start of the 1-MT Loose Backfill Calculation . . . . .	64
3.6 Shear, Thrust, and Bending Moment for Selected Sections Through the Structure at a Time of 55 ms after the start of the 10-KT Dense Backfill Calculation . . . . .	65
3.7 Shear, Thrust, and Bending Moment for Selected Sections Through the Structure at a Time of 60 ms after the start of the 10-KT Dense Backfill Calculation . . . . .	66
3.8 Shear, Thrust, and Bending Moment for Selected Sections Through the Structure at a Time of 60 ms after the start of the 10-KT Loose Backfill Calculation . . . . .	67
3.9 Shear, Thrust, and Bending Moment for Selected Sections Through the Structure at a Time of 62.5 ms after the start of the 10-KT Loose Backfill Calculation . . . . .	68
3.10 Shear, Thrust, and Bending Moment for Selected Sections Through the Structure at a Time of 67.5 ms after the start of the 10-KT Loose Backfill Calculation . . . . .	69
4.1 Rotations of the Chord Formed by the Two Bottom Corners of the Structure; 10-KT Yield, 1000-psi Nominal Overpressure, Dense Backfill Calculation. . . . .	123
4.2 Shear, Thrust, and Bending Moment for Selected Sections Through the Structure at a Time of 40 ms after the start of the 10-KT dense Backfill Calculation . . . . .	124
5.1 Shear, Thrust, and Bending Moment for Selected Sections Through the Structure at a Time of 360 ms after the start of the 10-KT "Pseudo" Static Dense Backfill Calculation . . . . .	140

	<u>Page</u>
6.1 Modulus and Wave Speed Data for Backfill	
Materials and Concrete . . . . .	157
6.2 Stress Arrival Times at Element 278 Calculated	
from Material Wave Speeds, Assuming a Path	
Through the Structure . . . . .	158
6.3 Comparison of DLF from 2D Calculations with	
Those for Damped SDF Systems . . . . .	159
A.1 Calculated Natural Frequencies from In Vacuo	
Analyses with Higher Order Element Description. . . . .	177
A.2 Calculated Natural Frequencies from In Vacuo	
Analyses with Constant Strain Element Description . . . . .	178
A.3 Elastic Properties of Materials Used in	
Embedded Analyses . . . . .	179
A.4 Calculated Natural Frequencies for Embedded	
Analyses . . . . .	180

# EFFECT OF BACKFILL PROPERTY AND AIRBLAST VARIATIONS ON THE EXTERNAL LOADS DELIVERED TO BURIED BOX STRUCTURES

## CHAPTER 1

### INTRODUCTION

#### 1.1 BACKGROUND

Large amounts of backfill must be placed around and over buried hardened facilities for hardening against nuclear airblast and ground shock environments. The condition of the backfill around present facilities ranges from very well compacted to poorly compacted backfill. Reference 1 presents the results of a series of two-dimensional (2D), dynamic finite element (FE), structure-medium interaction (SMI) code calculations, which were conducted to parametrically investigate the effect of variations in constitutive properties of the backfill region around a hypothetical plane-strain idealization of a simple, shallow-buried, box-type protective structure. In this reference, the differences in the dynamic response of the structure due to a long-duration, 50-psi (3.45-bar) surface airblast loading\* caused by changing the surrounding backfill from a dense (or well-compacted) glacial till to the same material in a loose (or poorly compacted) condition were examined. A second study, identical with the first except that dense and loose clay shale materials were simulated, is also reported.

The calculations performed in Reference 1 indicated that for the particular idealized problem investigated, the use of loose backfill rather than dense backfill results in (1) increased vertical deflections in the backfill, (2) increased loads on, deflections of, and thrusts, shears, and bending moments within the structure, and (3) increased amplitudes of the shock spectra for points on the inside surface of the structure.

Because of the long airblast positive-phase duration, negligible

---

\* Due to a 1-MT surface burst.

stress attenuation occurred in the loose backfill calculation in spite of the high hysteresis of that material. This should not be the case for short-duration airblast loadings.

Under the present study, Defense Nuclear Agency (DNA) Subtask SC062, Work Unit 01, "Influence of Backfill on Structural Response," five 2D dynamic and one 2D static FE, SMI code calculations were performed with the HONDO<sup>2,3</sup> code to determine the effect of soil backfill property variations and surface airblast loading options on the transient ground shock environments experienced by a hypothetical protective structure at much higher overpressure levels than those studied in Reference 1. The results are primarily intended to (1) determine the effect of soil property variations and surface loading options on the transient ground shock environments experienced by a hypothetical shallow-buried structure, and (2) provide a tangible example to structure analysts of the type of structure/backfill interaction information that can be obtained for their use in vulnerability assessments.

Prior to performing these calculations, a series of in vacuo modal analyses was conducted with the SAP IV elastic FE code<sup>4</sup> to (1) determine the effects of using basic isoparametric quadrilateral elements (i.e., the type employed by the HONDO code), instead of high order elements, on calculated natural frequencies, and (2) aid in determining the minimum number of elements needed across structural sections in order to adequately model the response of the structure. Embedded modal analyses were also performed to (1) determine the effect of material property variations on the natural frequencies of the buried structure, and (2) assist in planning the follow-on structure/backfill interaction calculations. The results of the modal analyses were previously submitted in a letter report to DNA\* and are included herein as Appendix A.

---

\* J. O. Curtis and J. E. Windham, "In Vacuo and Embedded Modal Analyses for Hypothetical Structure in Plane Strain," SC062/01 informal report to HQ DNA, April 1976, U. S. Army Engineer Waterways Experiment Station, CE, Vicksburg, Mississippi.

A first series of HONDO code calculations consisting of four large 2D, SMI calculations were performed on a CDC 7600 computer. These calculations involve two surface loadings (e.g., nominal 300-psi (20.7-bar) overpressure pulses for 1-MT and 10-KT weapons) over two backfill conditions (i.e. loose and dense shale backfill cases<sup>1</sup>). A detailed plan of study for this first series of calculations has previously been submitted.\* A fifth dynamic calculation, essentially identical to the other dense shale backfill calculations except for the surface blast loading that was a nominal 1000-psi (68.9-bar) overpressure pulse from a 10-KT detonation, was also conducted. Finally, a calculation was conducted with the HONDO code in which the structure surrounded by dense backfill was slowly loaded with a monotonically increasing load from 0 to 300 psi (20.7 bars). The stress rate was applied slow enough so that the results at any stress level would closely approximate that of a static solution. In order to maximize correlation with previous results, the site profile, excavation, and structure configurations were identical to those in Reference 1.

## 1.2 PURPOSE AND SCOPE

The purposes of this code calculation study are to (1) determine the effect of selected soil backfill property variations and surface loading options on the high overpressure, airblast-induced ground shock environments experienced by a hypothetical shallow-buried structure, and (2) provide a tangible example to structural analysts of the type of backfill-structure interaction information that can be obtained for use in buried structure vulnerability assessments. This report (1) outlines the plan of analyses, (2) describes the FE code calculations, (3) presents their results, (4) reports comparative analyses of the effects of the independent variables, and (5) discusses the implications of these results. The analyses are essentially limited to the results of the six HONDO code

---

\* J. E. Windham, "Plan of Study for First Series of Structure/Backfill Interaction Calculations," WES informal report on DNA Subtask SC062, Work Unit 01, April 1976.

calculations that are the key elements of this study.

A supplementary study is reported in Appendix B. A simple method for producing the rigid body motion of a buried box structure is presented in Reference 5. This method is applied to the 1-MT, 300-psi (20.7-bar) dense backfill case. The calculated vertical motion of the structure was found to be in good agreement with the HONDO code calculated structure motion time histories.

## CHAPTER 2

### DESCRIPTION OF FIRST CALCULATION SERIES

#### 2.1 OVERALL PLAN

The objective of the first series of calculations was a parametric study to determine the effects of both (1) soil backfill property variations (due to either diverse construction conditions or data uncertainties), and (2) surface airblast loading options (due to selection of different weapon yields) on the transient ground shock environments experienced by a hypothetical protective structure located at a given overpressure contour. In order to maximize correlation with previous results, the site/excavation/structure configuration is identical with that reported in Reference 1. A total of four large calculations were performed on a CDC 7600 computer with the HONDO<sup>2,3</sup> dynamic FE code; these calculations involve two surface loadings (e.g., nominal 300-psi (20.7-bar) overpressure pulse for 1-MT and 10-KT weapons) over each of two different backfills (loose and dense shale).

Figure 2.1 illustrates the geometry of the plane-strain problem investigated. The free-field medium is postulated as a four-layered soil profile consisting of clayey sand over clay shale (Material No. 1 through 4). The structure is assumed to be constructed of reinforced concrete (Material No. 5), which is idealized as a linear elastic material. It is laterally supported and covered by a compacted soil backfill (Material No. 6), whose constitutive properties are independent variables in this study.

#### 2.2 FINITE ELEMENT GRID

The FE grid that was employed is shown in Figure 2.1 and consisted of 1048 constant strain rectangular and triangular elements. The elements located in the structure are 1.0 foot (0.30 metre) by 1.25 feet (0.38 metre), 1.0 foot (0.30 metre) by 2.5 feet (0.76 metre), and 1.25 feet (0.38 metre) by 2.0 feet (0.61 metre); each structural member

has four elements across its section. In the backfill, the elements range from 1.25 feet (0.38 metre) by 2.5 feet (0.76 metre) to 2.5 feet (0.76 metre) by 10 feet (3.05 metres). In the stiffer and deeper earth materials, the elements are larger. The largest elements are in the corners of the grid and are 20 feet (6.10 metres) by 20 feet (6.10 metres). The grid was chosen as a compromise between (1) the desire for fine resolution, and (2) the need to keep computer memory and running time (and, hence, cost) requirements within reason.

### 2.3 HYPOTHETICAL STRUCTURE

The idealized structure is covered by 5 feet (1.52 metres) of backfill and is supported on undisturbed shale at a depth of 30 feet (9.14 metres); the structure has outside dimensions of 40 feet (12.19 metres) and 25 feet (7.62 metres). Its roof and floor are 5 feet (1.52 metres) thick. Its sidewalls are 4 feet (1.22 metres) thick. The exterior structure elements are treated as being fully bonded to those of the backfill and underlying shale, as no slip element capability existed in the U. S. Army Engineer Waterways Experiment Station (WES) version of the HONDO code when these calculations were performed.\* The structure is treated as a linear elastic material with a bulk modulus  $K$  of 1330 ksi (91,700 bars) and a shear modulus  $G$  of 800 ksi (55,200 bars). The structure is assumed to have a mass density of 145 pcf ( $2.32 \text{ g/cm}^3$ ). Whether or not a real reinforced concrete structure of the dimension adopted would remain operational in the overpressure environments used in this study is doubtful. However, since (1) the purpose of the planned calculations was to show only the relative effect of weapon yield on the loads transmitted to a hypothetical structure for a wide range of backfill materials, and (2) it was desirable for comparison purposes to use the same structure as that used in previous calculations,<sup>1</sup> the decision was made to use the section thicknesses indicated in Figure 2.1.

---

\* A slip debonding line capability has recently been added to the code.

## 2.4 CONSTITUTIVE PROPERTIES

All of the earth materials were represented in the calculations by nonlinear hysteretic soil cap models of the type used by the Site Defense Ground Motion Working Group (SDGMWG).<sup>6</sup> However, for the SDGMWG analyses, uniaxial strain (UX) relations were only modeled to a vertical stress  $\sigma_z$  of 1000 psi (68.9 bars). For the current study, it was necessary to extend the cap model fits to a  $\sigma_z$  in UX of 5000 psi (344.7 bars). The extended constitutive model fits for the in situ or free-field materials (Material Nos. 1 through 4) are shown in Figures 2.2 through 2.9; values of the fitting constants that were actually used as calculational input are presented in Table 2.1.

The backfill material properties chosen for this study were the same as those previously used to represent a crushed shale backfill placed in very loose and very dense conditions. The cap model fits for the loose and dense backfill materials, which are extended from 160 psi (11.0 bars) to 5000 psi (344.7 bars) for the current study, are shown in Figures 2.10 through 2.13; values of the fitting constants are also listed in Table 2.1. The UX  $\sigma_z$  versus vertical strain  $\epsilon_z$  relations for the loose and dense backfills are compared in Figure 2.14. The initial constrained modulus  $M_i$  for the loose backfill material is 1500 psi (103.4 bars) and for the dense material is 6000 psi (413.7 bars). The secant moduli to 300 psi (20.7 bars) for the loose and dense backfill materials are 2500 psi (172.4 bars) and 7500 psi (517.2 bars), respectively.

A review of UX data from tests conducted on backfill materials from 19 sites (including MINUTEMAN, HEST, and high-explosive test event sites) showed that the average secant loading modulus to 300 psi (20.7 bars) ranged from 5000 psi (344.7 bars) to 13,900 psi (958.6 bars). Backfill density control specifications were in effect at all of these sites. Thus, the dense shale properties proposed for use in this study are clearly within the range produced by good construction practice. However, it is also clear that the dense backfill should be considered as "typical" rather than as an upper bound to the backfill stiffness that can be obtained. The

loose shale properties are considered to be typical of poor construction practice or expedient construction.

## 2.5 SURFACE OVERPRESSURE

Two traveling surface airblast overpressure functions were used in the calculations. The loading portions for both are defined by a linear rise to peak pressure in a constant time of 10 ms; the decay portions are fits to Brode's<sup>7</sup> equations for 10-KT and 1-MT weapons detonated at a zero height of burst and at a distance from the structure that will cause a 300-psi (20.7-bar) surface overpressure over the centerline of the structure. The variations of the pressure time histories for both cases as the airblast traverses the 240-foot (73.2-metre) distance from the left to the right boundary of the problem are shown in Figure 2.15. The pressure time histories over the left boundary, the structure centerline, and right boundary for the two weapon yields are plotted at larger scales for comparison purposes in Figures 2.16, 2.17, and 2.18, respectively. Artificial 10-ms rise times appended to the Brode overpressure pulses increase the impulse at the 300-psi (20.7-bar) level by 2.8 percent for the 1-MT case and 12.9 percent for the 10-KT case; at higher overpressure levels, the added percentage is even larger. Based on criteria developed for the limiting frequencies that can be propagated in 1D elastic wave propagation problems,<sup>8</sup> even longer rise times should be employed if the lowest moduli for the backfill materials are used to calculate the elastic wave speeds and the FE grid remains as defined in Figure 2.1. However, appending a longer rise time to the airblast functions would unrealistically distort the impulse. The desired frequency resolution could be fully satisfied by increasing the number of elements used to zone the problem; but this would be cost-prohibitive. Thus, a 10-ms rise time is a compromise value, which may be artificially increased by the FE grid after the stress wave has propagated a short distance into the backfill media.

The duration of each of the calculations was 200 ms. At 200 ms, the

surface overpressures for the 10-KT and 1-MT loadings were approximately 5 psi (0.34 bars) and 65 psi (4.48 bars), respectively. Reflections from the bottom and right boundaries reached the structure at a time of approximately 100 ms. After that time, there was some influence of the boundary on structure/backfill interaction, but the influence should be nearly the same in all four problems since the first reflected signals travel primarily through the nonvaried free-field materials.

## 2.6 OUTPUT DATA

The output data from the calculations consisted of (1) time histories of stress and motion at selected locations in the structure and in the earth media, (2) plots of the normal stress on the exterior surfaces of the structure, (3) plots of deflected shape of the structure's neutral axis, and (4) tabulated bending moment, axial thrust, and shear at selected structure cross sections for selected times. The locations for which time histories of motion and stress were saved are shown in Figure 2.19. Approximately 260 motion and 200 stress time histories were involved for each calculation. Forty-seven plots (or snapshots) of normal stress on the external surface of the structure and of the deflected shape of the structure, and the tables of bending moment, axial thrust, and shear were made at 2.5-ms time increments between 10 and 100 ms and at 10-ms increments between 100 and 200 ms. The 28 structural sections for which bending moments, axial thrusts, and shear were tabulated are indicated in Figure 2.20.

## 2.7 TIME INCREMENT AND FREQUENCY TRANSMISSION

Each calculation was run for 2000 time steps of 0.1 ms each. This time step was chosen to satisfy the Courant criteria\* and was controlled

---


$$* \quad \Delta t \leq \frac{\Delta x_{\min}}{C_{p_{\max}}} \leq \frac{1.0 \text{ ft}}{8.76 \text{ ft/ms}} \leq 0.114 \text{ ms}$$

where  $\Delta t$  = time increment;  $\Delta x_{\min}$  = minimum element size;  $C_{p_{\max}}$  = maximum P-wave velocity.

by the minimum FE dimension and P-wave velocity within the elastic structure. The lowest frequencies that can be fully transmitted are given by the reciprocal of the calculation pulse duration, i.e., 1/200 ms or 5 Hz. The lowest modal frequency determined from an embedded modal analysis (see Appendix A) using lower bound moduli for all materials was 4.315 Hz, while a similar analysis using upper bound moduli gave a first-mode frequency of 11.99 Hz. Thus, the duration of the calculations were long enough to permit peak displacement responses in the lowest mode of the system. The highest frequencies that can be fully transmitted cannot exceed the reciprocal of the loading rise time, i.e., 1/10 ms or 100 Hz. As a practical matter, however, credible frequencies probably did not exceed one-half of this value or 50 Hz.

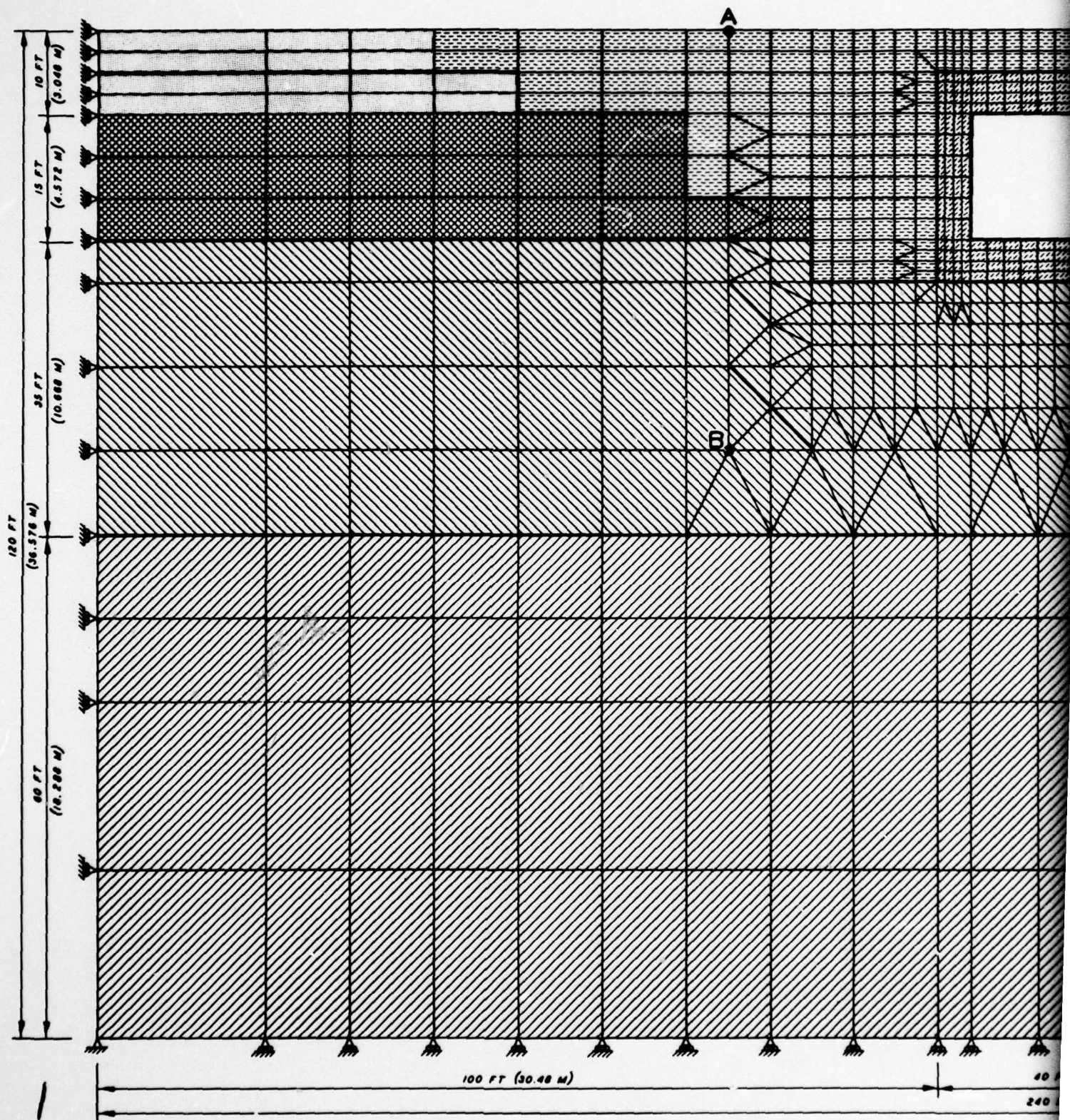
The FE grid for the backfill material immediately surrounding the structure can transmit frequencies through the dense backfill up to 68 Hz based on the formula

$$f_{\max} = \frac{C_{p_{\min}}}{\pi \Delta x_{\max}} \quad (2.1)$$

By similar calculation, however, the loose backfill can only transmit frequencies up to 24 Hz. Thus, the cutoff frequencies were assumed to be on the order of 50 Hz for the two dense backfill calculations and 25 Hz for the two loose backfill calculations. The embedded modal analyses presented in Appendix A using upper bound moduli gave a 20th-mode frequency of 49.11 Hz; the calculated frequency for the 25th mode based on lower bound moduli was only 14.35 Hz. Thus, the calculations were judged to have a sufficient range of frequency response to permit an adequate assessment of the stress and motion patterns that would occur within the hypothetical structure/backfill system under the postulated airblast environments.

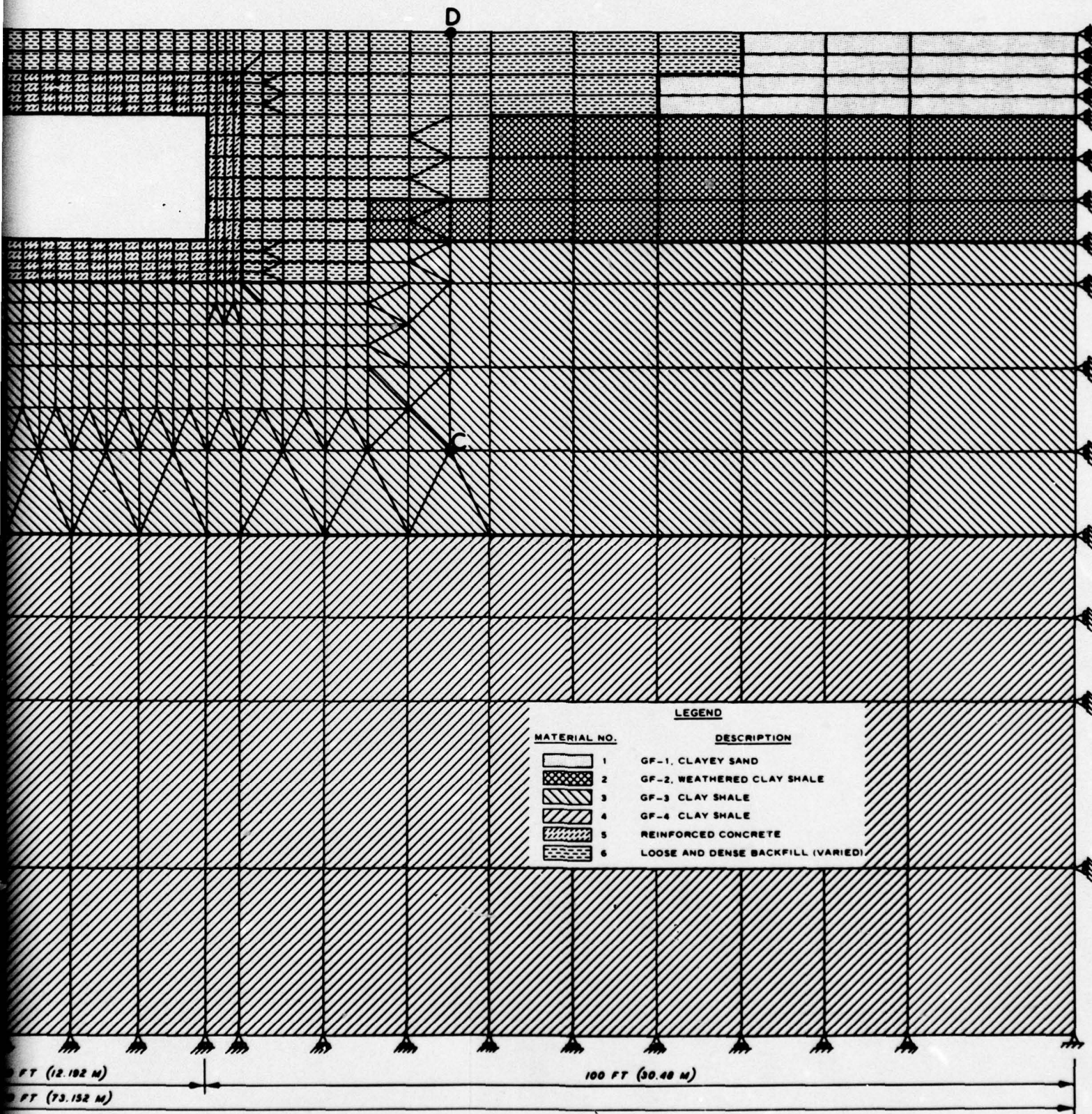
Table 2.1 Material Constants for Cap Model Fits for Free-Field and Backfill Materials (Figure 2.1).

Term	Units	1	2	3	4	Dense Backfill (6)	Loose Backfill (6)
AA	$N/M^2$	$2.316523033 \times 10^6$	$2.587473494 \times 10^6$	$3.02526877 \times 10^6$	$3.741598363 \times 10^6$	$3.582337404 \times 10^6$	$2.388224936 \times 10^6$
AB	$(N/M^2)^{-1}$	$7.7352 \times 10^{-8}$	$1.2909 \times 10^{-7}$	$1.3779 \times 10^{-7}$	$2.1757 \times 10^{-7}$	$1.3054 \times 10^{-7}$	$1.0878 \times 10^{-7}$
AC	$N/M^2$	$2.188476377 \times 10^6$	$2.309628619 \times 10^6$	$2.3509950101 \times 10^6$	$2.129684419 \times 10^6$	$3.383088846 \times 10^6$	$2.308249736 \times 10^6$
AR		0.55	0.9	0.9	0.85	2.8	1.0
ARI		5.0	3.0	3.0	3.0	0.786	2.0
ARR	$(N/M^2)^{-1}$	$5.0766 \times 10^{-7}$	$4.3513 \times 10^{-7}$	$2.8284 \times 10^{-7}$	$7.2522 \times 10^{-9}$	$7.2522 \times 10^{-7}$	$1.4504 \times 10^{-7}$
AW		0.061	0.0159	0.00275	0.00162	0.133	0.267
AD	$(N/M^2)^{-1}$	$8.9928 \times 10^{-8}$	$1.8856 \times 10^{-7}$	$3.459 \times 10^{-7}$	$2.0306 \times 10^{-7}$	$5.0766 \times 10^{-8}$	$5.8018 \times 10^{-8}$
AAD		0.836	0.9	0.7	0.8	1.0	-1.8
AD1	$(N/M^2)^{-1}$	$1.23113 \times 10^{-7}$	$2.0306 \times 10^{-7}$	$3.0604 \times 10^{-7}$	$26108 \times 10^{-7}$	$1.4504 \times 10^{-1}$	$2.1757 \times 10^{-7}$
AD2	$(N/M^2)^{-2}$	$2.1038 \times 10^{-12}$	$7.3633 \times 10^{-13}$	$1.0519 \times 10^{-12}$	$1.0098 \times 10^{-13}$	0.0	0.0
AWF	$(N/M^2)^{-2}$	$7.9945 \times 10^{-15}$	$8.4152 \times 10^{-16}$	$2.4825 \times 10^{-16}$	0.0	$-1.0519 \times 10^{-16}$	$1.0519 \times 10^{-15}$
ADF	$(N/M^2)^{-1}$	$9.4279 \times 10^{-7}$	$5.2491 \times 10^{-7}$	$6.0919 \times 10^{-7}$	0.0	$1.1604 \times 10^{-7}$	$1.4504 \times 10^{-7}$
ADMAX	$N/M^2$	$5.438313596 \times 10^8$	$3.491927583 \times 10^9$	$4.826089652 \times 10^9$	$5.618947237 \times 10^9$	$1.809783619 \times 10^9$	$9.483235166 \times 10^8$
AK1		0.781	0.1	0.154	0.122	0.9571	0.924
AK2	$(N/M^2)^{-1}$	$1.4509 \times 10^{-9}$	$1.4504 \times 10^{-10}$	$3.6261 \times 10^{-9}$	$3.6261 \times 10^{-9}$	$3.6261 \times 10^{-8}$	$4.3513 \times 10^{-8}$
AK3	$(N/M^2)^{-2}$	$2.7349 \times 10^{-14}$	$2.1038 \times 10^{-15}$	$3.1557 \times 10^{-14}$	$3.1557 \times 10^{-14}$	0.0	0.0
AK4	$(N/M^2)$	$1.792547585 \times 10^9$	0.0	$3.447206894 \times 10^9$	$1.034162068 \times 10^{10}$	$1.551243102 \times 10^9$	$2.068324136 \times 10^9$
AK5	$(N/M^2)^{-2}$	$1.6830 \times 10^{-16}$	0.0	$1.2623 \times 10^{-15}$	$1.9986 \times 10^{-15}$	$2.1038 \times 10^{-16}$	$7.3633 \times 10^{-16}$
ACMAX	$N/M^2$	$5.143232686 \times 10^8$	$3.447206894 \times 10^9$	$3.791927543 \times 10^9$	$5.515531031 \times 10^9$	$7.756215512 \times 10^8$	$5.72236344 \times 10^8$
AGR		0.9	0.4	0.194	0.335	0.8933	0.6
AG1	$(N/M^2)^{-1}$	$5.8018 \times 10^{-7}$	$1.3054 \times 10^{-6}$	$2.1757 \times 10^{-6}$	$2.1757 \times 10^{-6}$	$4.3513 \times 10^{-7}$	$3.6261 \times 10^{-7}$



PRECEDING PAGE BLANK

Figure 2.1 Geome



metry of problem and FE grid representation.

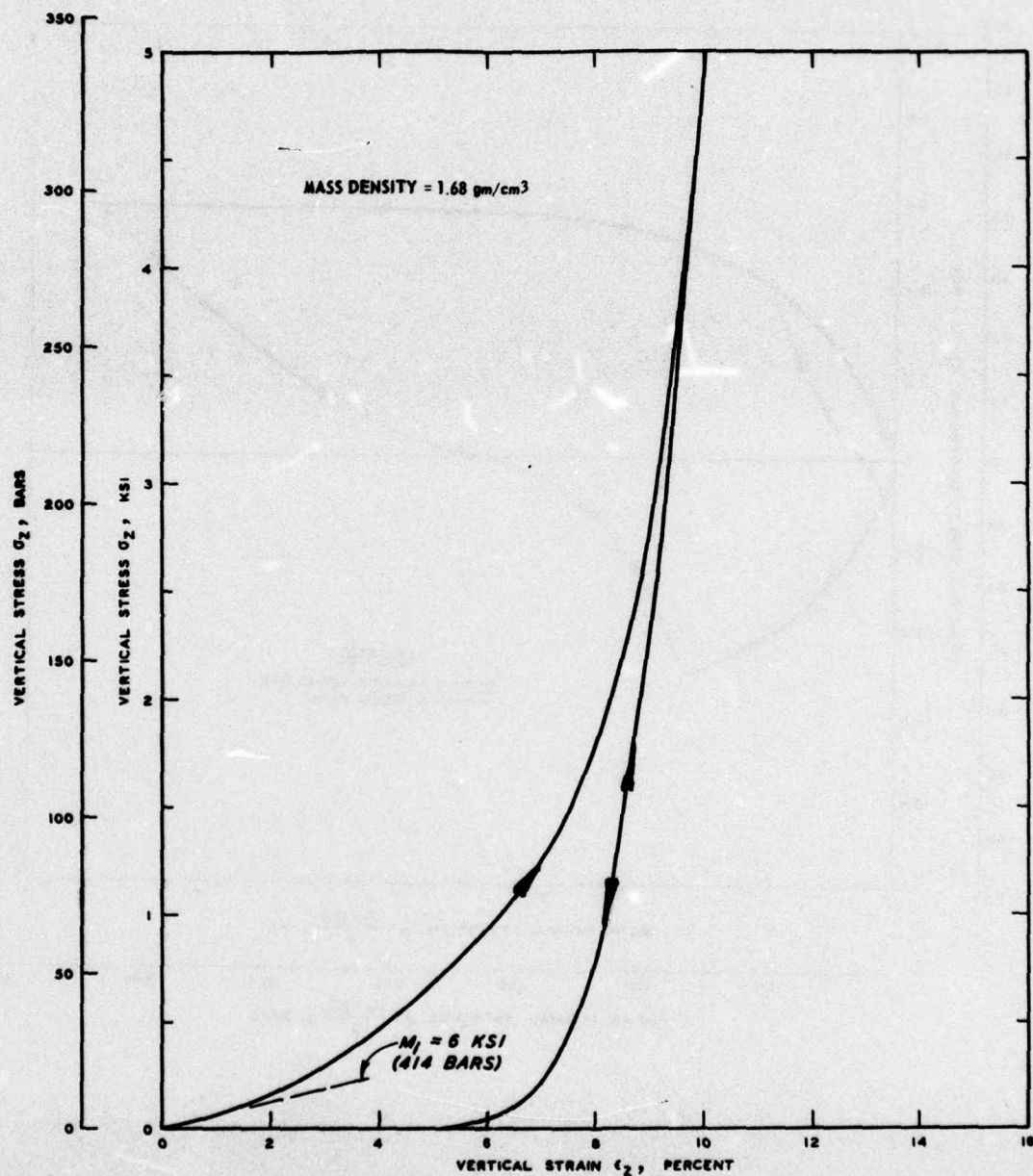


Figure 2.2 UX stress-strain curve for free-field layer 1 produced by the constitutive model.

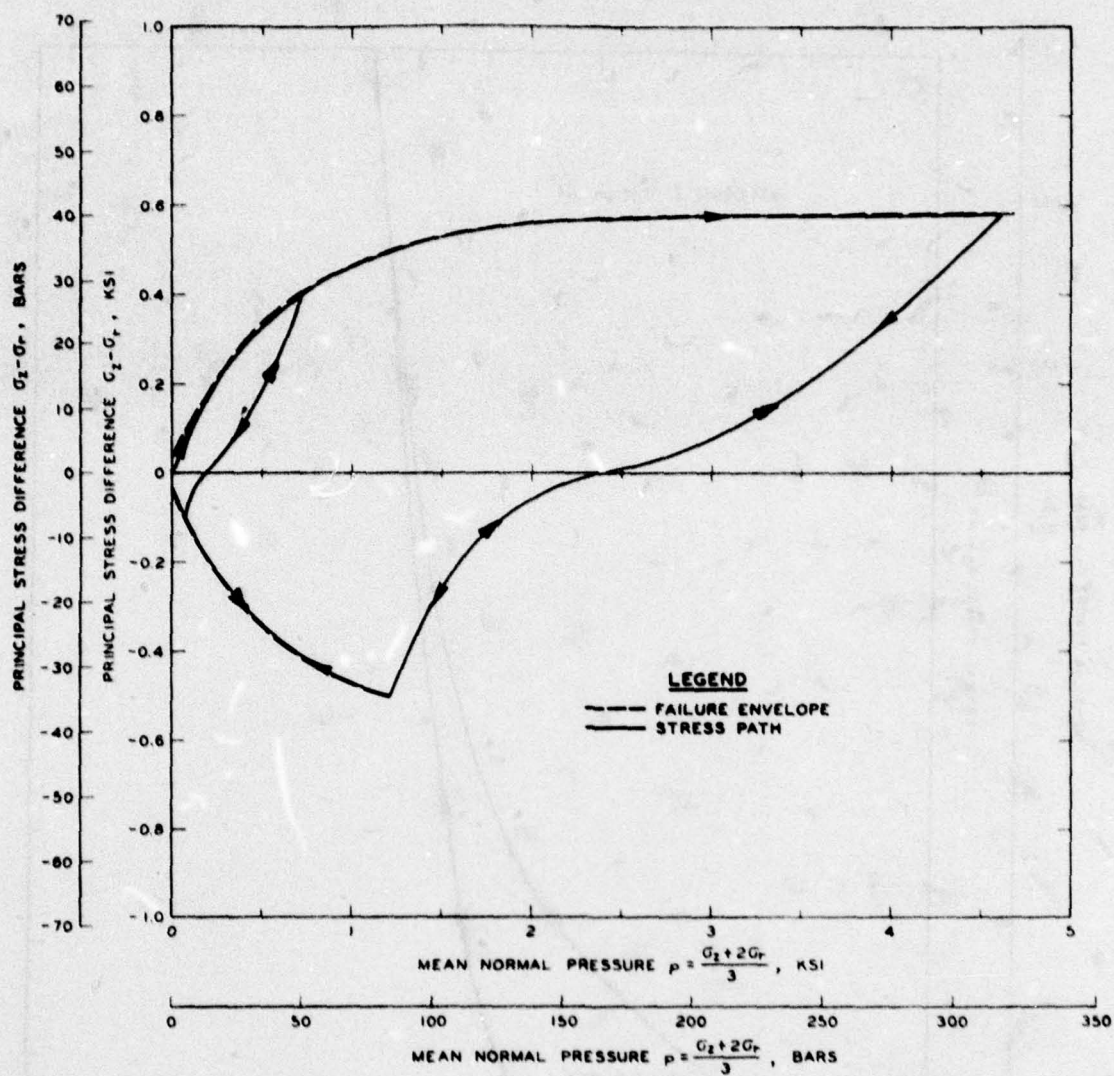


Figure 2.3 Failure envelope and UX stress path for free-field layer 1 produced by the constitutive model.

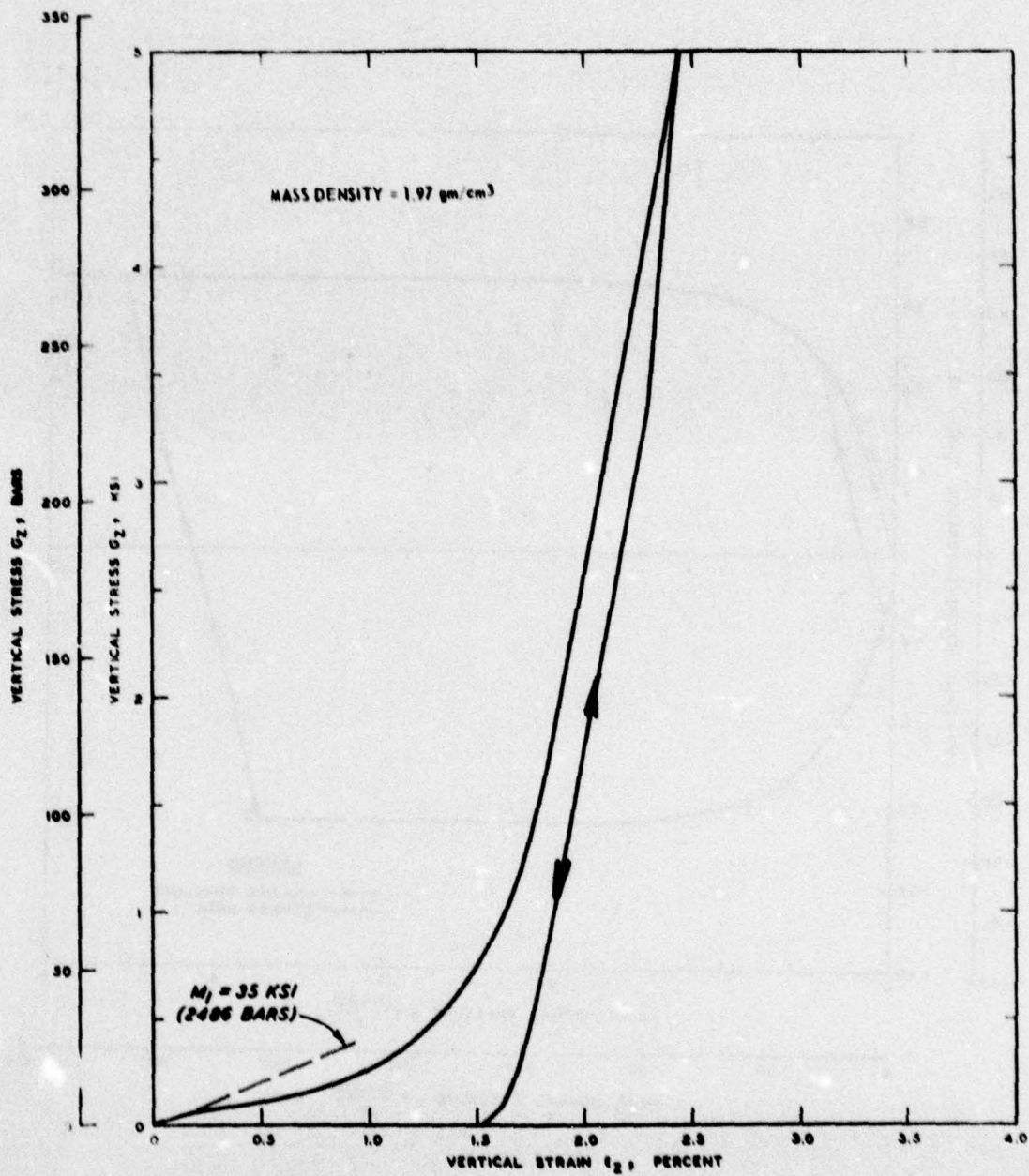


Figure 2.4 UX stress-strain curve for free-field layer 2 produced by the constitutive model.

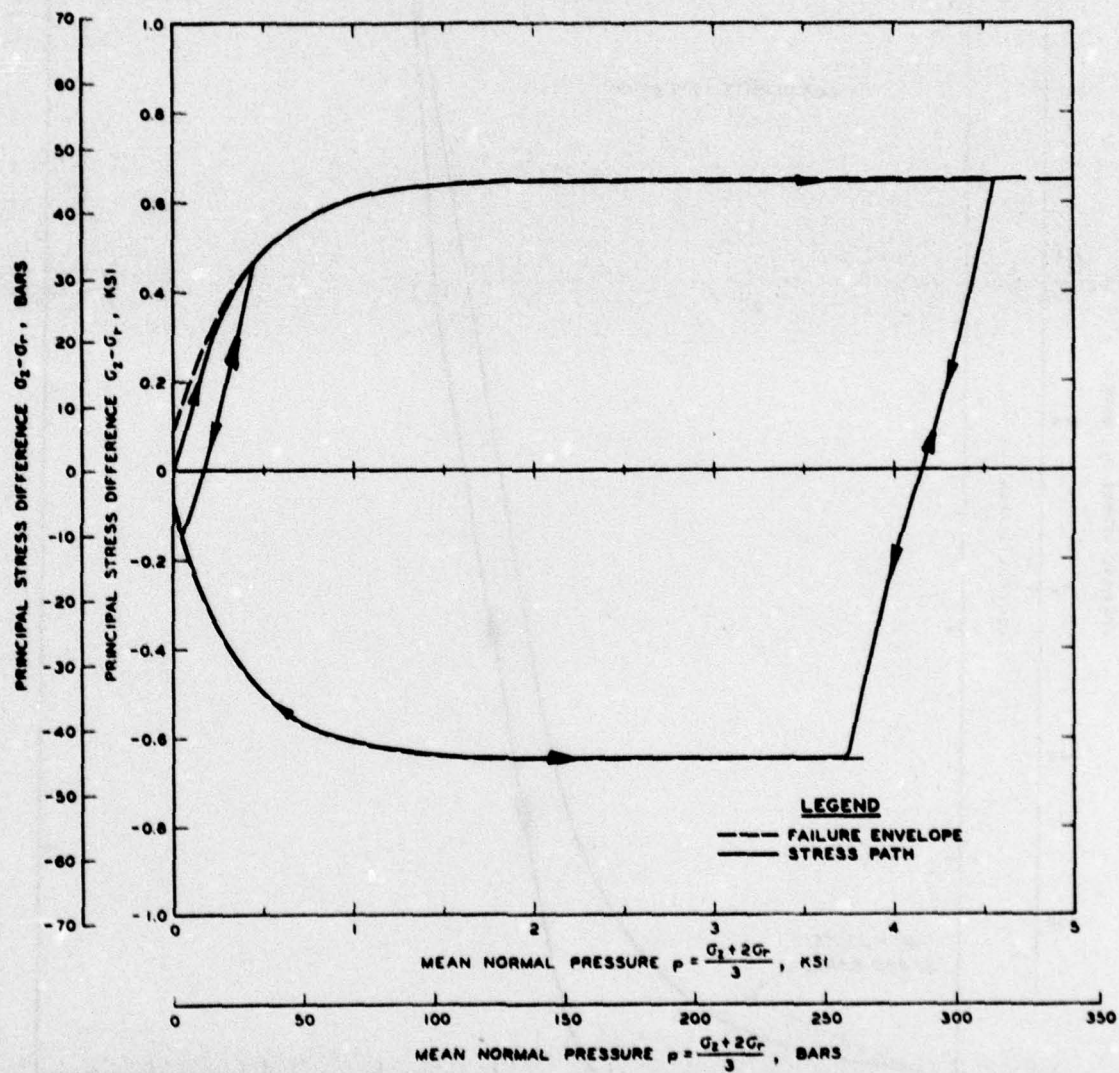


Figure 2.5 Failure envelope and UX stress path for free-field layer 2 produced by the constitutive model.

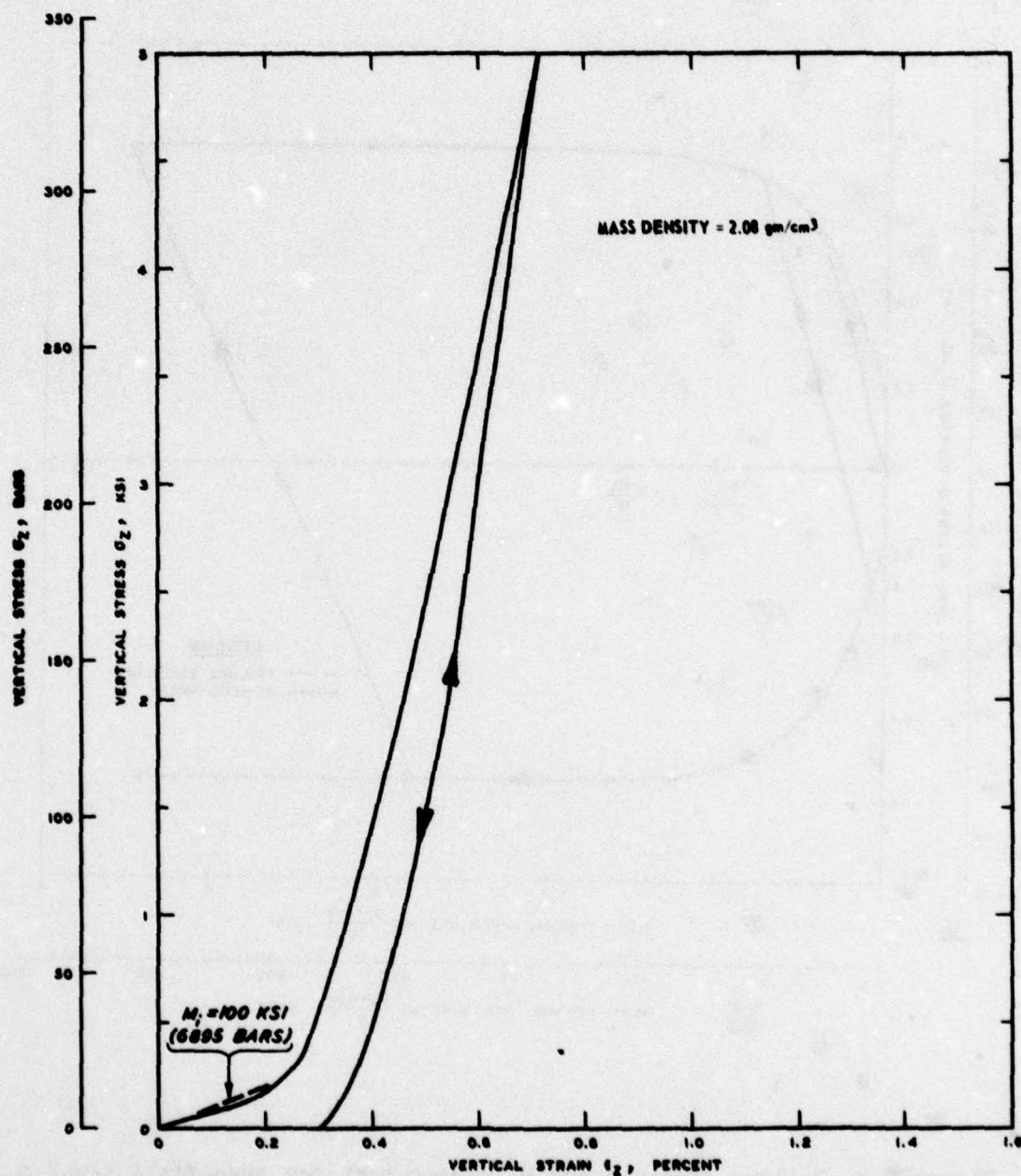


Figure 2.6 UX stress-strain curve for free-field layer 3 produced by the constitutive model.

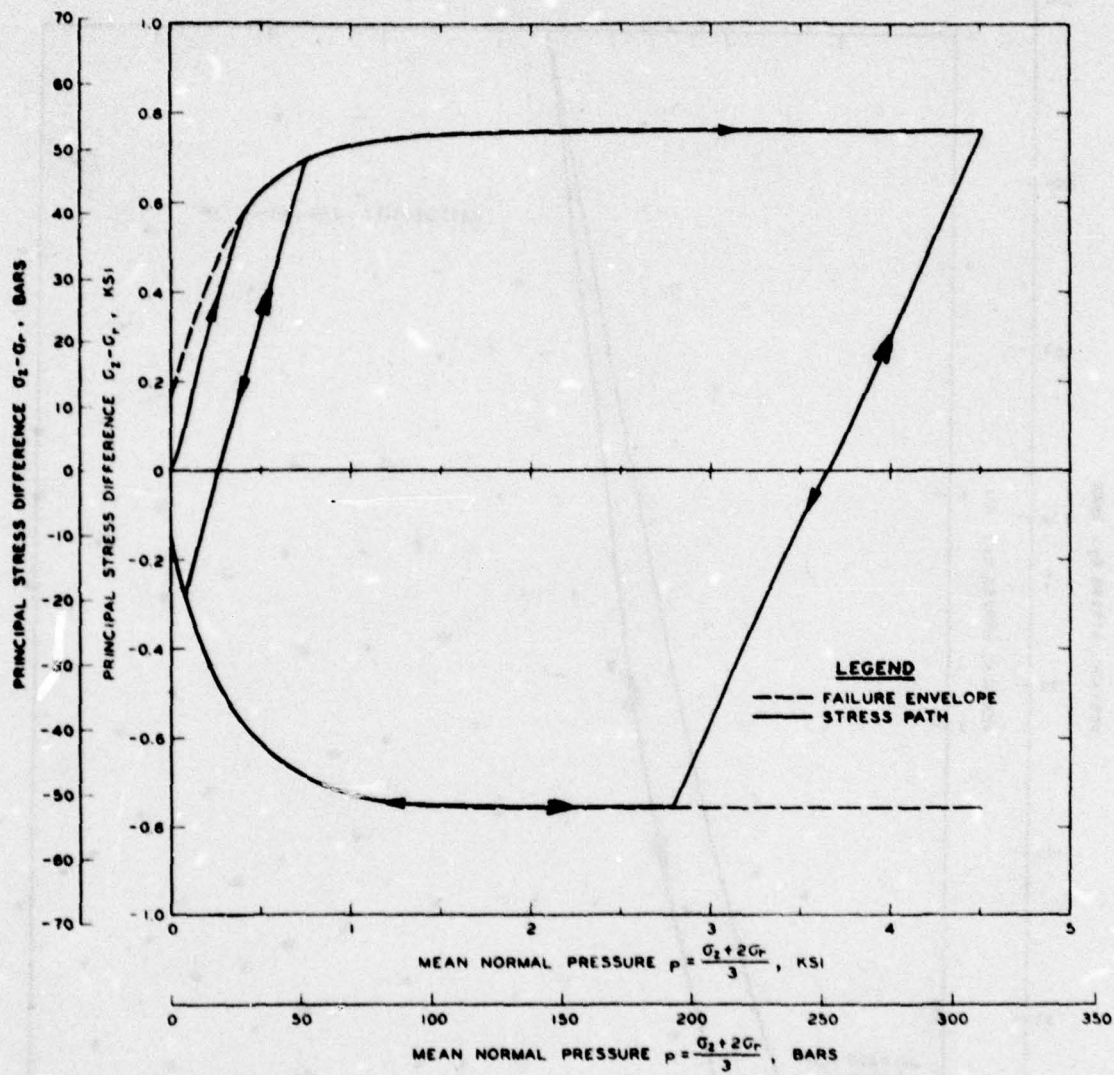


Figure 2.7 Failure envelope and UX stress path for free-field layer 3 produced by the constitutive model.

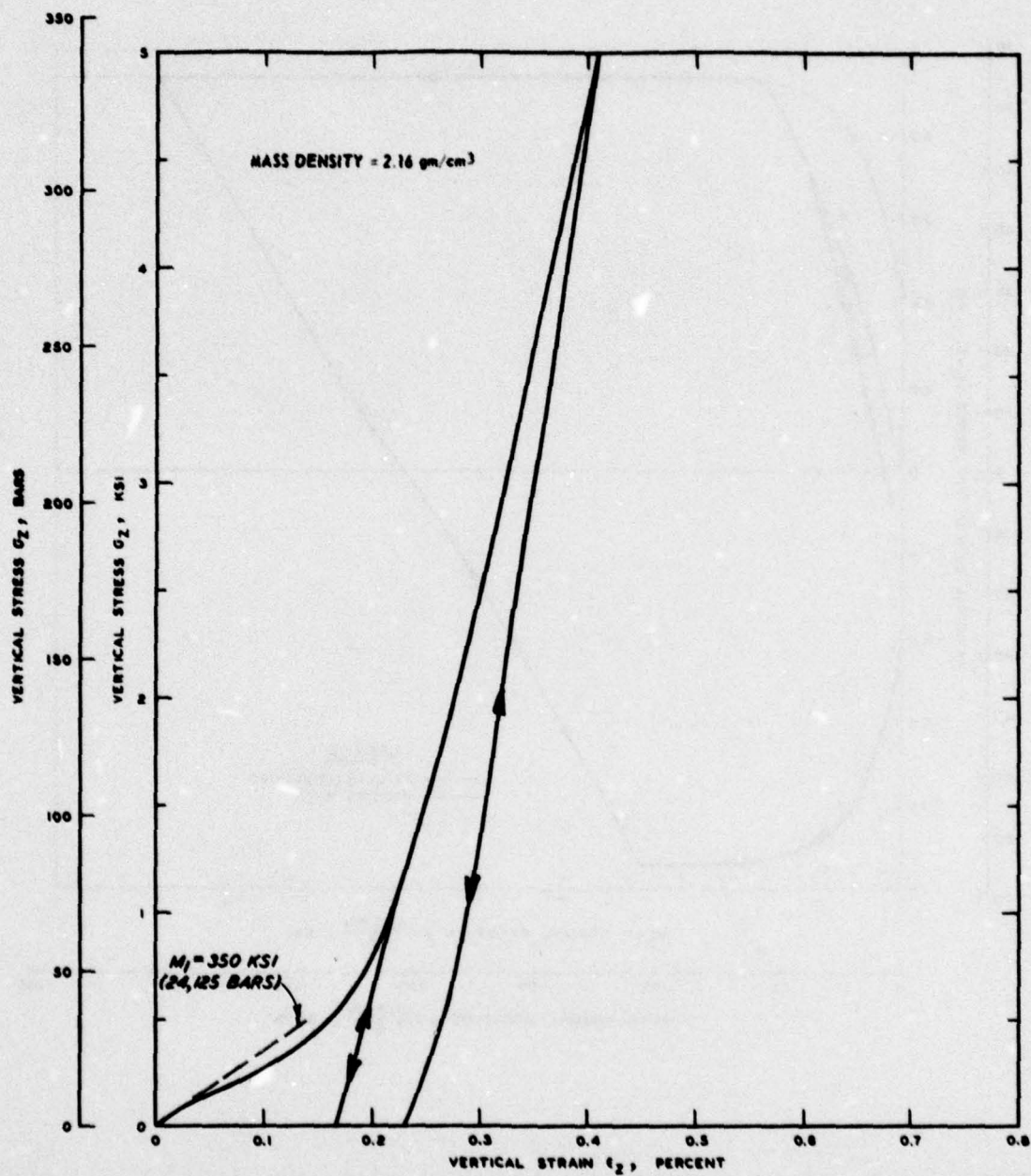


Figure 2.8 UX stress-strain curve for free-field layer 4 produced by the constitutive model.

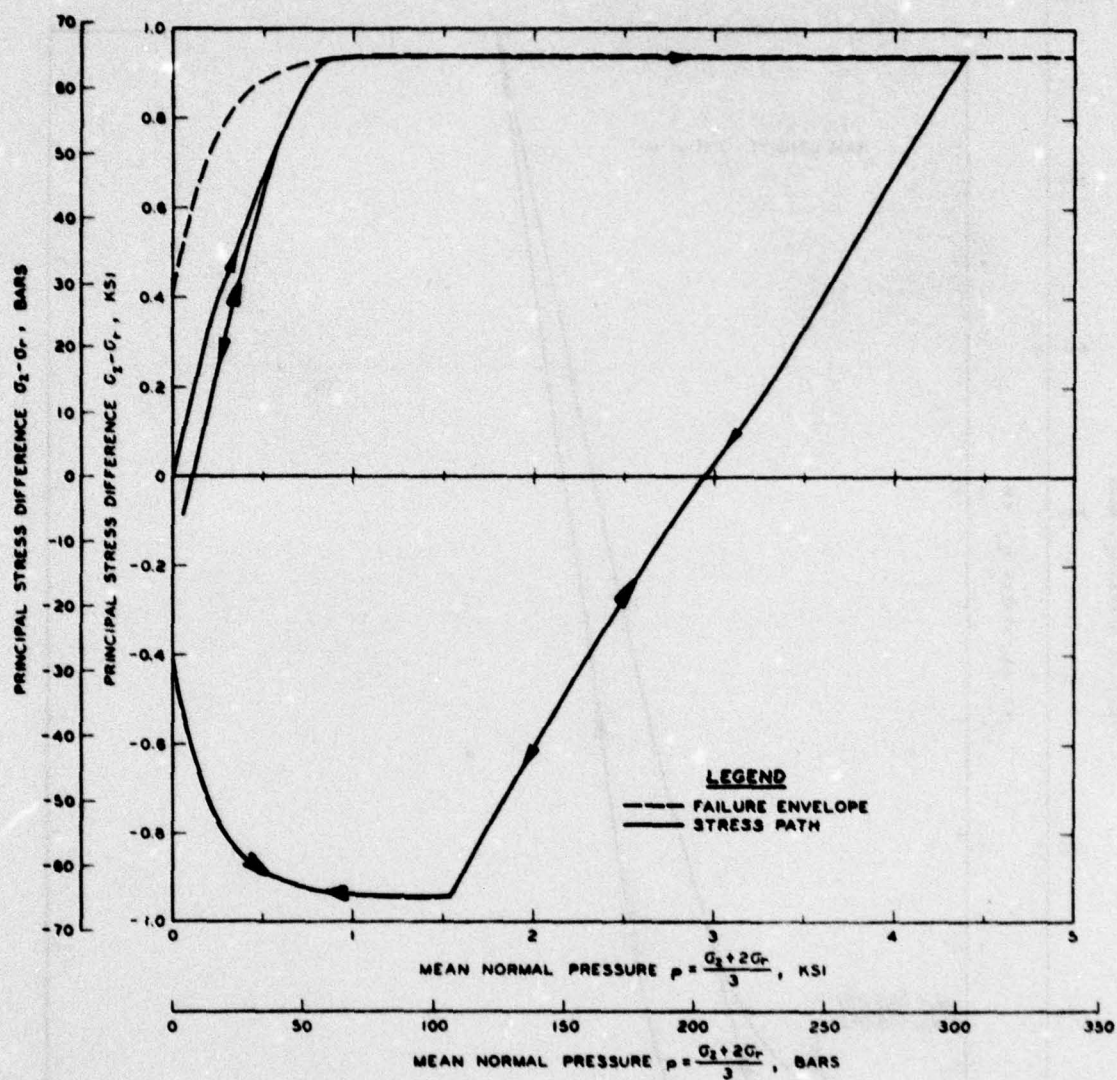


Figure 2.9 Failure envelope and UX stress path for free-field layer 4 produced by the constitutive model.

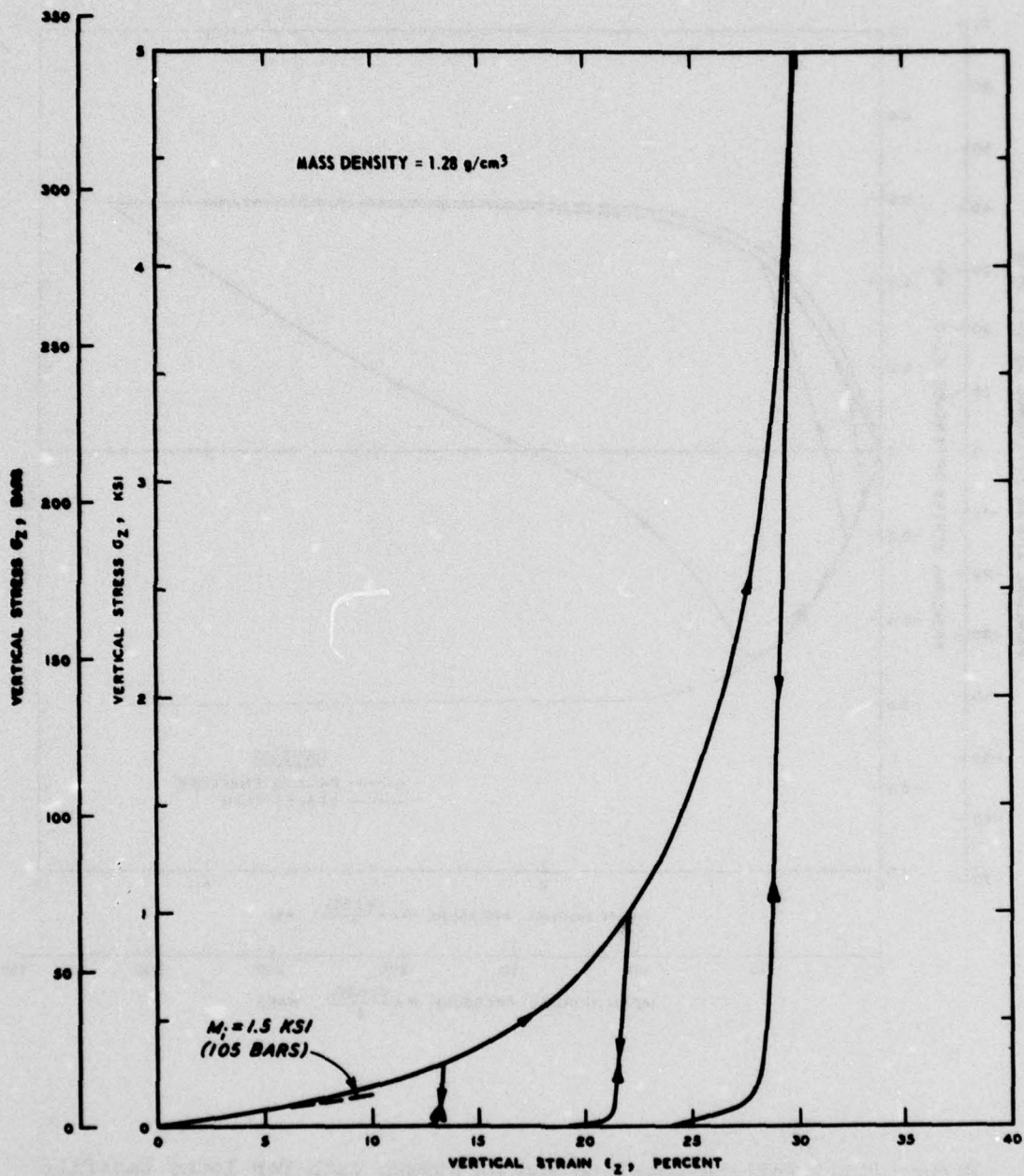


Figure 2.10 UX stress-strain curve for loose backfill produced by the constitutive model.

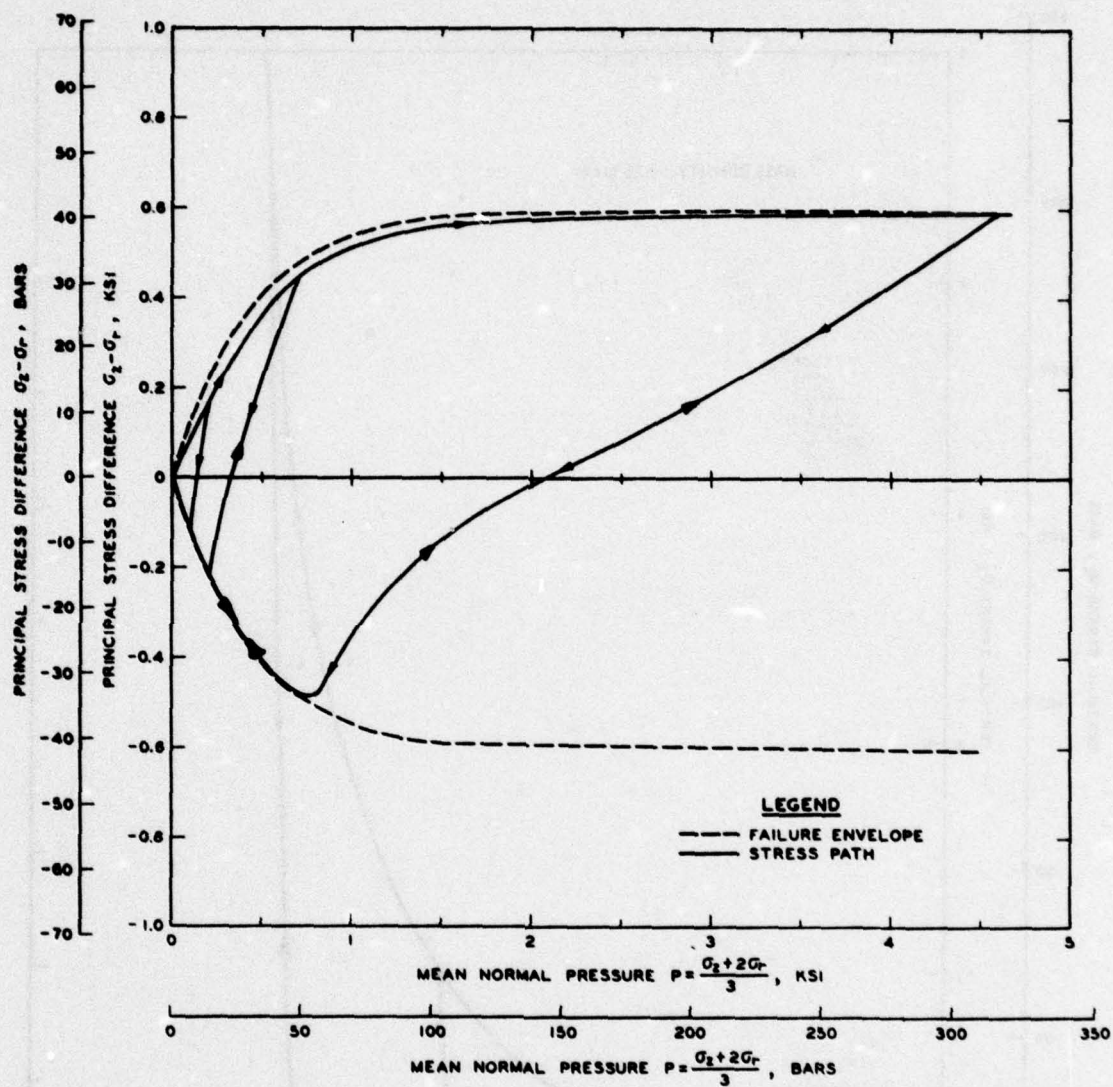


Figure 2.11 Failure envelope and UX stress path for loose backfill produced by the constitutive model.

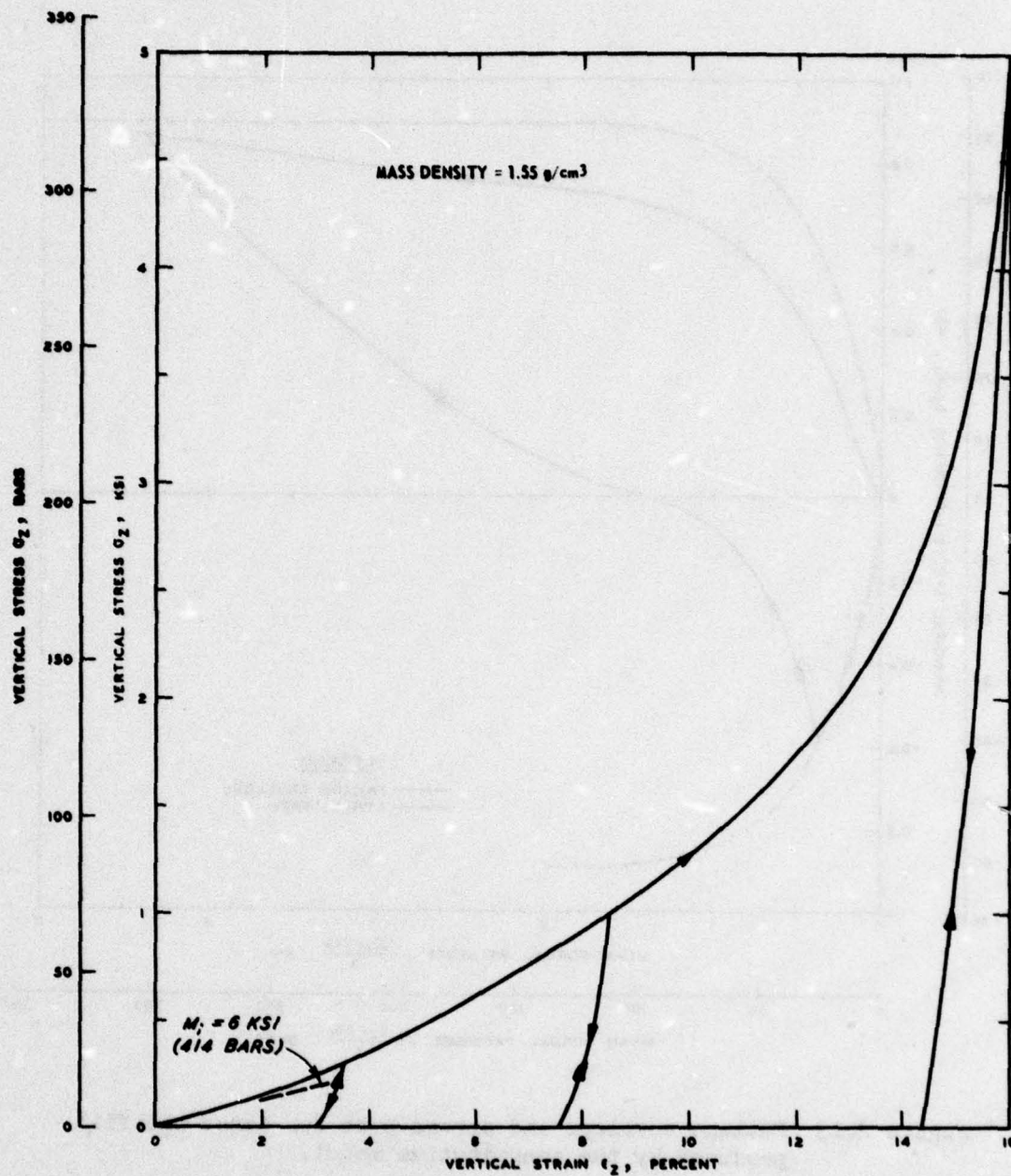


Figure 2.12 UX stress-strain curve for dense backfill produced by the constitutive model.

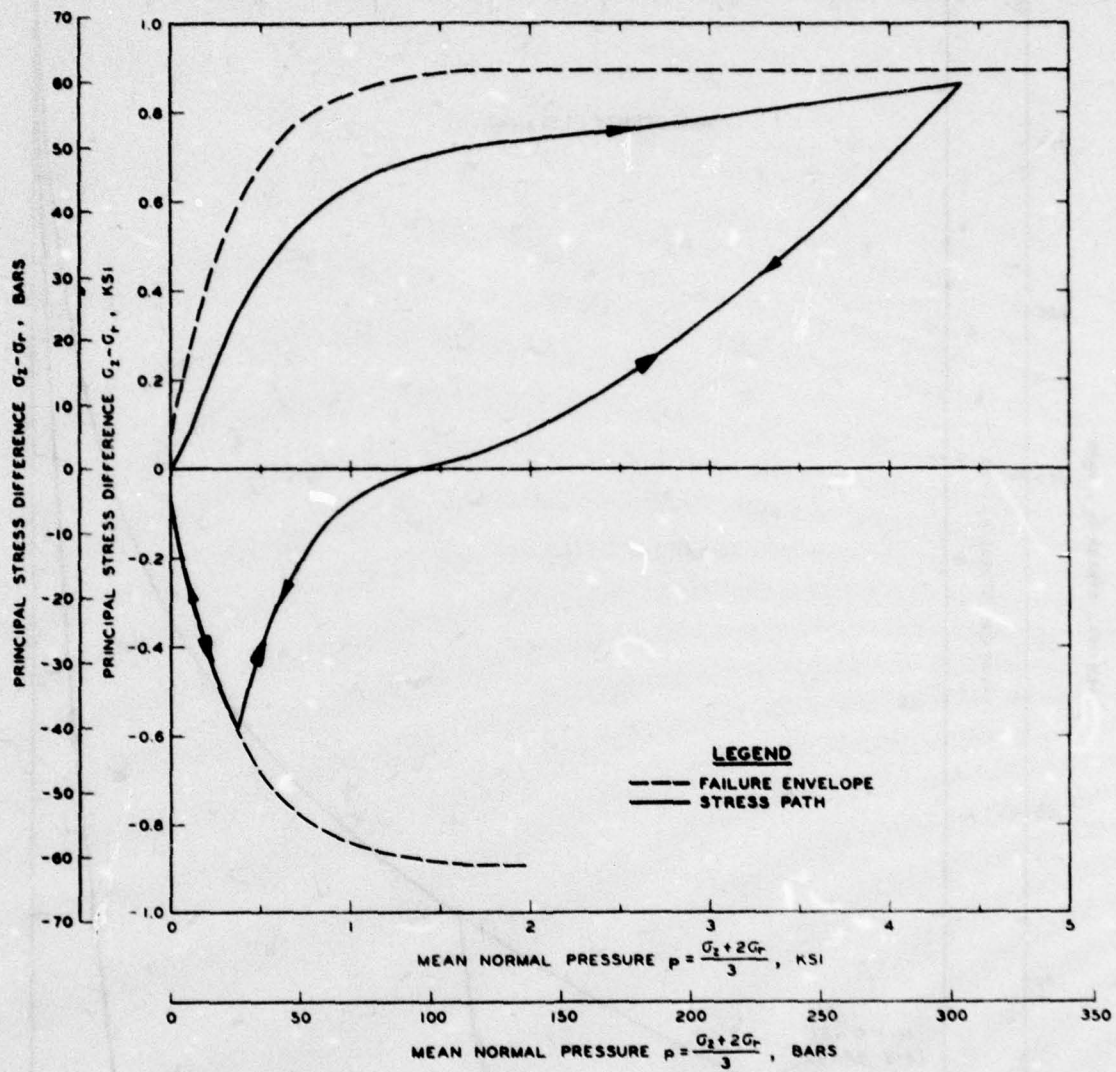


Figure 2.13 Failure envelope and stress path for dense backfill produced by the constitutive model.

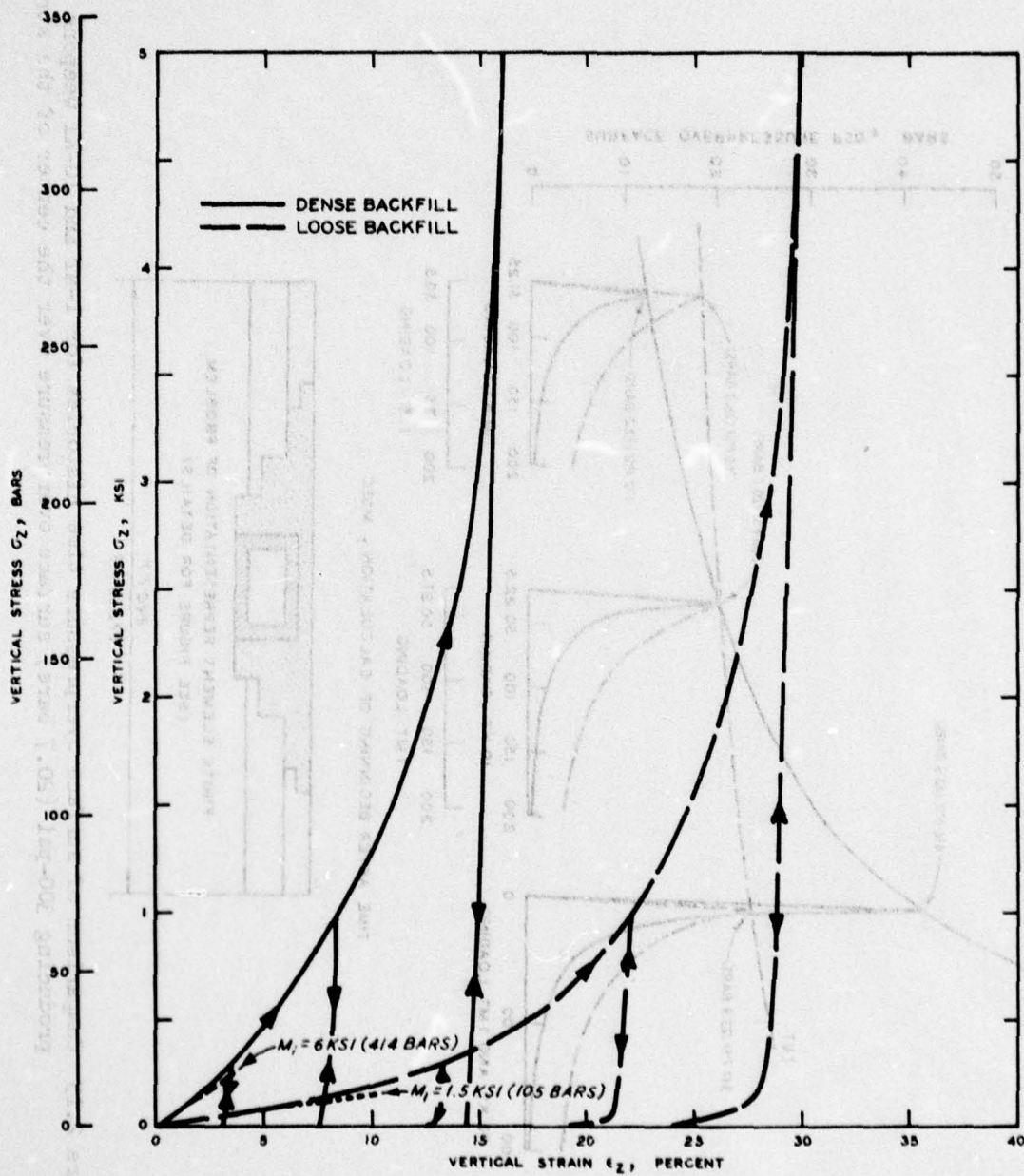


Figure 2.14 Comparison of UX stress-strain curves for loose and dense backfills produced by the constitutive model.

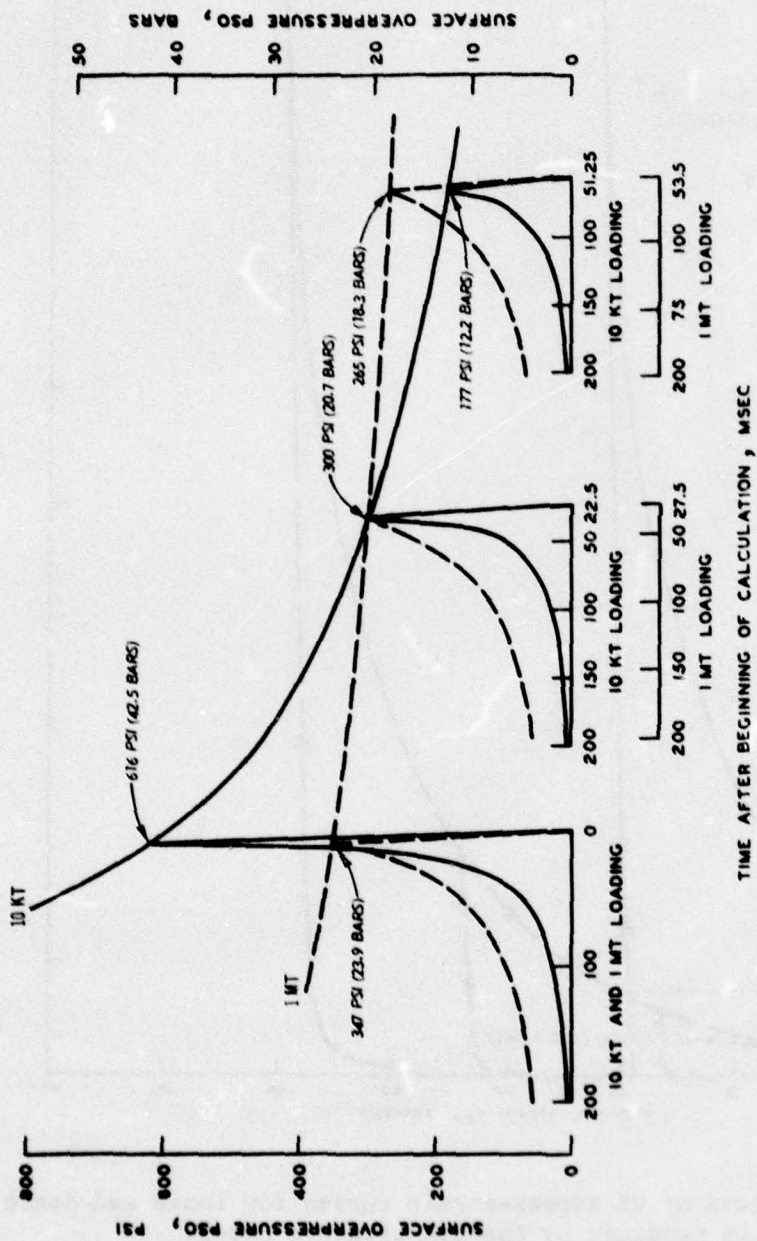


Figure 2.15 Comparison of surface overpressure time histories for 1-MT and 10-KT weapons producing 300-psi (20.7 bars) surface overpressure over the center of the structure.

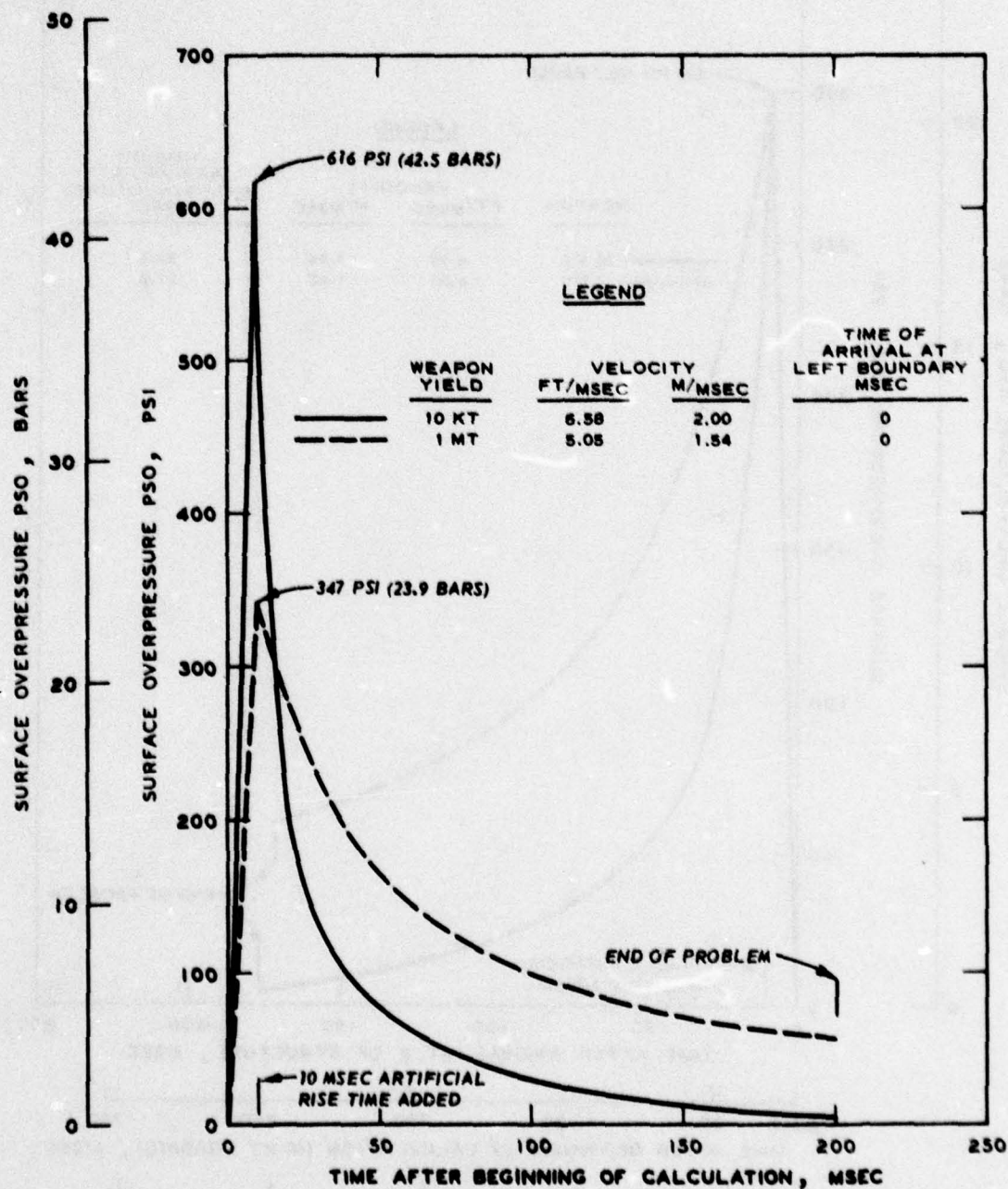


Figure 2.16 Surface overpressure time history over the left boundary of problem for 1-MT and 10-KT weapons.

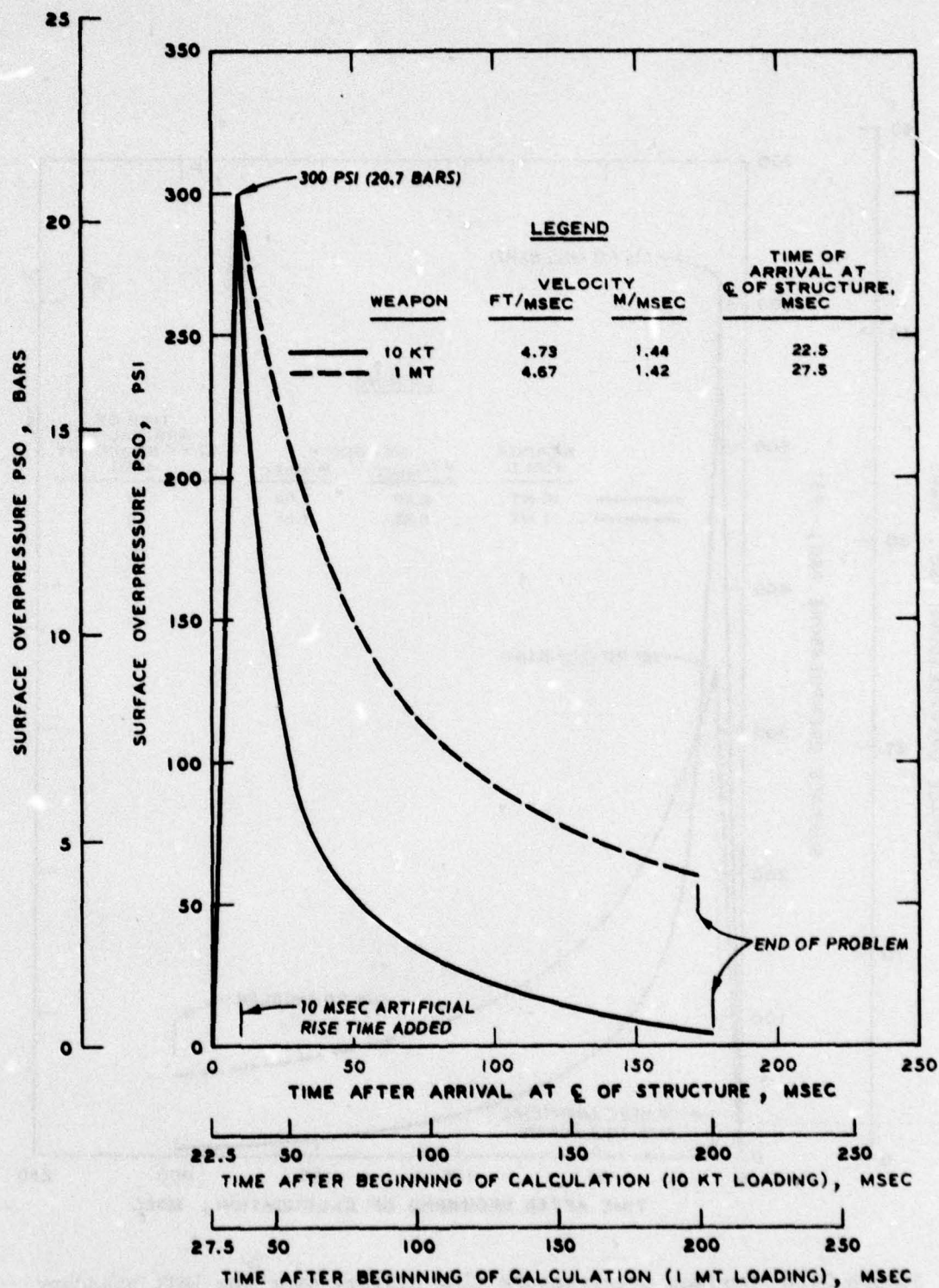


Figure 2.17 Surface overpressure time history over the centerline of the structure for 1-MT and 10-KT weapons.

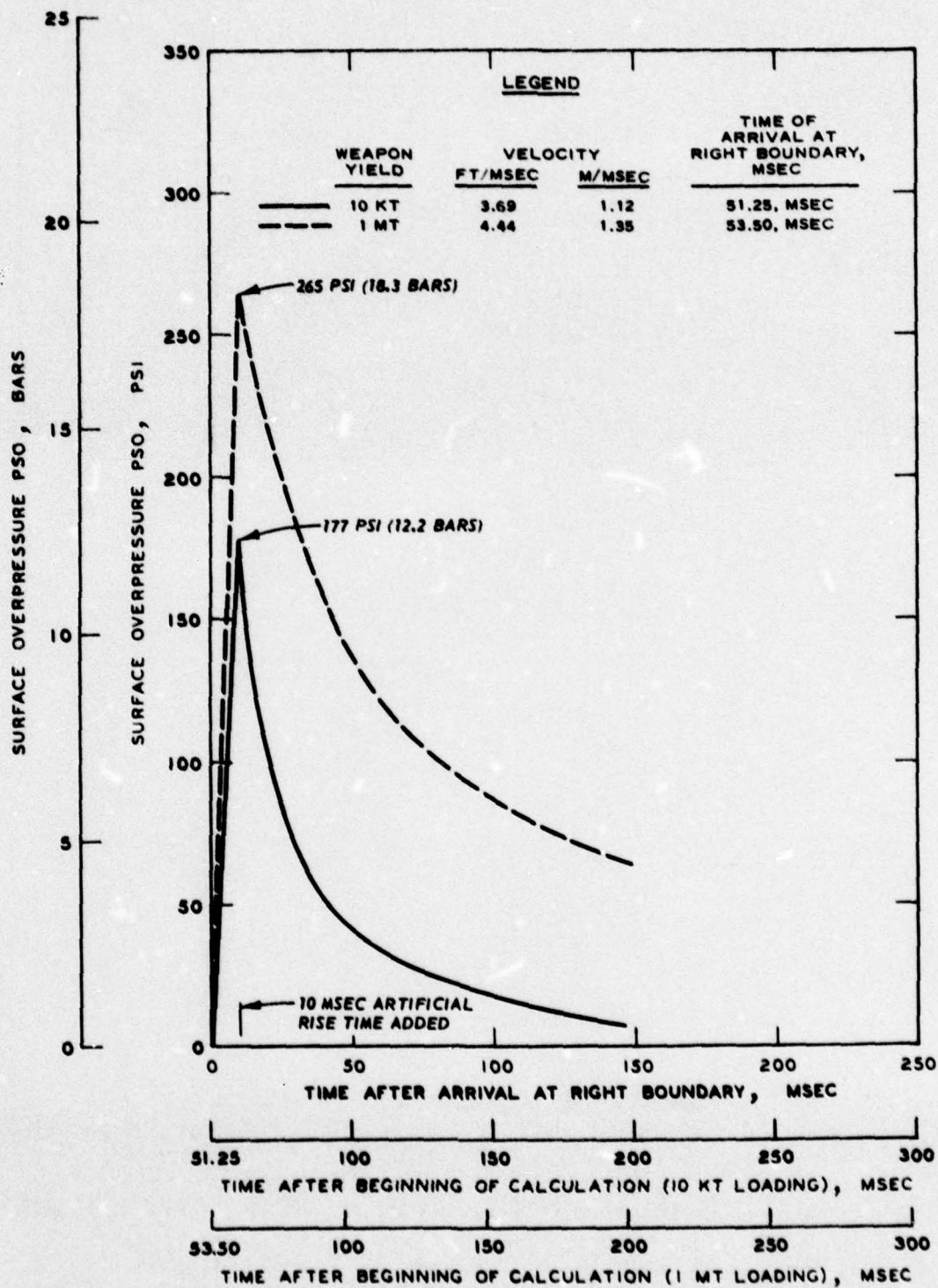


Figure 2.18 Surface overpressure time history over the right boundary of the problem for 1-MT and 10-KT weapons.

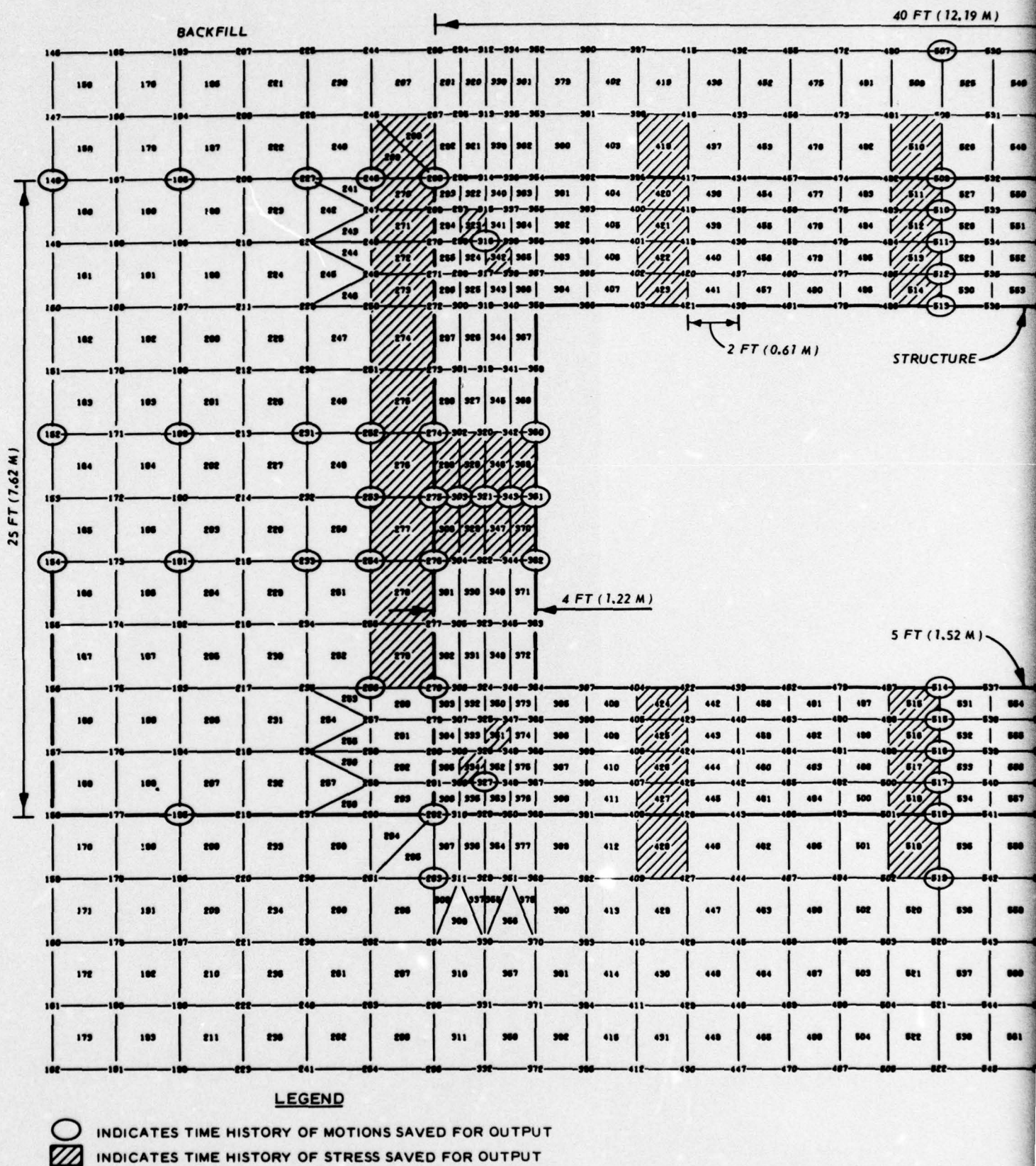
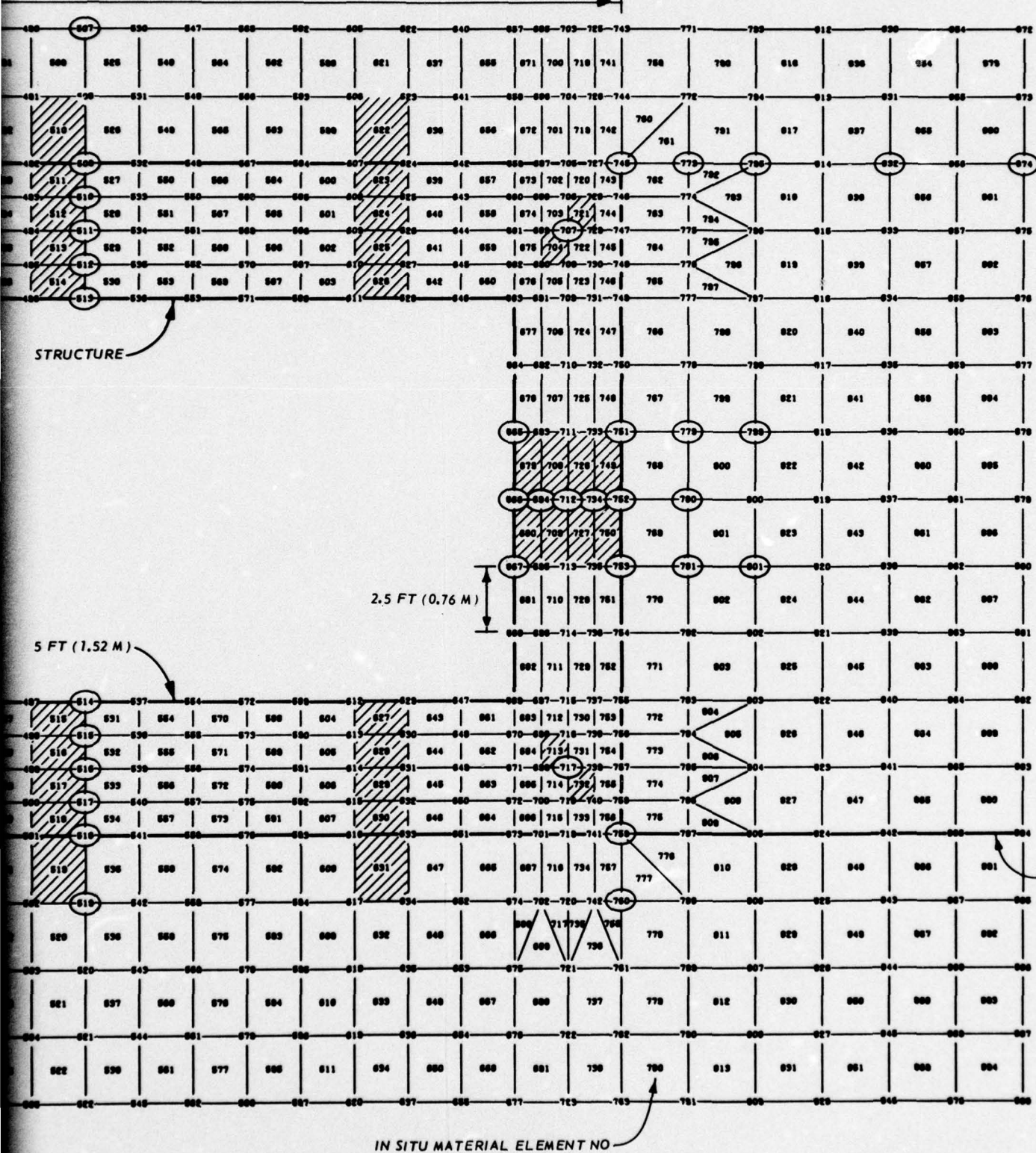


Figure 2.19 Detailed layout of the FE grid in the vicinity

40 FT (12.19 M)



In the vicinity of the structure showing time history output locations.

2

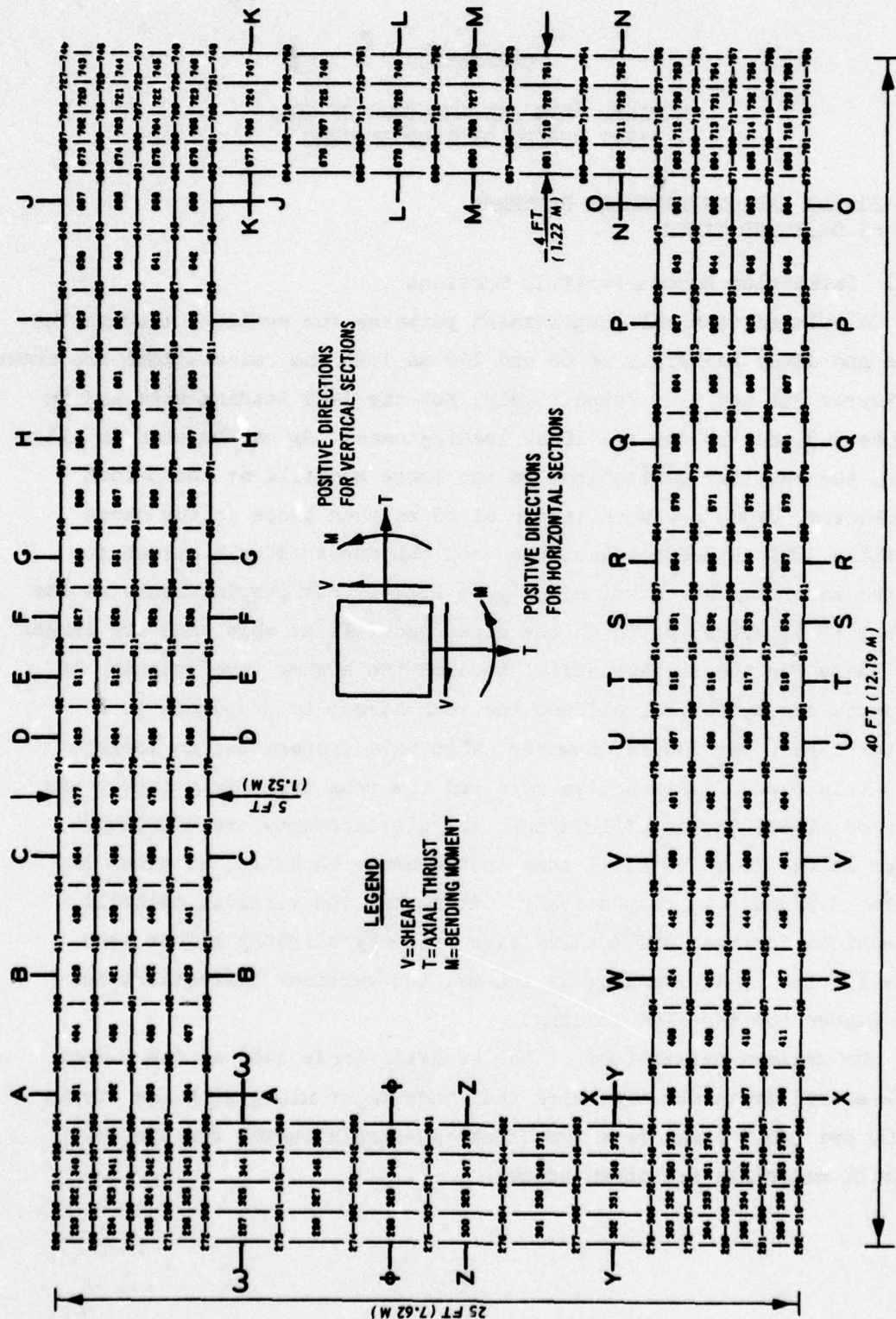


Figure 2.20 Structure sections for which shear, moment, and thrust will be calculated.

## CHAPTER 3

### RESULTS FROM AND ANALYSIS OF THE FIRST SERIES OF COMPUTATIONS

#### 3.1 STRESS AND DISPLACEMENT PATTERNS AT SELECTED TIMES

##### 3.1.1 Deflection Across Backfill Sections

Calculated vertical displacement patterns for sections through the loose and dense backfills at 60 and 100 ms into the calculations are shown in Figures 3.1 and 3.2, respectively, for the 1-MT loading case and in Figures 3.3 and 3.4 for the 10-KT loading case. As can be seen in all cases, the vertical deflections in the loose backfill at the 5-foot (1.52-metre) depth are much larger at 60 ms than those in the dense backfill. This appears reasonable when the stress-strain curves for the two materials are examined (Figure 2.14). But displacements at the 15-foot (4.57 metre) depth in the dense backfill at this time are larger than those for the loose backfill because the higher wave velocity of the dense shale fill has allowed the peak stress to propagate to a greater depth. At 100 ms, however, when wave propagation no longer plays this type of interactive role and the peak free-field stress has occurred at all depths of interest, the displacements are everywhere larger in the loose backfill than in the dense backfill, as shown in Figures 3.2 and 3.4, respectively. At 60 ms, the vertical backfill deflections for the 1-MT loading case are only slightly higher than those for the 10-KT loading; at 100 ms, the vertical deflections are much higher for the 1-MT loading.

The maximum deflections of the backfill (node 148) at the 5-foot (1.52-metre) depth and the times that they occur along with the strain at 200 psi (20.7 bars) from the UX stress-strain curves for the two backfill materials are shown below:

Backfill Case	Vertical Strain at 20.7-bar Vertical Stress in UX %	Deflection at 5-ft (1.52-m) Depth Node 148			
		1-MT Weapon Yield		10-KT Weapon Yield	
		Peak Deflection	Time	Peak Deflection	Time
		cm	ms	cm	ms
Dense	3.6	24	85	18	88
Loose	13.4	76	120	53	115

As can be seen in the table, the deflection at the 5-foot (1.52-metre) depth increases as weapon yield increases and as backfill quality decreases. For each weapon yield, the deflection at the 5-foot (1.52-metre) depth for the loose backfill case is approximately three times that for the dense backfill case. The deflections in the backfill for the 1-MT weapon yields over loose and dense backfills are a factor of 1.4 and 1.3 times the deflections for the 10-KT weapon yields over loose and dense backfills, respectively. These trends are reasonable when the stress-strain properties of the backfill materials and the differences in propagation speeds and impulse for the two airblast loadings are considered.

The interface between the backfill and structure should have been treated computationally by some type of slip element so that the relatively compressible backfill could deflect vertically with respect to the concrete structure (which is founded on very stiff undisturbed clay shale). This type of element was not available when these calculations were performed. Since the structure and backfill were "welded" together, it is inevitable that very little deflection would occur near the structure walls. Of course, this is not the case in the real world. However, the backfill vertical deflections did maximize at a distance of approximately 6 to 10 metres from the structure (Figures 3.1 through 3.4) for all cases. Deflections close to but perhaps less than the maximum shown for the backfill (because of wall friction) should be expected close to the structure. The deflections calculated in the loose shale backfill would be considered very severe for cables or pipes that might be connected to the structure at some point along the sidewall.

### 3.1.2 Stresses on the Exterior Structure Surfaces and Deflections of the Neutral Axis

Figures 3.5, 3.7, 3.8, 3.9, and 3.10 show the stresses normal to the exterior surfaces of the structure and the deflection of the neutral axis of the structural members for all four calculations at times of 40, 80, 100, 150, and 200 ms, respectively. Figure 3.6 shows the same normal stress and deflection information for the times that the vertical deflection at the center of the roof of the structure has maximized for each calculation. Maximum deflections occur between 60 and 70 ms for all calculations. In actuality, the stresses are the vertical or horizontal stresses in the middle of the soil "cells" adjacent to the structure.

At a time of 40 ms as shown in Figure 3.5, the roof loading is triangular except in the 10-KT dense backfill case. At 40 ms, the peak overpressure for the 10-KT dense backfill simulation has already been applied to the structure roof, while the stress in the other cases is still increasing. The amplitude of the stress normal to the roof at this time is a function of the velocity of the traveling airblast and the wave speed of the backfill. The average propagation velocity of the 10-KT airblast for locations upstream of the center of the structure is faster than that of the 1-MT airblast (i.e., the local propagation velocity is 2.0 m/ms versus 1.54 m/ms at the left (upstream) boundary of the problem), and the wave speed of dense backfill (0.195 m/ms) is greater than that of the loose backfill (0.115 m/ms). At the time that the peak centerline deflections of the roof occur, the roof loading varies irregularly with position, but generally the differences among the four calculations are less than 20 bars (Figure 3.6). For subsequent times, i.e., 80, 100, 150, and 200 ms as shown in Figures 3.7 through 3.10, the normal stress on the roof decreases with increasing time and tends toward a pattern of uniform loading over most of the roof with stress concentrations above the side-walls. At 200 ms, the stresses normal to the roof for the 1-MT weapon-yield cases are higher than those for the 10-KT cases because the airblast from the 10-KT weapon decays at a faster rate than does the airblast from the 1-MT weapon.

The normal stresses on the blastward sidewall from the two dense backfill calculations at 40 msec, as shown in Figure 3.5, are higher than those for the loose backfill calculations; the higher wave velocity of the dense backfill materials has permitted significant stress to propagate further down the backfill. Figure 3.6 also shows this trend. At 80 ms, as shown in Figure 3.7, the stress normal to the blastward sidewall is nearly equal for both backfill cases.

At 40 ms, the stress normal to the structure floor shows a concentration under the blastward sidewall for all cases because significant stress has just propagated to this depth on the blastward side of the structure. The load distribution shown in Figure 3.5 causes a rotation in the counter-clockwise direction. At the time that the peak deflection of the roof is occurring, the stress normal to the floor of the structure is concentrated under the sidewalls and is at a minimum near the center. For subsequent times, as shown in Figures 3.7 through 3.10, the stresses under the sidewalls decrease. At 150 ms, as shown in Figure 3.9, tensile stresses are occurring under the left portion of the floor of the structure. It is separating from the soil, and a clockwise rotation of the structure is taking place at this time.

The deflected shape of the structure at 40 ms, as shown in Figure 3.5, indicates that the left portion of the roof and floor of the structure are deflecting downward. The deflections are greatest for the 10-KT dense backfill calculation and the least for the 1-MT loose backfill calculation. This is consistent with the stresses normal to the structure at this time (Figure 3.5). Figure 3.6 shows the deflected shape of the structure at the time that the peak downward deflection of the roof centerline occurs in each calculation. Also, in Figure 3.6, the roof centerline is deflecting downward with respect to the sidewalls in all cases, and the magnitude of the deflection increases with increase in weapon yield and with loose backfill. The total maximum downward motion of the roof centerline for the 1-MT dense, 1-MT loose, 10-KT dense, and 10-KT loose calculations are 10.9, 13.0, 7.2, and 8.4 centimetres, respectively. The maximum relative

downward displacements of the roof centerline (i.e., measured vertically from a line drawn through the two upper corners of the structure), are 5.3, 7.4, 3.4, and 4.6 centimetres, respectively. The maximum relative deflections for the 1-MT case are 56 percent and 61 percent greater than those for the 10-KT loading cases for the dense and loose backfills, respectively. The loose backfill caused maximum relative deflections 40 percent higher for the 1-MT loading case and 35 percent higher for the 10-KT loading case than did the dense backfill.

At 80 ms, the roof structure is rebounding upward with respect to the top corners, while the structure as a whole is moving downward (Figure 3.7). The roof has rebounded more for the 10-KT loading cases than for the 1-MT loading cases; this phenomenon is compatible with the stress distributions normal to the structure roof shown in Figure 3.7.

At 100 ms, as shown in Figure 3.8, the roof has rebounded in all cases, and the downward deflection of the centerline of the floor is "catching up" with the sidewalls. At this time, the structure has moved downstream and an inflection has developed in the blastward sidewall (i.e., the top of the wall has moved further downstream than the bottom). At 200 ms, as shown in Figure 3.10, for the 10-KT loading cases, the structure has essentially returned to an undeformed condition but has been moved downstream and rotated in the clockwise direction. At the same time, the roof and the floor of the structure have deflected inward, and the sidewalls have deflected outward for the 1-MT loading cases. The structure has been deflected downward further into the clay shale and undergone less clockwise rotation for the 1-MT cases than for the 10-KT loading cases.

### 3.1.3 Rotation of the Structure

The rotations of the chord formed by the two bottom outside corners of the structure are presented in Table 3.1 for all calculations. In all cases, the structure initially undergoes a counterclockwise rotation; then, as the airblast passes, it rotates through the upright or "zero position" and undergoes a clockwise rotation. For both loading conditions, at

200 ms, the structure remains rotated in a clockwise position. However, for the 1-MT cases at 200 ms, the clockwise rotation is less than the maximum; whereas, for the 10-KT calculations the maximum clockwise rotation occurs at 200 ms. The maximum counterclockwise rotations are higher for the higher weapon yields and for loose backfill conditions. The maximum rotation of 0.00246 radians for the 10-KT simulation represents only 3 centimetres of differential displacement over the length of the structure.

#### 3.1.4 Thrusts, Shear and Bending Moments Within the Structure

Axial thrust, bending moment, and shear per unit width of the structure at selected times were calculated from the output data and were tabulated in Tables 3.2 through 3.10 for the structural section shown in Figure 2.20. The sign convention for these tabulated values is designated in the figure. Shear and moment diagrams for each calculation were plotted for the roof and floor at the times that the horizontal stress in elements 514 and 515 (Figure 2.20) maximized and for the blastward and leeward sidewalls at the time that the vertical stresses in elements 369 and 679 maximized (i.e., when bending moment maximized at the midsections of these structural elements). The shear and moment diagrams for the roof and floor are plotted in Figures 3.11 and 3.12, respectively, while those for the blastward and leeward sidewalls are plotted in Figure 3.13. The times for which the moment and shear diagrams were plotted for each member are shown in the appropriate figure. The signs for the moments, shears, and thrusts are those of a right-handed sign convention.

In Figure 3.11, the maximum moment occurs near the center of the roof of the structure for all calculations and is positive. The maximum moment in the floor of the structure is negative and occurs slightly downstream from the center of the floor of the structure as shown in Figure 3.12. The maximum moments in the sidewalls occur near the top of the sidewalls as shown in Figure 3.13. The general trend is for moments to increase with increase in weapon yield and with loose backfill.

The calculated moments and thrusts for specific sections are compared with thrust-moment interaction diagrams in Figures 3.14 and 3.15. Figure 3.14 shows a thrust-moment interaction diagram for yield of a structural section that might be typical of those for the roof and floor in the idealized structure, and Figure 3.15 presents the same type thrust-moment interaction diagram for the sidewalls. The thrust-moment interaction diagrams were determined by the methods of Section 8.3 of ASCE Manual 42<sup>9</sup> and by assuming a concrete strength of 4.0 ksi (277 bars), a yield strength of steel of 52 ksi (3600 bars), and 1 percent of reinforcing steel in each face. Also shown in Figure 3.14 are the maximum thrusts and moments on Sections FF (through the roof) and Section RR (through the floor), and in Figure 3.15, those on Sections ww and KK (through the sidewalls). As further noted in Figure 3.14, an increase in weapon yield and a change from dense to loose backfill caused an increase in thrusts and moments. The same trend was seen in Figure 3.15 with the exception of Section KK for the 10-KT case. The increases in thrust and moments due to changes in the type of backfill were larger for 1-MT cases than for the 10-KT cases.

What do the increases in thrusts, moments, and shears, which have been shown to occur as backfill quality decreases, mean in terms of structural integrity, strength design criteria, and resulting costs? The structure idealized here would probably undergo significant permanent deformation and might even be totally unusable if subjected to the loading assumed. Because the idealized structure is linear elastic, the calculation cannot possibly demonstrate that type of behavior. The trends in Figure 3.14 indicate that structural integrity could possibly be threatened by an increase in weapon yield or decreases in backfill quality. (This trend is more evident for the roof than for the floor of the structure.) The same statement can be made concerning the trends shown in Figure 3.15. (For the sidewalls, the trend is more evident for the 1-MT loading case.)

### 3.2 SELECTED TIME HISTORIES

Figures 3.6 through 3.42 present comparisons of selected stress or motion time histories for the four calculations. In each figure, the element and/or node locations are sketched. The sign convention for these figures is as follows: upward and outward movements and tensile stresses are considered positive.

Comparisons of the vertical displacement and velocity time histories for the center of the roof span are shown in Figures 3.16 and 3.17, respectively. As can be seen in the figures, both peak downward velocities and peak downward displacements increase for loose backfill conditions and higher weapon yields. The maximum displacements varied more with the weapon yield than with the backfill properties, while for the peak particle velocities, the reverse was true. After the first relative maximum displacement, the period of the oscillation in the motion of this point ranged from 60 to 65 ms. This corresponds to a frequency range of 15 to 17 Hz. Within or very close to this same range are the first (15.1) and second (18.2) frequencies determined in the in vacuo modal analyses\* and with the second (16.7), third (17.2), and fourth (17.4) frequencies determined during the embedded nodal analyses\*\* using the upper bound material properties. The deflected shapes of the structure at the times that the vertical deflection at this point maximize and at the 100 msec time, as shown in Figures 3.6 and 3.8, respectively, can be approximated as a combination of the mode shapes associated with these frequencies.

Figures 3.18 and 3.19 show the horizontal stresses at points three-fourths of the way from the neutral axis to the top and bottom fibers of the roof, respectively. As can be seen, the peak stresses above and below the neutral axis are of opposite sign and are notably higher for the loose backfill and higher weapon-yield cases.

The vertical and horizontal velocity time histories for the upper blastward corner of the structure are shown in Figures 3.20 and 3.21,

---

\* See Figure A.3 of Appendix A.

\*\* See Figure A.7 of Appendix A.

respectively. The peak downward velocities for the loose backfill calculations are slightly higher than those for the dense backfill calculations for both weapon yields. The peak outward velocity for the 10-KT loose backfill calculations is only slightly greater than that for the 10-KT dense backfill calculation; however, the peak outward velocity for the 1-MT loose backfill calculation is much greater (a factor of 2 higher) than that for the 1-MT dense backfill calculation.

Vertical and horizontal displacement time histories for a point (node 361) near the midheight of the blastward sidewall of the structure are shown in Figures 3.22 and 3.23, respectively. The type of backfill has little effect on the vertical displacements, as shown in Figure 3.22; however, the peak downward displacements for the calculations with 1-MT loading are approximately 50 percent higher than those for the calculations with 10-KT loading. The peak inward displacement at the midheight of the structure is highest for the loose backfill and largest weapon yield.

Figures 3.24 through 3.29 compare vertical deflection time histories of points on the blastward face of the structure with those for adjacent points in the backfill for three different depths. As also noted, the maximum vertical deflections of points on the structure are not affected by changes in backfill or vertical location along the wall. (The deflections of the structure for the calculations with 10-KT loading and 1-MT loading are 5.0 and 7.5 centimetres, respectively.) The reason for this is that the vertical deflection of the structure as a whole is mainly controlled by the applied loading and the properties of the relatively incompressible material upon which it rests. The figures further show that the relative displacements between the loose backfill and the structure are much greater than the relative displacements between the dense backfill and the structure. The points in the backfill examined were only 10 feet (3.05 metres) from the structure, and backfill deflections in these figures at these locations are probably less than they should be because the backfill elements are welded to the structural

elements at the soil-structure interface (see Section 3.1.1). Nevertheless, the important influence of backfill properties on relative displacement sensitive items, such as pipes, cables, and connections to the structure, is clearly evident.

At middepth of the structure, shown in Figures 3.26 and 3.27, the structure moves down with respect to the backfill at early times. The phenomenon occurs because a significant stress has not propagated to this depth through the backfill materials, while significant stress has been applied to the roof of the structure, which is only 5 feet (1.52 metres) below the ground surface and is very quickly transmitted into the foundation causing it to deform. The fact that for certain cases the structure has been shown to deflect downward with respect to the backfill at early times could be a very significant consideration when designing cable or pipe connections to protective structures. The loose backfill and higher weapon-yield cases present the most severe conditions for relative displacement of the structure-backfill system in either vertical directions.

In Appendix B, the vertical deflection of the base of the structure (the average of the two bottom corners) is compared to the rigid body motion of the structure as predicted by methods outlined in Reference 5 for the 1-MT/300-psi (20.7-bar) dense backfill case. Good agreement is demonstrated, and the structure is shown to be deflected downward nearly twice the free-field deflection at a point that is the same depth as, but upstream of the base of, the structure.

Figures 3.30 and 3.31 show the time histories of horizontal stress on the blastward sidewall at points near its top and midpoint, respectively. The horizontal stress arrives sooner in the dense backfill calculations than in the loose backfill calculations due to the higher wave speed in the dense backfill. Both the peak stress and the impulse per unit area delivered to the structure are higher in the loose backfill cases.

Figures 3.32 through 3.37 present comparisons of selected stress time histories of stress components within the blastward sidewall for

all the calculations. Figure 3.38 compares vertical stress time histories for an element on the inside of the leeward sidewall near the midheight. Figure 3.39 compares horizontal stress time histories for an element on the top of the floor near the center. In all cases, the maximum stresses increase with an increase in weapon yield and for the loose backfill condition.

Examination of the time histories of stress and motion shows the presence of frequencies up to 250 Hz in the wave forms for points in the structure. The highest frequencies that can possibly be faithfully represented are given by the reciprocal of the rise time, i.e., 1/10 ms or 100 Hz. As a practical matter, however, credible frequencies will probably not exceed one-half this value or 50 Hz. The FE grid for the backfill material immediately surrounding the structure can transmit frequencies through the dense backfill up to about 70 Hz. However, for the case of the loose backfill, the grid can only transmit frequencies up to about 25 Hz. Thus, the cutoff frequencies are on the order of 50 Hz for the two dense backfill calculations and 25 Hz for the two loose backfill calculations.

### 3.3 SHOCK SPECTRA ANALYSES

The effects of backfill variations on the response of possible equipment mounting points on the roof, sidewalls, and on the floor can be considered by examining the shock spectra for the motion wave forms calculated for these locations. Figures 3.43 through 3.46 present the 2 percent damped shock spectra calculated for the velocity wave forms in Figures 3.17 and 3.14 through 3.42. The inside of the roof of the structure (node 513) has the most severe calculated shock environment of those points examined. In the credible frequency range, the shock environment worsens for the loose backfill and the higher weapon yield. The center of the floor of the structure has the smallest shock environment (Figure 3.46). This is probably due to the fact that the floor rests on the undisturbed stiff shale and is somewhat shielded from the direct

effects of airblast-induced ground shock.

The maximum response of the sidewalls and the roof of the structure over the credible frequency range occurs at frequencies of 15 to 17 Hz. This frequency range, of course, coincides with the frequency range observed for structural motion time histories and supports the discussion concerning mode shapes and frequencies in paragraph 2 of Section 3.2. The maximum response of the floor of the structure occurs at frequencies ranging from 12 to 15 Hz. This response could possibly be controlled by the properties of the clay shale upon which the floor rests.

#### 3.4 SUMMARY

The results of the calculations presented herein demonstrate that both loose backfill and higher weapon yield tend to increase the load on, the stresses and bending moments within, and the deflections of the structure.

The results of the shock spectra analyses also show that the shock environments for the roof, sidewalls, and floor of the structure are worsened by the loose backfill and the higher yield conditions.

The frequencies observed for selected motion time histories of the structure and the deflected shape of the structure at selected times indicate that the structure is responding as in the first two in vacuo modes and/or the second, third, and fourth embedded modes as calculated with upper bound properties. These observed frequencies range from 15 to 17 Hz and are well within the range of credible frequencies of the calculations as controlled by the airblast rise time and duration, the FE grid, and the controlling wave speeds of the materials.

Table 3.1 Maximum and Final Rotations of the Chord Formed by the Two Bottom Corners of the Structure; 300-psi Nominal Overpressure, Dynamic 1-MT and 10-KT Calculations.

Type Rotation	<u>Loose Backfill</u>		<u>Dense Backfill</u>	
	<u>rad</u>	<u>time, ms</u>	<u>rad</u>	<u>time, ms</u>
<u>1-MT Calculations</u>				
Counterclockwise max	0.00164	55	0.00131	44
Return to upright position	0	70	0	100
Clockwise max	0.00155	145	0.00107	173
Final (clockwise)	0.00098	200	0.00090	200
<u>10-KT Calculations</u>				
Counterclockwise max	0.00123	52	0.00107	45
Return to upright position	0	65	0	82
Clockwise max	0.00246	200	0.00246	200
Final (clockwise)	0.00246	200	0.00246	200

Table 3.2 Shear, Thrust, and Bending Moment for Selected Sections Through the Structure at a Time of 62.5 ms after the start of the 1-MT Dense Backfill Calculation.

SECTION	SHEAR FORCE N/M	AXIAL THRUST N/M	BENDING MOMENT N-M/M
AA	-.102376E+08	-.419787E+07	-.473455E+07
BB	-.842209E+07	-.260066E+07	.616023E+07
CC	-.558145E+07	-.108749E+07	.141402E+08
DD	-.233285E+07	-.582594E+06	.190783E+08
EE	-.167006E+06	-.404017E+06	.198071E+08
FF	.166431E+07	-.423725E+06	.193666E+08
GG	.339878E+07	-.436804E+06	.177922E+08
HH	.590060E+07	-.114740E+07	.125775E+08
II	.877934E+07	-.298414E+07	.465592E+07
JJ	.113601E+08	-.443199E+07	-.672029E+07
KK	.270988E+07	-.197473E+08	-.103222E+08
LL	.134079E+07	-.206890E+08	-.750289E+07
MM	.881774E+06	-.213870E+08	-.640362E+07
NN	.884999E+06	-.218552E+08	-.497088E+07
OO	-.832790E+07	.195321E+07	-.229006E+07
PP	-.295019E+07	.280952E+07	-.798783E+07
QQ	-.105504E+07	.327231E+07	-.993590E+07
RR	.320701E+06	.354529E+07	-.104811E+08
SS	.115094E+07	.345789E+07	-.100973E+08
TT	.140339E+07	.343907E+07	-.925915E+07
UU	.199849E+07	.349103E+07	-.815804E+07
VV	.269904E+07	.357057E+07	-.516528E+07
WW	.304686E+07	.342147E+07	-.193066E+07
XX	.685241E+07	.155480E+07	.209488E+07
YY	.601668E+06	-.209155E+08	.509323E+07
ZZ	-.659680E+06	-.196589E+08	.542107E+07
PH	-.978072E+06	-.190817E+08	.629803E+07
OM	-.199715E+07	-.172102E+08	.946443E+07

Table 3.3 Shear, Thrust, and Bending Moment for Selected Sections Through the Structure at a Time of 67.5 ms after the start of the 1-MT Dense Backfill Calculation.

SECTION	SHEAR FORCE N/M	AXIAL THRUST N/M	BENDING MOMENT N-M/M
AA	-.105408E+08	-.374327E+07	-.445841E+07
BB	-.830187E+07	-.279306E+07	.628365E+07
CC	-.541504E+07	-.250716E+07	.140169E+08
DD	-.238525E+07	-.265022E+07	.184372E+08
EE	-.927898E+06	-.266036E+07	.192059E+08
FF	.931420E+06	-.245843E+07	.189098E+08
GG	.281309E+07	-.233132E+07	.176433E+08
HH	.574132E+07	-.245642E+07	.127427E+08
II	.810962E+07	-.296525E+07	.497010E+07
JJ	.110148E+08	-.416021E+07	-.574760E+07
KK	.229079E+07	-.184130E+07	-.108205E+08
LL	.163122E+07	-.192156E+08	-.773167E+07
MM	.120306E+07	-.195514E+08	-.641475E+07
NN	.487381E+06	-.196719E+08	-.474711E+07
OO	-.828929E+07	.151226E+07	-.240470E+07
PP	-.280095E+07	.203062E+07	-.792474E+07
QQ	-.939922E+06	.196075E+07	-.989753E+07
RR	.400944E+05	.218987E+07	-.101598E+08
SS	.619620E+06	.212733E+07	-.994286E+07
TT	.832944E+06	.236858E+07	-.921564E+07
UU	.155073E+07	.275304E+07	-.824304E+07
VV	.217587E+07	.373303E+07	-.561876E+07
WW	.270879E+07	.424453E+07	-.229156E+07
XX	.696349E+07	.260226E+07	.174157E+07
YY	.355575E+05	-.216697E+08	.531669E+07
ZZ	-.186319E+06	-.209106E+08	.566889E+07
PH	-.649240E+06	-.201778E+08	.631605E+07
OH	-.182424E+07	-.184929E+08	.930553E+07

Table 3.4 Shear, Thrust, and Bending Moment for Selected Sections Through the Structure at a Time of 65 ms after the start of the 1-MT Loose Backfill Calculation.

SECTION	SHEAR FORCE N/M	AXIAL THRUST N/M	BENDING MOMENT N-M/M
AA	-.141963E+08	-.520878E+07	-.595056E+07
BB	-.108962E+08	-.414780E+07	.830392E+07
CC	-.728103E+07	-.276500E+07	.183627E+08
DD	-.343906E+07	-.176086E+07	.241612E+08
EE	-.136180E+07	-.150918E+07	.254624E+08
FF	.932809E+06	-.161729E+07	.257662E+08
GG	.329538E+07	-.154365E+07	.245845E+08
HH	.617370E+07	-.106124E+07	.184952E+08
II	.895037E+07	-.404154E+06	.958375E+07
JJ	.128761E+08	-.979693E+05	-.388827E+07
KK	.560826E+06	-.184591E+08	-.155290E+08
LL	.283360E+07	-.177870E+08	-.130873E+08
MM	.339794E+07	-.178012E+08	-.107252E+08
NN	.441126E+07	-.186154E+08	-.461006E+07
OO	-.677665E+07	.747343E+07	-.539721E+07
PP	-.236499E+07	.709201E+07	-.100923E+08
QQ	-.555661E+06	.609523E+07	-.121351E+08
RR	.453260E+06	.614428E+07	-.121088E+08
SS	.112561E+07	.589591E+07	-.119727E+08
TT	.220010E+07	.618898E+07	-.109922E+08
UU	.294998E+07	.634900E+07	-.958381E+07
VV	.310014E+07	.678928E+07	-.581641E+07
WW	.337758E+07	.627631E+07	-.218816E+07
XX	.444350E+07	.522094E+07	.114505E+07
YY	-.244108E+07	-.189039E+08	.462251E+07
ZZ	-.181801E+07	-.200371E+08	.762922E+07
PH	-.229627E+07	-.205974E+08	.893792E+07
OM	-.364321E+07	-.204530E+08	.135893E+08

Table 3.5 Shear, Thrust, and Bending Moment for Selected Sections Through the Structure at a Time of 70 ms after the start of the 1-MT Loose Backfill Calculation.

SECTION	SHEAR FORCE N/M	AXIAL THRUST N/M	BENDING MOMENT N-M/M
AA	-.126100E+08	-.542594E+07	-.361896E+07
BB	-.998340E+07	-.463273E+07	.900363E+07
CC	-.669010E+07	-.331368E+07	.195888E+08
DD	-.286998E+07	-.263861E+07	.254194E+08
EE	-.854766E+06	-.244692E+07	.266279E+08
FF	.106663E+07	-.259695E+07	.268819E+08
GG	.347018E+07	-.306256E+07	.258397E+08
HH	.882408E+07	-.412874E+07	.191881E+08
II	.120943E+08	-.516794E+07	.692681E+07
JJ	.149694E+08	-.602264E+07	-.881551E+07
KK	.469836E+07	-.227296E+08	-.152649E+08
LL	.286651E+07	-.230255E+08	-.928701E+07
MM	.108774E+07	-.235379E+08	-.775057E+07
NN	.699506E+06	-.242016E+08	-.700114E+07
OO	-.109216E+08	.261314E+07	-.295817E+07
PP	-.400304E+07	.370663E+07	-.102317E+08
QQ	-.113149E+07	.446511E+07	-.123803E+08
RR	.365951E+06	.401589E+07	-.125332E+08
SS	.916139E+06	.398654E+07	-.119339E+08
TT	.673871E+06	.413670E+07	-.112768E+08
UU	.120950E+07	.440977E+07	-.105219E+08
VV	.201341E+07	.541392E+07	-.777864E+07
WW	.234823E+07	.569884E+07	-.484150E+07
XX	.561569E+07	.574191E+07	-.394862E+06
YY	-.327899E+07	-.216749E+08	.534396E+07
ZZ	-.207601E+07	-.204812E+08	.970450E+07
PH	-.223268E+07	-.197005E+08	.115246E+08
OM	-.137432E+07	-.187048E+08	.144245E+08

Table 3.6 Shear, Thrust, and Bending Moment for Selected Sections Through the Structure at a Time of 55 ms after the start of the 10-KT Dense Backfill Calculation.

SECTION	SHEAR FORCE N/M	AXIAL THRUST N/M	BENDING MOMENT N-M/M
AA	-.708742E+07	-.310741E+07	-.298061E+07
BB	-.560417E+07	-.226156E+07	.398263E+07
CC	-.383507E+07	-.190823E+07	.913651E+07
DD	-.143084E+07	-.173256E+07	.119213E+08
EE	-.344119E+06	-.170868E+07	.123111E+08
FF	.658962E+06	-.196648E+07	.122437E+08
GG	.136859E+07	-.214758E+07	.115836E+08
HH	.259869E+07	-.239354E+07	.937212E+07
II	.524131E+07	-.252498E+07	.513587E+07
JJ	.823865E+07	-.317721E+07	-.301177E+07
KK	.133345E+07	-.120698E+08	-.823104E+07
LL	.127646E+07	-.116914E+08	-.638933E+07
MM	.137604E+07	-.113797E+08	-.543467E+07
NN	.146687E+07	-.109227E+08	-.315412E+07
OO	-.434710E+07	.163597E+07	-.243390E+07
PP	-.208855E+07	.180915E+07	-.610923E+07
QQ	-.101039E+07	.244167E+07	-.789129E+07
RR	.411891E+06	.295934E+07	-.835217E+07
SS	.101774E+07	.295137E+07	-.810272E+07
TT	.159040E+07	.312223E+07	-.709599E+07
UU	.204698E+07	.317425E+07	-.588824E+07
VV	.269139E+07	.300242E+07	-.312572E+07
WW	.274200E+07	.256782E+07	-.985271E+06
XX	.386048E+07	.107701E+07	.261117E+07
YY	.302986E+06	-.126995E+08	.371076E+07
ZZ	-.371355E+06	-.125087E+08	.413848E+07
PH	-.157152E+06	-.124280E+08	.435202E+07
OM	-.114092E+07	-.119751E+08	.524757E+07

Table 3.7 Shear, Thrust, and Bending Moment for Selected Sections Through the Structure at a Time of 60 ms after the start of the 10-KT Dense Backfill Calculation.

SECTION	SHEAR FORCE N/M	AXIAL THRUST N/M	BENDING MOMENT N-M/M
AA	-.5667139E+07	-.225562E+07	-.279653E+07
BB	-.539512E+07	-.132093E+07	.445817E+07
CC	-.368965E+07	-.581998E+06	.100221E+08
DD	-.129289E+07	.185881E+06	.129685E+08
EE	.225718E+06	.102783E+06	.133841E+08
FF	.147794E+07	.482639E+05	.129637E+08
GG	.268416E+07	.440422E+05	.117832E+08
HH	.468136E+07	-.295944E+06	.752211E+07
II	.598219E+07	-.155648E+07	.177484E+07
JJ	.524790E+07	-.259686E+07	-.493959E+07
KK	.129277E+07	-.117827E+08	-.654546E+07
LL	.461067E+06	-.123938E+08	-.511871E+07
MM	.110455E+06	-.127101E+08	-.474634E+07
NN	.351496E+06	-.129674E+08	-.405265E+07
OO	-.565722E+07	.528942E+06	-.176414E+07
PP	-.244739E+07	.114866E+07	-.621389E+07
QQ	-.952297E+06	.152115E+07	-.798445E+07
RR	.138497E+06	.190272E+07	-.842318E+07
SS	.525538E+06	.219664E+07	-.801676E+07
TT	.102066E+07	.231309E+07	-.743547E+07
UU	.150731E+07	.260704E+07	-.639638E+07
VV	.230882E+07	.303057E+07	-.359870E+07
WW	.289801E+07	.238635E+07	-.573209E+06
XX	.481748E+07	.924269E+06	.274108E+07
YY	.729793E+06	-.152492E+08	.396570E+07
ZZ	-.247014E+06	-.143632E+08	.383059E+07
PH	-.508312E+06	-.135841E+08	.436164E+07
OH	-.101516E+07	-.118931E+08	.589363E+07

Table 3.8 Shear, Thrust, and Bending Moment for Selected Sections Through the Structure at a Time of 60 ms after the start of the 10-KT Loose Backfill Calculation.

SECTION	SHEAR FORCE N/M	AXIAL THRUST N/M	BENDING MOMENT N-M/M
AA	-.837063E+07	-.251423E+07	-.401623E+07
BB	-.681801E+07	-.152348E+07	.477527E+07
CC	-.505923E+07	-.548072E+06	.115312E+08
DD	-.267273E+07	.390536E+06	.158846E+08
EE	-.128864E+07	.658117E+06	.169397E+08
FF	.876684E+05	.644790E+06	.172788E+08
GG	.147724E+07	.600936E+06	.167531E+08
HH	.456443E+07	.382205E+06	.129557E+08
II	.659144E+07	.616610E+05	.576993E+07
JJ	.702297E+07	-.472293E+06	-.270264E+07
KK	-.761095E+06	-.902724E+07	-.952087E+07
LL	.765878E+06	-.100209E+08	-.100927E+08
MM	.260108E+07	-.105343E+08	-.885179E+07
NN	.417948E+07	-.115581E+08	-.300420E+07
OO	-.387288E+07	.591771E+07	-.470427E+07
PP	-.157752E+07	.610769E+07	-.808221E+07
QQ	.200900E+06	.624570E+07	-.924654E+07
RR	.131810E+07	.614102E+07	-.848592E+07
SS	.154511E+07	.583787E+07	-.779471E+07
TT	.191239E+07	.544645E+07	-.692124E+07
UU	.190125E+07	.501453E+07	-.586036E+07
VV	.201557E+07	.430022E+07	-.339583E+07
WW	.292207E+07	.294156E+07	-.103812E+07
XX	.370098E+07	.185016E+07	.212183E+07
YY	-.475672E+06	-.124928E+08	.330415E+07
ZZ	-.125977E+07	-.121930E+08	.452473E+07
PH	-.157706E+07	-.121891E+08	.557428E+07
OM	-.194803E+07	-.115975E+08	.845751E+07

Table 3.9 Shear, Thrust, and Bending Moment for Selected Sections Through the Structure at a Time of 62.5 ms after the start of the 10-KT Loose Backfill Calculation.

SECTION	SHEAR FORCE N/M	AXIAL THRUST N/M	BENDING MOMENT N-M/M
AA	-.930198E+07	-.347173E+07	-.367252E+07
BB	-.719139E+07	-.300188E+07	.603143E+07
CC	-.477745E+07	-.230685E+07	.127901E+08
DD	-.207519E+07	-.162004E+07	.165662E+08
EE	-.728168E+06	-.125374E+07	.172502E+08
FF	.799313E+06	-.985063E+06	.171375E+08
GG	.192589E+07	-.645301E+06	.161367E+08
HH	.390547E+07	-.300309E+06	.124087E+08
II	.610161E+07	-.180732E+06	.633213E+07
JJ	.884546E+07	-.225686E+06	-.305396E+07
KK	.542127E+06	-.119822E+08	-.104574E+08
LL	.154763E+07	-.116976E+08	-.884029E+07
MM	.226166E+07	-.113745E+08	-.755339E+07
NN	.299993E+07	-.108358E+08	-.364068E+07
OO	-.428738E+07	.380711E+07	-.351084E+07
PP	-.171237E+07	.403637E+07	-.736229E+07
QQ	-.845657E+06	.424938E+07	-.894381E+07
RR	.250787E+06	.486314E+07	-.938042E+07
SS	.923567E+06	.515836E+07	-.893055E+07
TT	.178687E+07	.518465E+07	-.820425E+07
UU	.245262E+07	.530228E+07	-.686940E+07
VV	.239131E+07	.474244E+07	-.411292E+07
WW	.299119E+07	.373610E+07	-.165638E+07
XX	.302489E+07	.331989E+07	.201365E+07
YY	-.147808E+07	-.126736E+08	.347480E+07
ZZ	-.106456E+07	-.130285E+08	.541136E+07
PH	-.145509E+07	-.133681E+08	.626215E+07
OM	-.194711E+07	-.129644E+08	.900207E+07

Table 3.10 Shear, Thrust, and Bending Moment for Selected Sections Through the Structure at a Time of 67.5 ms after the start of the 10-KT Loose Backfill Calculation.

SECTION	SHEAR FORCE N/M	AXIAL THRUST N/M	BENDING MOMENT N-M/M
AA	-.774121E+07	-.292338E+07	-.167174E+07
BB	-.596176E+07	-.293576E+07	.666854E+07
CC	-.382717E+07	-.261453E+07	.125872E+08
DD	-.137209E+07	-.217855E+07	.156633E+08
EE	-.108191E+06	-.227178E+07	.163542E+08
FF	.131357E+07	-.251108E+07	.162448E+08
GG	.281744E+07	-.271210E+07	.151872E+08
HH	.512011E+07	-.321084E+07	.109112E+08
II	.724939E+07	-.377357E+07	.375025E+07
JJ	.838037E+07	-.402683E+07	-.550379E+07
KK	.241597E+07	-.127474E+08	-.882071E+07
LL	.120910E+07	-.136723E+08	-.505524E+07
MM	.404682E+06	-.142650E+08	-.531307E+07
NN	.198027E+06	-.150610E+08	-.515472E+07
OO	-.672730E+07	.304101E+06	-.194052E+07
PP	-.270490E+07	.583297E+06	-.690150E+07
QQ	-.895387E+06	.947876E+06	-.873050E+07
RR	-.728234E+05	.118034E+07	-.907855E+07
SS	.448222E+06	.121415E+07	-.884865E+07
TT	.910445E+06	.143501E+07	-.834929E+07
UU	.134963E+07	.177211E+07	-.759809E+07
VV	.157545E+07	.322431E+07	-.518750E+07
WW	.291679E+07	.337939E+07	-.316076E+07
XX	.312490E+07	.427564E+07	.120567E+07
YY	-.208479E+07	-.132260E+08	.366948E+07
ZZ	-.134446E+07	-.129743E+08	.664752E+07
PH	-.906459E+06	-.127276E+08	.764057E+07
OM	-.116194E+06	-.119210E+08	.837061E+07

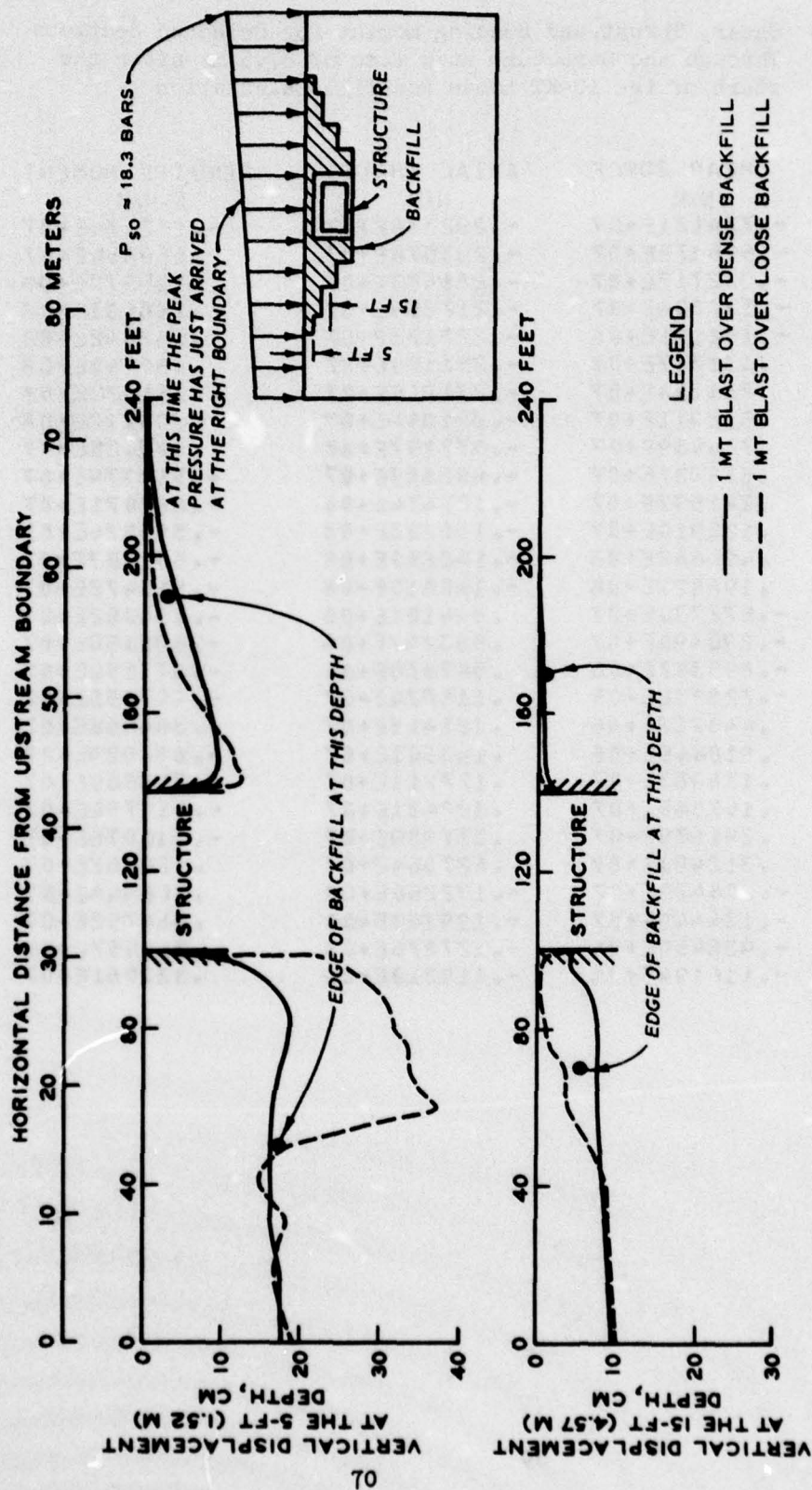


Figure 3.1 Instantaneous pattern of vertical displacements along two lines through the backfill at 60 ms after the start of the problem, 1 MT loading.

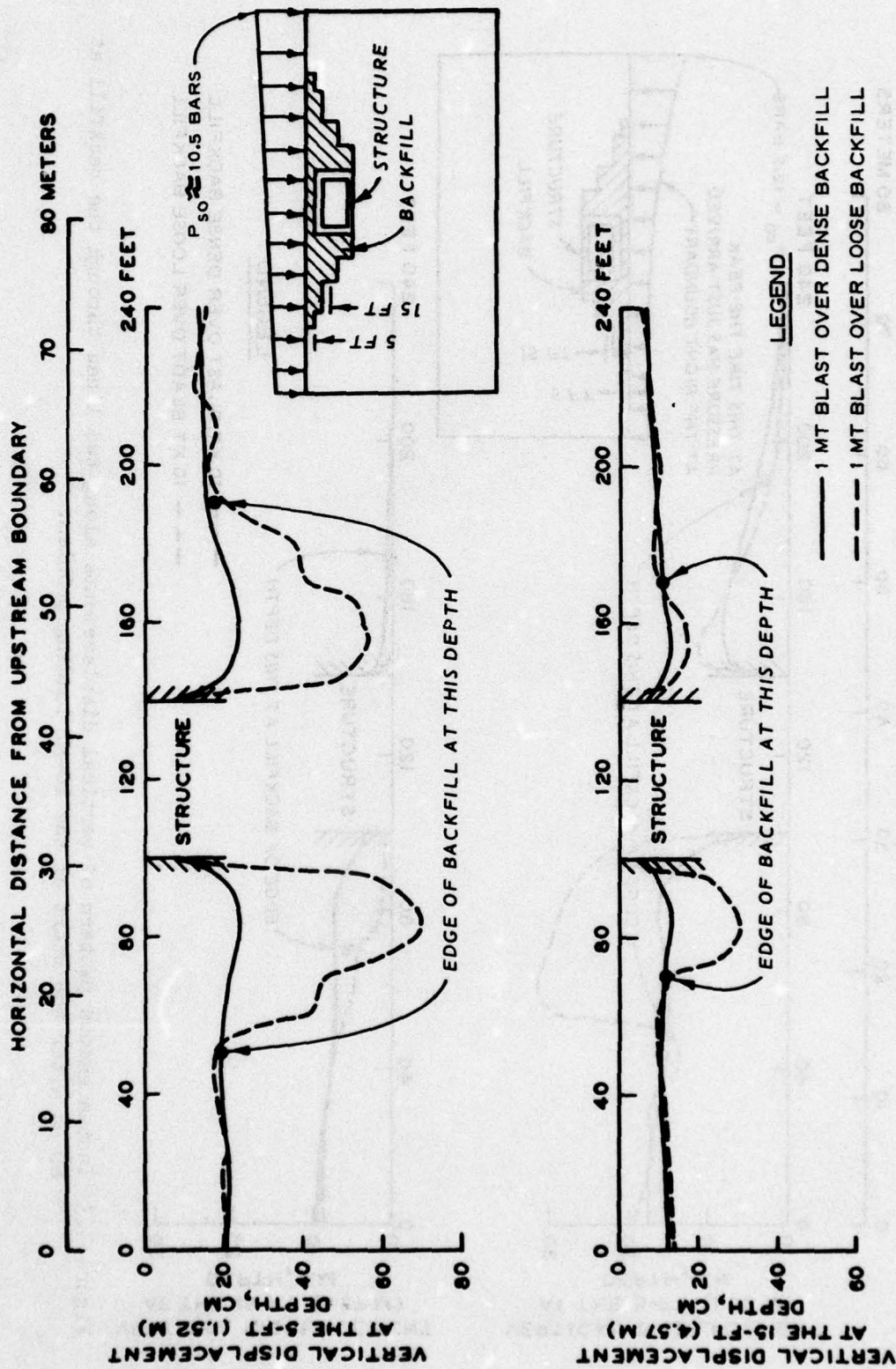


Figure 3.2 Instantaneous pattern of vertical displacements along two lines through the backfill at 100 ms after the start of the 1-MT loading problem.

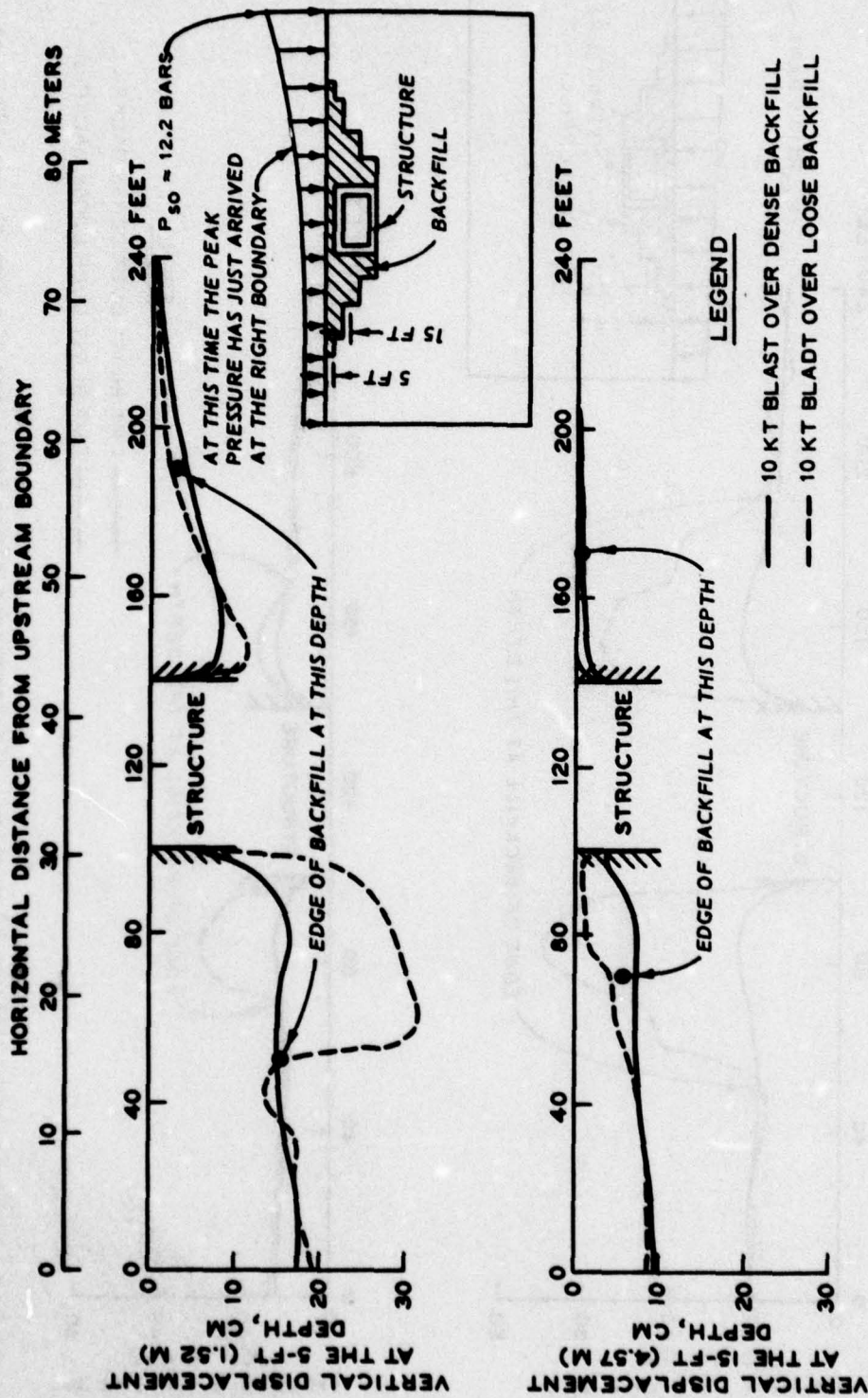


Figure 3.3 Instantaneous pattern of vertical displacements along two lines through the backfill at 60 ms after the start of the 10-KT loading problem.

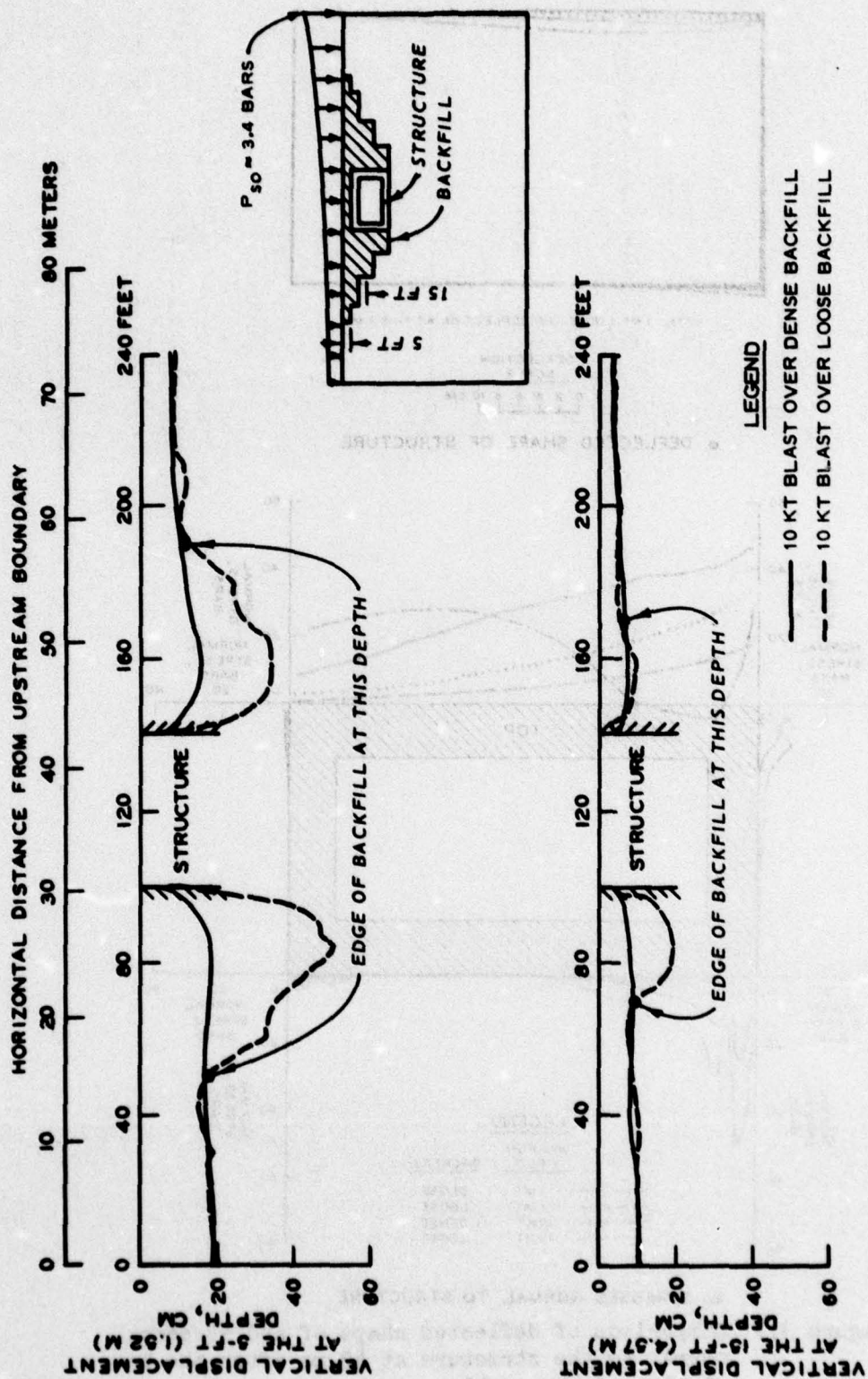
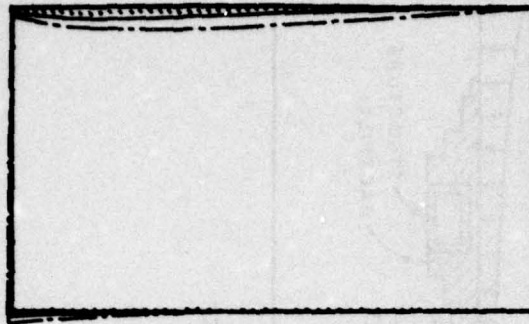


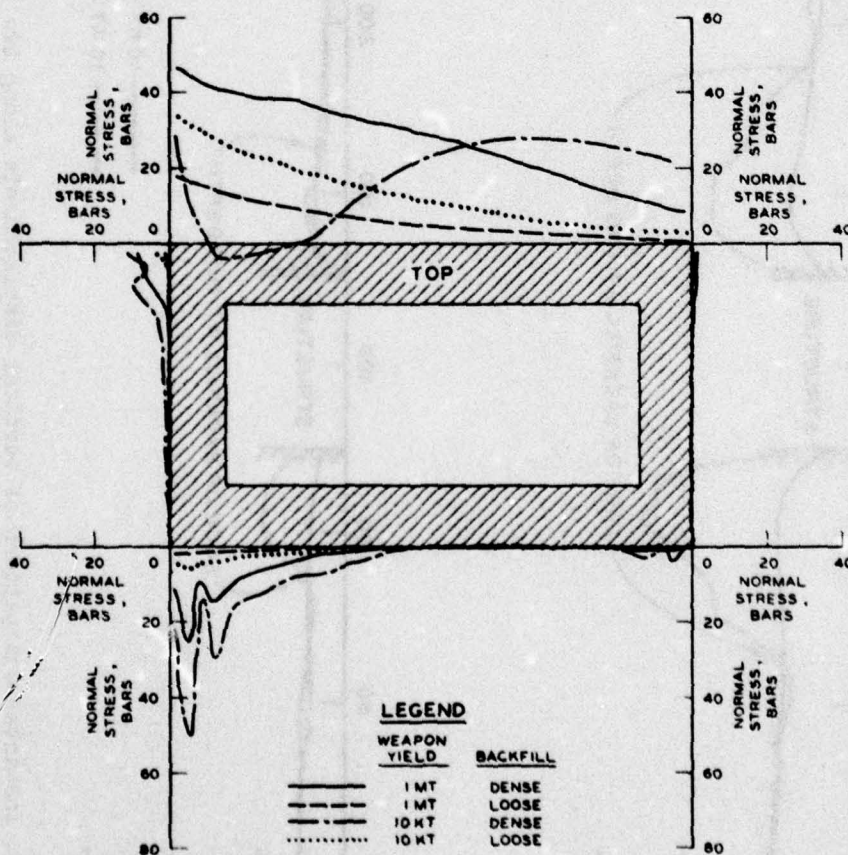
Figure 3.4 Instantaneous pattern of vertical displacements along two lines through the backfill at 100 ms after the start of the 10-KT loading problem.



NOTE: 1 MT LOOSE - NO DEFLECTION AT THIS TIME

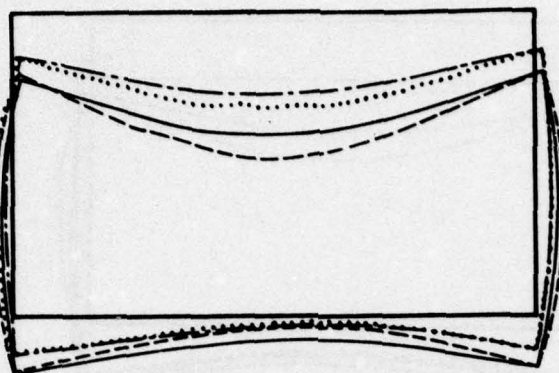
DEFLECTION  
SCALE  
0 2 4 6 8 10 CM

a. DEFLECTED SHAPE OF STRUCTURE



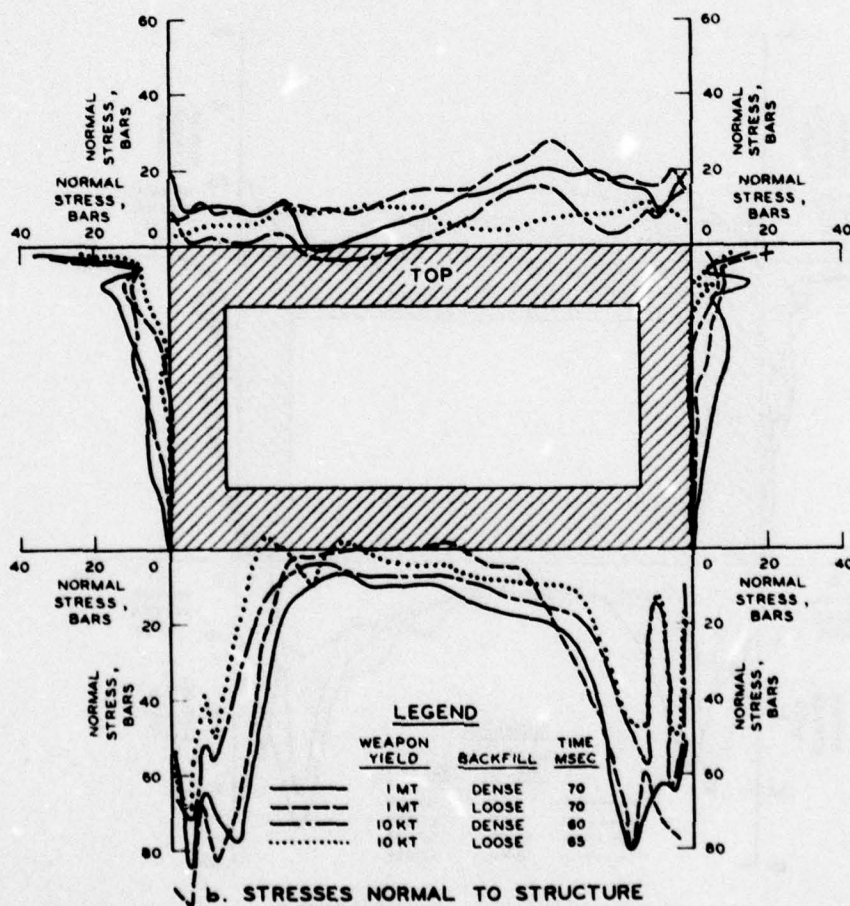
b. STRESSES NORMAL TO STRUCTURE

Figure 3.5 Comparison of deflected shape of and stresses normal to the structure at 40 ms after the beginning of the problem.



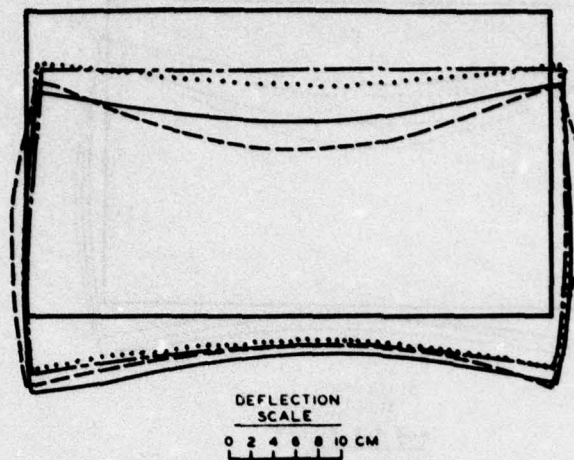
DEFLECTION  
SCALE  
0 2 4 6 8 10 CM

a. DEFLECTED SHAPE OF STRUCTURE

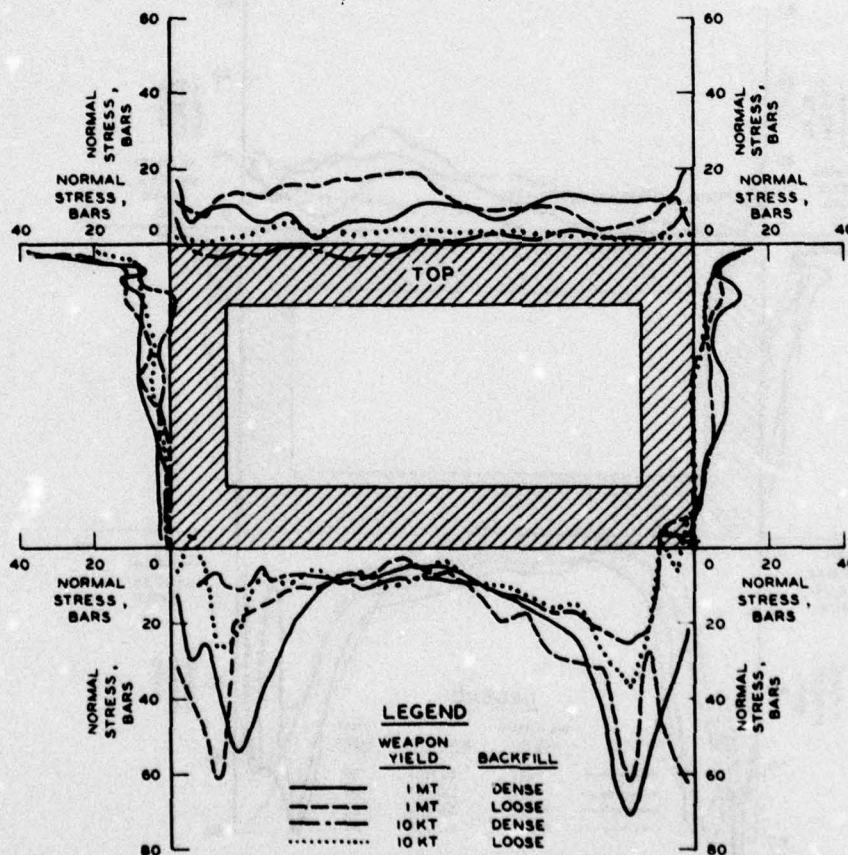


b. STRESSES NORMAL TO STRUCTURE

Figure 3.6 Comparison of deflected shape of and stresses normal to the structure at the times that the maximum relative deflection of the center of the roof occurs.

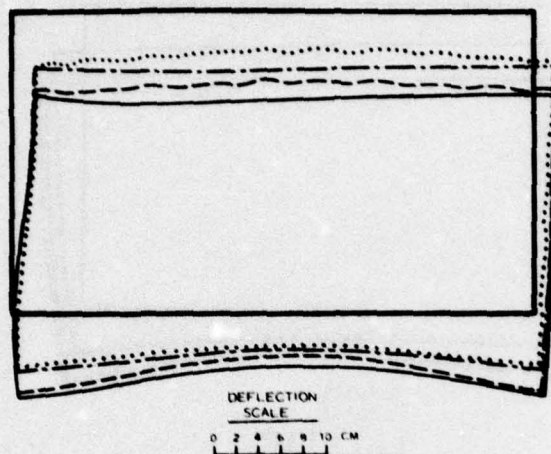


a. DEFLECTED SHAPE OF STRUCTURE

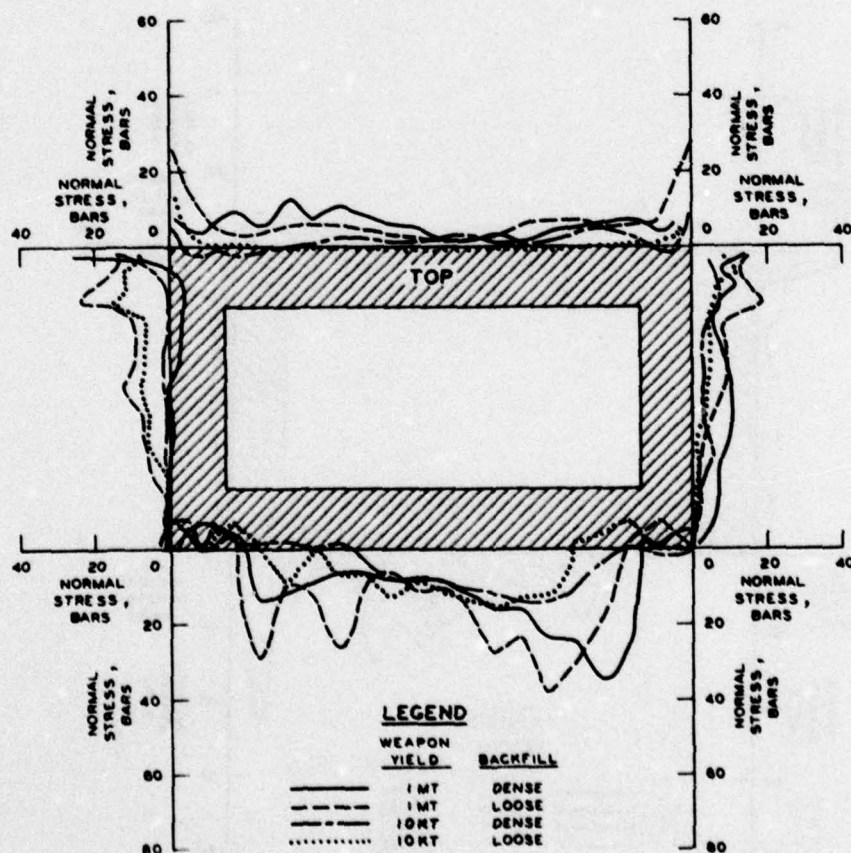


b. STRESSES NORMAL TO STRUCTURE

Figure 3.7 Comparison of deflected shape of and stresses normal to the structure at 80 ms after the beginning of the problem.

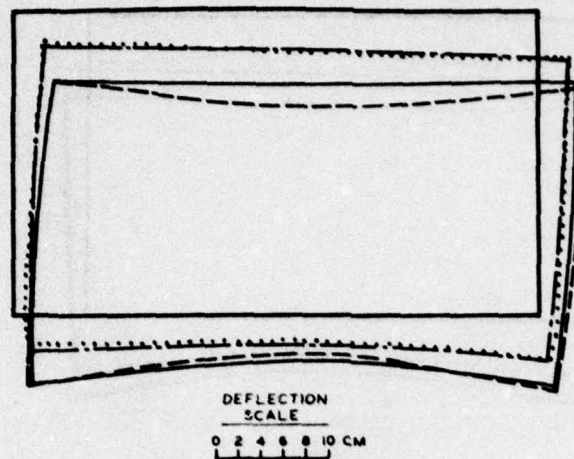


a. DEFLECTED SHAPE OF STRUCTURE

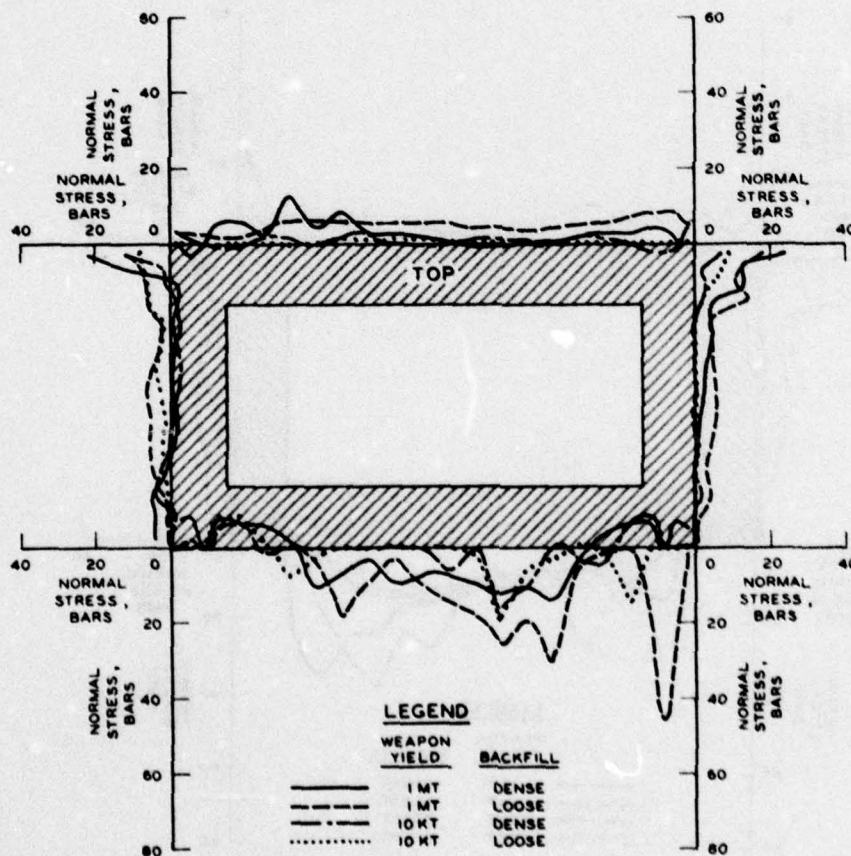


b. STRESSES NORMAL TO STRUCTURE

Figure 3.8 Comparison of deflected shape of and stresses normal to the structure at 100 ms after the beginning of the problem.

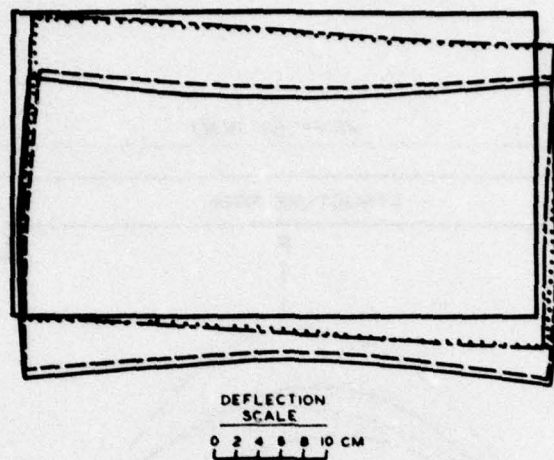


a. DEFLECTED SHAPE OF STRUCTURE

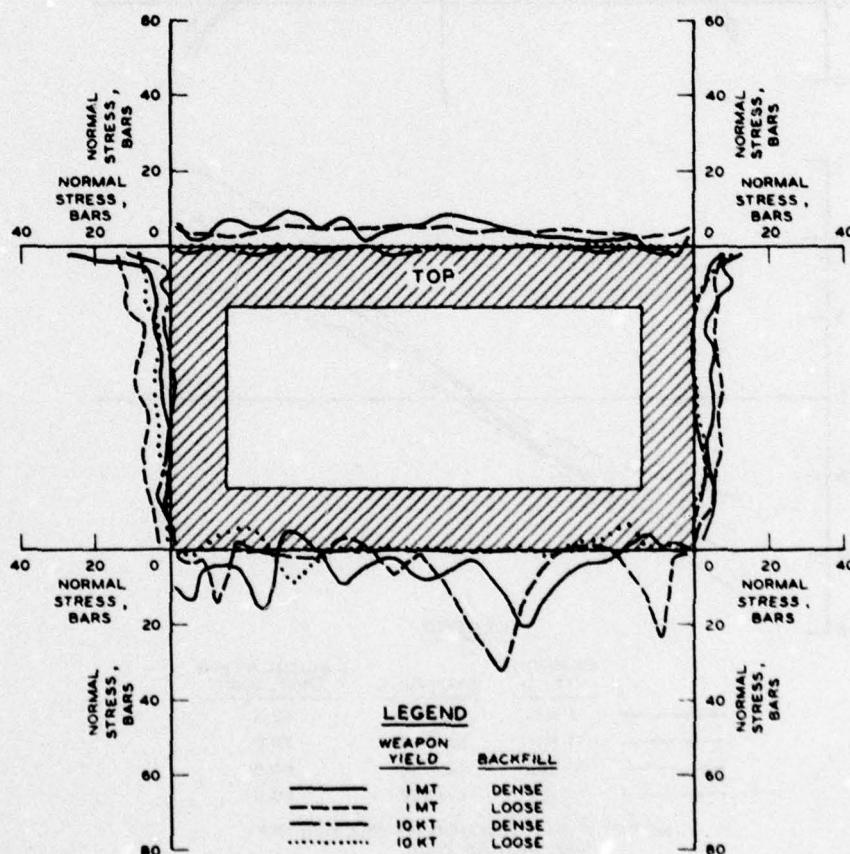


b. STRESSES NORMAL TO STRUCTURE

Figure 3.9 Comparison of deflected shape of and stresses normal to the structure at 150 ms after the beginning of the problem

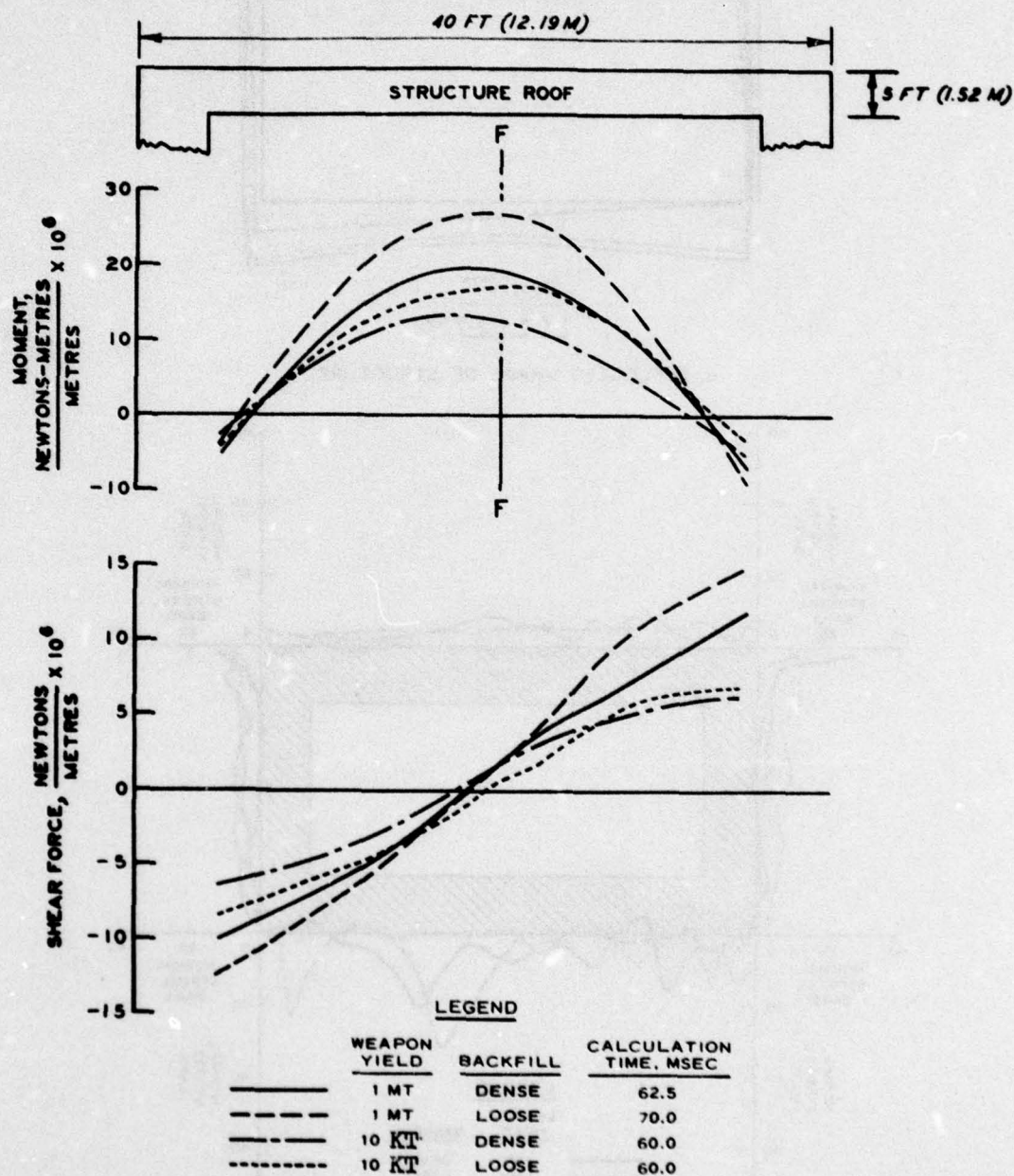


a. DEFLECTED SHAPE OF STRUCTURE



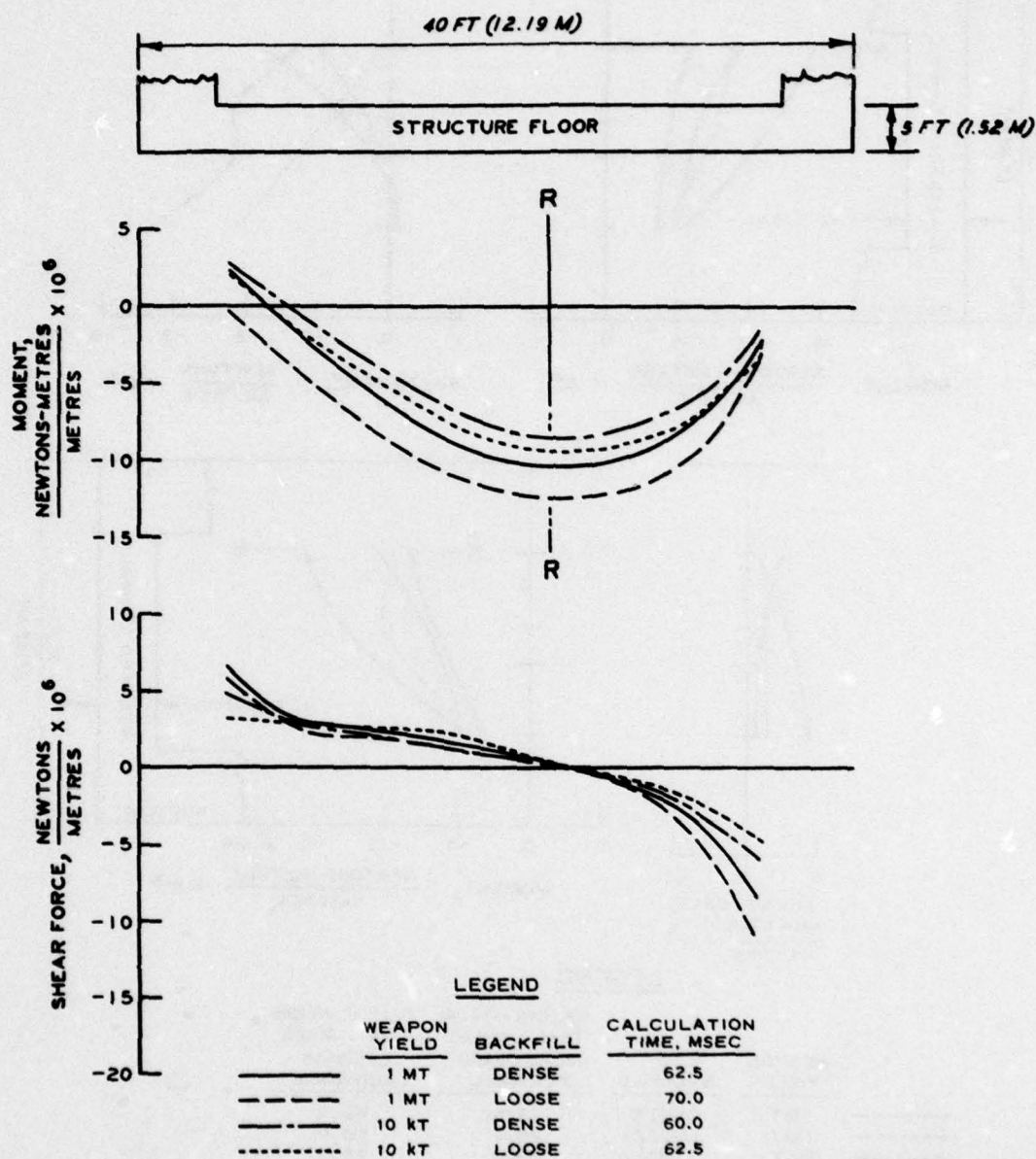
b. STRESSES NORMAL TO STRUCTURE

Figure 3.10 Comparison of the deflected shape of and stresses normal to structure at 200 ms after the beginning of the problem.



NOTE: FOR LOCATION OF SECTION FF  
SEE FIGURE 2.20.

Figure 3.11 Comparison of moment and shear diagrams for selected roof sections at the time that the radial stress in element 514 (Figure 2.20) maximizes.



NOTE: FOR LOCATION OF SECTION RR  
SEE FIGURE 2.20

Figure 3.12 Comparison of moment and shear diagrams for selected floor sections at the time that the radial stress in element 515 (Figure 2.20) maximizes.

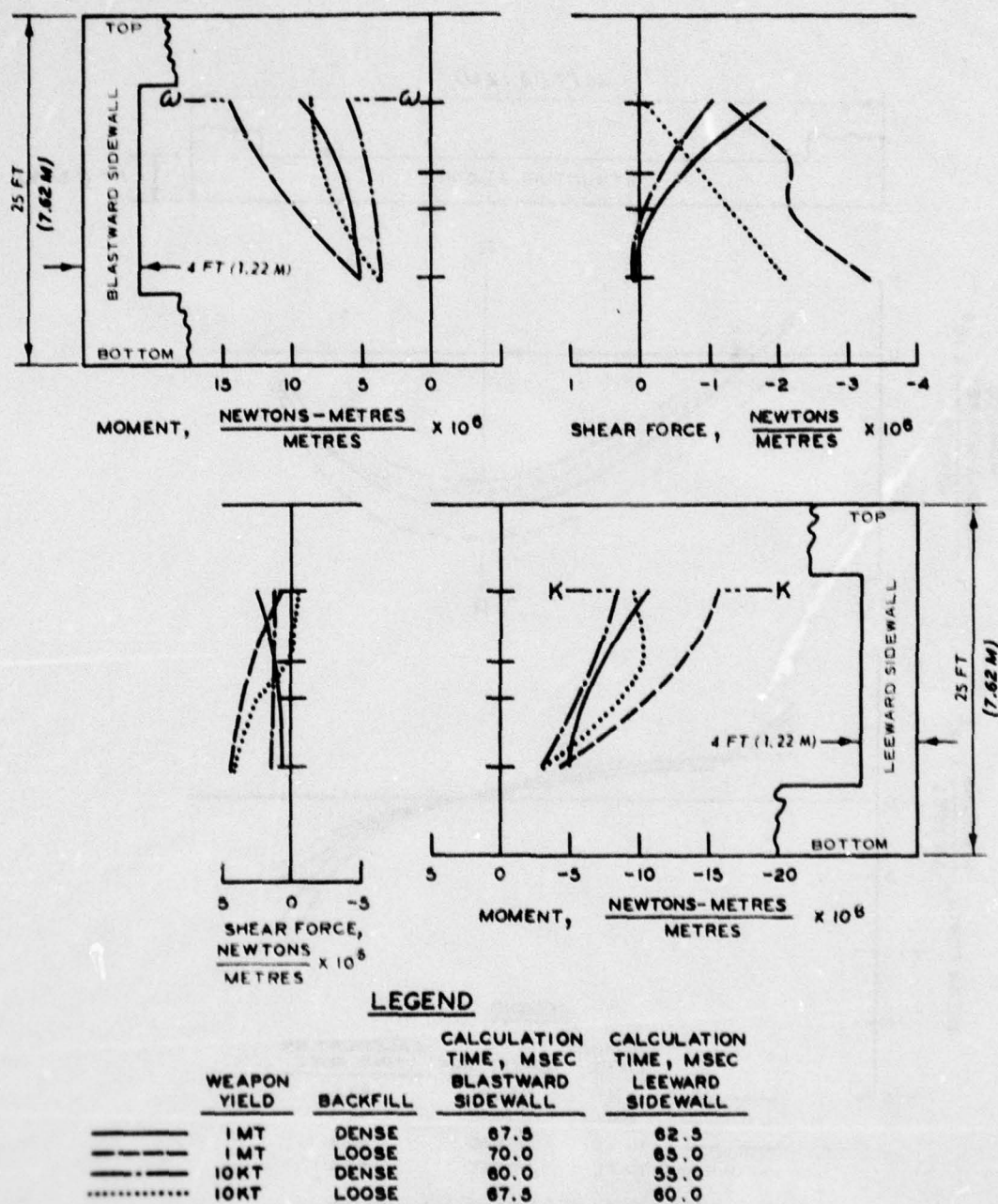


Figure 3.13 Comparison of maximum moment and shear diagrams for selected sidewall sections at the time that the vertical stress in elements 369 and 679 maximize in the blastward and leeward sidewalls, respectively.

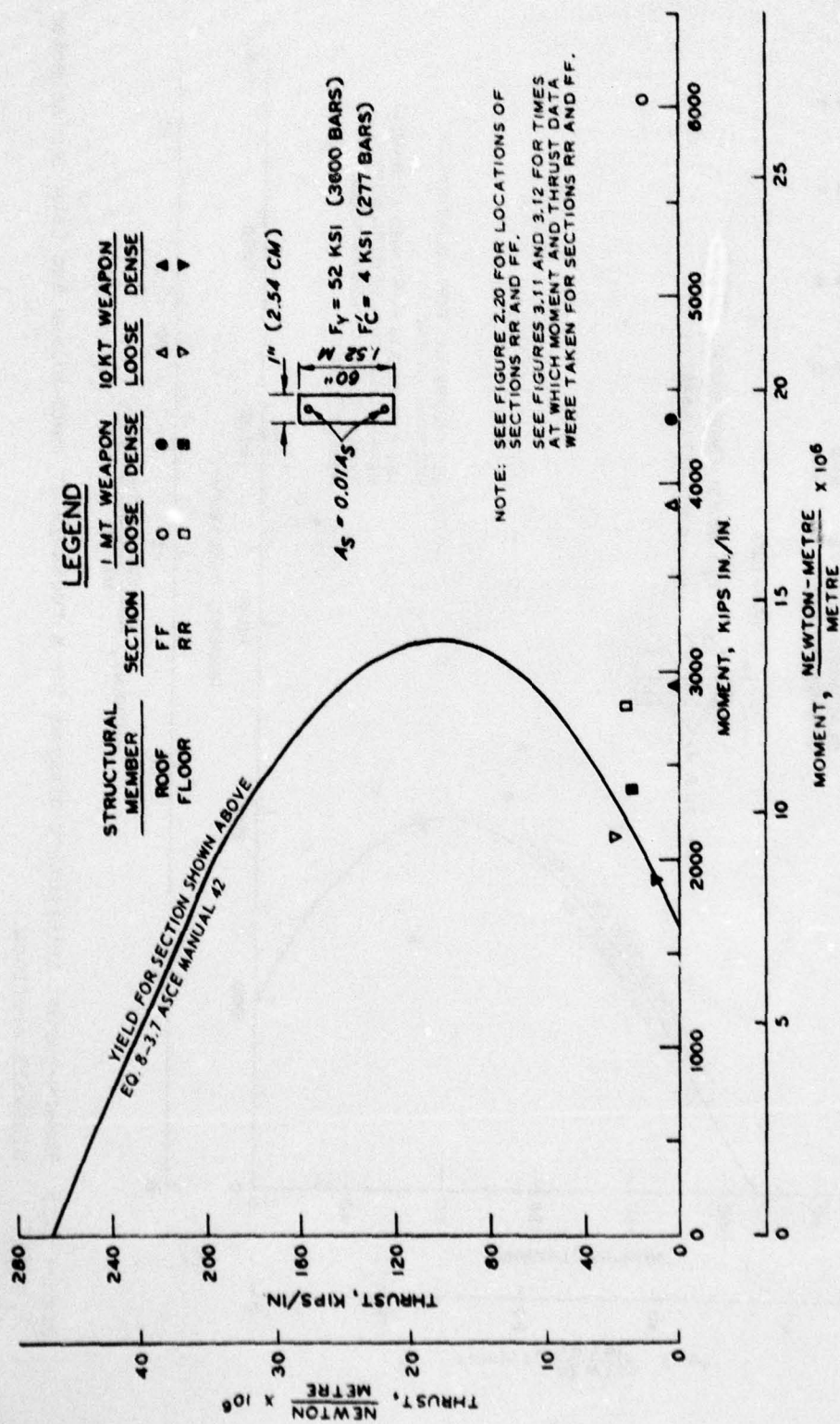


Figure 3.14 Moment-thrust interaction diagram for a rectangular beam-column and data for selected roof and floor sections.

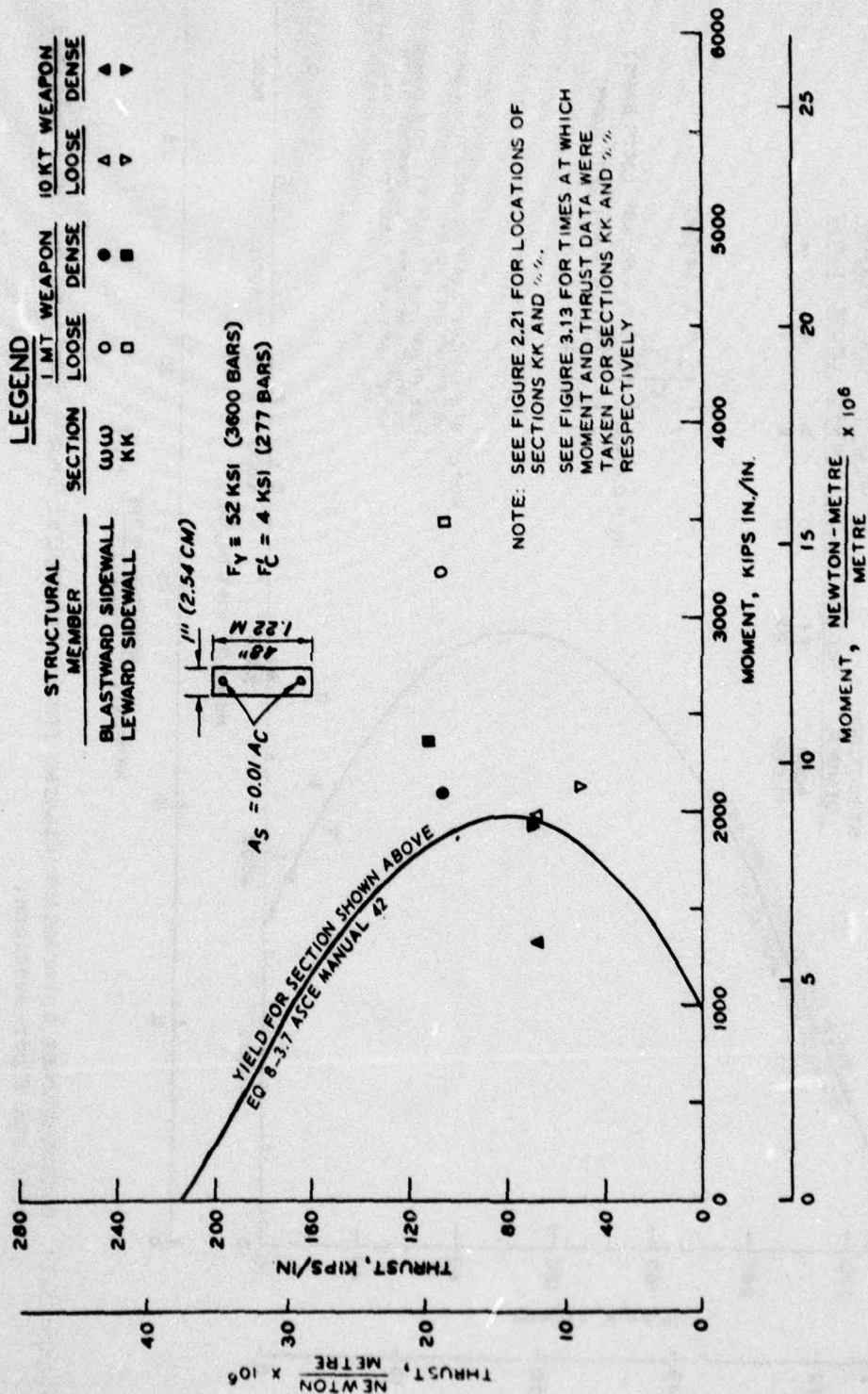


Figure 3.15 Moment-thrust interaction diagram for a rectangular beam-column and data for selected sidewall sections.

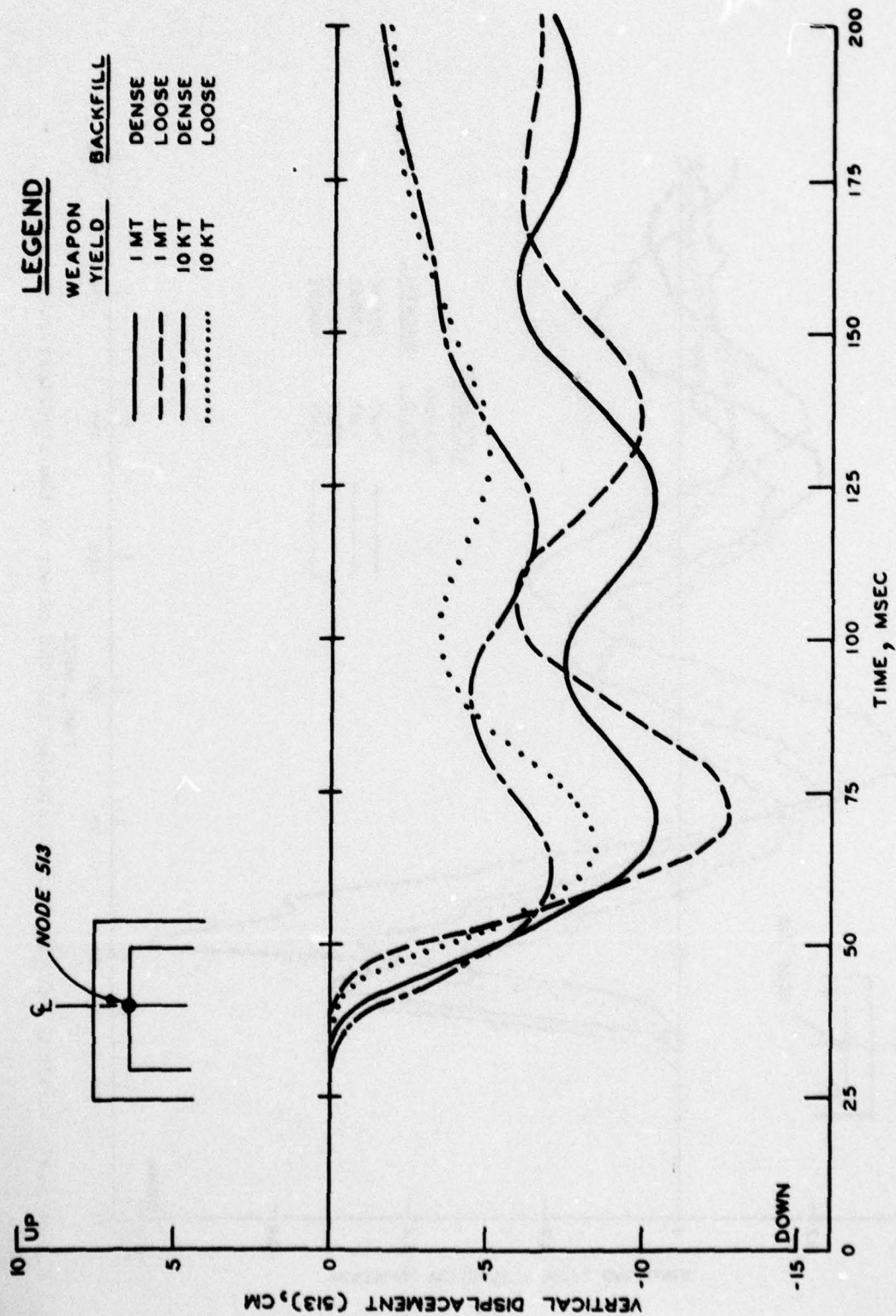
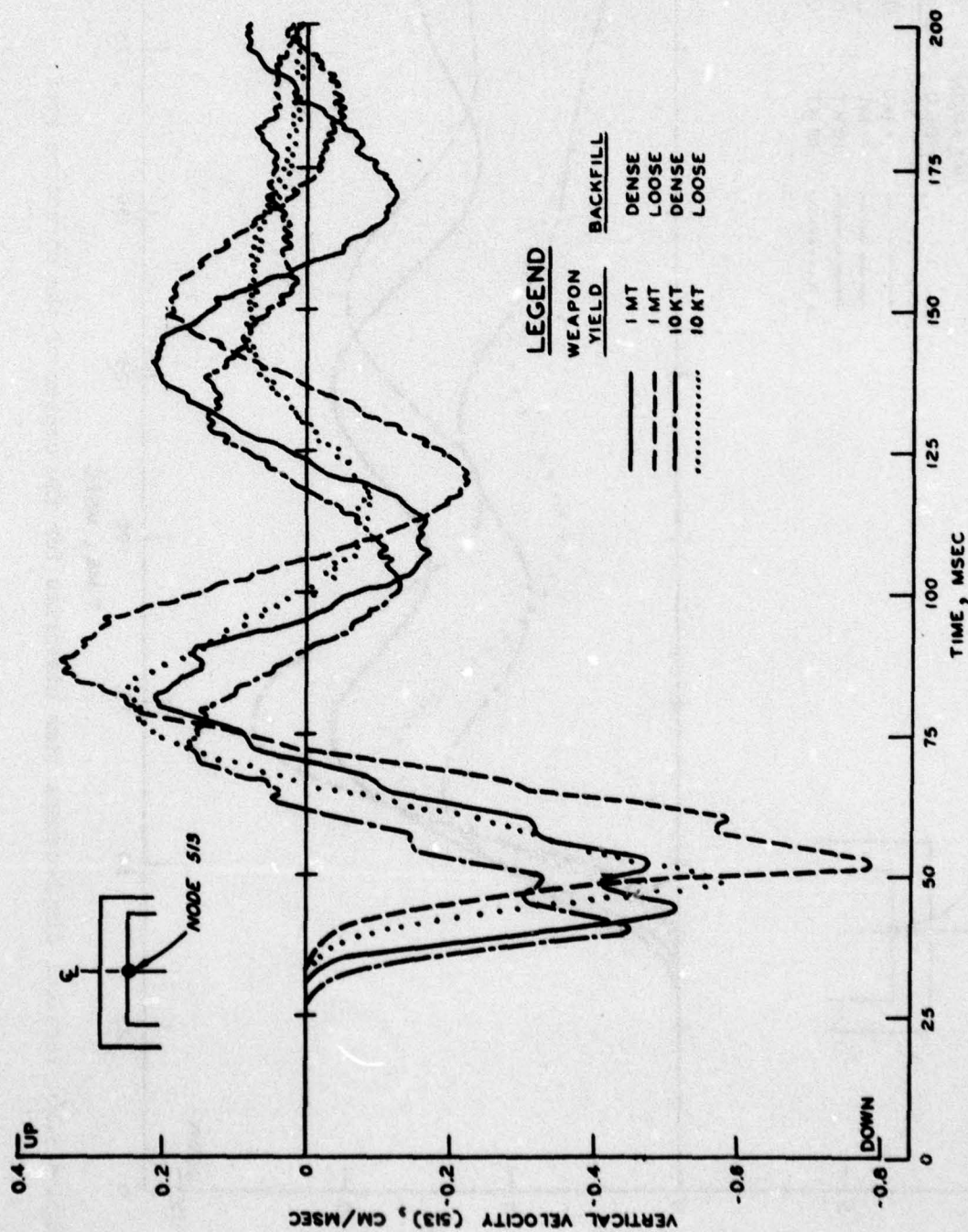
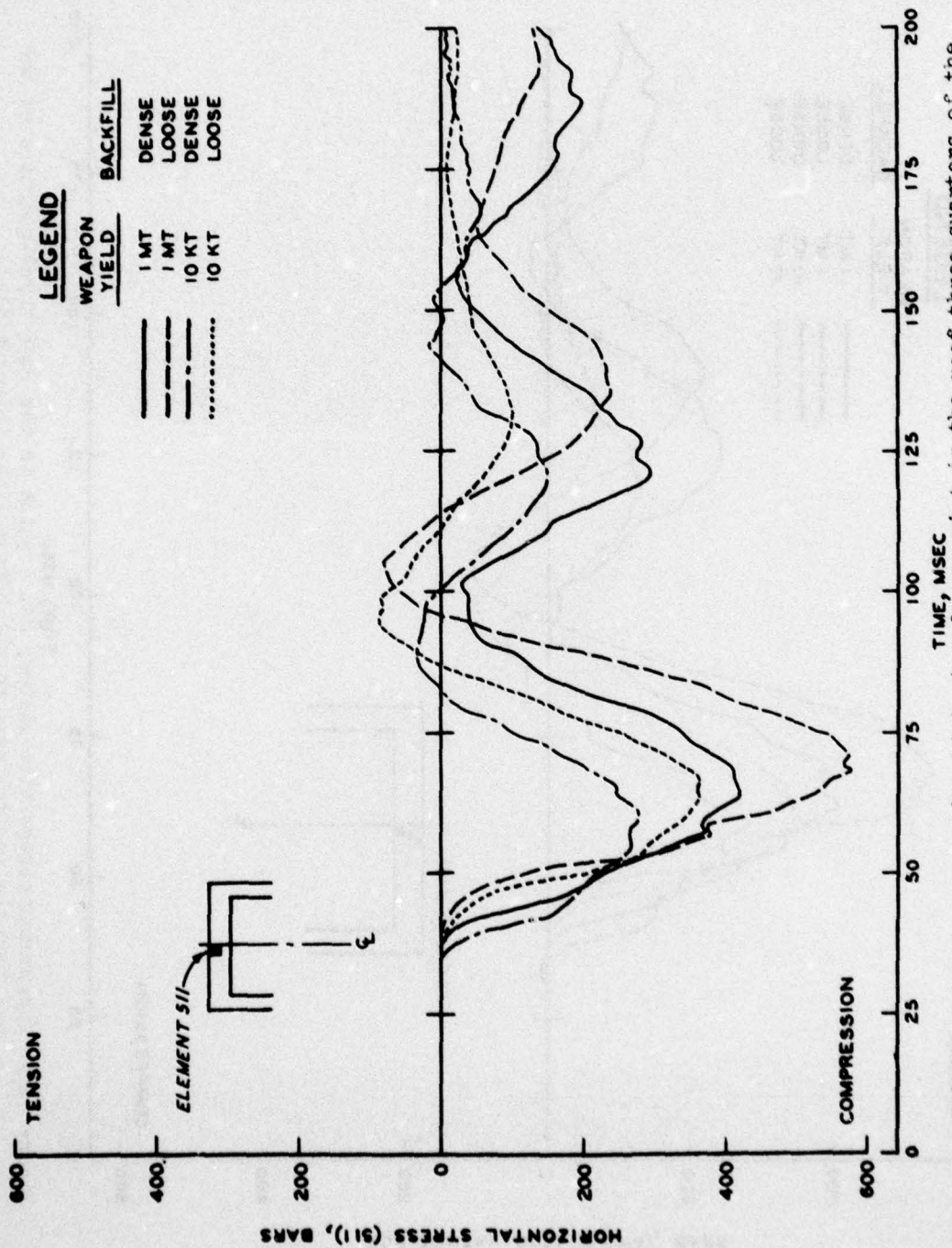
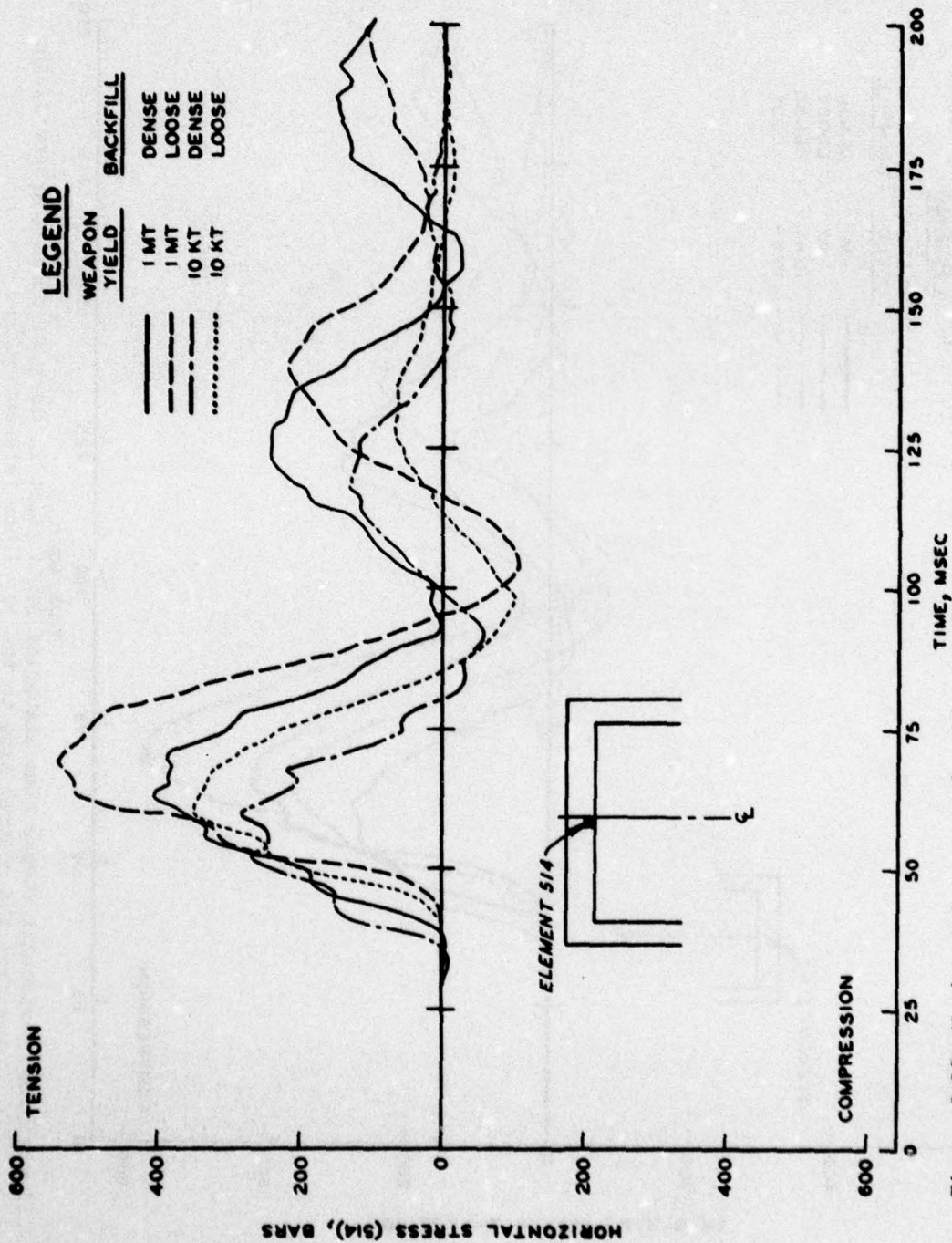


Figure 3.16 Vertical displacement time histories for the center of the structure roof.







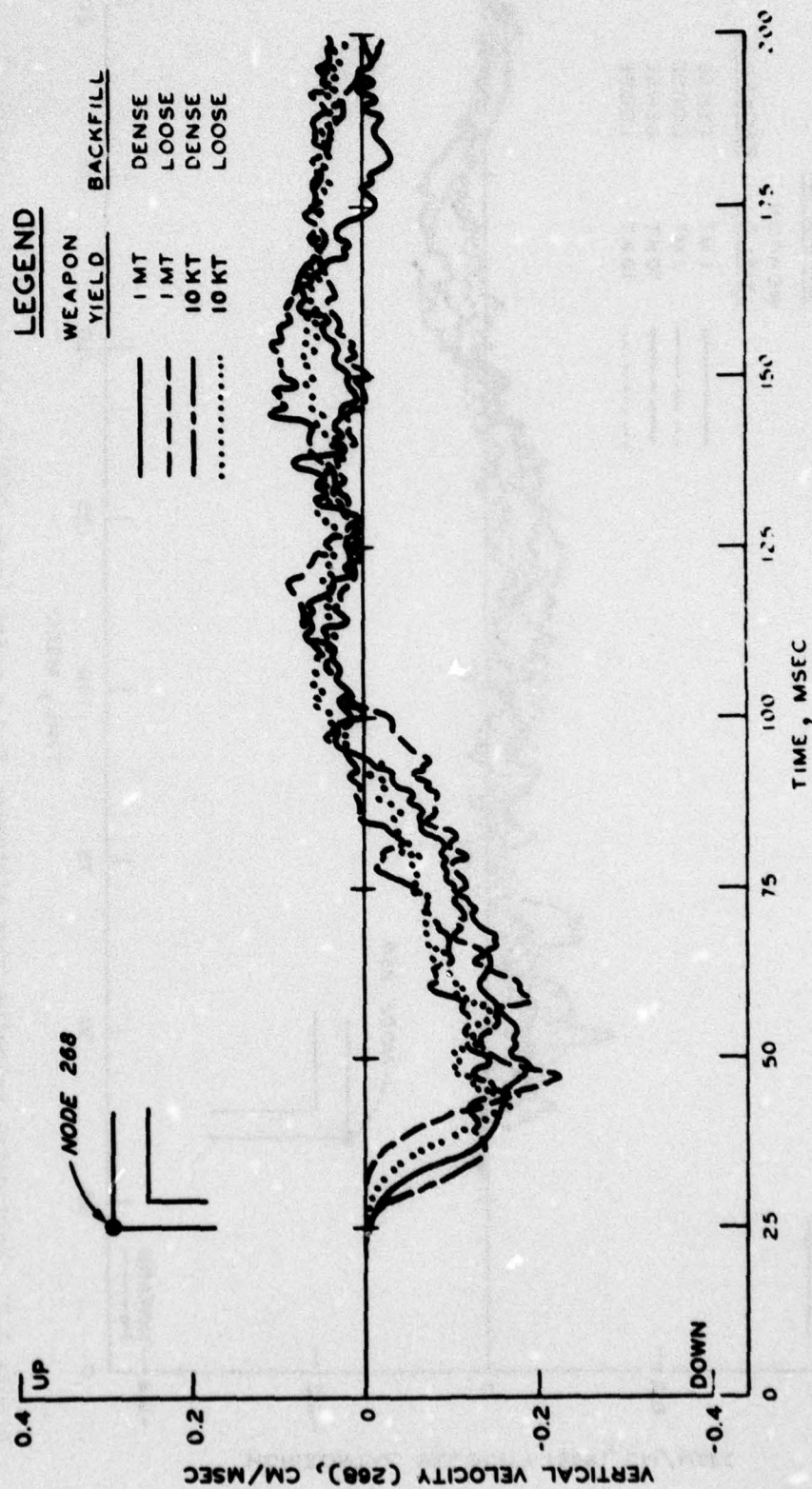


Figure 3.20 Vertical velocity time histories for a point (node 268) on the blastward sidewall.

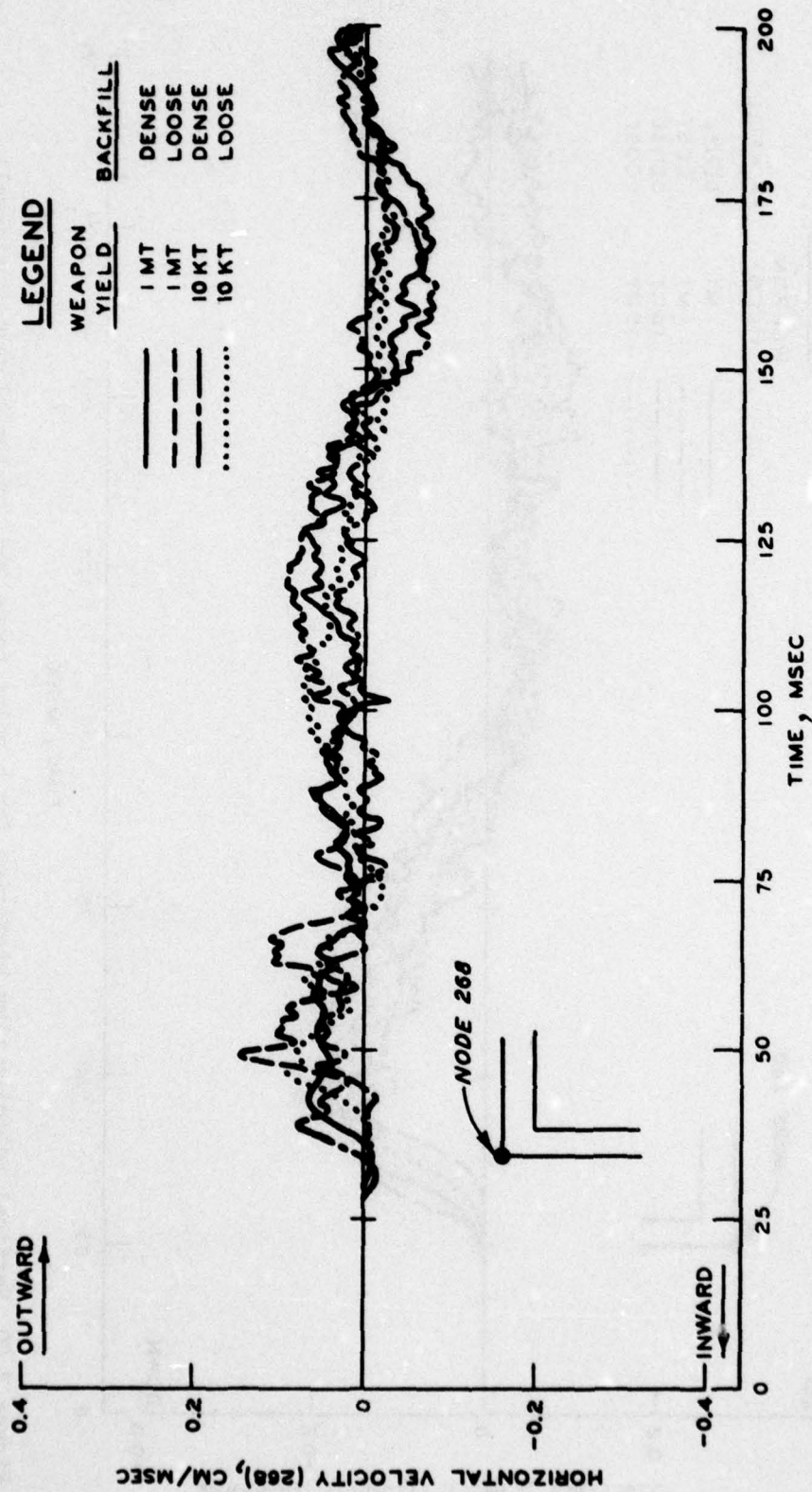


Figure 3.21 Horizontal velocity time histories for a point (node 268) on the blastward sidewall.

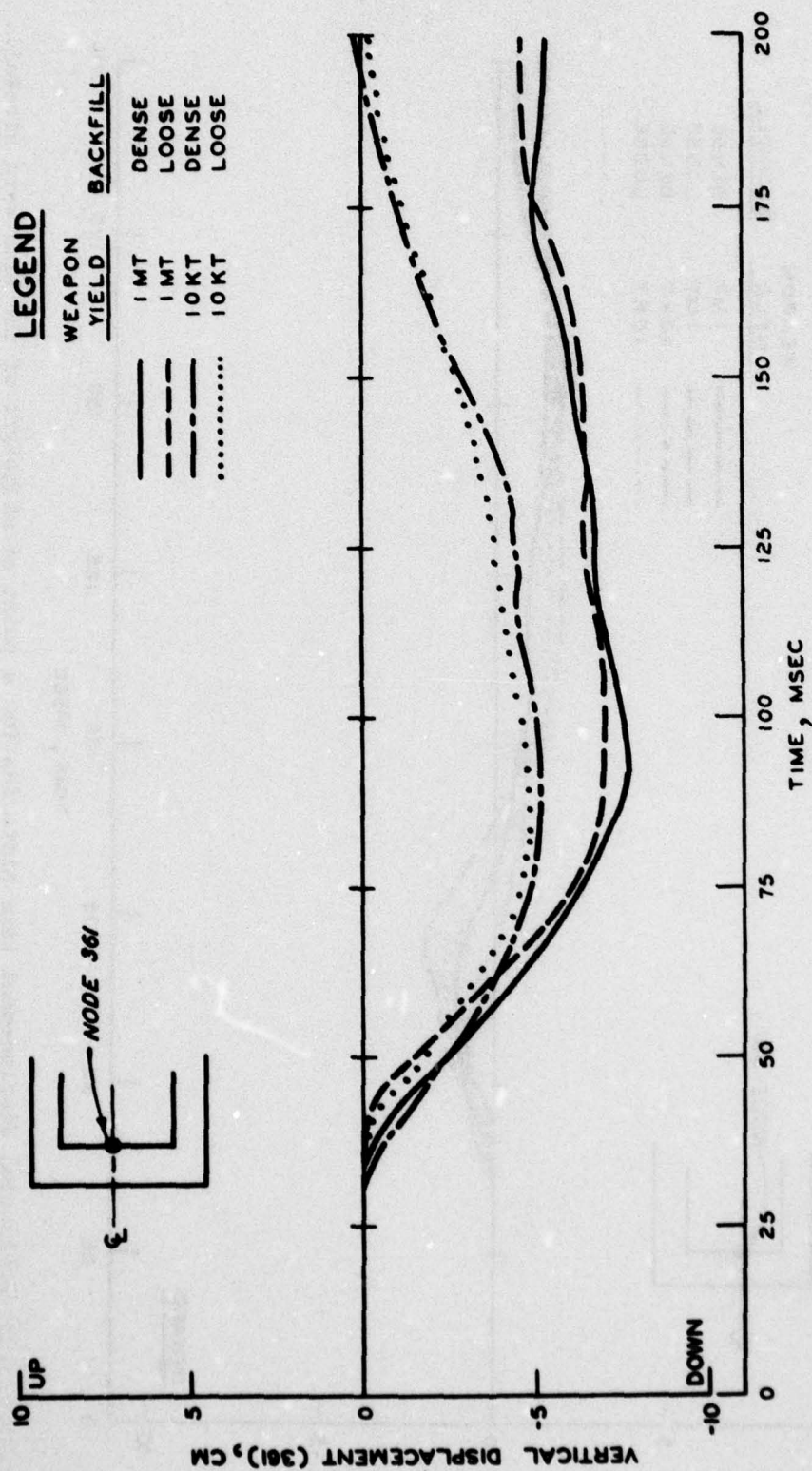


Figure 3.22 Vertical displacement time histories for a point at the midheight of the blastward sidewall.

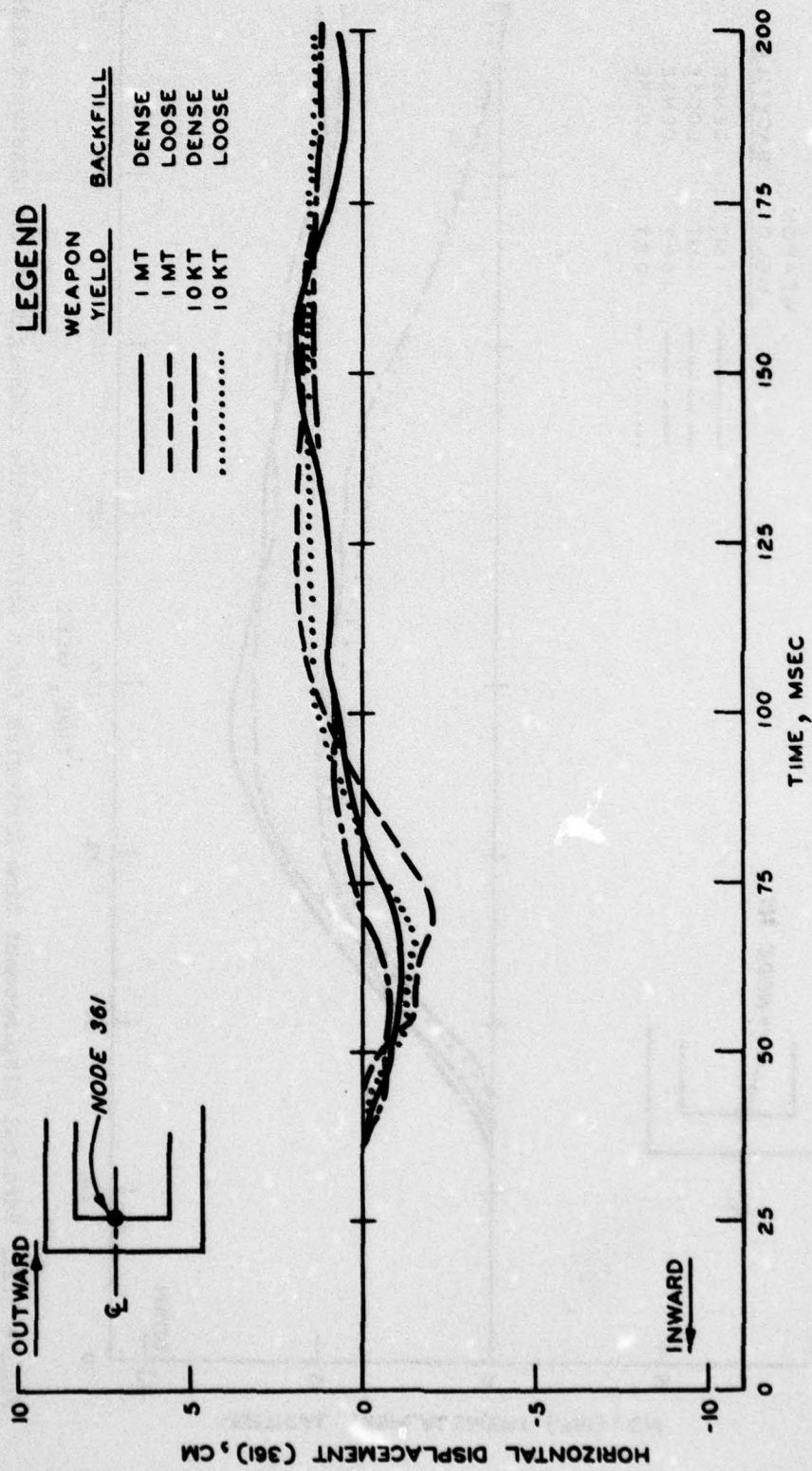


Figure 3.23 Horizontal displacement time histories for a point at midheight of the blastward sidewall.

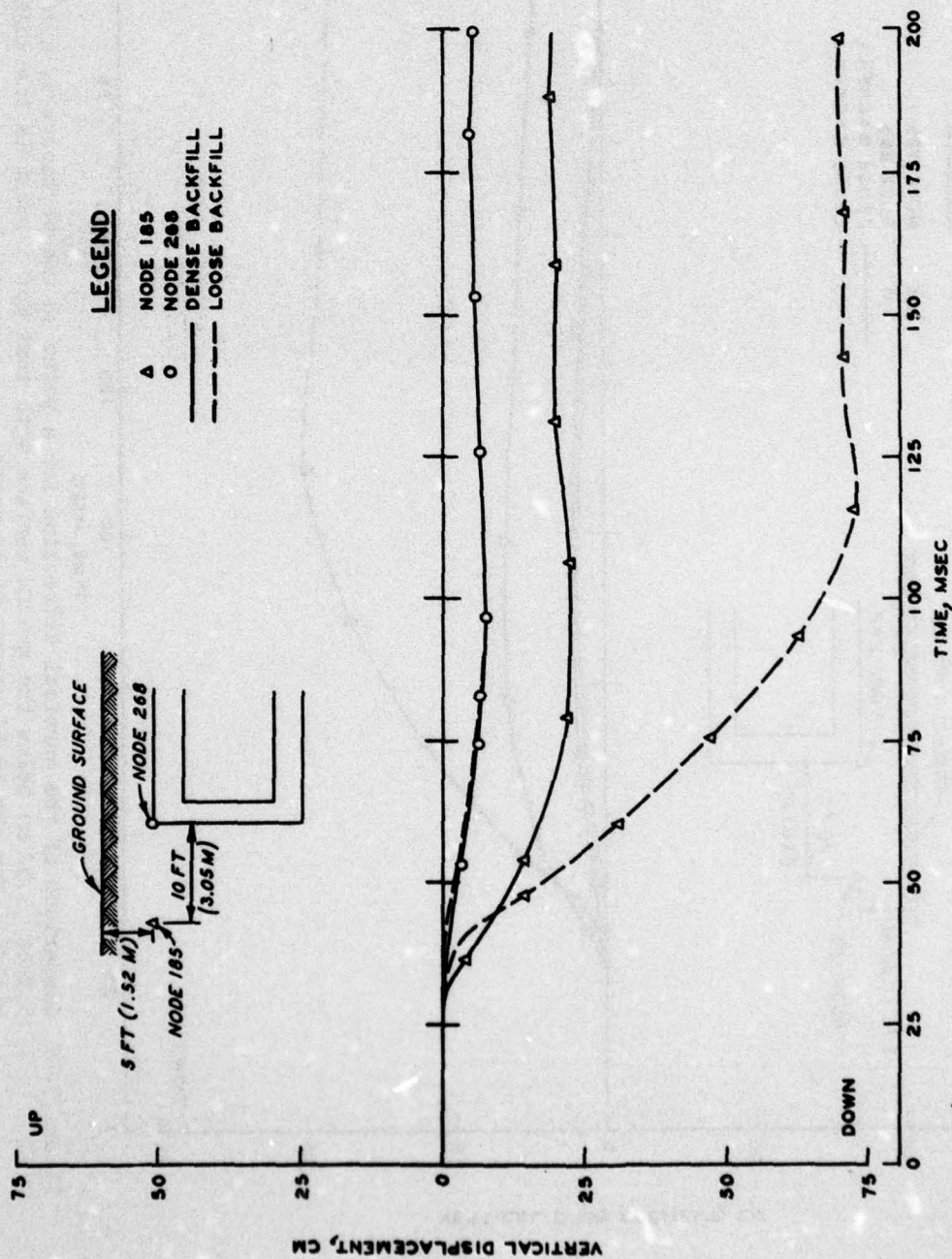


Figure 3.24 Comparison of the vertical deflection for a point on the structure at a depth of 5 feet (1.52 m) below the ground surface with that for a point in the adjacent backfill for the 1-MT weapon-yield cases.

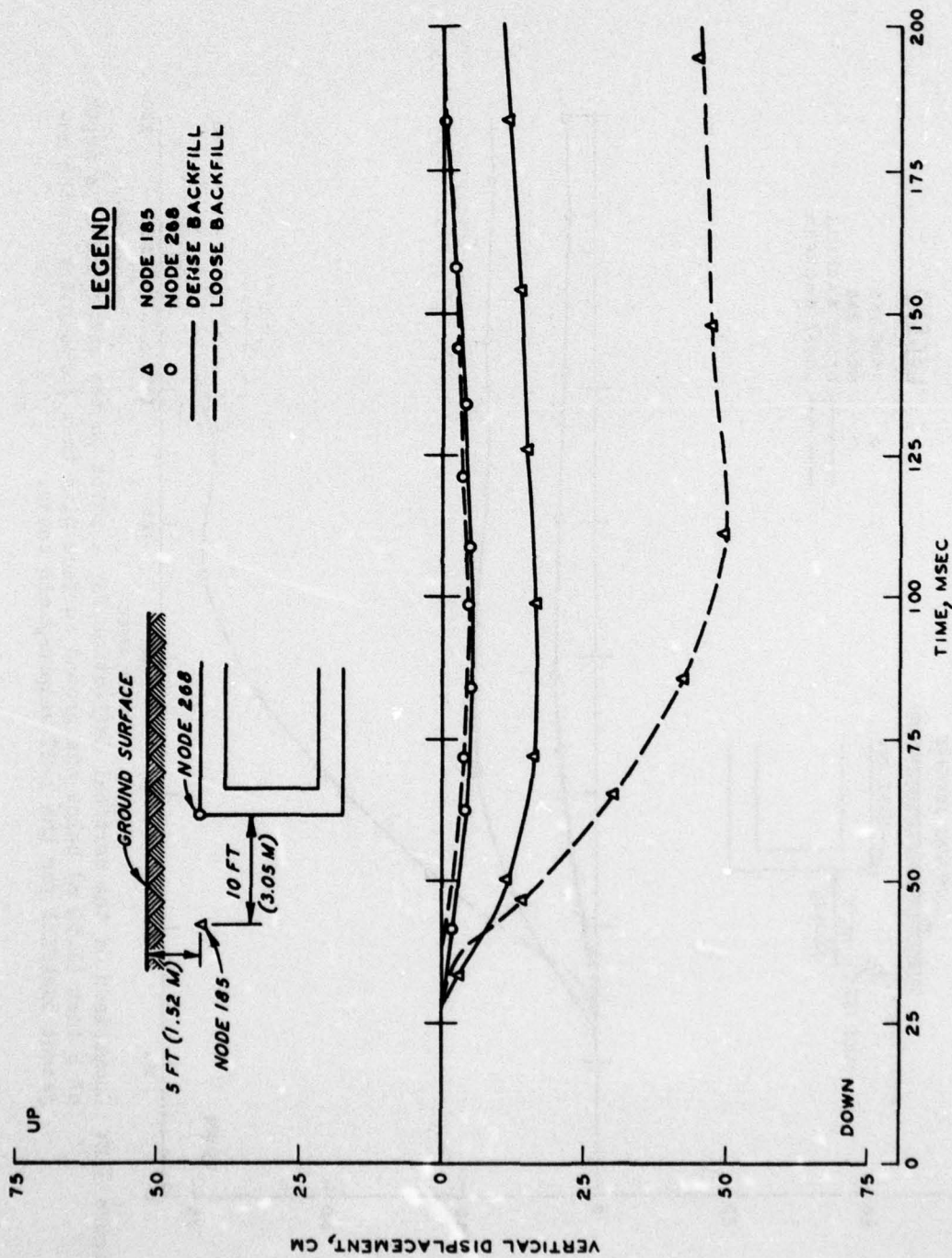


Figure 3.25 Comparison of the vertical deflection for a point on the structure at a depth of 5 feet (1.52 m) below the ground surface with that for a point in the adjacent backfill for the 10-KT weapon-yield cases.

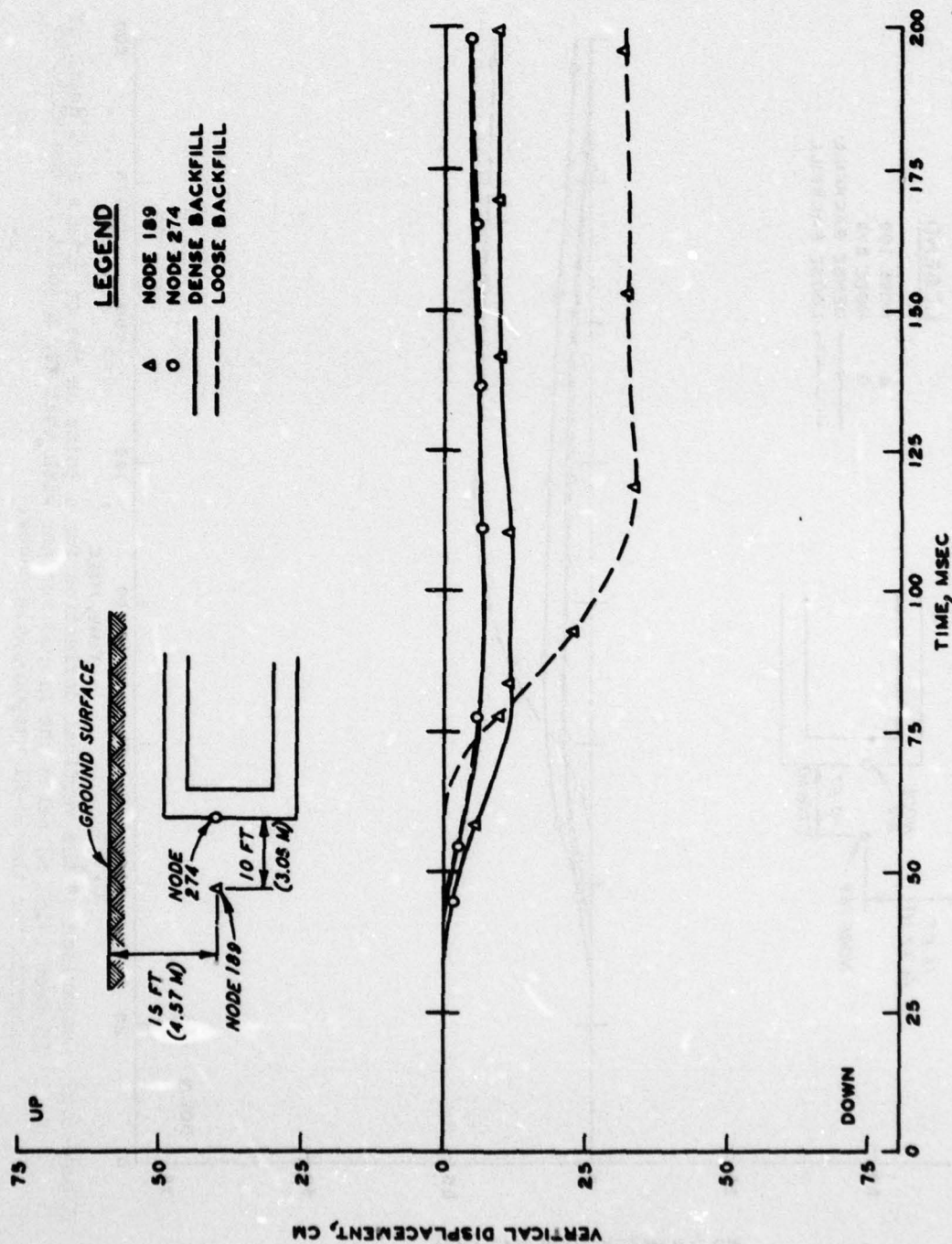


Figure 3.26 Comparison of the vertical deflection for a point on the structure at a depth of 15 feet (4.57 m) below the ground surface with that for a point in the adjacent backfill for the 1-MT weapon-yield cases.

AD-A058 669

ARMY ENGINEER WATERWAYS EXPERIMENT STATION VICKSBURG MISS F/G 18/3  
EFFECT OF BACKFILL PROPERTY AND AIRBLAST VARIATIONS ON THE EXTE--ETC(U)  
JUN 78 J E WINDHAM, J O CURTIS

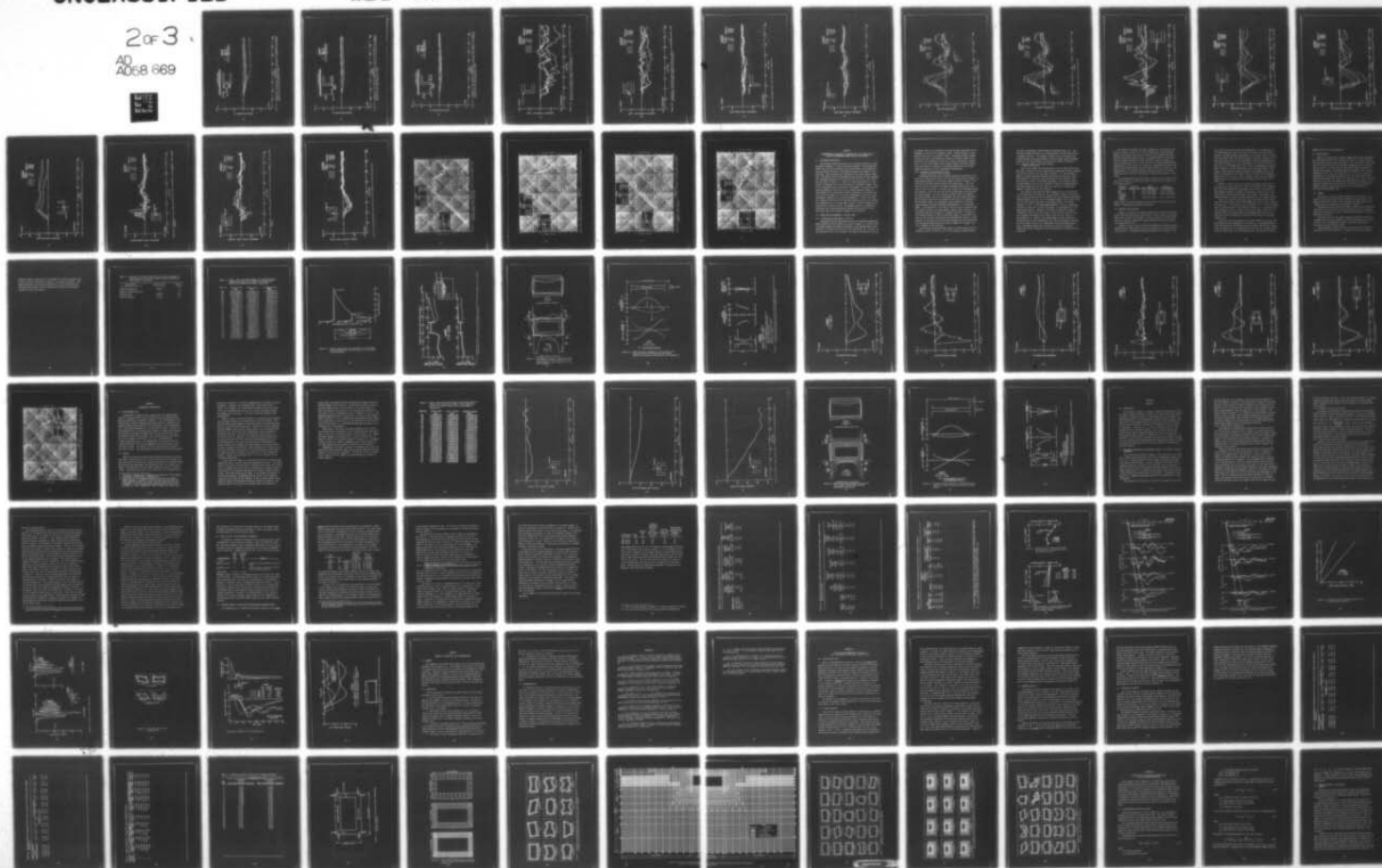
UNCLASSIFIED

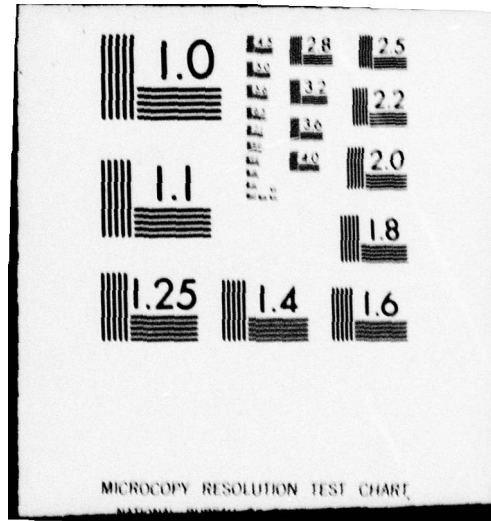
WES-TR-S-78-5

NL

2 of 3

AD  
A058 669





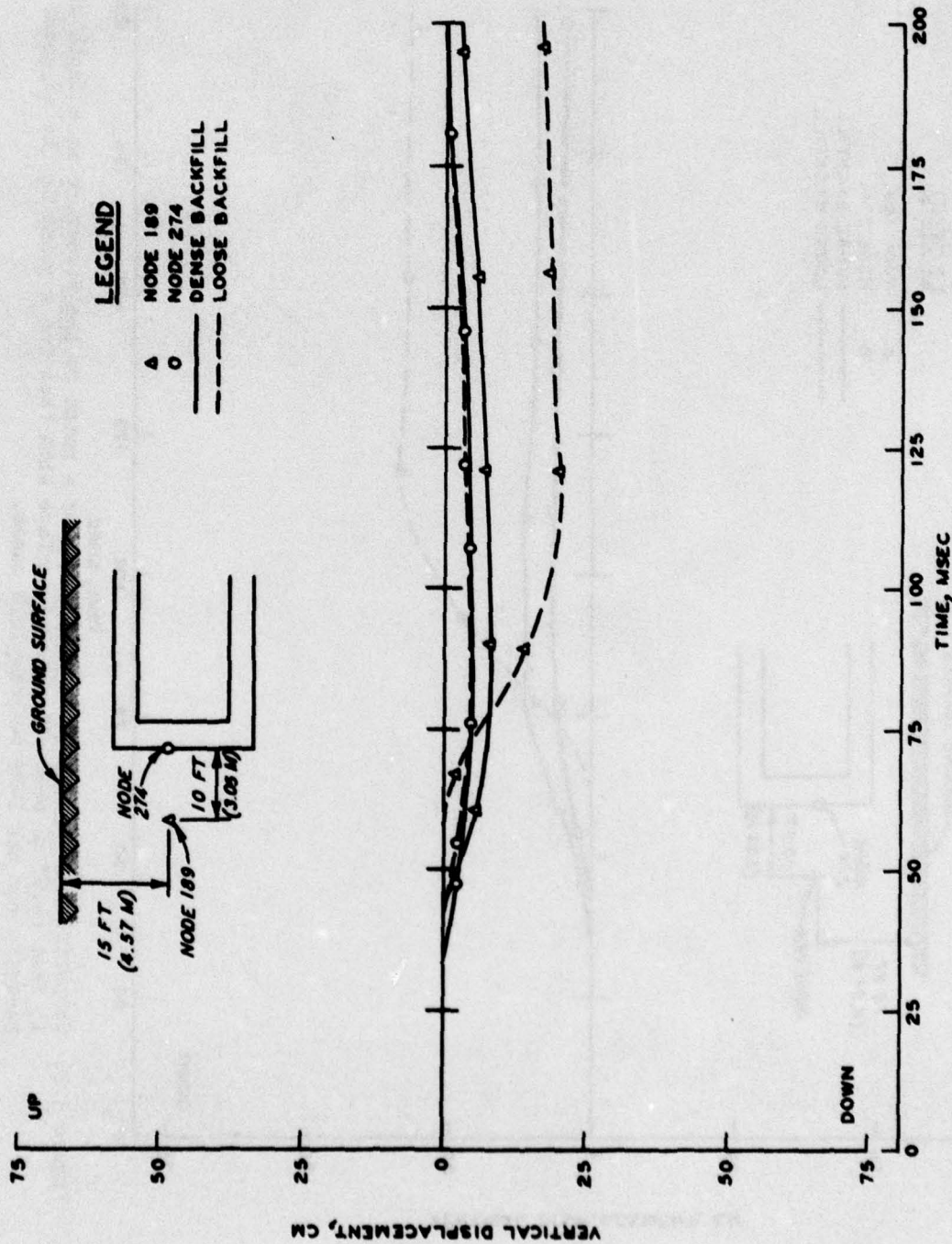


Figure 3.27 Comparison of the vertical deflection for a point on the structure at a depth of 15 feet (4.57 m) below the ground surface with that for a point in the adjacent backfill for the 10-KT weapon-yield cases.

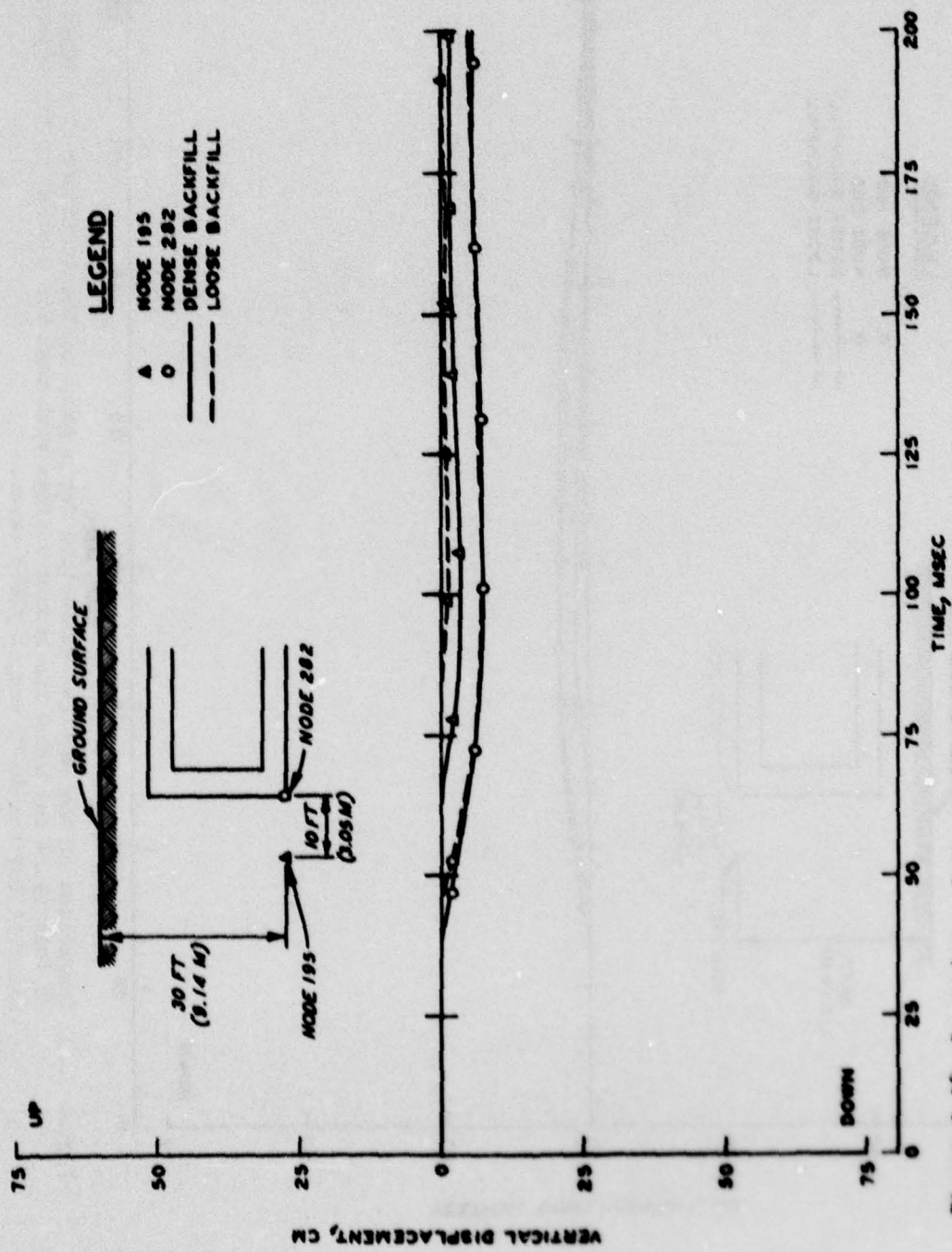


Figure 3.28 Comparison of the vertical deflection for a point on the structure at a depth of 30 feet (9.14 m) below the ground surface with that for a point in the adjacent backfill for the 1-MT weapon-yield cases.

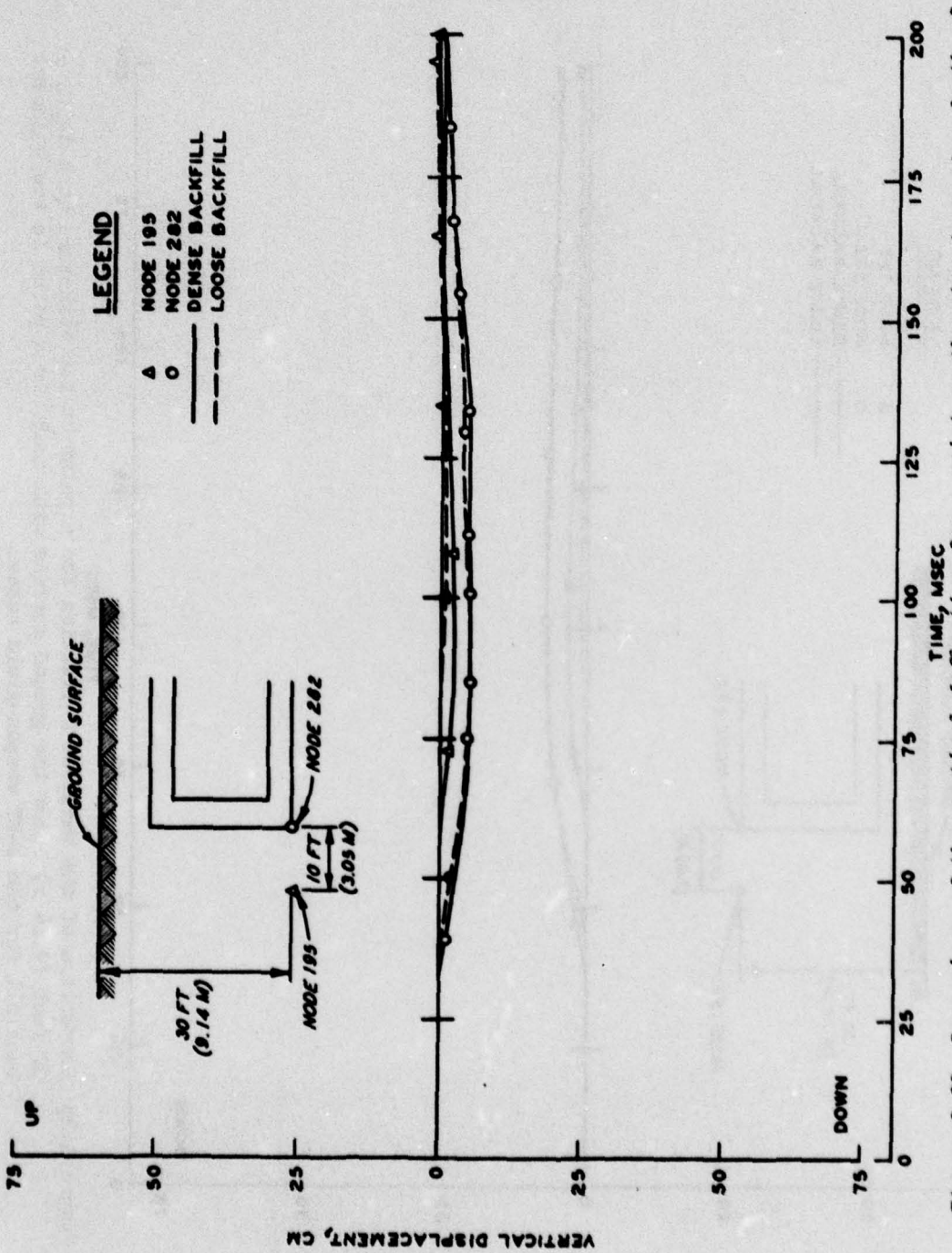


Figure 3.29 Comparison of the vertical deflection for a point on the structure at a depth of 30 feet (9.14 cm) below the ground surface with that for a point in the adjacent backfill for the 10-KT weapon-yield cases.

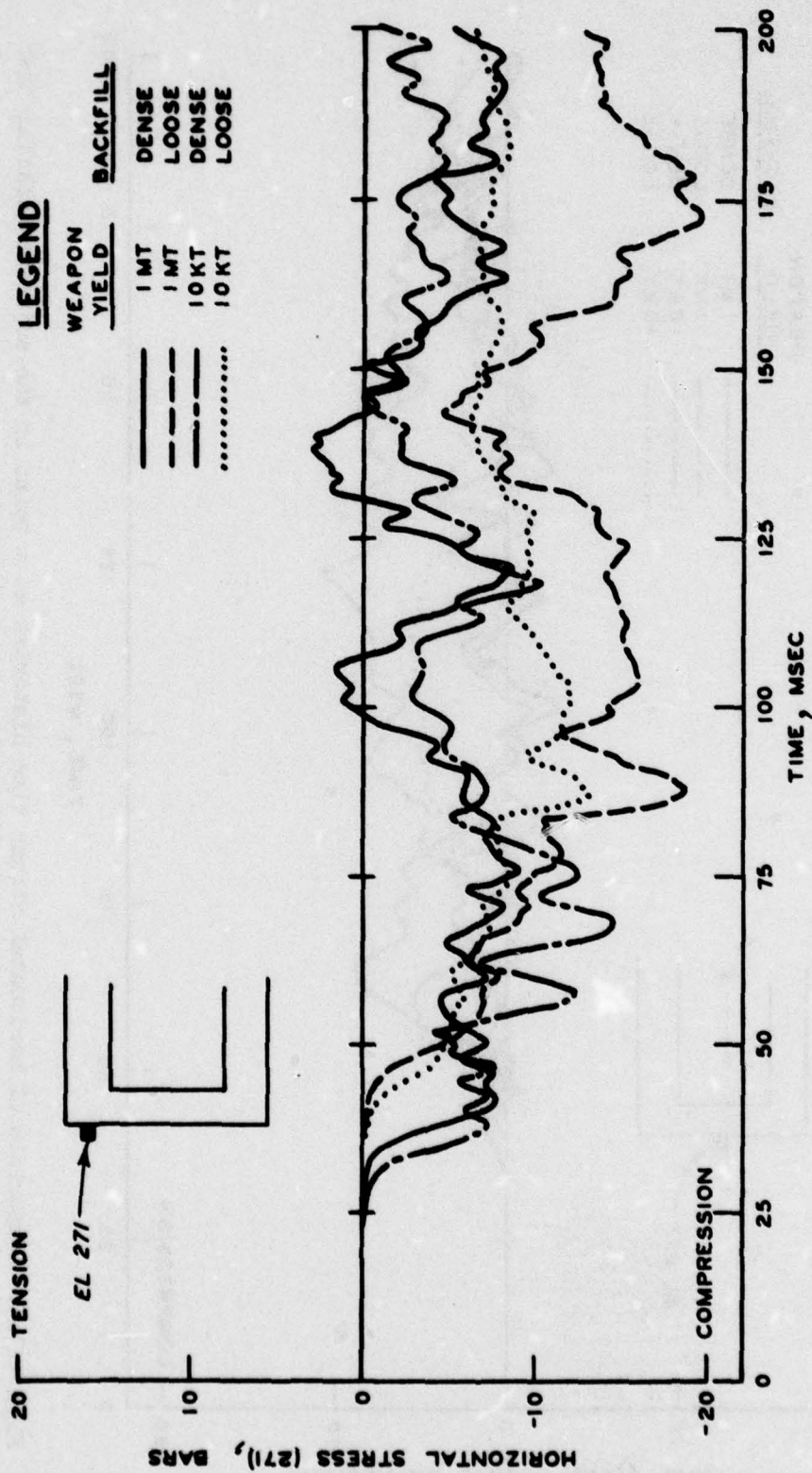


Figure 3.30 Comparison of horizontal stress time histories at a point in the adjacent backfill near the top of the blastward sidewall of the structure.

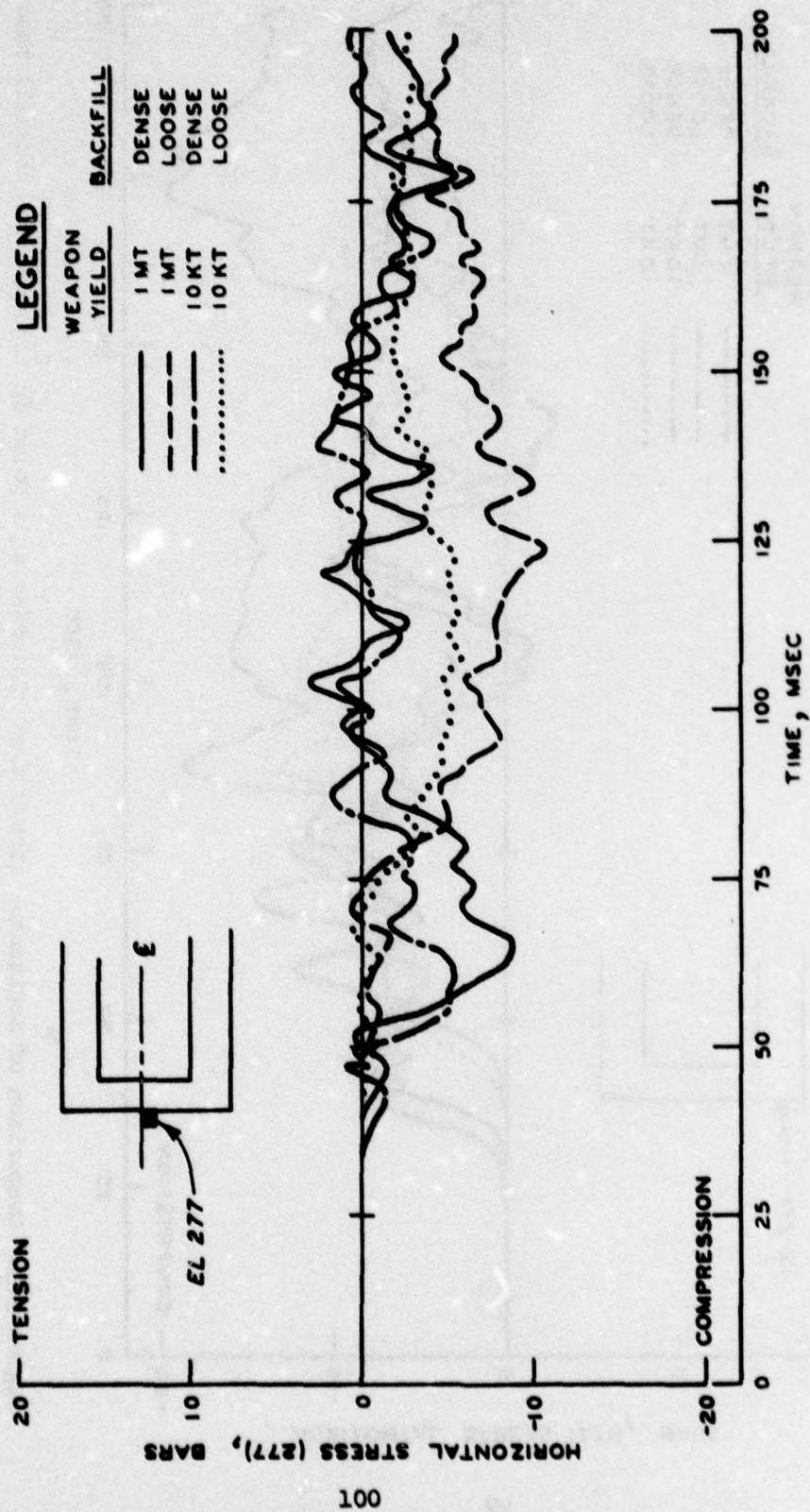


Figure 3.31 Comparison of horizontal stress time histories at a point in the adjacent backfill near the midheight of the blastward sidewall of the structure.

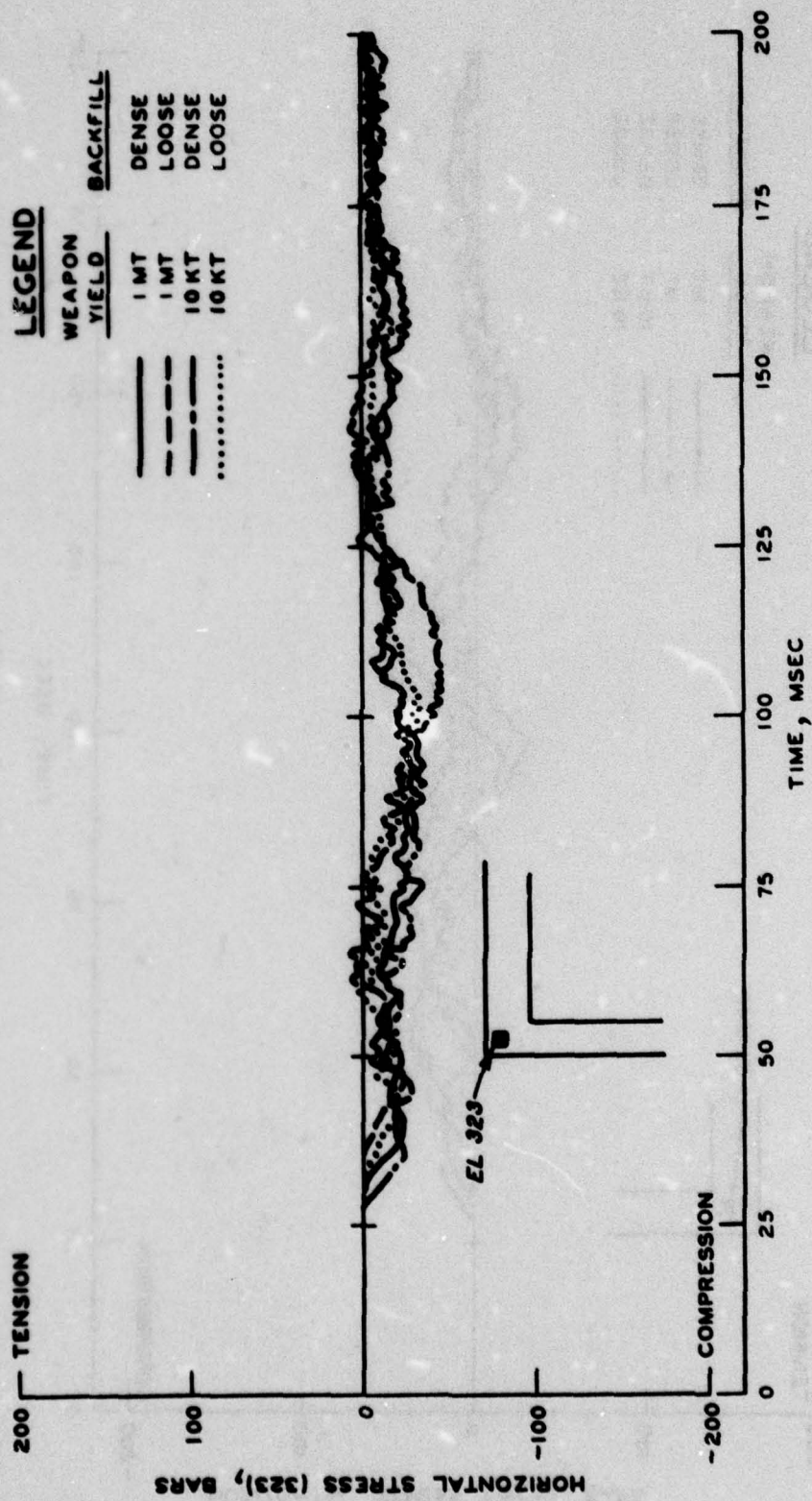


Figure 3.32 Horizontal stress time histories for element 323.

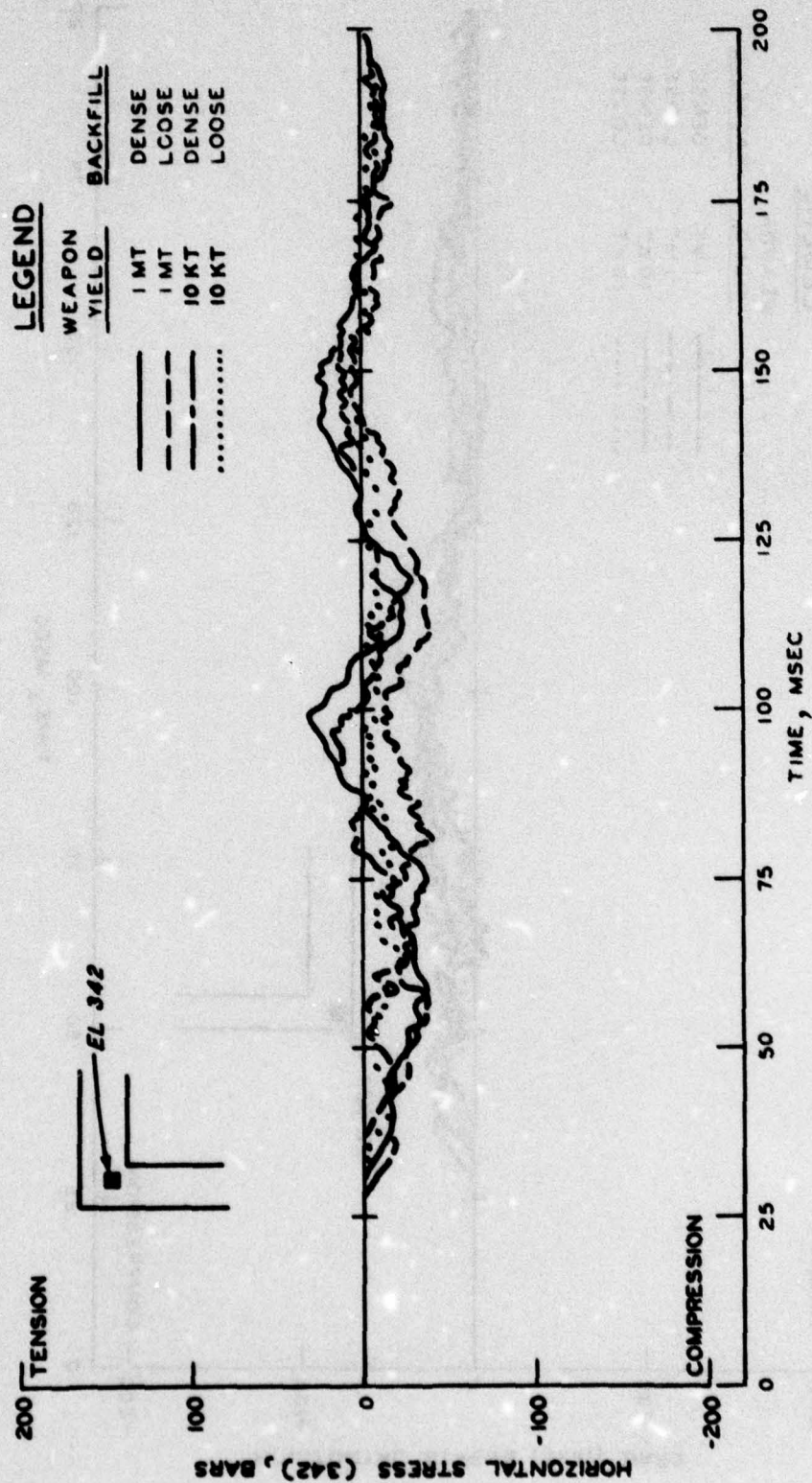


Figure 3.33 Horizontal stress time histories for element 342.

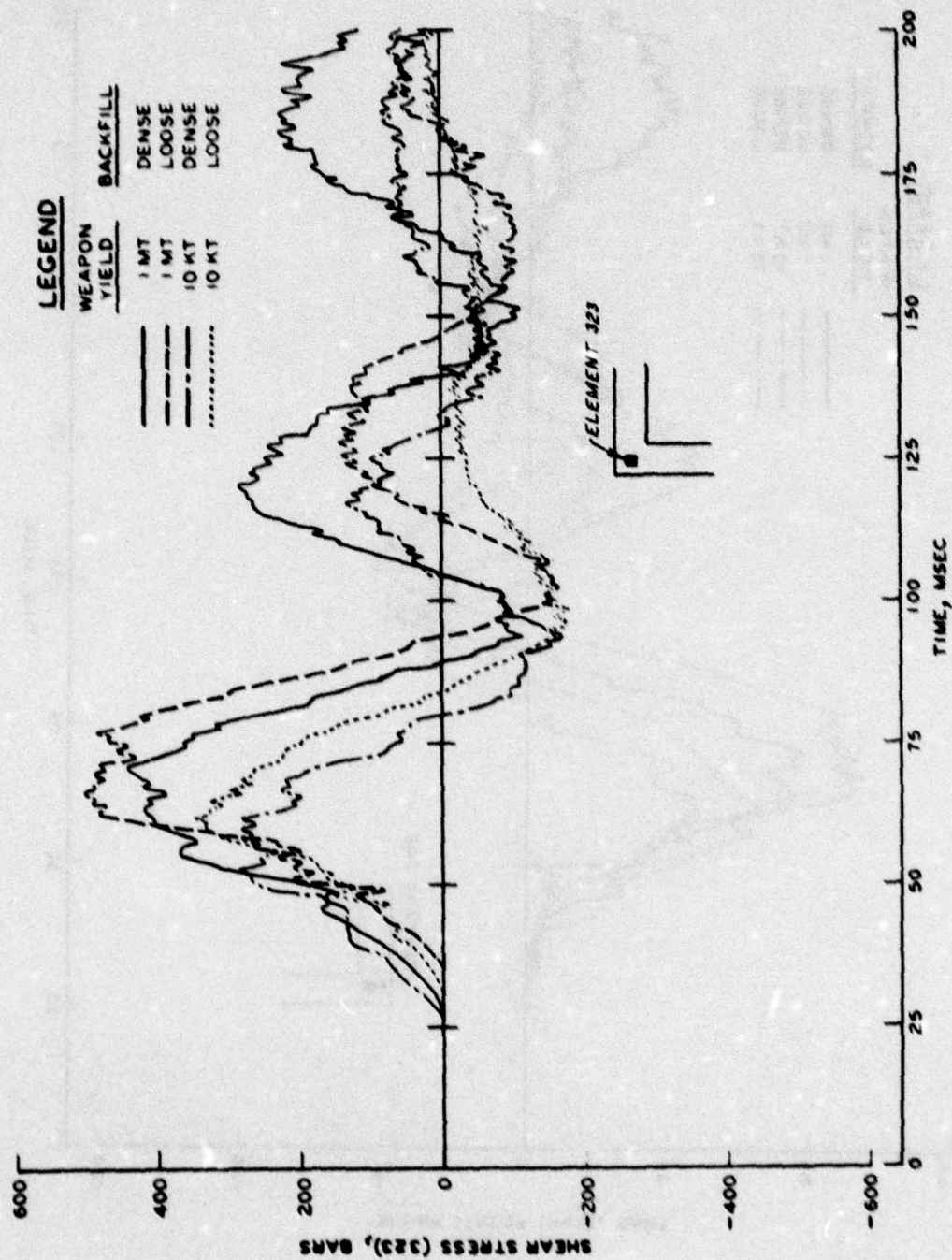


Figure 3.34 Shear stress time histories for element 323.

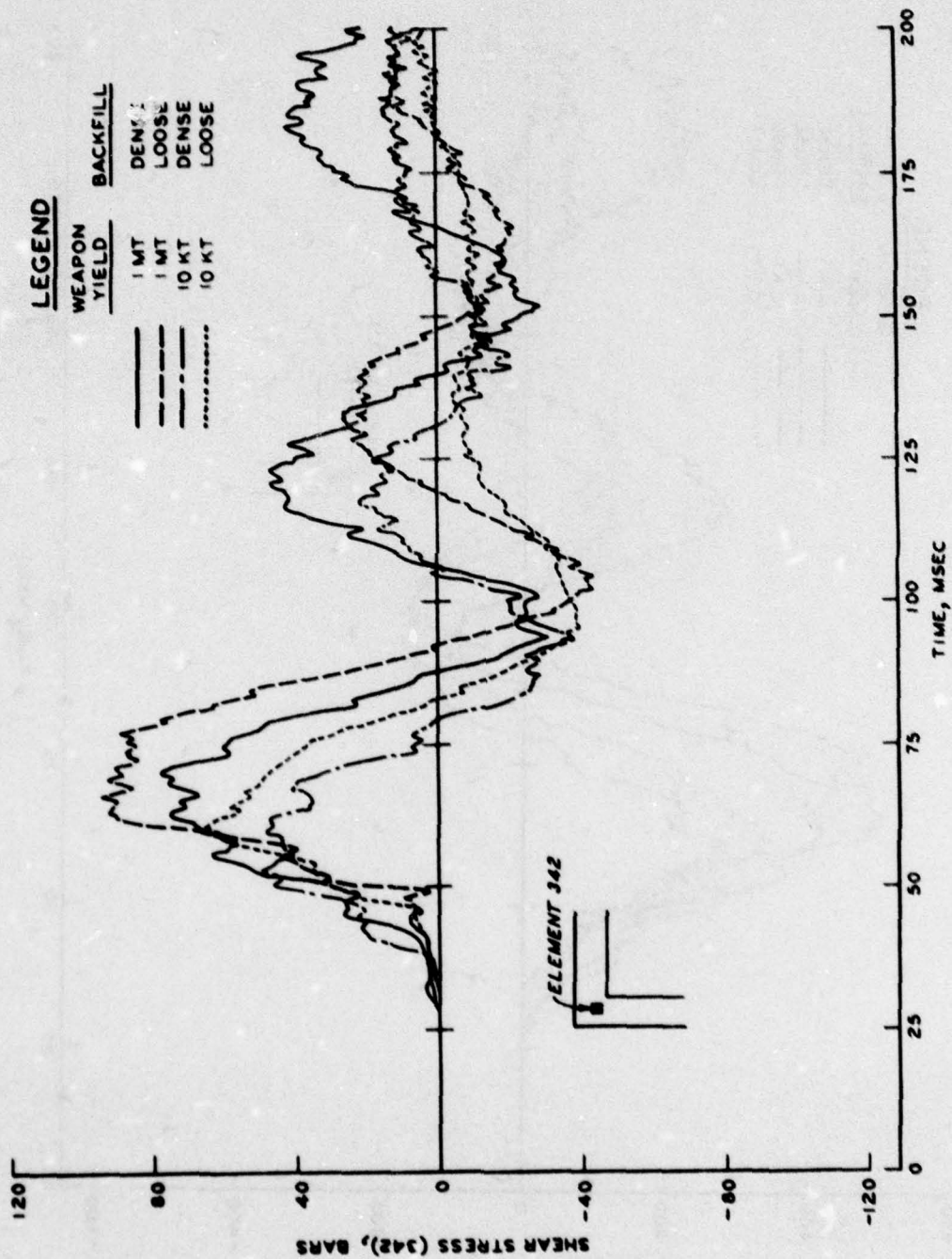


Figure 3.35 Shear stress time histories for element 342.

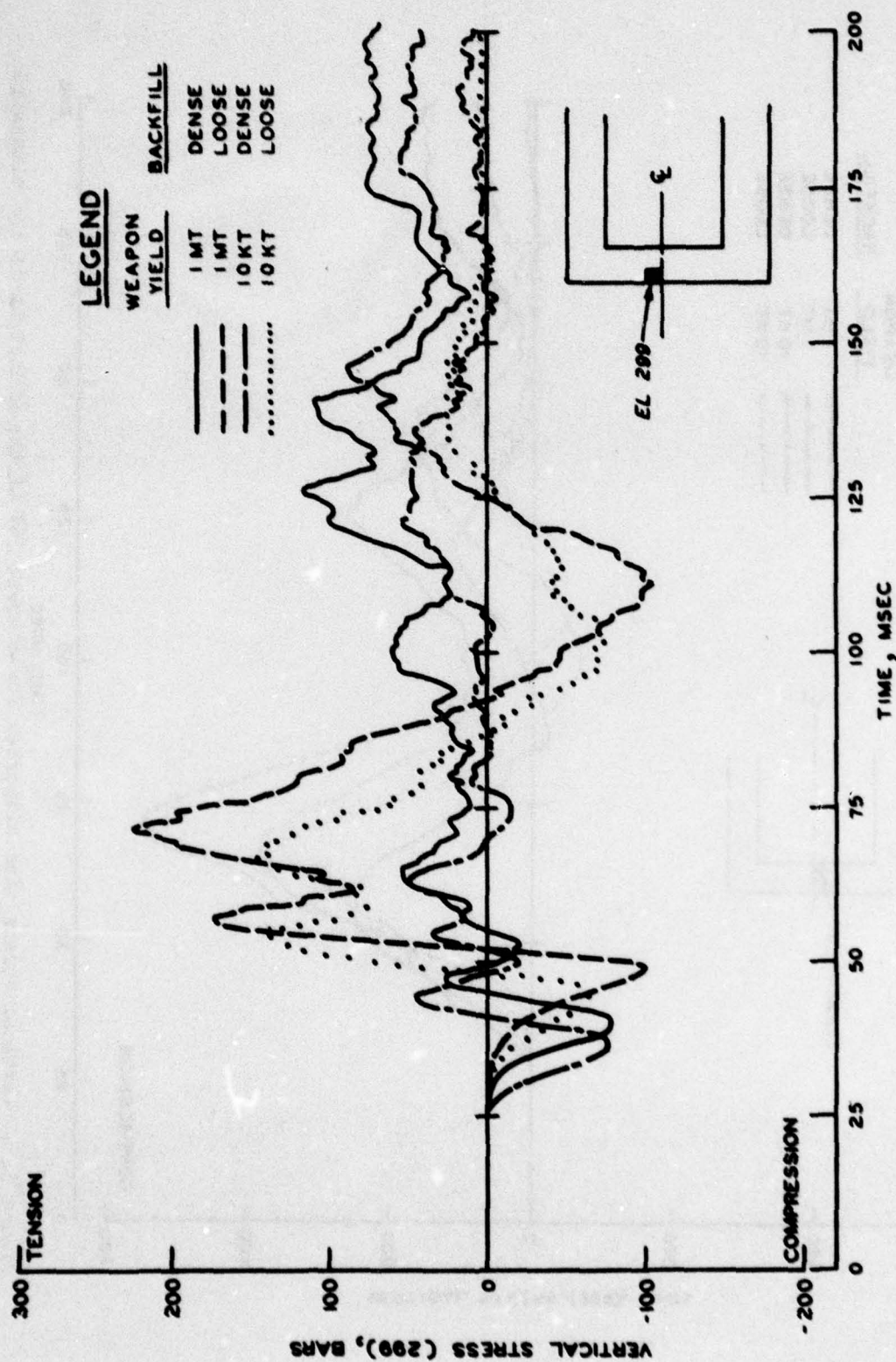


Figure 3.36 Vertical stress time histories for element 299 at the midheight of the blastward sidewall.

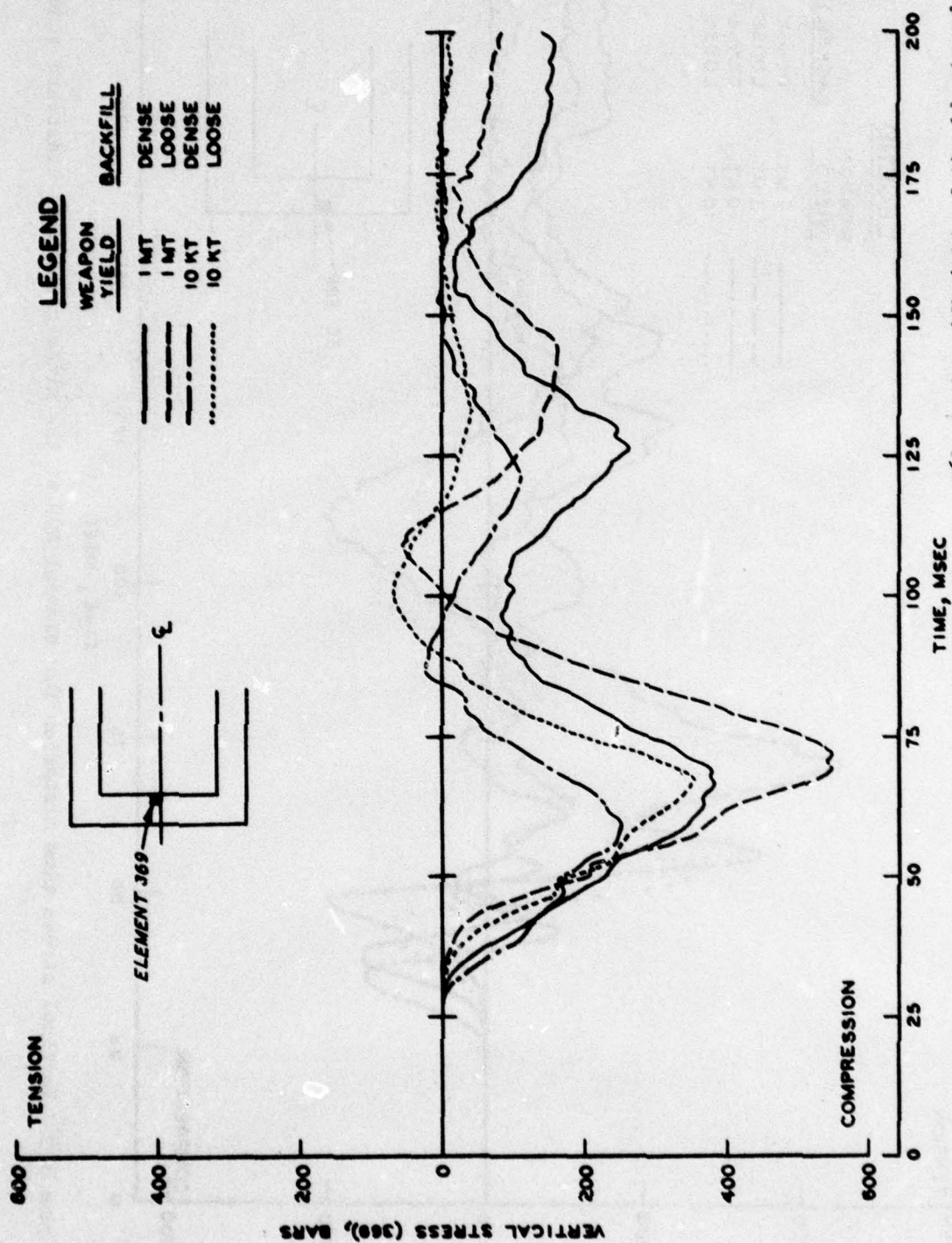
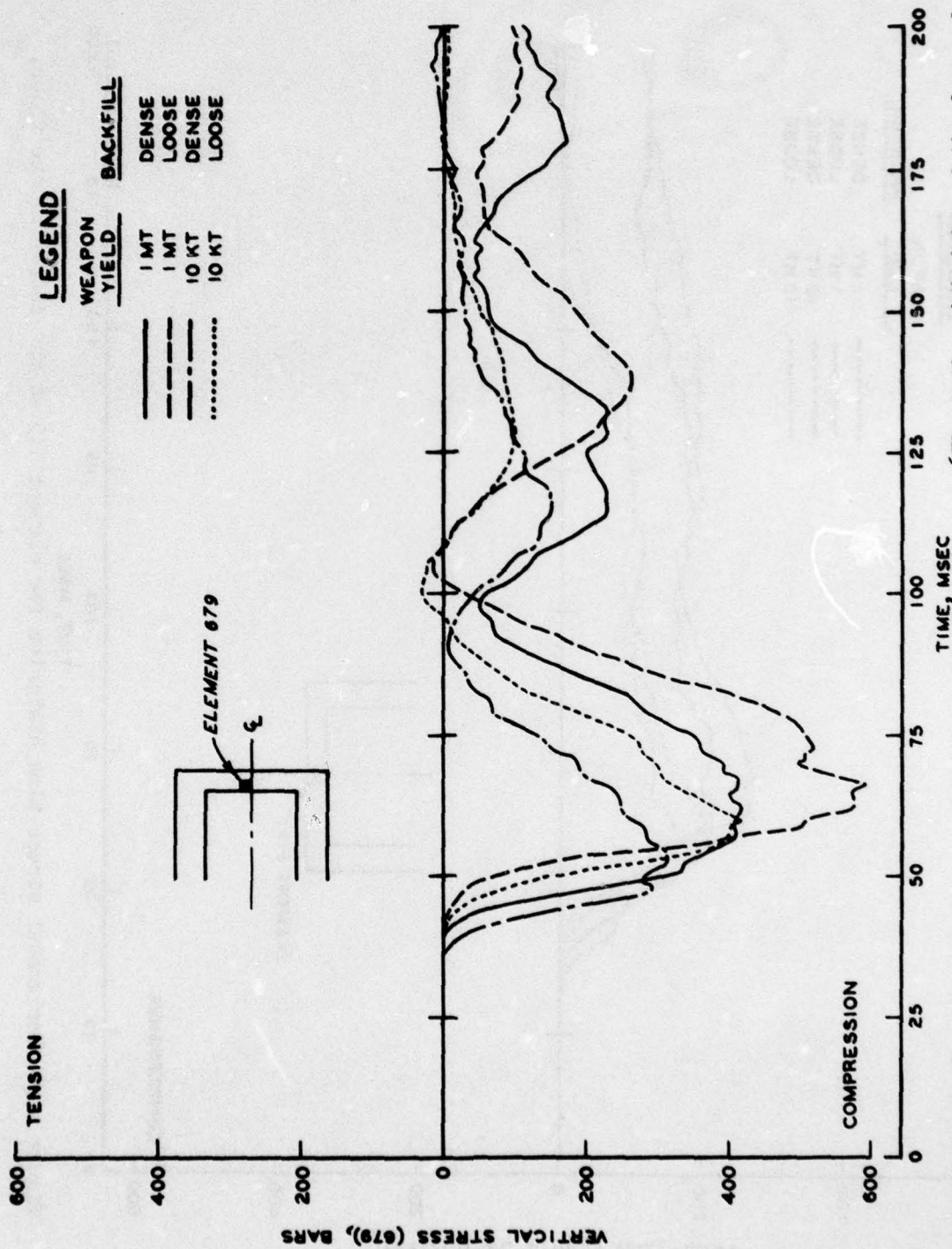
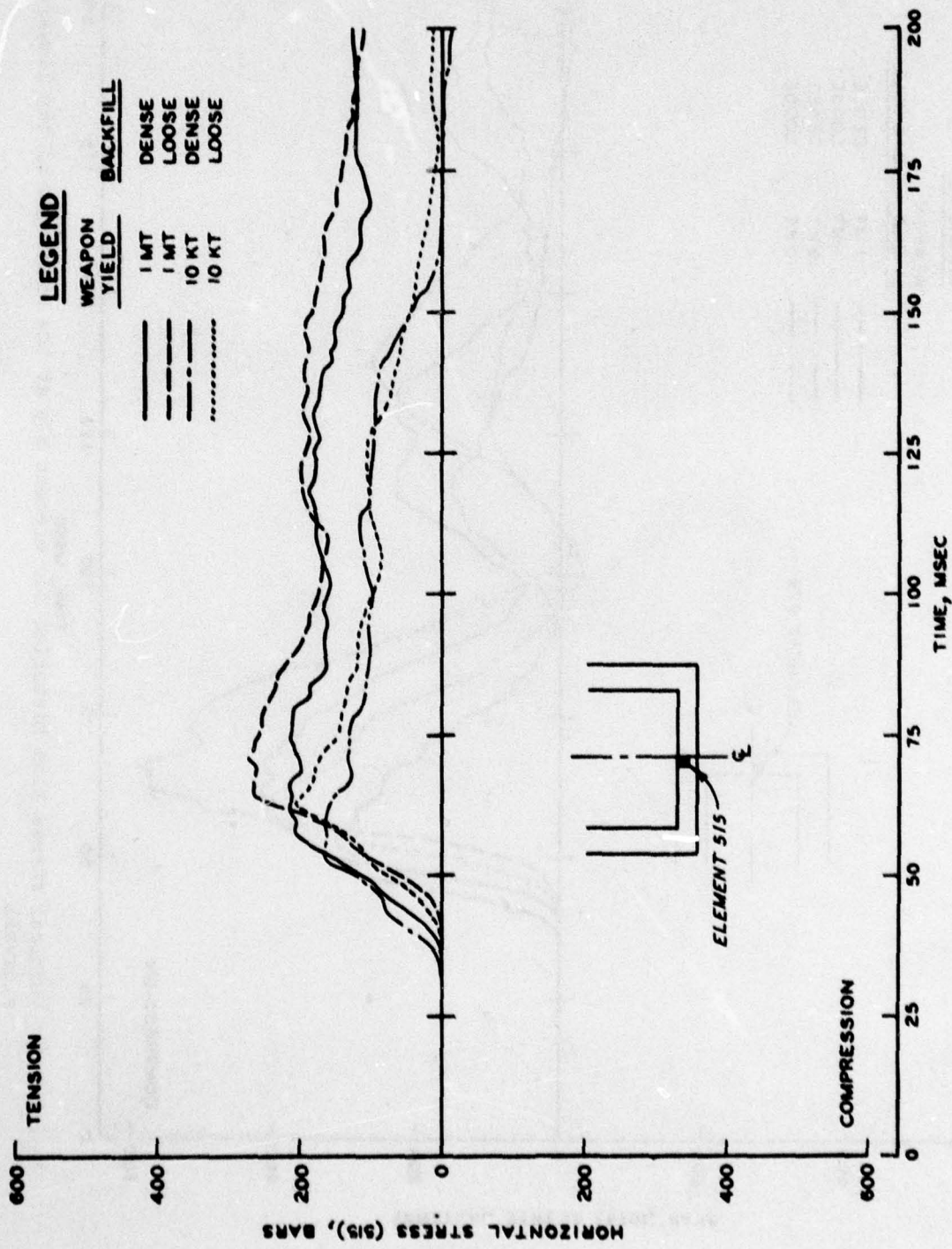


Figure 3.37 Vertical stress time histories for element 369 at the midheight of the blastward sidewall.





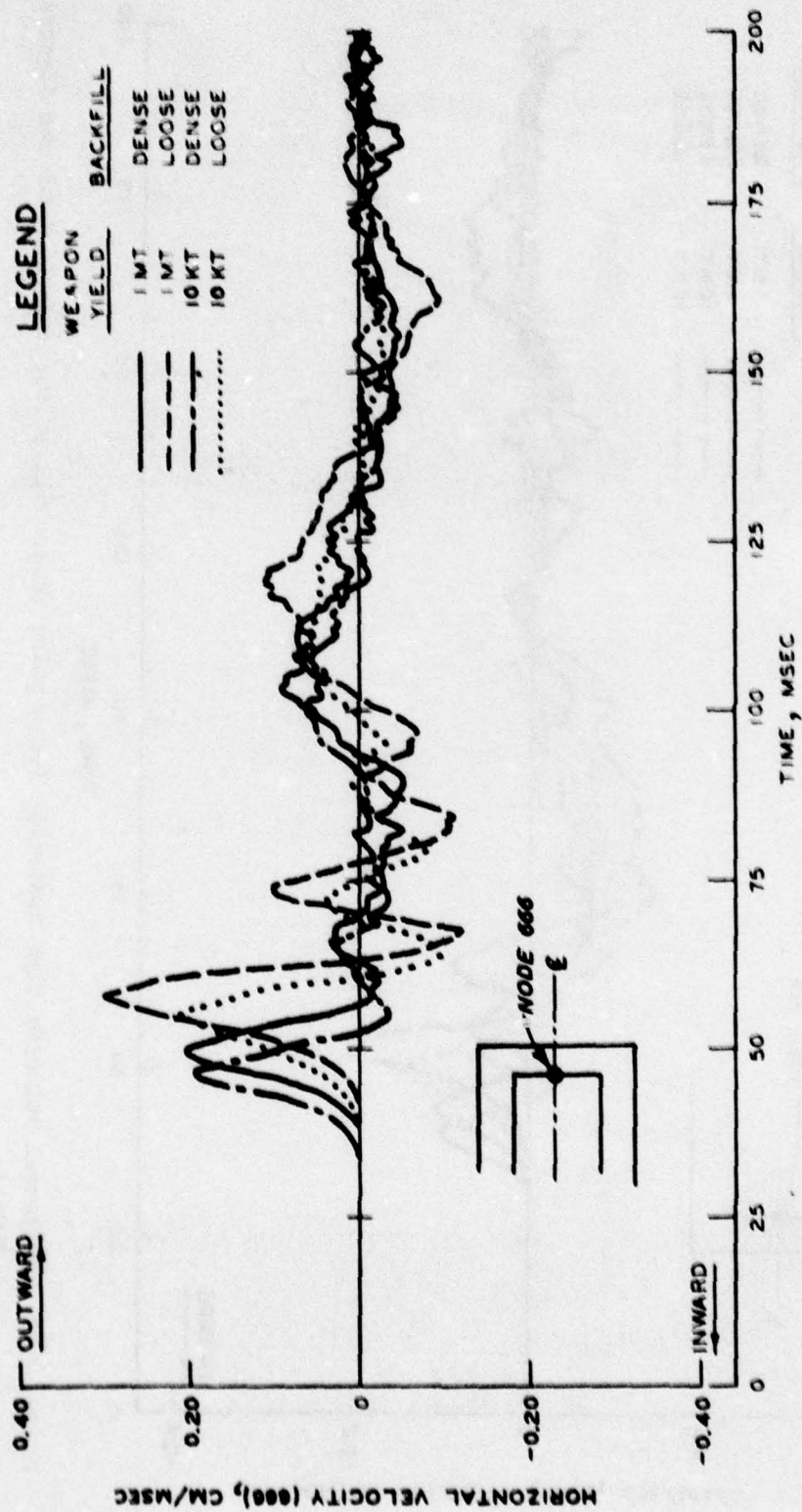


Figure 3.40 Horizontal velocity time histories for a point (node 666) at the midheight of the leeward sidewall.

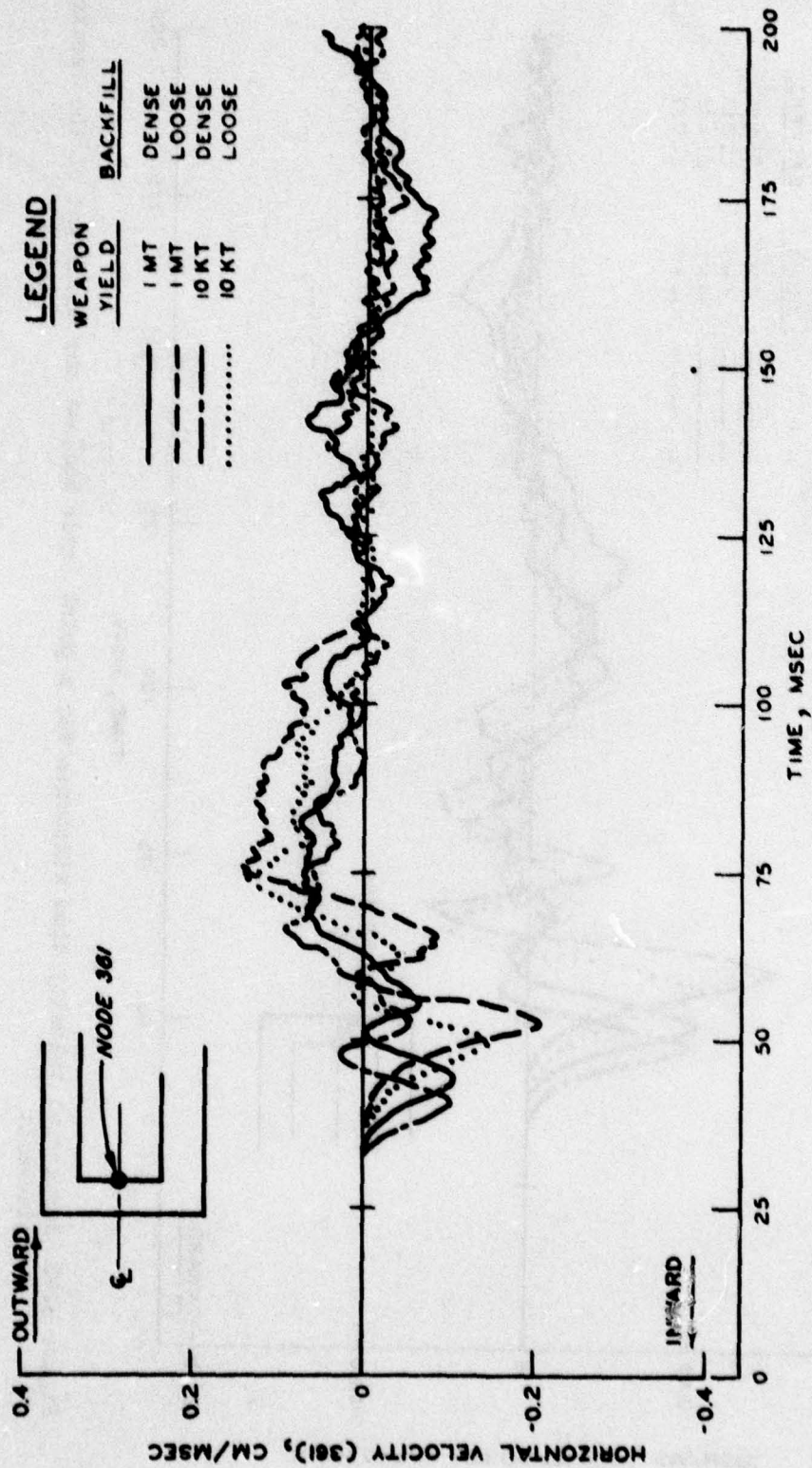


Figure 3.41 Horizontal velocity time histories for a point (node 361) at the midheight of the blastward sidewall.

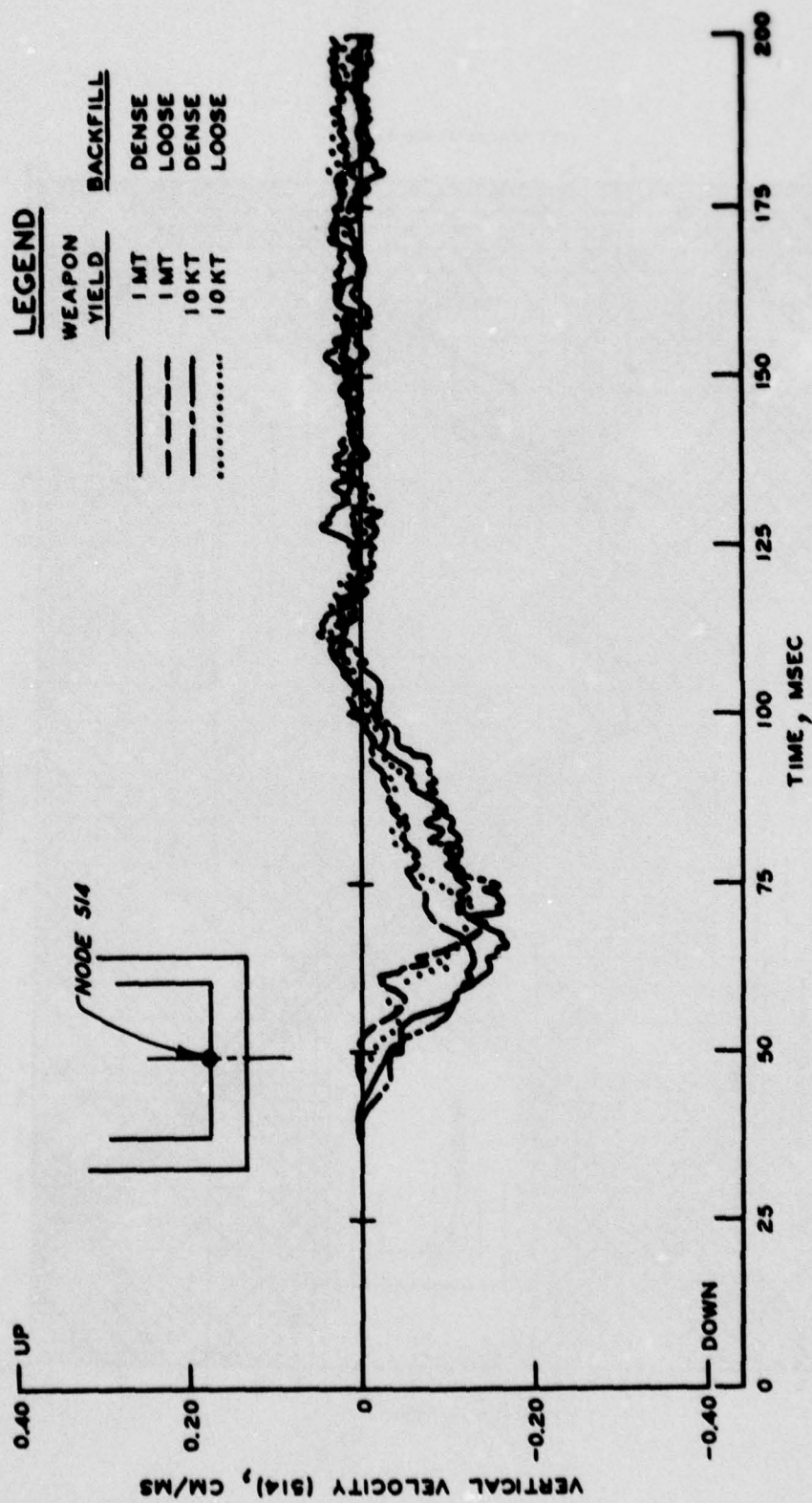


Figure 3.42 Vertical velocity time histories for the centerline of the structure floor.

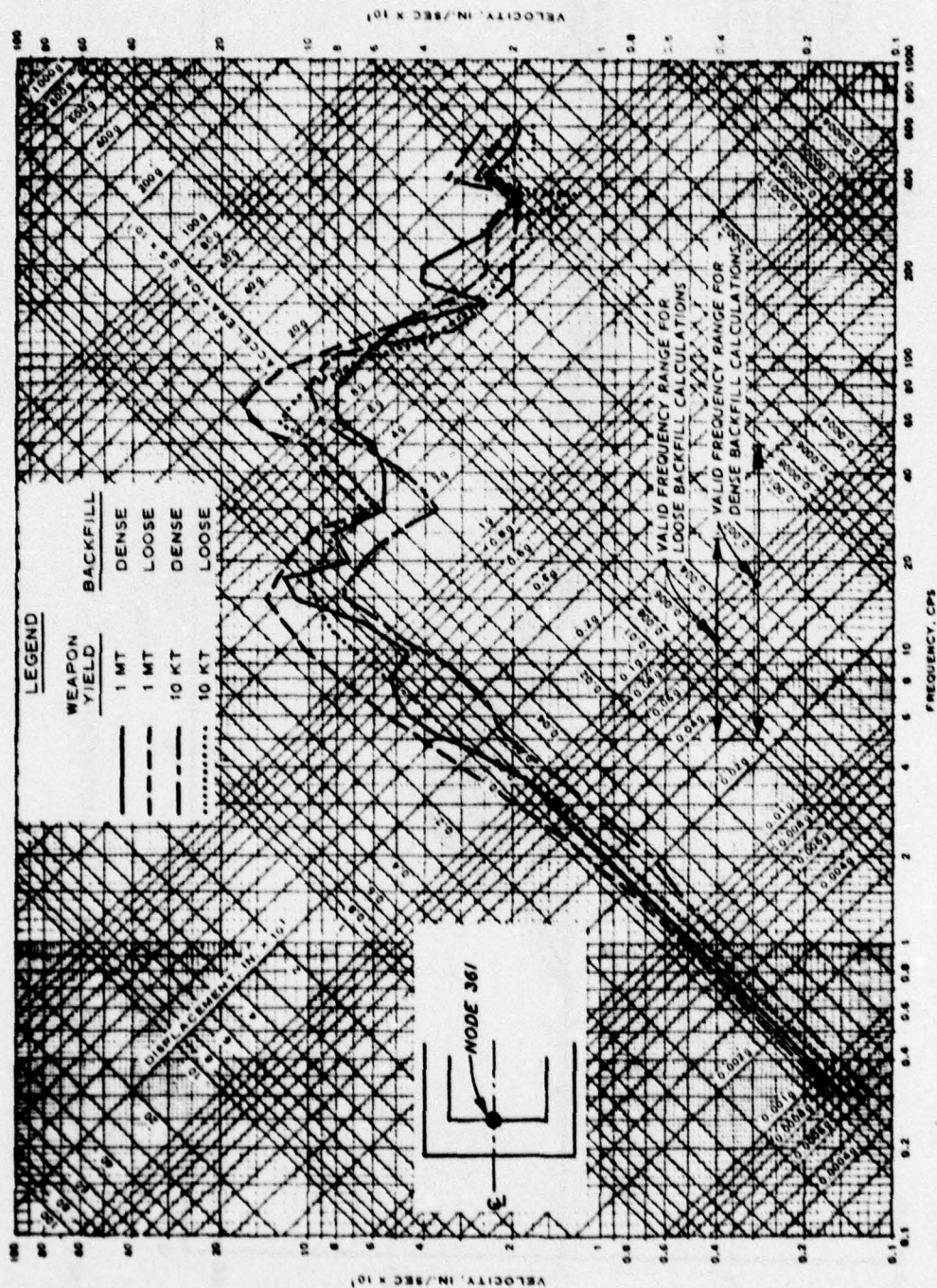


Figure 3.43 Horizontal shock spectra for a point (node 361) on the inside of the blastward sidewall of the structure.

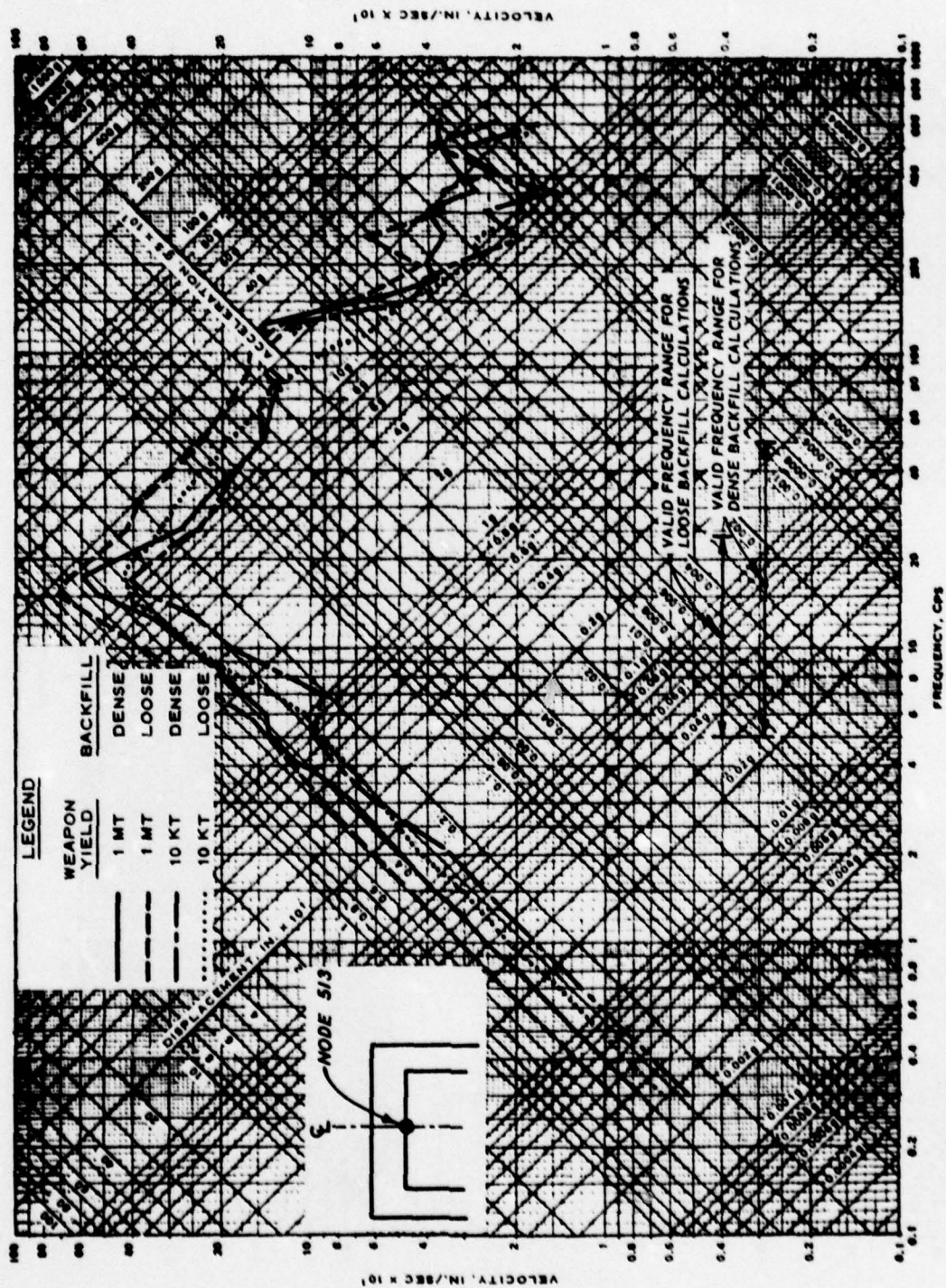


Figure 3.44 Vertical shock spectra for a point (node 513) on the inside of the structure roof.

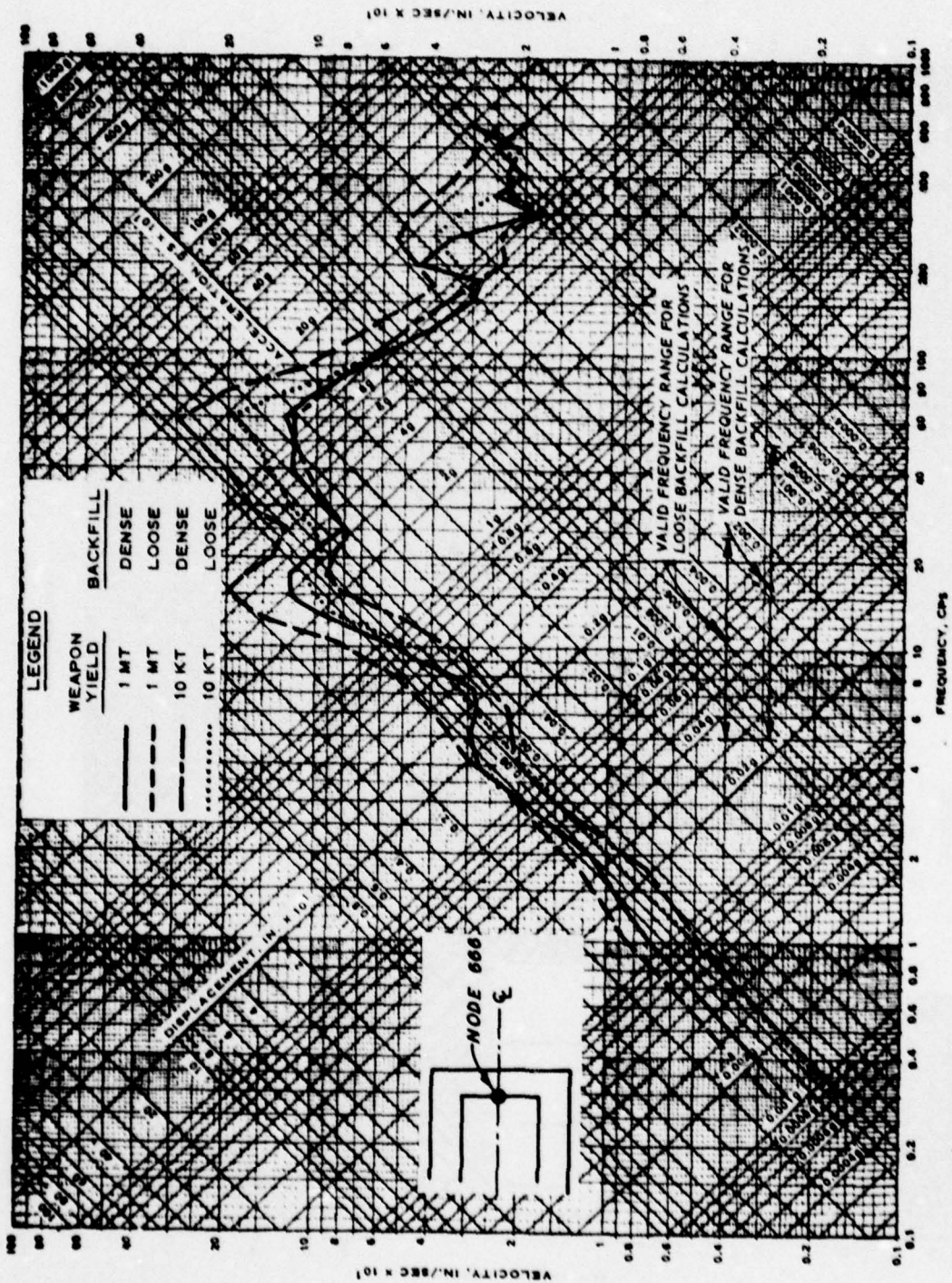


Figure 3.45 Horizontal shock spectra for a point (node 666) on the inside of the leeward sidewall of the structure.

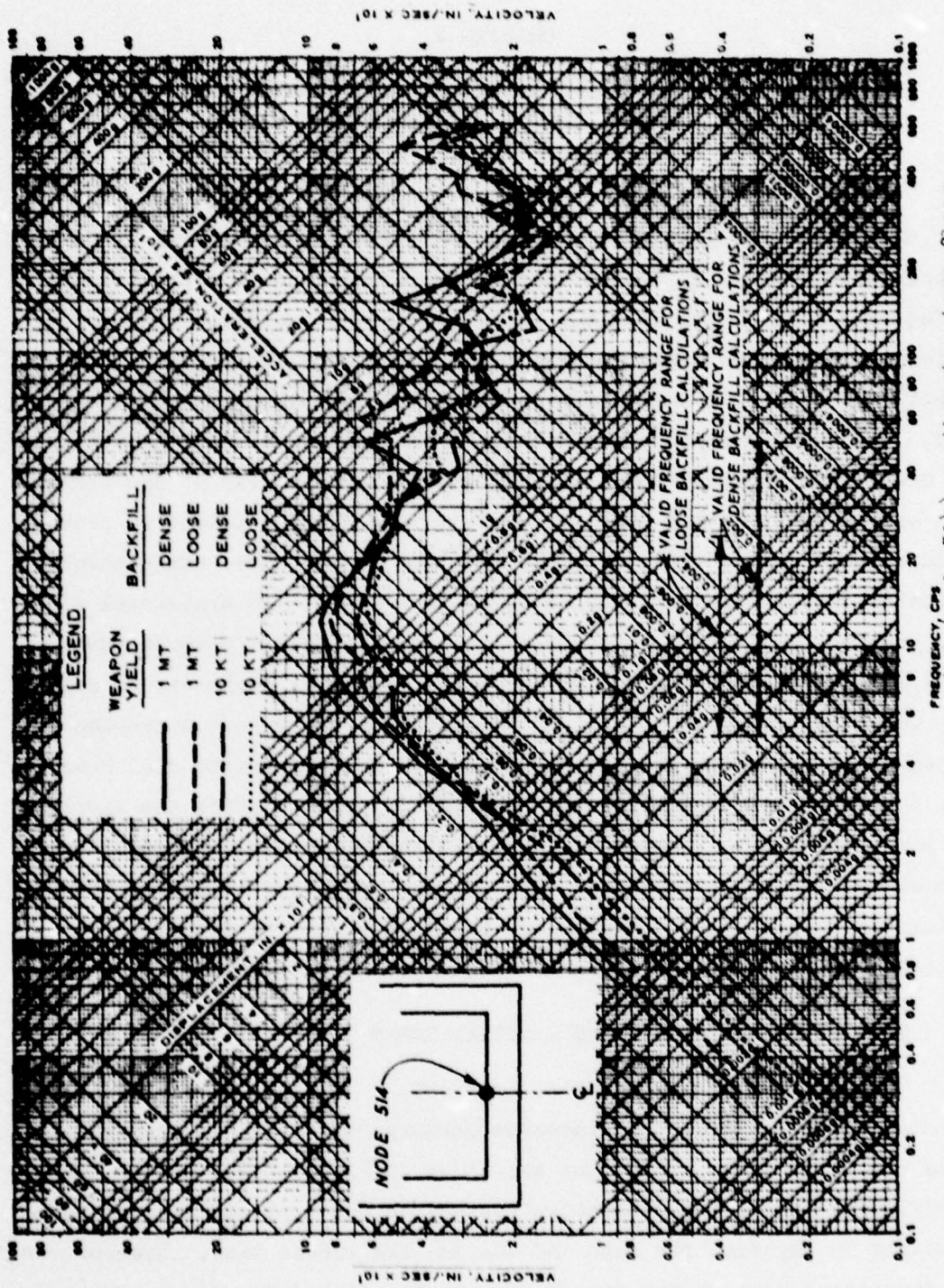


Figure 3.46 Vertical shock spectra for a point (node 514) on the structure floor.

## CHAPTER 4

### PRESENTATION AND ANALYSES OF RESULTS FOR 10-KT WEAPON YIELD, 1000-PSI OVERPRESSURE DENSE BACKFILL CALCULATION

#### 4.1 CALCULATION DESCRIPTION

An additional dynamic calculation was conducted identical to those described in Chapter 2, except the surface boundary of the problem was loaded with a traveling airblast from a 10-KT weapon, which produced a nominal 1000-psi (68.9-bar) overpressure loading on the center of the structure. This calculation was conducted for the dense backfill case only. The applied surface overpressure time histories over the upstream and downstream boundaries of the grid and over the center of the structure are shown in Figure 4.1. There is a very large gradient in peak surface overpressure (10x) over the 240-foot (73.2-metre) range covered by the calculation grid as indicated in the figure. No artificial rise time was appended to the front of this loading function because the added impulse for a 10-KT yield, 1000-psi (68.9-bar) overpressure relation would be too great if a rise time commensurate with the frequency transmission capability of the grid was appended. A finite rise time will develop in the media due to the grid limitations after the airblast has propagated into it for some small distance. Credible frequencies probably will not exceed 50 Hz. The maximum objective of adding this calculation was to gain qualitative insight into the effect of this additional case on the external loading on the structure.

#### 4.2 STRESS AND DISPLACEMENT AT SELECTED TIMES

##### 4.2.1 Deflections Across Backfill Sections

Calculated vertical displacement patterns for sections through the dense backfills at 40 and 100 ms are shown in Figure 4.2. At the 5-foot (1.52-metre) depth, the deflection pattern on the upstream side of the structure is the same for both the 40- and the 100-ms time. However, on the downstream side of the structure, the backfill deflections at 100 ms

are greater than at 40 ms because at 40 msec the peak stress has not yet propagated to the 5-foot (1.52-metre) depth. Similar behavior is also shown for the 15-foot (4.57-metre) depth. The maximum backfill deflection at the 5-foot (1.52-metre) and 15-foot (4.57-metre) depths in the vicinity of the structure at 100 ms are 23 and 12 centimetres, respectively. For the 10-KT weapon yield, nominal 300-psi (20.7-bar) loading over dense backfill calculation, the maximum deflections at the same depths and time were 19 and 7 centimetres, respectively.

#### 4.2.2 Stresses on and Deflection of the Exterior Surfaces of the Structure

Instantaneous distribution of normal stresses on the exterior surfaces of the structure at 40, 70, 150, and 200 ms are shown in Figure 4.3. Instantaneous patterns of deflection along the exterior surfaces of the structure at the same times are shown in the same figure. The 40-ms time is close to the time (45 ms) that the maximum deflection of the center of the roof occurs. At 40 ms, the stresses are concentrated under the sidewalls. The floor and the roof are bowing inward, and the walls are bowing outward. At 70 ms, the high stresses under the sidewalls have been relieved, the roof is rebounding, and the downward deflection of the center of the floor is catching up with that of the sidewalls. The blastward sidewall is undergoing a shear deformation, while the leeward sidewall has about rebounded approximately to its undeformed shape. At 150 and 200 ms, the stress on the structure is relieved, and the complete structure is moving upward, taking a shape similar to its unstressed shape and rotating in a clockwise direction. The patterns of calculated stresses on and the deflected shapes of the exterior surfaces of the structure observed here are qualitatively similar to those observed for the structure for the 10-KT, 300-psi (20.7-bar) dense backfill calculation whose results are shown in Figures 3.6 through 3.10.

#### 4.2.3 Rotation of the Structure

The structure follows the same trends in rotation during this calculation, as shown in Table 4.1, as it did during the nominal 300-psi

(20.7-bar) overpressure, dense backfill calculation (Table 3.1). The structure rotates initially in a counterclockwise direction and then in a clockwise direction. The maximum rotation in this calculation was 0.00328 radians and is approximately one-third greater than the maximum rotation in the 10-KT/300-psi (20.7-bar)/dense backfill calculation.

#### 4.2.4 Thrusts, Shears, and Bending Moments Within the Structure

Axial thrust, shear, and bending moment per unit depth of the structure were calculated from the output data and tabulated at 10-ms intervals for the 28 structural sections shown in Figure 2.20. From the data in Table 4.2, shear and moment diagrams were plotted for the roof, floor, and sidewalls for times very near those when the axial stress in elements near the center of each member maximized. This time was found to be approximately 40 ms for all components. Figure 4.4 presents moment and shear diagrams for the structure floor and roof at 40 ms, while Figure 4.5 shows those for the sidewalls.

The trends in the moment and shear diagrams for the roof and floor of the structure are the same for this calculation (Figure 4.4) as they were for the calculations with the 300-psi (20.7-bar) nominal overpressure loading (Figures 3.11 and 3.12). The maximum moment at the center of the roof from the 300-psi (20.7-bar), 10-KT dense backfill calculation (Figure 3.11) was  $13 \times 10^6$  Newton-metres/metres. The maximum moment at the center of the roof from this calculation is approximately  $20 \times 10^6$  Newton-metres/metres. Therefore, the effect of raising the applied overpressure from 300 psi (20.7 bars) to 1000 psi (68.9 bars) for this case increased the moment at the center of the roof by a factor of approximately 1.5. However, the maximum moment for this case was not as high as that for the 1-MT/300-psi (20.7 bar)/loose backfill case and was about equal to that of the 1-MT/300-psi (20.7-bar)/dense backfill case. The maximum moment near the center of the roof occurred at Section EE for this calculation, and at Section FF for the previous calculations.

The trends of the moment and shear diagrams for the structure side-walls, as shown in Figure 4.5, for the 10-KT/1000-psi (68.9-bar)/dense backfill calculation, are similar to those for the sidewalls from the previous calculations (Figure 3.13). The maximum moments in the blastward and leeward sidewalls for this calculation occur at Sections  $\omega\omega$  and KK, respectively, were  $9.5 \times 10^6$  and  $10.8 \times 10^6$  Newton-metres/metres, respectively, and are factors of 1.6 and 1.3, respectively, greater than those from the 10-KT/300-psi (20.7-bar)/dense backfill calculation. The maximum shear in the leeward sidewall from this calculation is almost identical to that from the 1-MT/300-psi (20.7-bar)/dense backfill calculation.

The maximum moments and thrusts that occurred in the structure roof, floor, and sidewalls, as shown in Figures 4.4 and 4.5 and in Table 4.2, are tabulated below:

Structural Member	Section (Figure 2.20)	Moment N-m/m (kip-in./in.)	Thrust N/m (kip/in.)
Roof	EE	$20.7 \times 10^6$ (4650)	$0.17 \times 10^6$ (1)
Floor	RR	$11.4 \times 10^6$ (2580)	$5.2 \times 10^6$ (30)
Blastward Sidewall	$\omega\omega$	$9.4 \times 10^6$ (2130)	$19.88 \times 10^6$ (115)
Leeward Sidewall	KK	$10.8 \times 10^6$ (2420)	$17.9 \times 10^6$ (100)

These values of thrust and moment are very close to those for the 1-MT/300-psi (20.7-bar)/dense backfill calculation.

#### 4.3 SELECTED TIME HISTORIES

Figures 4.6 through 4.11 present comparisons of selected stress and motion time histories from the calculation. In each figure, the element and/or node locations are sketched. The sign convention for these figures is as follows: upward and outward movements and tensile stresses are considered positive.

Figures 4.6 and 4.7 show vertical displacement and vertical velocity time histories, respectively, for points on the center of the structure roof and floor. The maximum downward displacement of the center of the

roof (which includes some rigid body displacement of the structure) is 10.4 centimetres and occurs at a time of 45 ms after the start of the problem. The peak downward displacement for the center of the roof from the 10-KT/100-psi (68.9 bars)/dense backfill calculation (Figure 4.6) is about the same as that from the 1-MT/300-psi (20.7-bar)/dense backfill calculation (Figure 3.16). The peak downward velocity for the center of the roof is 0.77 centimetres/ms. This value is approximately 50 percent higher than that from the 1-MT/300-psi (20.7-bar)/dense backfill calculation. After the first relative maximum in displacement occurs, the period of oscillation at the center of the roof (node 513) was approximately 55 ms (i.e., 18 Hz). This is slightly higher than the frequency range observed for the previous four calculations (see Section 3.2 of Chapter 3).

Figures 4.8 and 4.9 show the horizontal displacement and velocity time histories, respectively, for points at the center of the sidewalls. The trend in the horizontal displacement versus time for the center of the blastward sidewall is similar to that shown in Figure 3.23 for the 1-MT/300-psi (20.7-bar)/dense backfill calculation. The center of the leeward sidewall is always deflected leewardly from its original position.

Figure 4.10 shows the horizontal stress time histories for points near the inside extreme fibers at the approximate centers of the structure roof and floor. Both the points are in tension at 40 ms. This is expected from the deflected shape of the structure (Figure 4.3). The maximum tensile horizontal stress for element 514, near the center of the roof, is 430 bars, which is about the same as the maximum tensile stress at the same point from the 1-MT/300-psi (20.7-bar)/dense backfill calculation (Figure 3.19).

Figure 4.11 shows the vertical stress time histories for points near the inside fiber and midheights of the sidewalls. The maximum compressive vertical stress, 420 and 480 bars, for elements 369 and 679, respectively, in Figure 4.11 are slightly greater than those at the same points from the 1-MT/300-psi (20.7-bar)/dense backfill calculations as shown in

Figures 3.37 and 3.38, respectively.

#### 4.4 SHOCK SPECTRA

Figure 4.12 presents the 2 percent damped shock spectra calculated from the velocity wave forms in Figures 4.7 and 4.9. As was observed for the previous calculations (see Section 3.3), the inside of the structure roof (node 513) has the most severe calculated shock environment, and the center of the floor has the least severe shock environment of those points examined. The maximum spectral response of the structure sidewalls and roof occurs at frequencies of 17 to 20 Hz. The range of frequencies for the maximum response for the roof and sidewalls from previous calculations (see Section 3.3) was from 15 to 17 Hz. The shock spectra for all structural members were made larger by a factor of 2 or less when compared with those from the 10-KT/300-psi (20.7-bar)/dense backfill case and compared well with those for the 1-MT/300 psi (20.7 bar)/dense backfill case.

#### 4.5 SUMMARY

The results of the calculations presented in this chapter (i.e., nominal 1000-psi (68.9-bar) surface overpressure loading from a 10-KT weapon and the dense backfill case) indicated the same trends as were observed from the calculations as presented in Chapter 3.

The maximum stresses and bending moments within and the maximum deflections of the structure for this calculation are about the same as those from the 300-psi (20.7-bar) 1-MT yield/dense backfill calculation presented in Chapter 3.

The results of the shock spectra analyses show that the shock environments for the roof, sidewalls, and floor are worsened by a factor of two or less by changing the nominal overpressure from 300 psi (20.7 bars) to 1000 psi (68.9 bars).

The predominant frequency observed in the motion time history of the center of the roof was 18 Hz. It falls well within the credible

frequency range as controlled by the airblast rise time and duration, the FE grid, and the controlling wave speeds of the backfill materials. The deflected shapes of the structure observed at various times during the calculation are similar to those observed in the previous calculations carried out under this project.

**Table 4.1** Rotations of the Chord Formed by the Two Bottom Corners of the Structure; 10-KT Yield, 1000-psi Nominal Overpressure, Dense Backfill Calculation.

Type Rotation	Rotation, rad	Time, ms
Counterclockwise max	0.00123	24
Return to upright position	0	70
Clockwise max	0.00328	176
Final (clockwise)	0.00312	200

Table 4.2 Shear, Thrust and Bending Moment for Selected Sections Through the Structure at a Time of 40 ms after the start of the 10-KT Dense Backfill Calculation.

SECTION	SHEAR FORCE N/M	AXIAL THRUST N/M	BENDING MOMENT N-M/M
AA	-.970859E+07	-.541680E+07	-.408502E+07
BB	-.870663E+07	-.171428E+07	.607642E+07
CC	-.615660E+07	-.927605E+06	.151129E+08
DD	-.160776E+07	-.501366E+06	.200325E+08
EE	.124174E+06	-.167116E+06	.207009E+08
FF	.172170E+07	.302729E+06	.202071E+08
GG	.292577E+07	.495732E+06	.189538E+08
HH	.644964E+07	.523796E+06	.137735E+08
II	.107631E+06	-.121334E+07	.410496E+07
JJ	.110387E+06	-.338164E+07	-.779473E+07
KK	.232482E+07	-.178677E+06	-.107817E+08
LL	.332394E+06	-.198668E+08	-.778599E+07
MM	.247887E+06	-.211645E+08	-.741297E+07
NN	.176505E+07	-.230606E+08	-.570598E+07
OO	-.847744E+07	.402579E+07	-.241303E+07
PP	-.311285E+07	.556348E+07	-.809022E+07
QQ	-.132354E+07	.541573E+07	-.107196E+08
RR	.417472E+06	.520379E+07	-.114540E+08
SS	.939866E+06	.485546E+07	-.111454E+08
TT	.130268E+07	.474169E+07	-.107059E+08
UU	.214474E+07	.467863E+07	-.979269E+07
VV	.293951E+07	.492979E+07	-.653778E+07
WW	.355583E+07	.389353E+07	-.353607E+07
XX	.884388E+07	.188051E+07	.180897E+07
YY	.771872E+06	-.253162E+08	.682902E+07
ZZ	-.436294E+06	-.231771E+08	.633421E+07
PH	-.728005E+06	-.222506E+08	.718449E+07
HM	-.103960E+07	-.198144E+06	.945024E+07

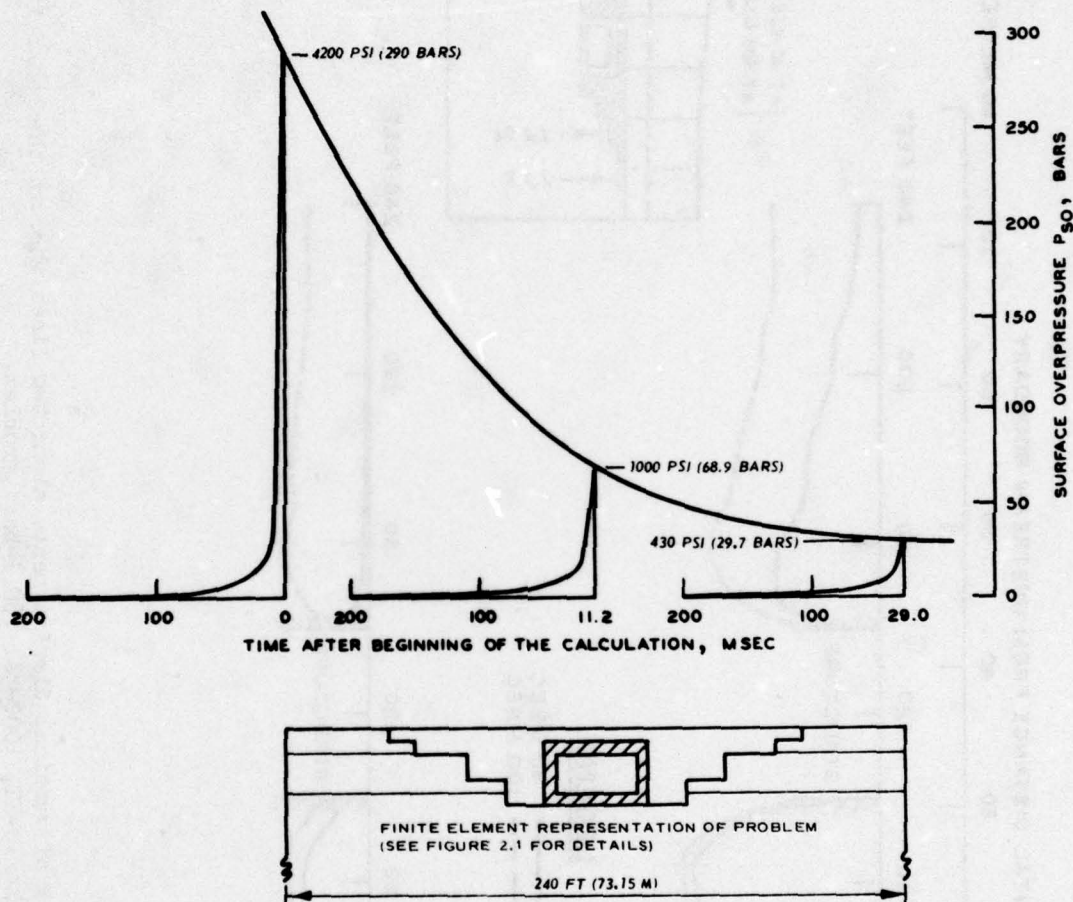


Figure 4.1 Surface overpressure time histories for 10-KT surface burst producing 1000 psi (68.9 bars) over the center of the structure.

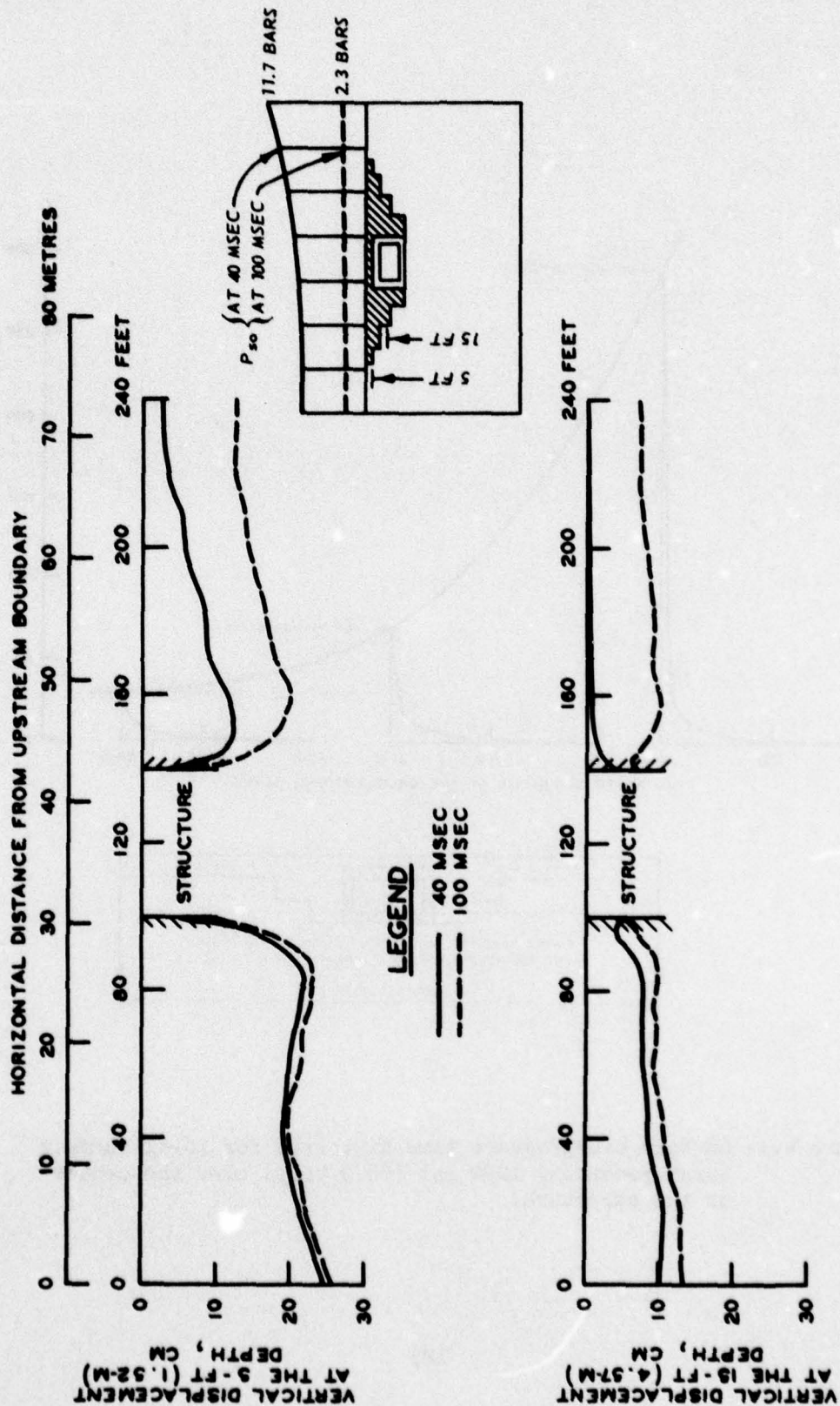
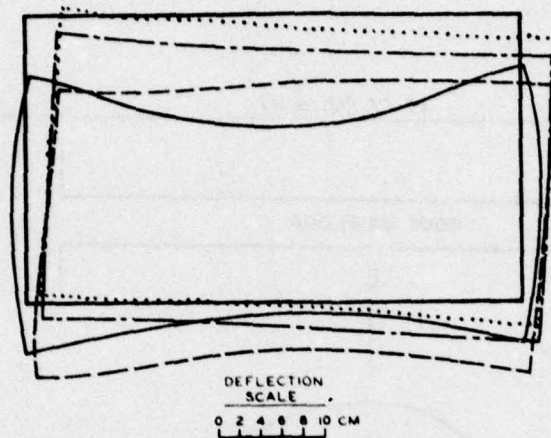
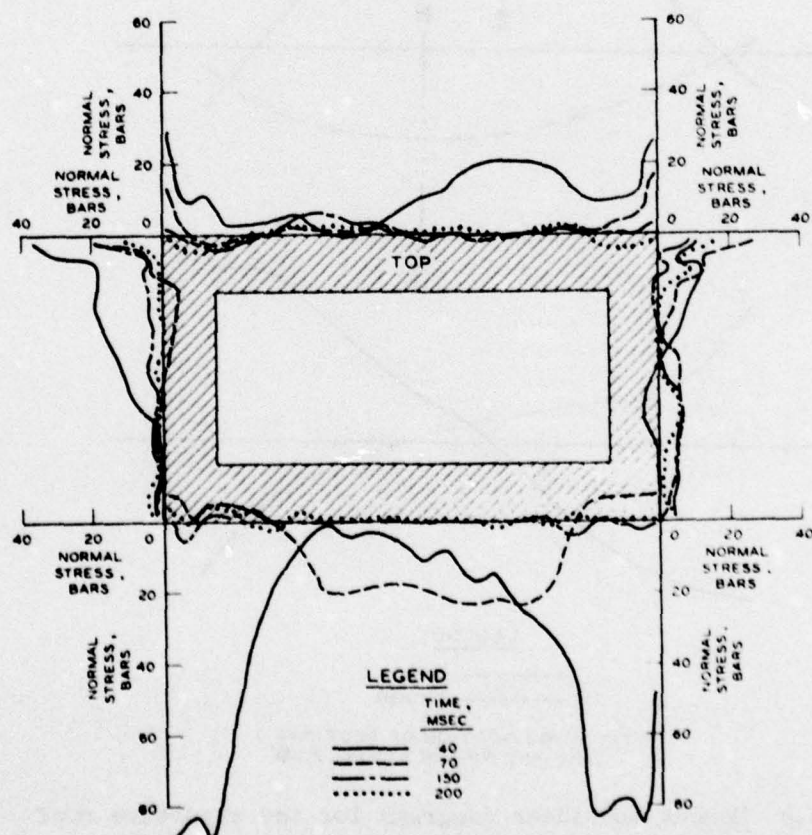


Figure 4.2 Instantaneous pattern of vertical displacements along two lines through the backfill at 40 and 100 ms after the start of the 10-KT, 1000-psi (68.9-bar) problem.

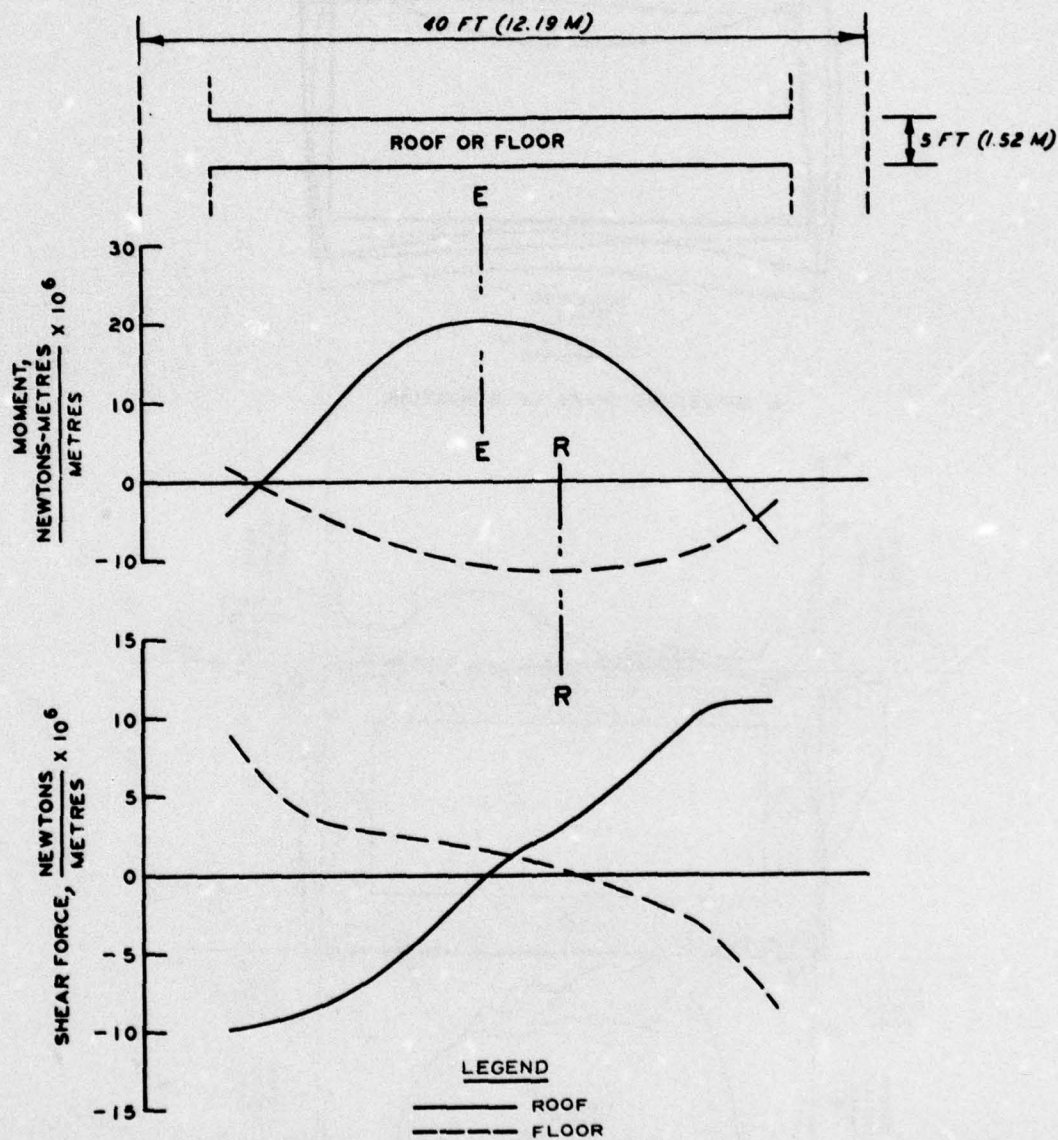


a. DEFLECTED SHAPE OF STRUCTURE



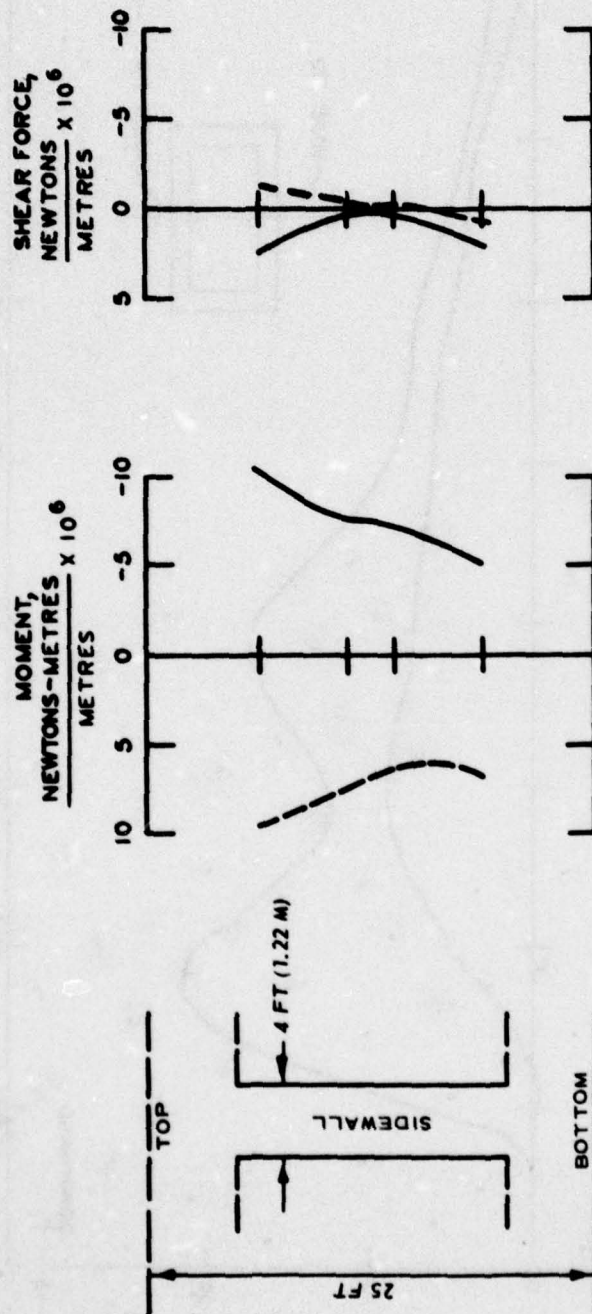
b. STRESSES NORMAL TO STRUCTURE

Figure 4.3 Instantaneous patterns of deflection of and distribution of normal stresses on the exterior surfaces of the structure at 40, 70, 150, and 200 ms.



NOTE: FOR LOCATION OF SECTIONS  
EE AND RR SEE FIGURE 2.20

Figure 4.4 Moment and shear diagrams for the structure roof and floor at 40 ms (the time that the radial stress at the center of the roof and floor maximized).



### LEGEND

- BLASTWARD SIDEWALL
- LEeward SIDEWALL

NOTE: THE MAXIMUM MOMENT OCCURS AT SECTIONS  $\omega-\omega$  AND KK FOR THE LEFT AND RIGHT SIDEWALL, RESPECTIVELY.

SEE FIGURE 2.21 FOR LOCATION OF SECTIONS  $\omega-\omega$  AND KK.

Figure 4.5 Moment and shear diagrams for the structure sidewalls at 40 ms (the time that the vertical stress at the center of the sidewalls maximized).

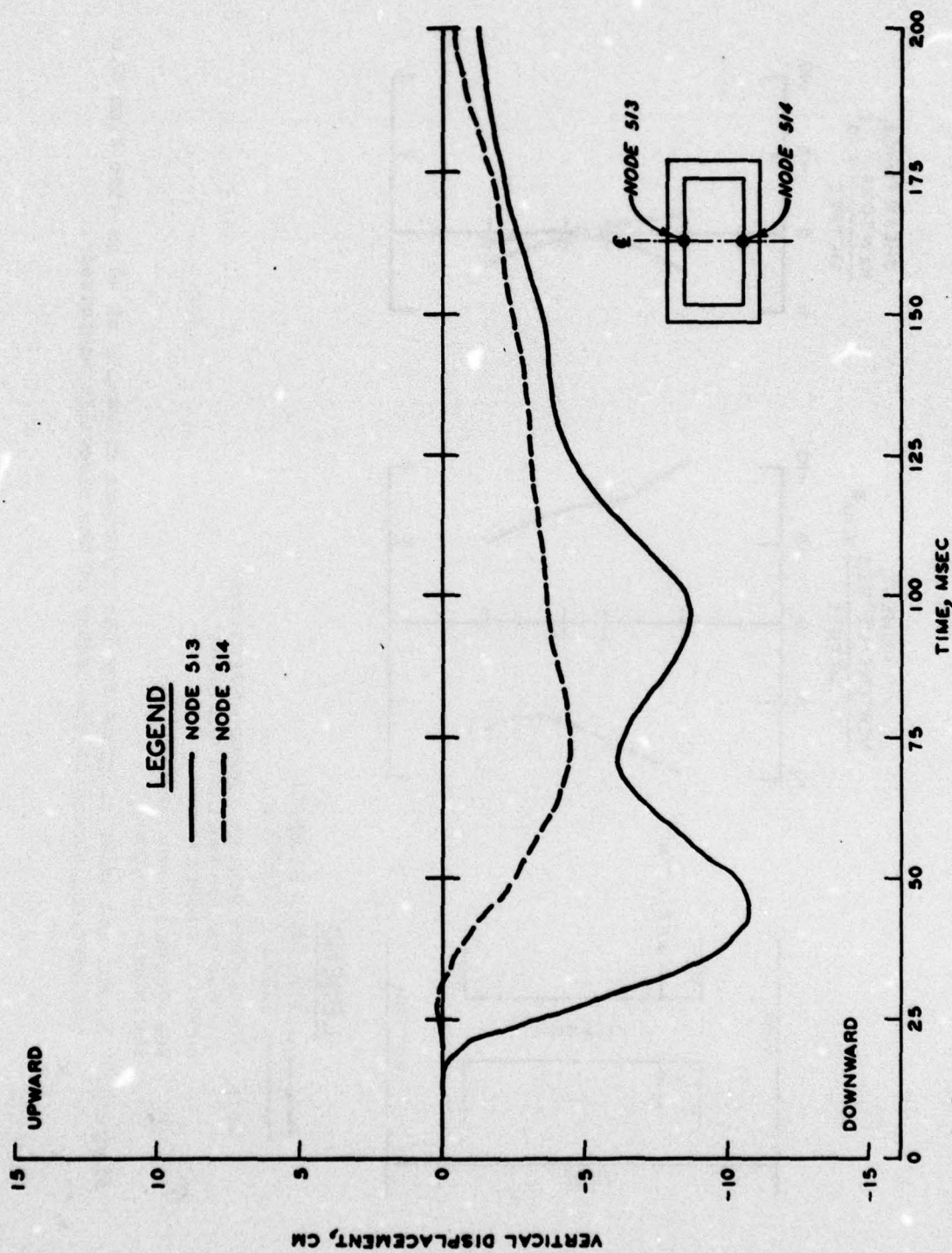


Figure 4.6 Vertical displacement time histories for points at the center of the structure roof and floor.

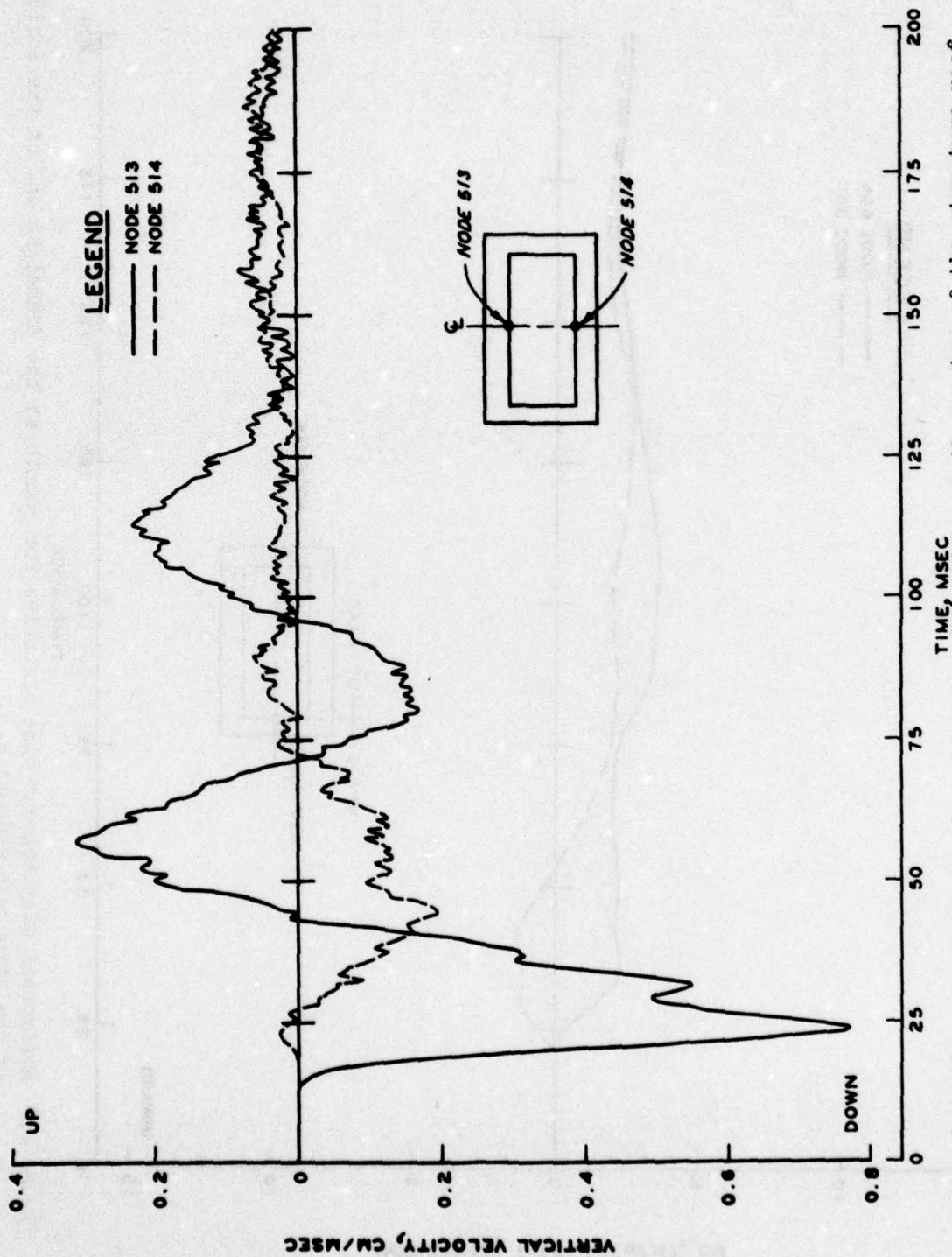


Figure 4.7 Vertical velocity time histories for points at the center of the structure roof and floor.

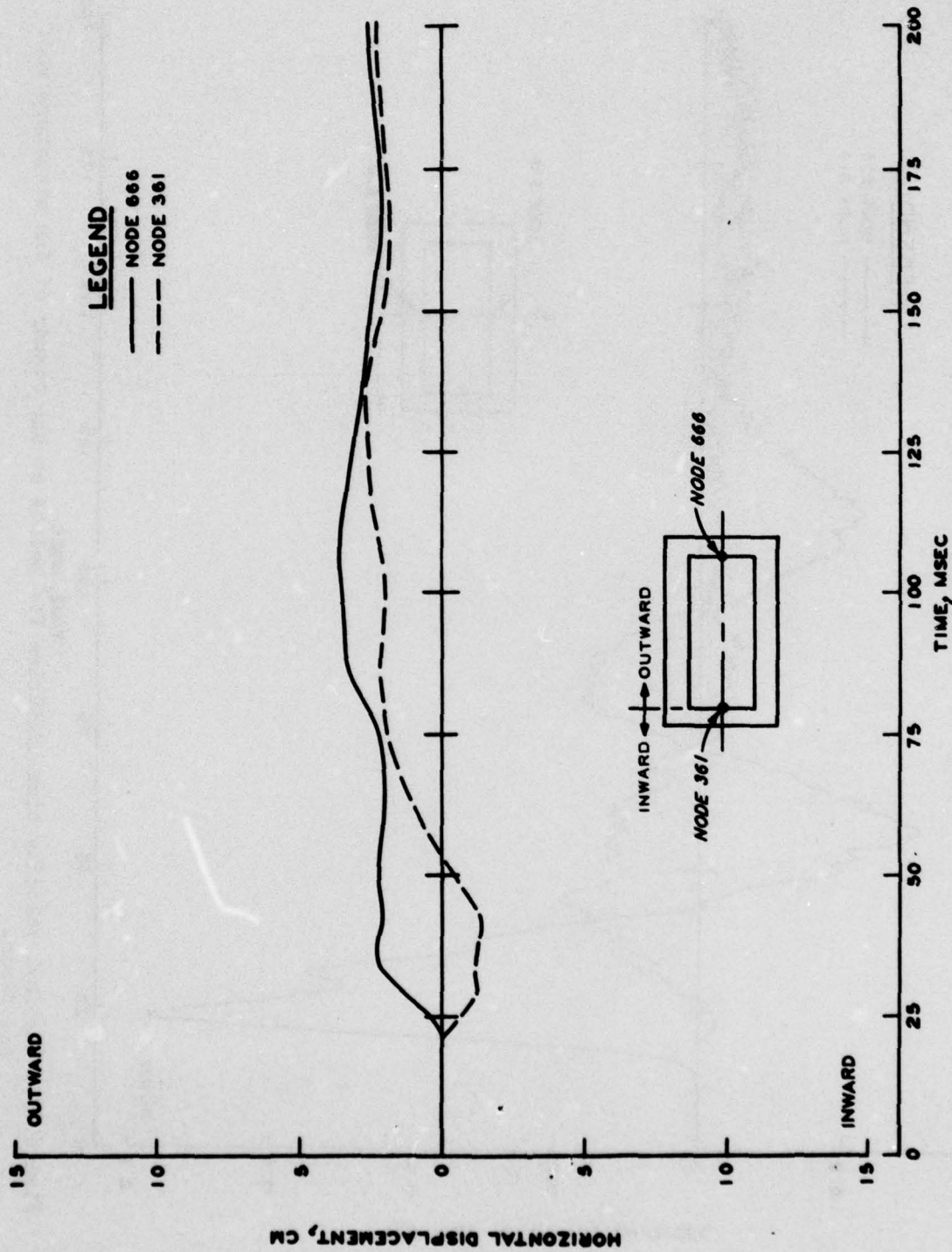


Figure 4.8 Horizontal displacement time histories for points at the midheight and on the inside of the structure sidewalls.

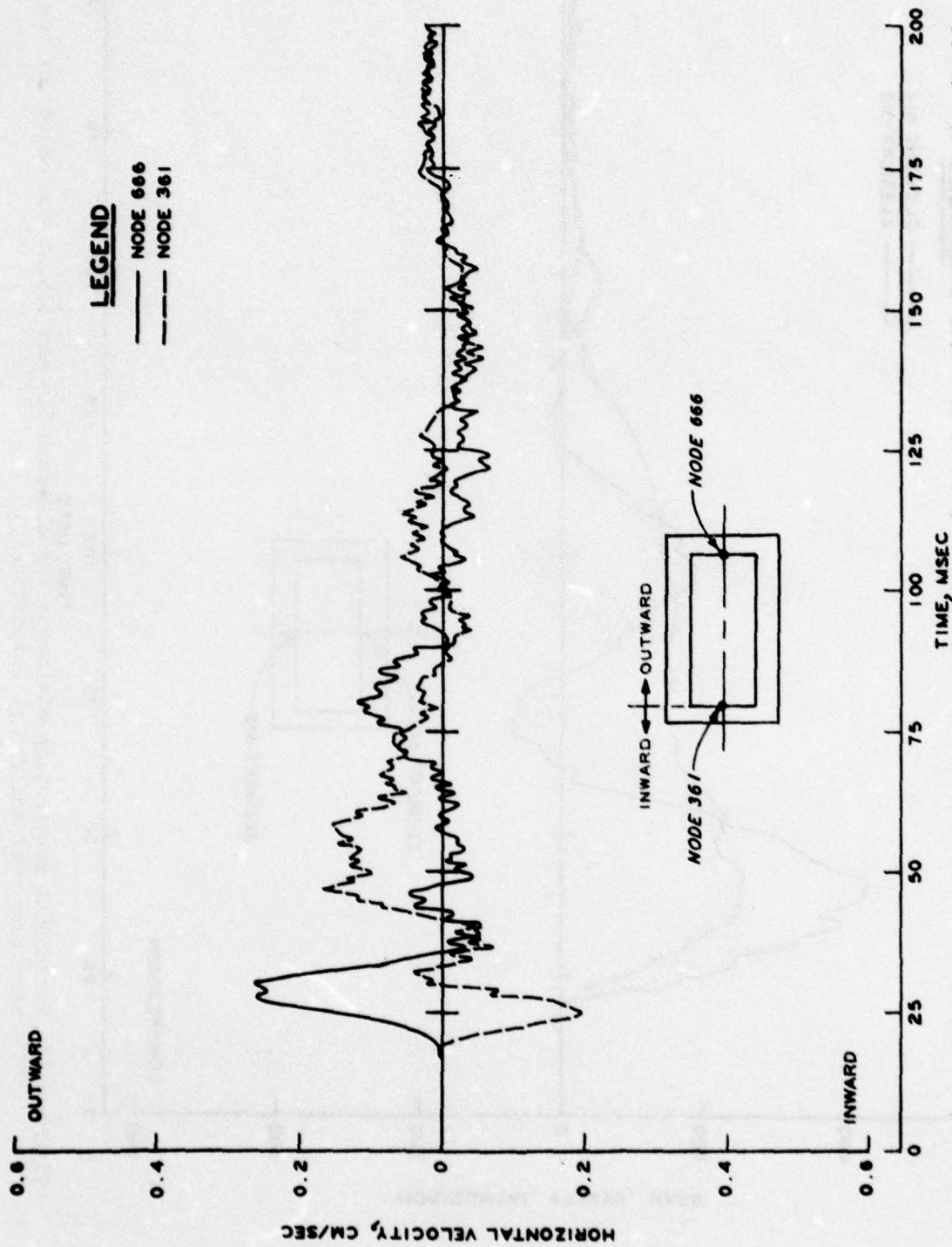


Figure 4.9 Horizontal velocity time histories for points at the midheight and on the inside of the structure sidewalls.

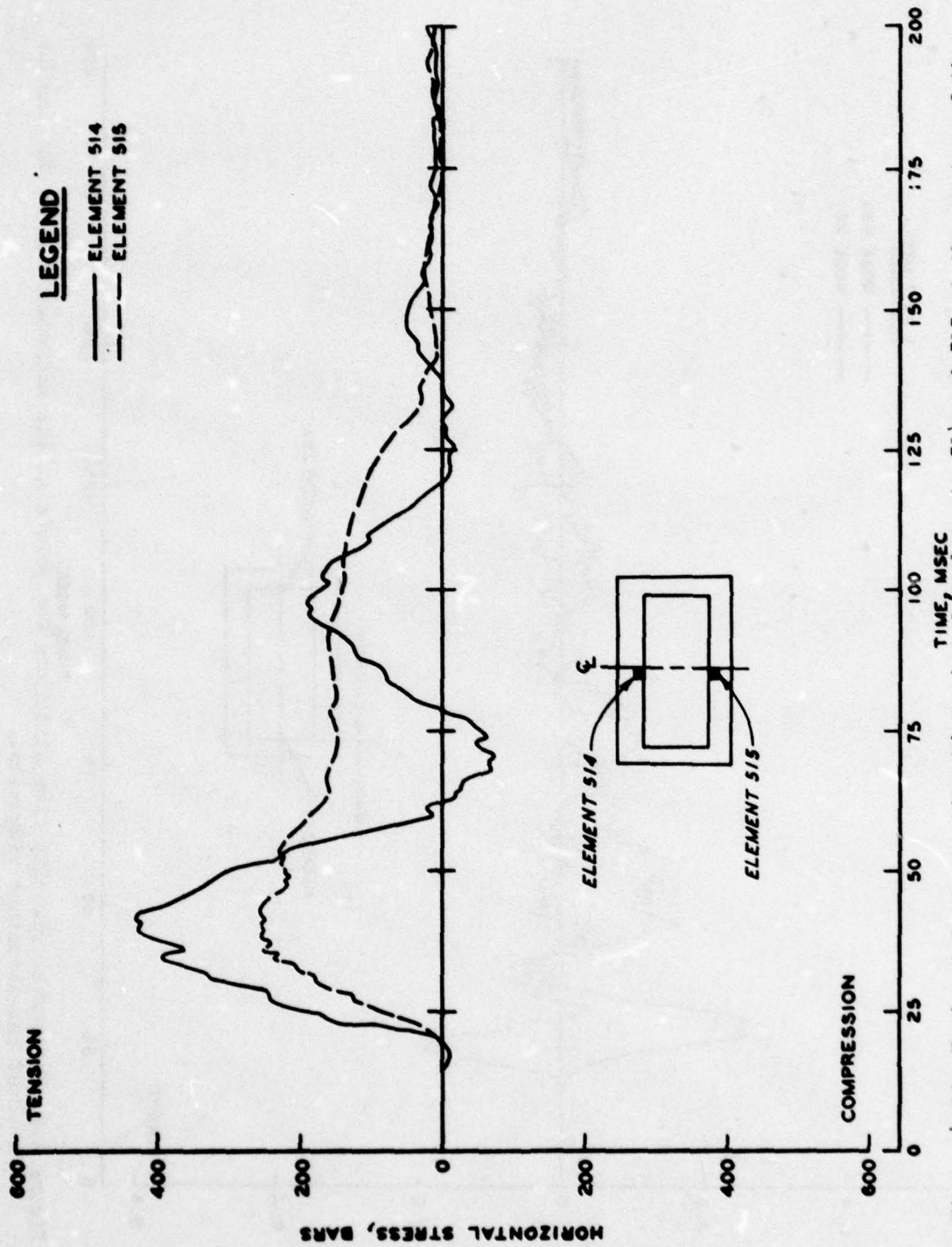


Figure 4.10 Horizontal stress time histories for elements 514 and 515 at the center of the structure roof and floor, respectively.

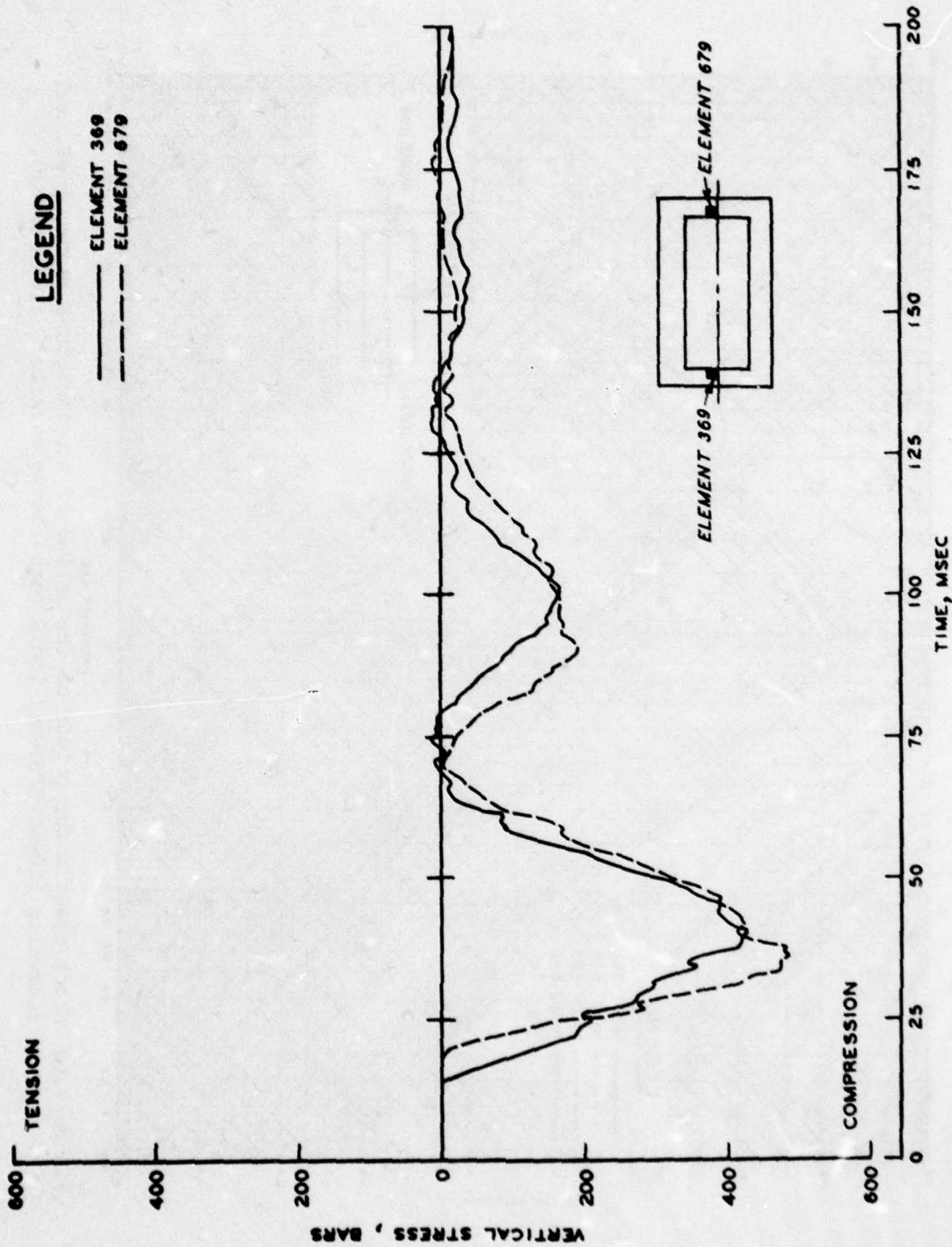


Figure 4.11 Vertical stress time histories for points at the midheight and on the inside of the structure sidewalls.

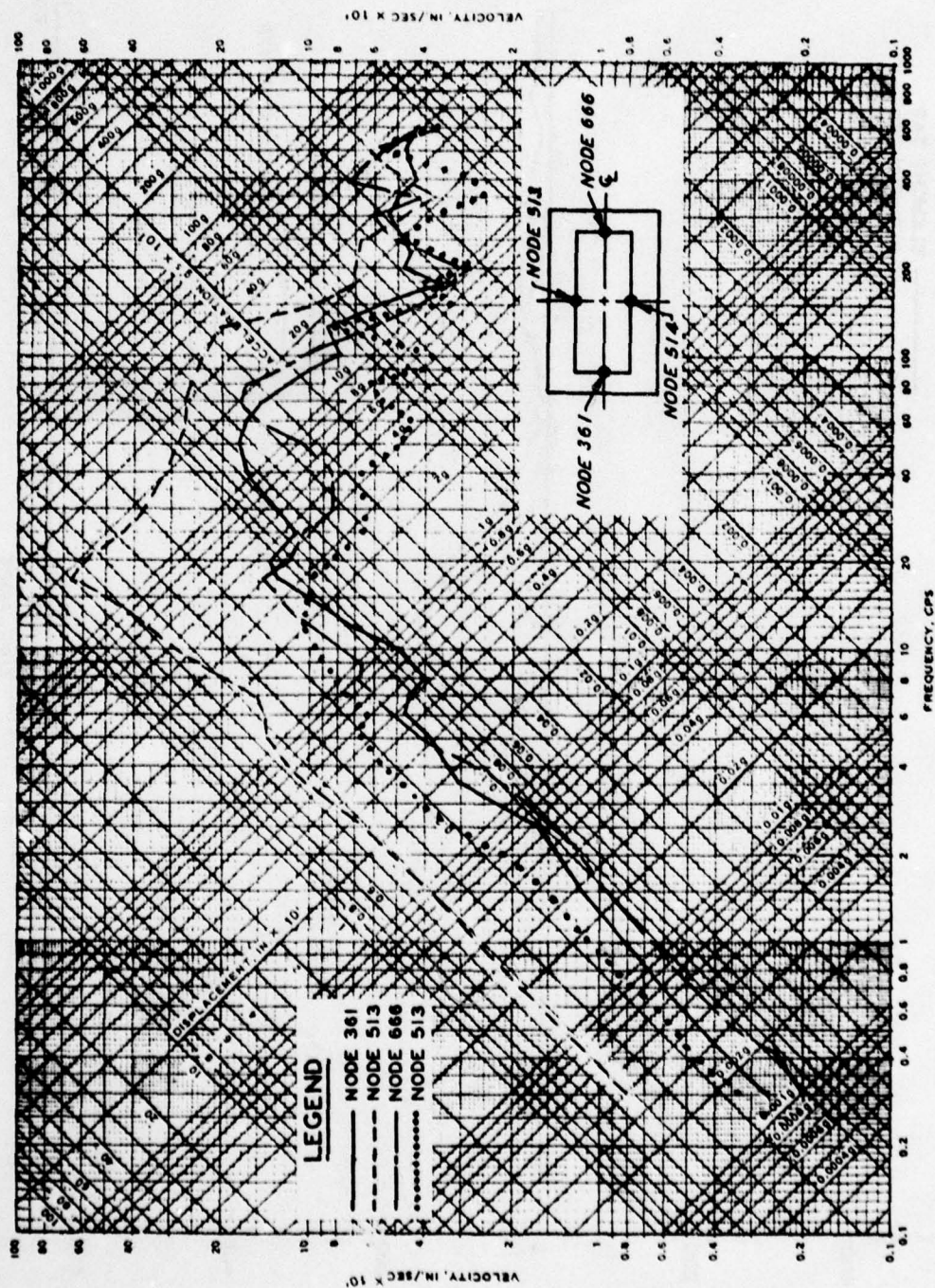


Figure 4.12 Shock spectra for points on the inside of the structure floor, roof, and sidewalls (10-KT/1000-psi (68.9 bars)/dense backfill calculations).

## CHAPTER 5

### PSEUDOSTATIC CALCULATION

#### 5.1 CALCULATIONAL PLAN

A pseudostatic calculation was conducted with the HONDO computer code for the dense backfill case, using the same FE representation and material properties as discussed in Chapter 2. The calculation was conducted with a linearly increasing (with time) vertical, uniformly distributed surface stress applied to the top surface of the FE representation. The stress increased from 0 to 300 psi (20.7 bars). A series of one-dimensional (1D) calculations was conducted to determine the smallest rise time and percentage of damping that could be used and still keep the particle velocities very small. By trial and error, a rise time of 250 ms and a damping coefficient,  $B_2^* = 0.3$ , were determined to give acceptable results. The pseudostatic 2D calculation was then conducted with this rise time and damping coefficient and with a total run time of 360 ms. The 300-psi (20.7-bar) stress was held constant from 250 to 360 ms. The time step was the same as in previous problems.\*\*

#### 5.2 RESULTS

Except for velocity and stress time histories for points at and near the center of the structure roof, all node point velocities became virtually zero after 350 ms, while all element stresses took on constant values. The velocity and displacement time histories of node 511, located at the center of the structure roof, are shown in Figures 5.1 and 5.2, respectively. They present the worst of the results as far as oscillations in

---

\* The type of damping used in HONDO and the definition of the damping coefficients are described in Reference 2.

\*\* While this is not a computationally efficient way of treating a static problem, it turned out to involve much less labor than reformulating the problem for a static code and, therefore, was more economical. It had the additional advantage that it ensured that in dynamic to static comparisons, "other things" were really equal.

velocity are concerned. In terms of displacements, the results are quite acceptable. Similarly, the horizontal stress time history shown in Figure 5.3 for element 511, located near an extreme fiber at the center of the roof, represents the worst case for stress oscillations during the pseudostatic calculation. It is also an entirely adequate static approximation.

Figure 5.4 shows the deflected shapes of structure and the distribution of normal stresses on the structure at 80, 160, and 360 ms. The vertical stress normal applied to the ground surface at these times were 6.6, 13.2, and 20.7 bars, respectively. However, the vertical stress in the soil elements just above the central portion of the structure at 80 and 160 ms was 6.0 and 12.5 bars, respectively, while the stress at 360 ms was 20.7 bars. The stress was increased linearly from 0 to 20.7 bars in 250 ms. Therefore, the stress was being increased at 80 and 160 ms while the 20.7-bar stress had been maintained for 110 ms at the 360-ms time. At the 80- and 160-ms times, the differences in applied stress at the boundary and stress normal to the structure were 9.1 and 5.3 percent, respectively. These differences were caused by the fact that the 250-ms rise time did not allow the applied surface stress to completely equalize throughout the problem due to wave propagation effects. However, the differences (i.e., 5.3 to 9.1 percent) are not considered significant.

As can be seen in Figure 5.4, the stress and deflection patterns are symmetrical about a vertical centerline through the structure. The normal stress on the roof of the structure is uniform at each stress level except over the sidewalls where the stress is increased due to negative arching. The stresses on the sidewalls increase with increase in applied surface stress. The stress distributions normal to the sidewall are concave to the structure sidewall and maximize near the center of the sidewalls. A portion of the stress on the sidewalls is due to partial passive earth pressure caused by the sidewalls bowing out against the backfill. The stresses normal to the base of the structure show a concentration of

stress under the sidewalls and are reasonable when compared with the deflected shape of the structure. The patterns of deflected shape of and the stresses normal to the structure at 360 ms are similar to those from previous calculations at the time that the deflection of the center of the roof maximized as shown in Figures 3.6 and 4.3. The maximum downward deflection of the center of the roof for the pseudostatic calculation is 10.5 centimetres, and the maximum relative deflection of the center of the roof (i.e., the deflection of the center of the roof with respect to a chord drawn through the top corners of the structure) is 4.4 centimetres.

Axial thrust, shear force, and bending moment per unit width of the structure were calculated at a time of 360 ms and are tabulated in Table 5.1 for the 28 structural sections shown in Figure 2.20. Moment and shear diagrams are plotted for the structure roof and floor in Figure 5.5 and for the structure sidewalls in Figure 5.6. The moments in the roof and floor appear to maximize near the center and ends of the spans indicating some degree of fixity due to the sidewalls.

Examination of Figures 5.1 through 5.6 indicates that results obtained from the pseudostatic HONDO calculation are reasonable approximations to a true static calculation. The results of this calculation will be used in the next chapter to establish ratios of dynamic to static response.

Table 5.1 Shear, Thrust, and Bending Moment for Selected Sections Through the Structure at a Time of 360 ms after the start of the 10-KT "Pseudo" Static Dense Backfill Calculation.

SECTION	SHEAR FORCE N/M	AXIAL THRUST N/M	BENDING MOMENT N-M/M
AA	-.923047E+07	-.450562E+07	-.531855E+07
BB	-.675940E+07	-.422561E+07	.421822E+07
CC	-.428842E+07	-.401663E+07	.107887E+08
DD	-.183878E+07	-.389373E+07	.144275E+08
EE	-.613314E+06	-.386882E+07	.151542E+08
FF	.613070E+06	-.386819E+07	.151520E+08
GG	.183805E+07	-.389188E+07	.144212E+08
HH	.428519E+07	-.401229E+07	.107769E+08
II	.675165E+07	-.421872E+07	.420824E+07
JJ	.921604E+07	-.449645E+07	-.531509E+07
KK	.300652E+07	-.156660E+08	-.846141E+07
LL	.154106E+07	-.166063E+08	-.442659E+07
MM	.852266E+06	-.169876E+08	-.328631E+07
NN	-.321412E+06	-.175200E+08	-.259351E+07
OO	-.527104E+07	-.307620E+06	.303815E+06
PP	-.219933E+07	.680402E+06	-.313843E+07
QQ	-.112358E+07	.128071E+07	-.463520E+07
RR	-.440771E+06	.157151E+07	-.534461E+07
SS	-.134424E+06	.162271E+07	-.548200E+07
TT	.134326E+06	.162285E+07	-.548296E+07
UU	.440775E+06	.157194E+07	-.534741E+07
VV	.112390E+07	.128218E+07	-.464083E+07
WW	.220072E+07	.682804E+06	-.314538E+07
XX	.527692E+07	-.305263E+06	.299292E+06
YY	.321168E+06	-.175327E+08	.259205E+07
ZZ	-.855713E+06	-.170009E+08	.328707E+07
PH	-.154607E+07	-.166195E+08	.443022E+07
OM	-.301470E+07	-.156780E+08	.847461E+07

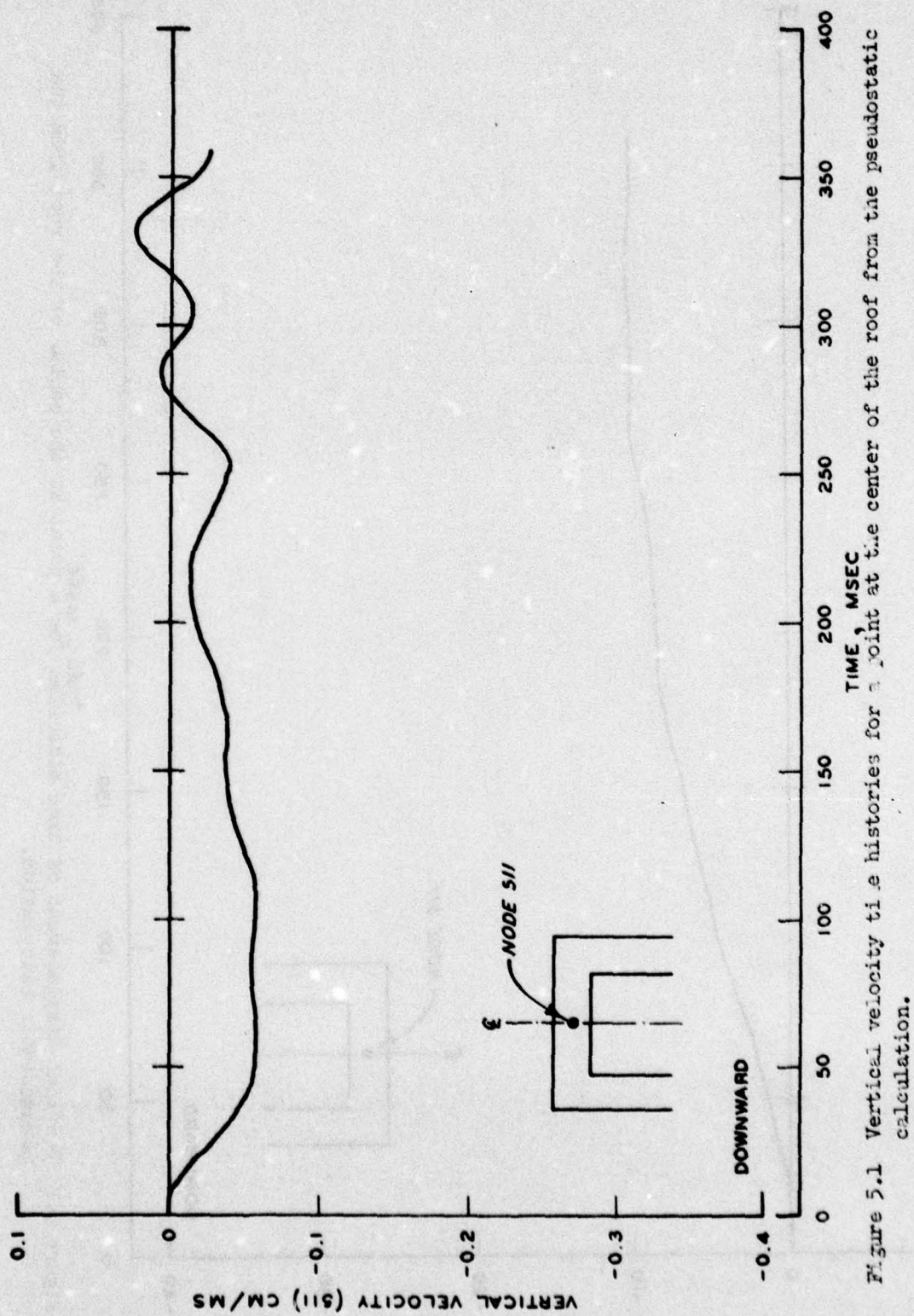


Figure 5.1 Vertical velocity time histories for a point at the center of the roof from the pseudostatic calculation.

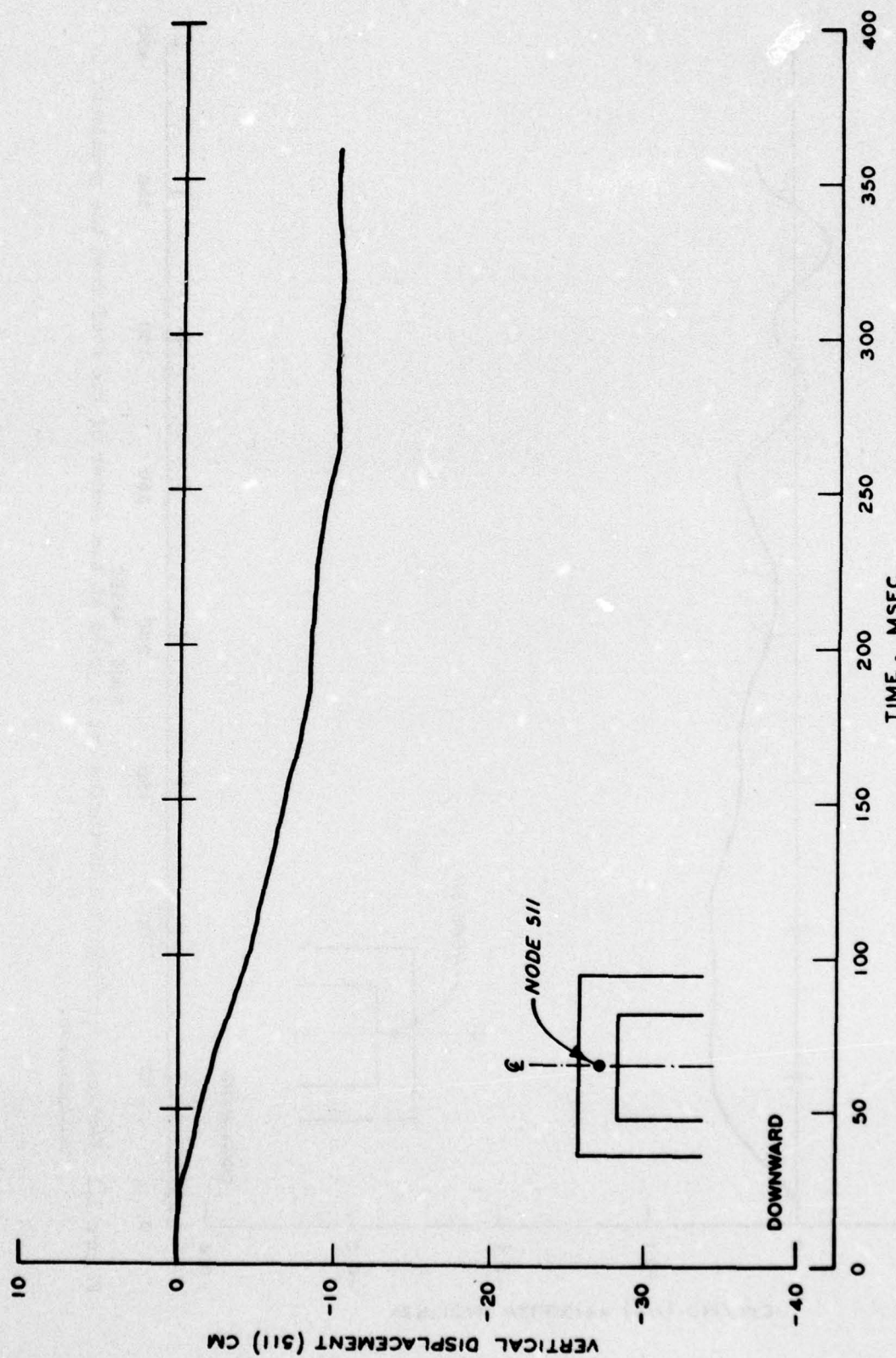


Figure 5.2 Vertical displacement of time histories for a point at the center of the roof from the pseudostatic calculation.

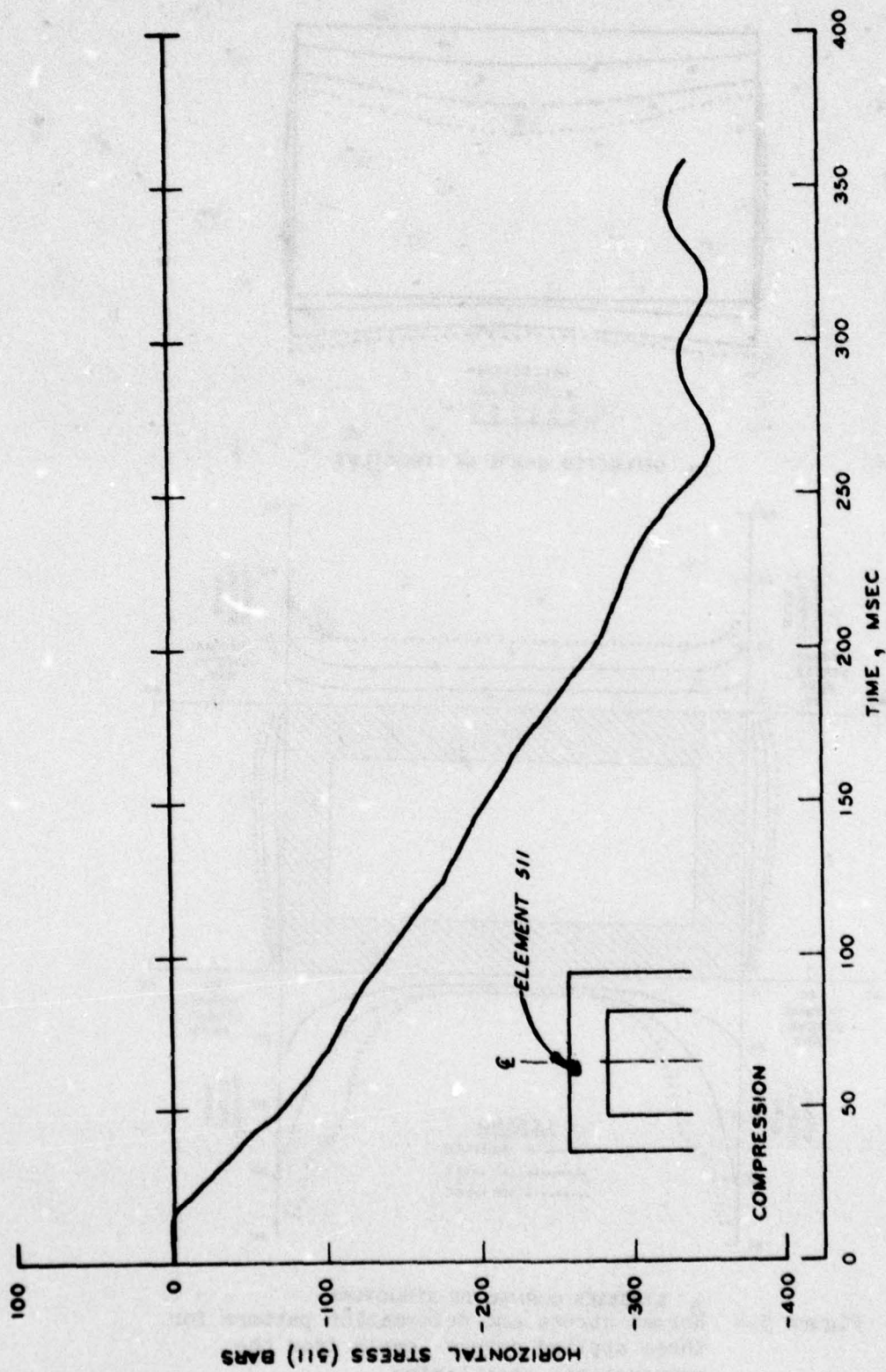


Figure 5.3 Horizontal stress time histories for element 511 from the pseudostatic calculation.

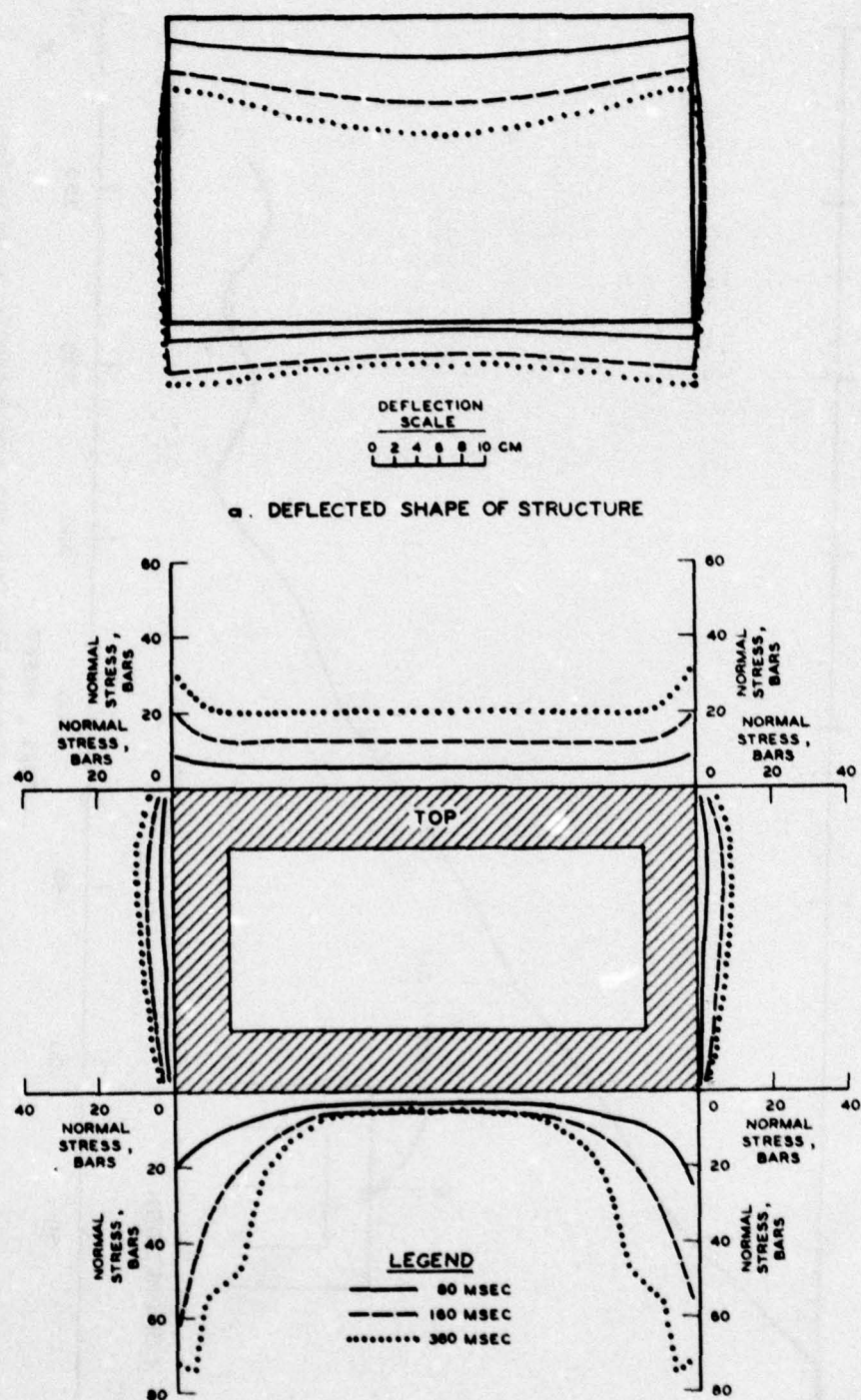


Figure 5.4 Normal stress and deformation pattern for three applied stress levels from the pseudostatic calculation.

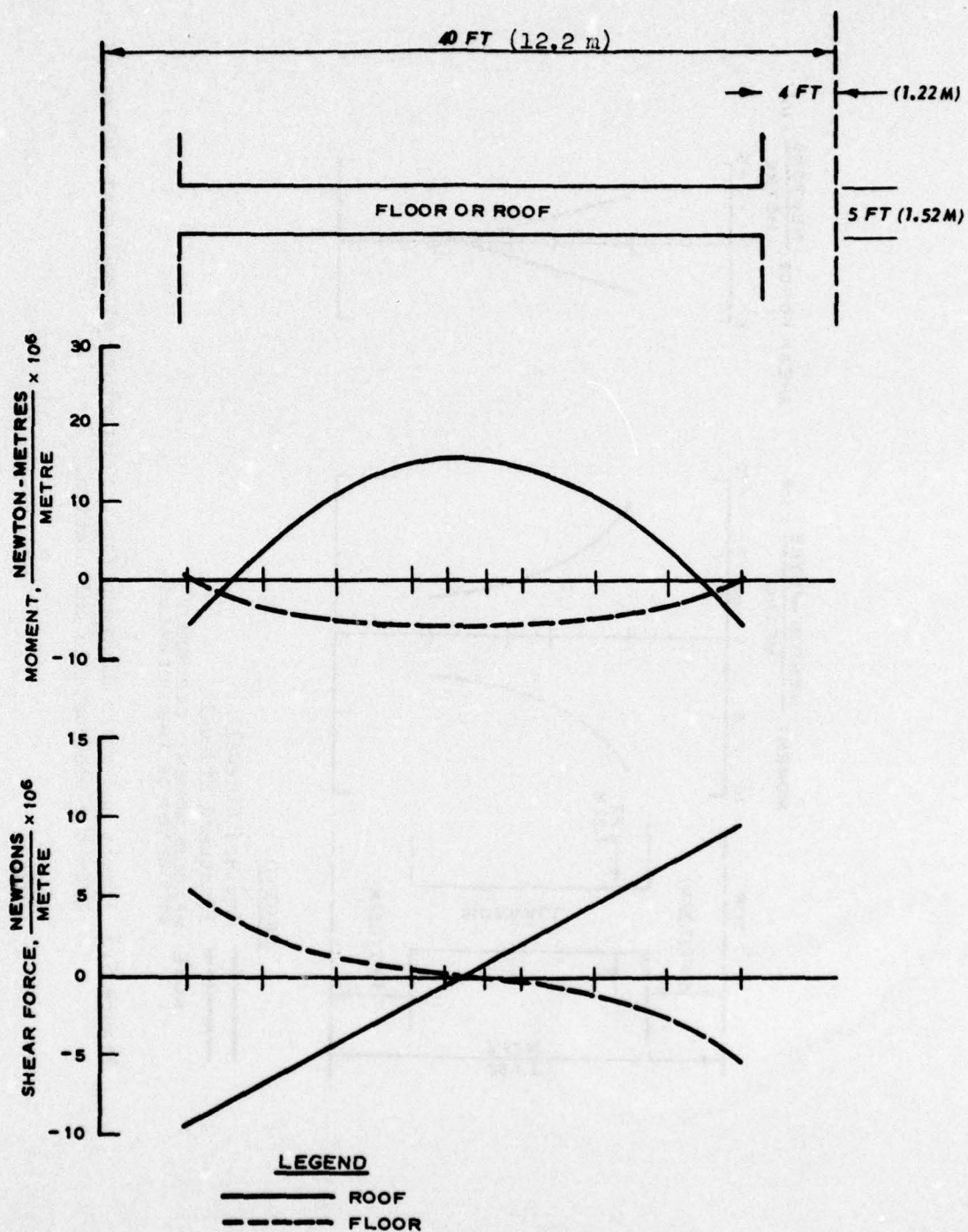


Figure 5.5 Moment and shear diagrams for the structure roof and floor at 360 ms from the pseudostatic calculation.

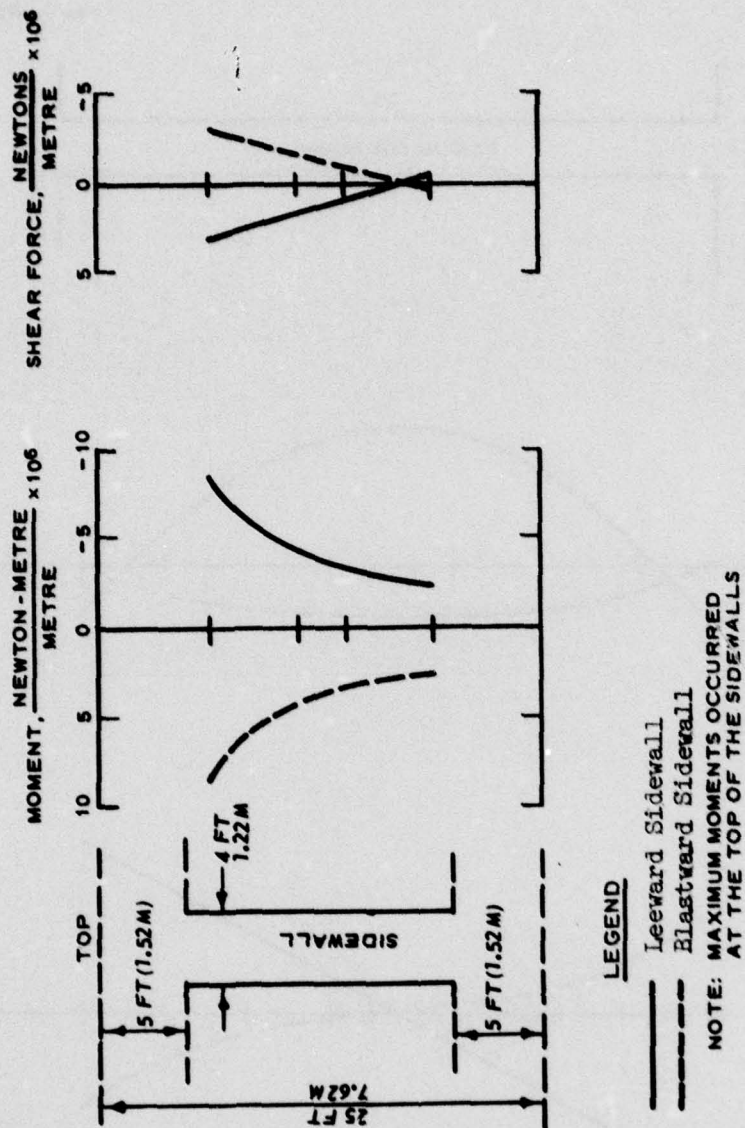


Figure 5.6 Moment and shear diagrams for the structure sidewalls at 360 ms from the pseudostatic calculation.

## CHAPTER 6

### ANALYSIS

#### 6.1 INTRODUCTION

As discussed in Chapter 3 a change in backfill properties from those of a poorly compacted material to those of the same material with a higher degree of compaction reduces the calculated load on and response of a shallow-buried box structure subjected to surface airblast loading. The first part of this chapter explores why this is so. The second portion of this chapter deals with the effects of overpressure ( $P_{so}$ ) and yield ( $W$ ) variations. Obviously, as  $P_{so}$  and  $W$  increase, so do the maximum amplitudes of structural response. This is well documented from linear elastic dynamic structural analyses of protective structures. The relatively small increase in response due to a 3.33 increase in  $P_{so}$  indicated in this study was considered surprising, and an effort was made to try to understand the phenomena that were responsible because, if true, this trend has implications on the accuracy required in targeting with low-yield weapons.

#### 6.2 PHENOMENA RESPONSIBLE FOR DIFFERENCES CAUSED BY A CHANGE IN BACKFILL PROPERTIES

The calculations described in Chapter 3 were conducted for two backfill conditions (loose and dense) and for two overpressure loading relations (i.e., nominal 300-psi (20.7-bar) airblast overpressure loading from 1-MT and 10-KT weapons). As far as response of the linear elastic idealized structure is concerned, the conclusion that may be drawn is that the effect of using loose rather than dense backfill properties for either weapon yield is to increase the calculated deflections of and the stresses within the structure by 25 to 40 percent. The purpose of this section is to examine the phenomena that could be responsible for these differences.

The deflections of the center of the roof, the moments in the roof,

and the bowing out of the sidewalls of the structure were greater for the loose backfill conditions. The dense backfill appears to cause more restraint on the structure sidewalls; therefore, the structure roof behaves more like a fixed beam when surrounded by dense backfill and more like a simply supported beam when surrounded by loose backfill. The greater lateral restraint on the sidewalls for dense backfill conditions could be caused by higher radial stresses transmitted to the structure through the dense backfill than through the loose backfill and/or by its greater strength and stiffness, which would provide larger partial-passive earth pressure per unit outward wall deflection.

#### 6.2.1 Vertical Stress Attenuation

The comparison of stress-strain properties for a state of UX for the loose and dense backfills shown in Figure 2.14 indicates that much more energy will be dissipated as the applied stress pulse passes through the loose backfill than through the dense. This is due to greater hysteresis in the loose backfill stress-strain relation. The practical impact of this is that the vertical airblast-induced stress should be attenuated more as it passed through the loose backfill material than through the dense backfill.

Figure 6.1 shows the variation of peak vertical stress with depth in the backfill from the 1-MT calculations at a point 3.5 metres upstream of the leading edge of the structure. As also noted in the figure, the maximum vertical stresses are roughly the same in the two calculations, which was not expected. The discrepancy may be explained in the following manner. Since the airblast positive phase durations were sufficiently long with respect to the depth of cover and the wave propagation properties of both backfill materials, the 1D wave propagation theory for linear hysteretic materials (Figure 6.2) indicates that stress attenuation at the depth of the roof should have been negligible in both cases. This is in agreement with the results presented in Figure 6.1. Hence, both theory and calculation results indicate that the maximum vertical free-field stress at the depth of the roof was almost the same

for the two backfill materials. Since the constitutive model is isotropic, it may be concluded that radial stress attenuation is not the primary cause of reduced lateral restraint on the sidewalls for the loose backfill condition.

#### 6.2.2 Lateral at Rest Earth Pressures

In addition to differences in stress-strain behavior, the backfills differ in their UX stress path behavior (Figures 2.11 and 2.13); however, this difference is small. Had the differences in the loading stress paths (whose slopes are  $\frac{3(1-2\nu)}{1+\nu}$ ) been significant, the at-rest lateral pressure coefficients  $K_0 = \frac{\sigma_{\text{horizontal}}}{\sigma_{\text{vertical}}} = \frac{\nu}{1-\nu}$  would have been different, and equal vertical stresses adjacent to the structure would have produced different lateral stresses on a rigid (nonmoving) structure. For the loose and dense backfills over the 0- to 20-bar range, the  $K_0$ 's are 0.50 and 0.44, respectively. This difference seems too small to have any significant effect on structure loading.

#### 6.2.3 Lateral Passive Earth Pressures

Figure 6.3 shows horizontal stress time histories for elements adjacent to the blastward structural sidewall from the 1-MT/300-psi (20.7-bar)/loose and dense backfill calculations. As also noted in the figure, the horizontal stress during the 50- to 75-ms time range is much greater for the dense backfill case than for the loose backfill case in spite of the fact that  $K_0$ 's are similar. This time range corresponds with the times at which the maximum downward deflection of the roof and the maximum outward deflection of the sidewalls occur as shown in Figure 3.6. This also is the time that the maximum moments, thrusts, and shears occur in the structure as shown in Figures 3.11 through 3.13. Figure 6.3 is consistent with the idea that the structure is being restrained more in the horizontal direction for the dense backfill case. This restraint would tend to cause the roof and floor to have a greater degree of end fixity. This would, in turn, account for the fact that the deflections of and stresses within the structure roof and floor are

less for the dense backfill.

After examining the wave speeds for the backfill material shown in Table 6.1, it is apparent that the stress is arriving for both backfill cases faster than it is possible for the stress to propagate downward through the backfill materials.\* After examining various paths for first arrivals, the conclusion was drawn that the path for the fastest arrival of stress at the middepth of the backfill adjacent to the structure is downward through the structure sidewall. The time for the stress to arrive at the center of element 278, located at a depth of 6.5 metres below the ground surface and 0.38 metres from the structure sidewall by taking a path through the structure sidewall, is shown in Table 6.2 for each of the backfill cases. The initial loading wave speeds were used for the backfill materials and the concrete. The arrival times at element 278 computed, as shown in Table 6.2, for the 300 psi/1-MT weapon yield/loose and dense backfills are 45.9 and 37.5 ms, respectively. These times compare favorably with the code calculated first arrival times of 48.0 and 39.0 ms shown in Figure 6.3. Lines showing the calculated times of arrival of stress through the backfill are presented in Figure 6.3. They show that the stress propagating vertically downward through the backfill is arriving much later than that which is coming through the structure. Figure 6.4 shows the same trends for the 10-KT loading case. From these analyses, it was concluded that much of the horizontal stress experienced by the elements shown in Figure 6.3 was due to causes other than wave propagation through the backfill. As the sidewall bows out against the backfill due to loading on the structure roof, passive earth pressure is developed. The passive resistance is much greater for the dense backfill case during the time that the maximum deflections and moments in structural sections occur (Figure 6.3) and accounts for the greater structural deflections and moments for the loose backfill cases.

---

\* The code and model are not in error; this was proven by the 1D calculations in which the expected propagation velocities were observed.

Figure 6.5 shows the shear failure surfaces for the two backfill materials. At a given mean normal stress level, the dense backfill has roughly twice the strength of the loose backfill. Since the maximum possible passive earth pressure that can be mobilized in a given material increases with strength, the trends in stresses in Figures 6.3 and 6.4 are consistent with passive earth pressure phenomena.

#### 6.2.4 Stress Wave Reflections off the Concrete

Another phenomenon that causes differences in structural response for the loose and dense backfill cases is reflection of stress on the roof due to the variation in stress-strain properties (Figure 2.14) of the backfill materials. Figure 6.6 shows the vertical stress time histories for points just above the structure roof in the loose and dense backfill calculations for 1-MT and 10-KT weapons. Also, in Figure 6.6, the vertical stress for both weapon yields and backfill conditions is highly oscillatory. This phenomenon is caused by reflection off the relatively stiff, thick roof structure at a depth of 1.52 metres and by the stress wave reflection at the free surface, i.e., the ground surface. The period of oscillation should be approximately  $4H/C_u$ , where  $H$  is depth to the top of the structure and  $C_u$  is the unloading-reloading wave velocity (Table 6.1). For the loose and dense backfill curves, the periods calculated by the formula are 10 and 7 ms, respectively. The average periods in Figure 6.6 are 9.5 and 8.5 ms for the loose and dense backfills, respectively. This oscillary stress time history phenomenon has been seen experimentally in the WES small blast load generator (Reference 10). Since there is a greater impedance mismatch between the loose backfill and the concrete than between the dense backfill and the concrete, the reflected vertical stresses for the loose backfill cases are greater than that for the dense backfill cases (Figure 6.6). Hence, for the same applied airblast loading at the ground surface, a greater vertical loading is experienced by the structure roof for the loose backfill cases than for the respective dense backfill cases. It is concluded that these differences in reflection phenomena coupled

with differences in passive earth pressure effects are the primary causes of larger structural deflections and moments, thrusts, and shears within the structures for the loose backfill cases.

### 6.3 EFFECT OF SOIL COVER ON NATURAL FREQUENCIES

In Appendix A, eigenvalue analyses of the box structure both in vacuo and embedded in elastic media are reported. Figure 6.7 shows the lower two calculated frequencies and corresponding mode shapes for the structure calculated during the eigenvalue analyses for the in vacuo and embedded (stiff) conditions. Summarized below are the results for the lower modes:

Case Studied	Side Sway Mode Hz	Roof-Floor Bending Mode Hz	Remarks
In Vacuo	15.1	18.2	
Embedded (Stiff)	12.0	16.7	Based on unloading moduli for earth media
Embedded (Soft)	5.1	6.8	Media 10 times softer than in stiff media embedded analysis
[Added Mass]	[11.7]	[14.2]	

Embedment causes a decrease in frequency; the softer the media the larger is the decrease. In simple terms, this decrease is occurring because the media contributes more to the mass of the system than to its stiffness. Reference 5 describes a way of estimating the added mass effect. Its application to the in vacuo modes is shown at the bottom of the tabulation above, and it produces results, which are in fairly good agreement, with the embedded analysis that employed elastic constants based on the unloading properties of the media. The deformed shapes of the structure (Figure 3.6) at times of maximum response appear to be a combination of the side sway and the roof-floor bending modes with the latter being predominant.

### 6.4 APPARENT DAMPING IN EQUIVALENT SINGLE-DEGREE-OF-FREEDOM SYSTEM

One elementary way of considering the dynamic response of the linear

elastic structure studied in this investigation is by means of a linear elastic single-degree-of-freedom (SDF) system analysis. If a single mode of the 2D structure is predominant in the 2D response calculations (and this is the case), an equivalent SDF model can be created, which has the natural frequency of this mode. Figure 6.8 shows the roof centerline deflection time histories for four of the five\* dynamic 2D calculations and the maximum deflection in the 300-psi (20.7-bar), pseudostatic surface load calculation. Also presented in the figure are the surface overpressure loading functions used in these calculations. From the deflection time histories, the periods of the oscillation can be scaled:

Peak Overpressure $P_{so}$ bars	Yield W MT	Backfill	Time from Airblast Arrival to Maximum Displacement ms	Period of First Post-Peak Oscillation ms
20.7	1	Dense	44 (11 Hz)	52 (19 Hz)
20.7	1	Loose	46 (11 Hz)	65 (16 Hz)
20.7	0.01	Dense	40 (13 Hz)	54 (19 Hz)
69.0	0.01	Dense	32 (16 Hz)	52 (19 Hz)

The post-peak frequency in the dense backfill cases are in fairly good agreement with the embedded (stiff) and in vacuo roof-floor bending modes. In the loose backfill case, the frequency is lower than in the dense, but the percentage change is much smaller than in the eigenvalue analyses discussed in Section 6.3.

In Figure 6.9, the deflection of the centerline of the roof relative to the average of the corners of the floors is plotted for the 1-MT/300-psi (20.7-bar)/dense backfill calculation. When the deflection of the underlying media is subtracted out, the relative deflection curve is seen to be oscillating about a curve similar in shape to the applied airblast loading function with a period slightly longer than that observed

---

\* The 10-KT loose backfill calculation was not considered here because cursory examination showed it would show similar loose and dense trends as the 1-MT calculations.

in the absolute deflection curve. All of the roof centerline deflection curves in Figure 6.8 were processed in this manner to obtain the periods given in Table 6.3.

The periods for the dense backfill cases in Table 6.3 are approximately 60 ms. A SDF system with an undamped natural period of 60 ms was subjected to a unit load whose time variations were the same as the overpressure functions shown in Figure 6.8. Dynamic responses were calculated for the cases of 0, 20, and 40 percent of critical damping. The dynamic load factors (DLF) from these calculations (i.e., the ratio of maximum deflection of the SDF system to the deflection of the same system under the same peak load applied statically) are given in Table 6.3 and can be seen to decrease significantly as the percent of critical damping increases. These DLF were compared with 2D DLF derived from the HONDO code calculations by the following formula:

$$2D \text{ DLF} = \frac{\text{maximum deflection of centerline of the roof relative to the floor corners in dynamic HONDO calculation}}{\text{relative deflection at the same surface stress level from the pseudostatic calculation}}$$

Since the structure itself is linear elastic, this comparison is legitimate and shows that in order to achieve responses similar to the 2D calculations, the SDF system must be 20 to 40 percent critically damped with higher percentage of damping being appropriate for the shorter duration (lower yield) external loadings.

Since there is no source of damping within the structure, what is the mechanism present in the 2D calculations that has the appearance of equivalent viscous damping? There are two possible sources: the energy absorbing (hysteresis) capacity of the surrounding inelastic media and radiation "damping," i.e., the propagation of energy away from the loaded boundary due to the presence of a large linear elastic (or inelastic) region. Reference 11 concludes that "all footing soil systems are strongly damped" because of the propagation of energy into the subsoil even if the subsoil behaves as a linear elastic medium. The box structure here can be viewed as a large mat footing sitting on a foundation material, and

its "rigid body" motion should be expected to be strongly damped. In fact, it is as shown by the dotted curve in Figure 6.9. The same phenomenon should have an effect on the nonrigid body modes of the structure and is certainly responsible for some of the apparent damping in the roof-floor bending mode seen in the calculated structural response (References 12 and 13). The hysteresis of the backfill should also cause absorption of energy. Neither of these factors are usually considered in SDF system analyses of shallow-buried protective structures subjected to airblast loadings.

While this study is not conclusive, it strongly suggests that SDF system models used in targeting analyses of shallow-buried structures should include a dissipative mechanism to account for the energy removed from the system via radiation and hysteresis. The appropriate damping appears to exceed 20 percent of critical for the class of problems studied here. In cases where the overpressure decays very slowly (the combination of low ( 100 psi) surface overpressures and high yields), ignoring this mechanism has little effect on the maximum response of the system. For high overpressure, and/or low yields, the decay time to one-half the peak overpressure can be less than the natural period of the system, and the system response can be strongly affected by the presence of dissipative mechanisms. The presence of these dissipative mechanisms is thought to be the reason why the differences in response of the 2D elastic structure due to a factor of 3 variation in overpressure were not as large as expected based on previous thinking (largely conditioned by undamped system analyses) about the problem.

As an example of the potential implications consider the following tabulation:

Overpressure psi (bar)	Yield MT	Distance from GZ km	Maximum Relative* Deflection of Roof Based on 0% of Damped SDF Model cm	Actual HONDO Code Relative Deflection cm	Overestimate of Structural Deformation by Undamped SDF System %
300 (20.7)	.01	.15	5.8	3.4	71
1000 (68.9)	.01	.09	10.9	5.6	95
300 (20.7)	1.00	.67	6.1	5.3	15

The undamped SDF system for the two 10-KT cases overestimated the structure roof deflection by a factor of nearly 2. If 6 centimetres of deflection were assumed to be the amount required to cause failure,\*\* one would have to achieve a 1000-psi (68.9-bar) overpressure over the structure to cause the failure that the SDF analysis would predict for the 300 psi (20.7 bars). The CEP would have to be reduced by a factor of 1.7 to maintain the same single-shot kill probability for the 10-KT yield. By introducing the appropriate percentage of damping into the analysis, this trend becomes apparent.

---

\* DLF of 0 percent damping x  $P_{so}/300$  psi x static deflection at 300 psi.

\*\* For a real structure, this would be a ridiculously small value.

Table 6.1 Modulus and Wave Speed Data for Backfill Materials and Concrete.

Material Type	Initial Loading Constrained Modulus		Secant Loading Constrained Modulus		Unloading Constrained Modulus		Initial Loading Wave Speed		Wave Speed for Peak Stress		Unloading Wave Speed	
	$M_i$ , bars	$M_L$ , bars	$M_L$ , bars	$M_u$ , bars	$M_u$ , bars	$M_u$ , bars	$C_i$ , m/ms	$C_p$ , m/ms	$C_p$ , m/ms	$C_u$ , m/ms	$C_u$ , m/ms	$C_u$ , m/ms
Loose Backfill	100	140	140	11,000	11,000	11,000	0.09	0.11	0.11	0.11	0.91	0.91
Dense Backfill	410	550	550	6,200	6,200	6,200	0.16	0.19	0.19	0.19	0.61	0.61
Concrete	165,500	165,500	165,500	165,500	165,500	165,500	2.44	2.44	2.44	2.44	2.44	2.44

Table 6.2 Stress Arrival Times at Element 278 Calculated from Material Wave Speeds, Assuming a Path Through the Structure.

Backfill Type	Weapon Yield	Time for Airblast to Arrive Over Blastward Sidewall	Calculated		Calculated		Calculated		Calculated		Arrival Time at Element 278 from Figure 6.3 and Figure 6.4 ms
			Travel Time Through 1.5 m of Backfill over Structure	ms	Travel Time Through 4.9 m of Concrete	ms	Travel from Sidewall to Center of Element 278	ms	Problem Time for Stress to Arrive at Element 278	ms	
Dense	1 MT	23	10.0		2.0		2.5		37.5		39.0
Loose	1 MT	23	16.7		2.0		4.2		45.9		48.0
Dense	10 KT	18	10.0		2.0		2.5		32.5		34.0
Loose	10 KT	18	16.7		2.0		4.2		40.9		42.0

Table 6.3 Comparison of DLF from 2D Calculations with Those for Damped SDF Systems.

Peak Overpressure psi	Yield bars	mt	Backfill	Relative Maximum Displacement of roof C - (A + B)/2 cm	2D DLF*	Periods of Relative Displacement		SDF System			
						1st Cycle	2nd Cycle	Damping 0%	Damping 20%	Damping 40%	
						ms	ms				
300	20.5	1	Dense	5.3	1.33	64	59	1.53	1.16	-	
300	20.5	.01	Dense	3.4	0.85	59	60	1.44	1.07	0.86	
1000	69.0	.01	Dense	5.6	0.42**	57	59	0.82	0.63	0.50	
300	20.5	Static	Dense	4.0	1.00	-	-	1.00	-	-	

\* 2D DLF = Maximum relative deflection of roof centerline in dynamic 2D calculation + deflection from pseudostatic calculation at same overpressure level.

\*\* DLF based on static deflection extrapolation from 300- to 1000-psi load.

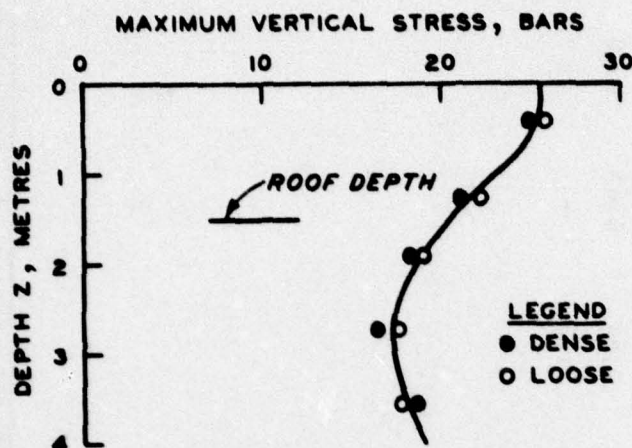


Figure 6.1 Maximum vertical stress versus depth for a station 3.5 m upstream of the structure, 1-MT case.

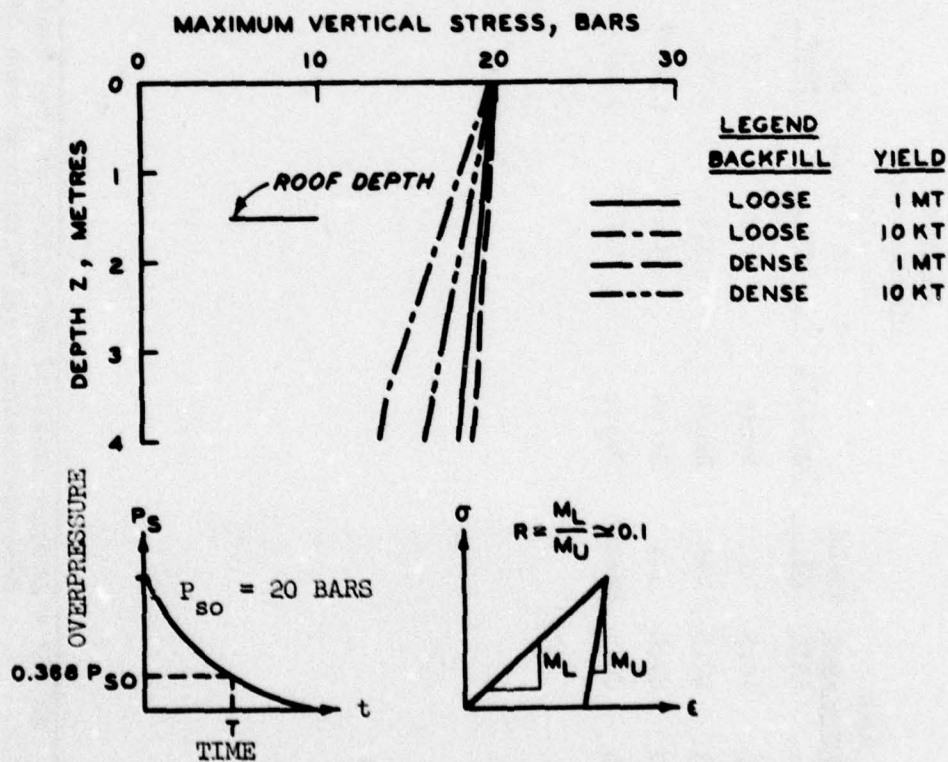


Figure 6.2 Stress attenuation in linear hysteretic media similar to loose and dense backfills for 20-bar airblast loadings.

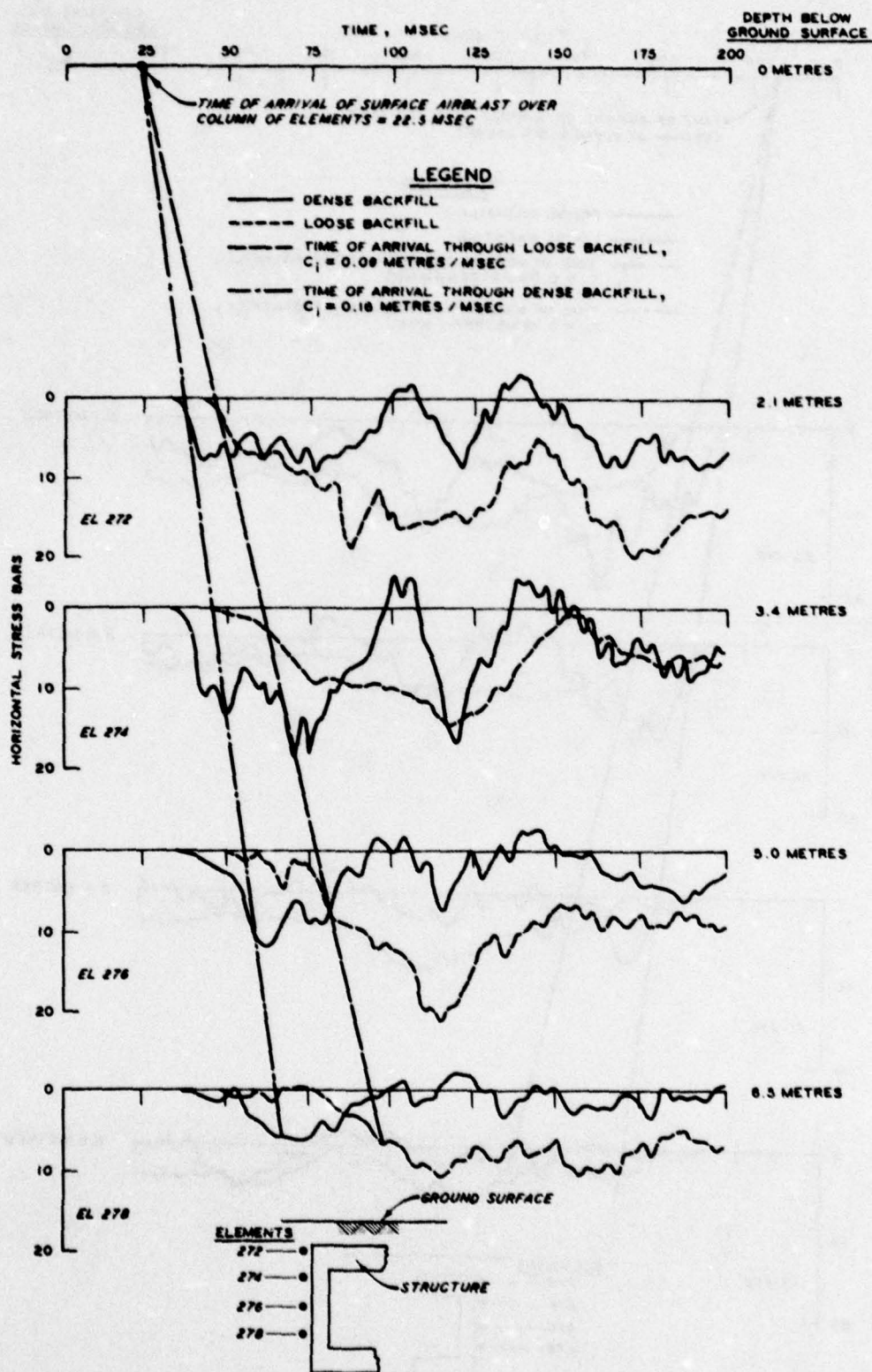


Figure 6.3 Horizontal stress time histories from 1-MT calculations for points adjacent to the blastward sidewall.

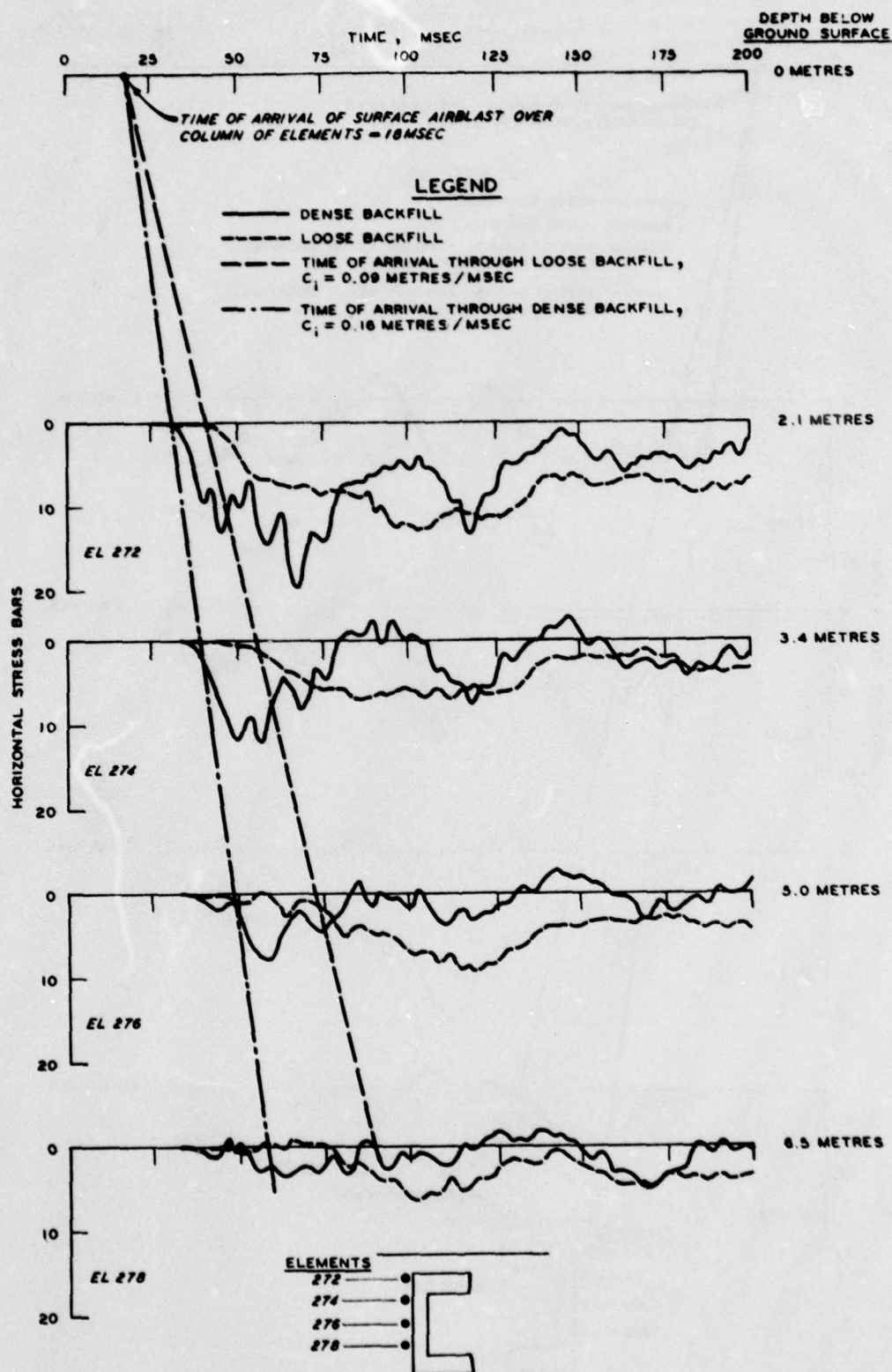


Figure 6.4 Horizontal stress time histories from 10-KT calculations for points adjacent to the blastward sidewall.

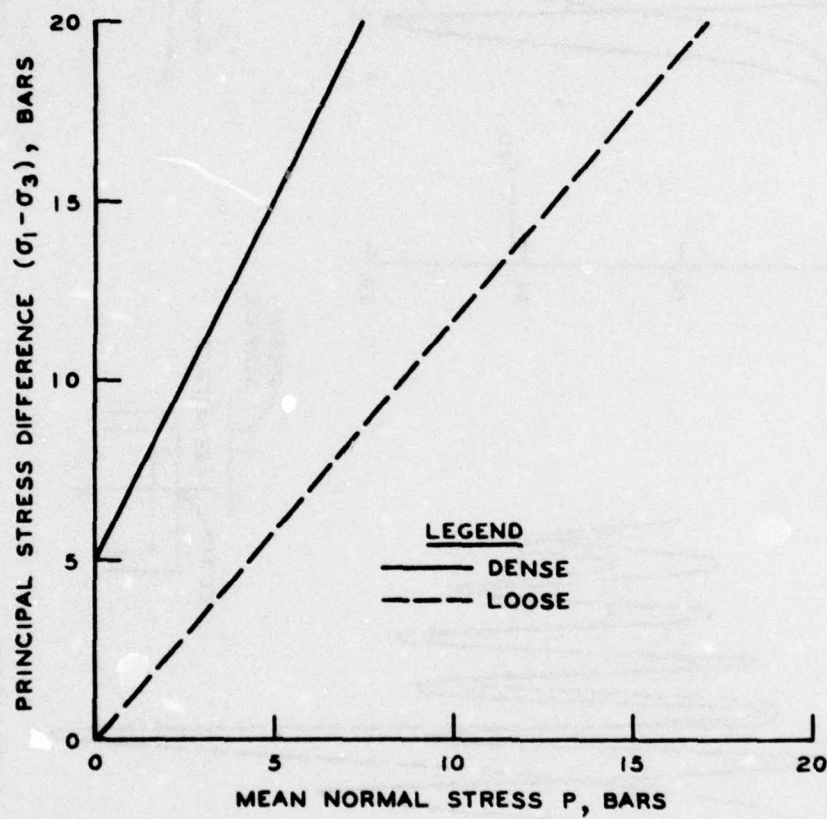


Figure 6.5 Comparison of shear strength envelopes for loose and dense backfills.

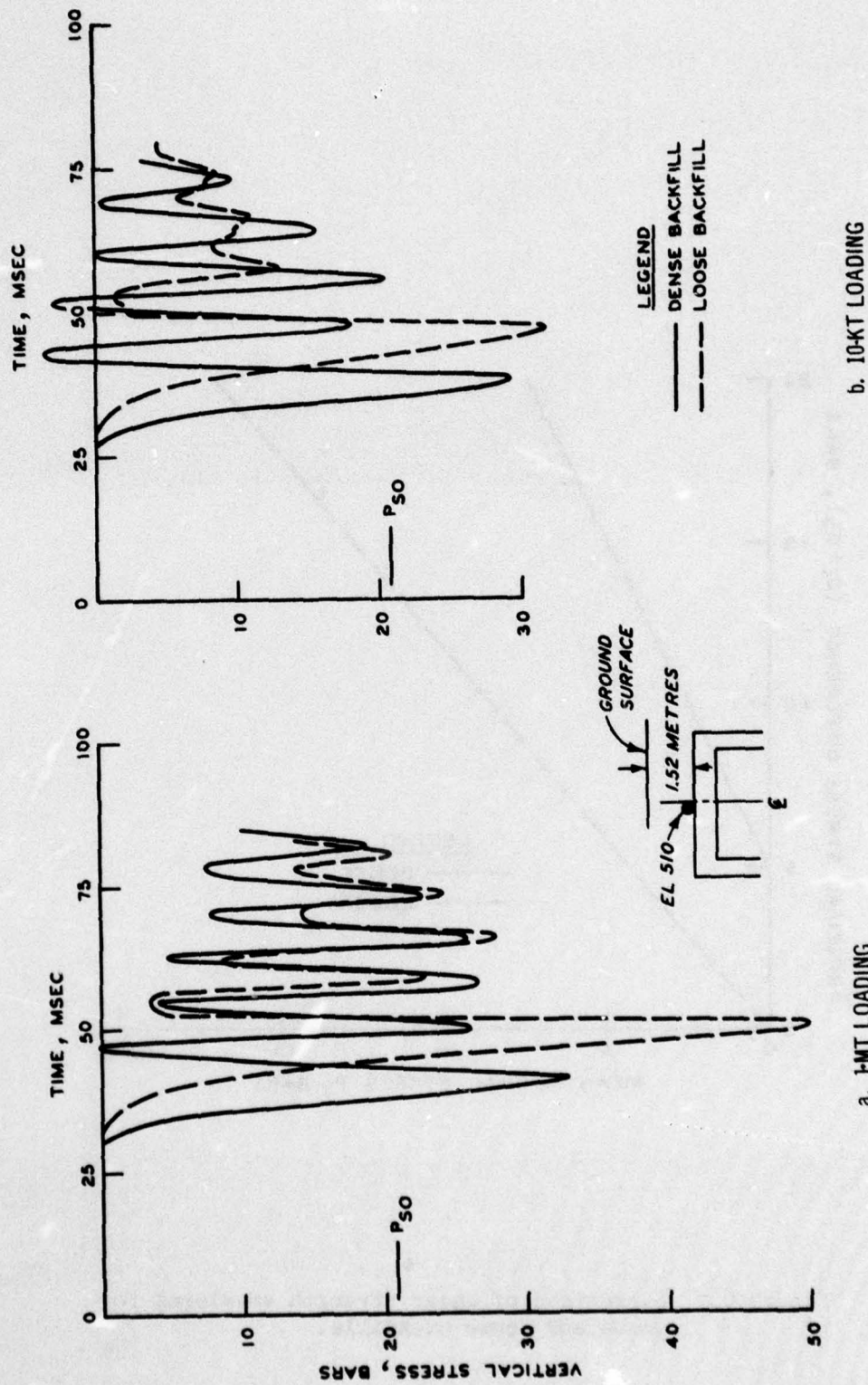
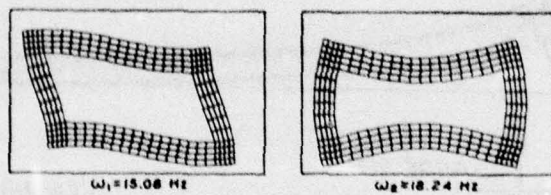
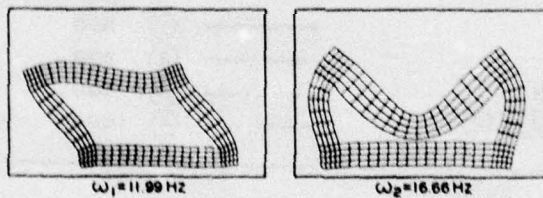


Figure 6.6 Stress on the roof versus time.



a. IN - VACUO



b. EMBEDDED (STIFF)

Figure 6.7 Side sway and roof-floor bending modes.

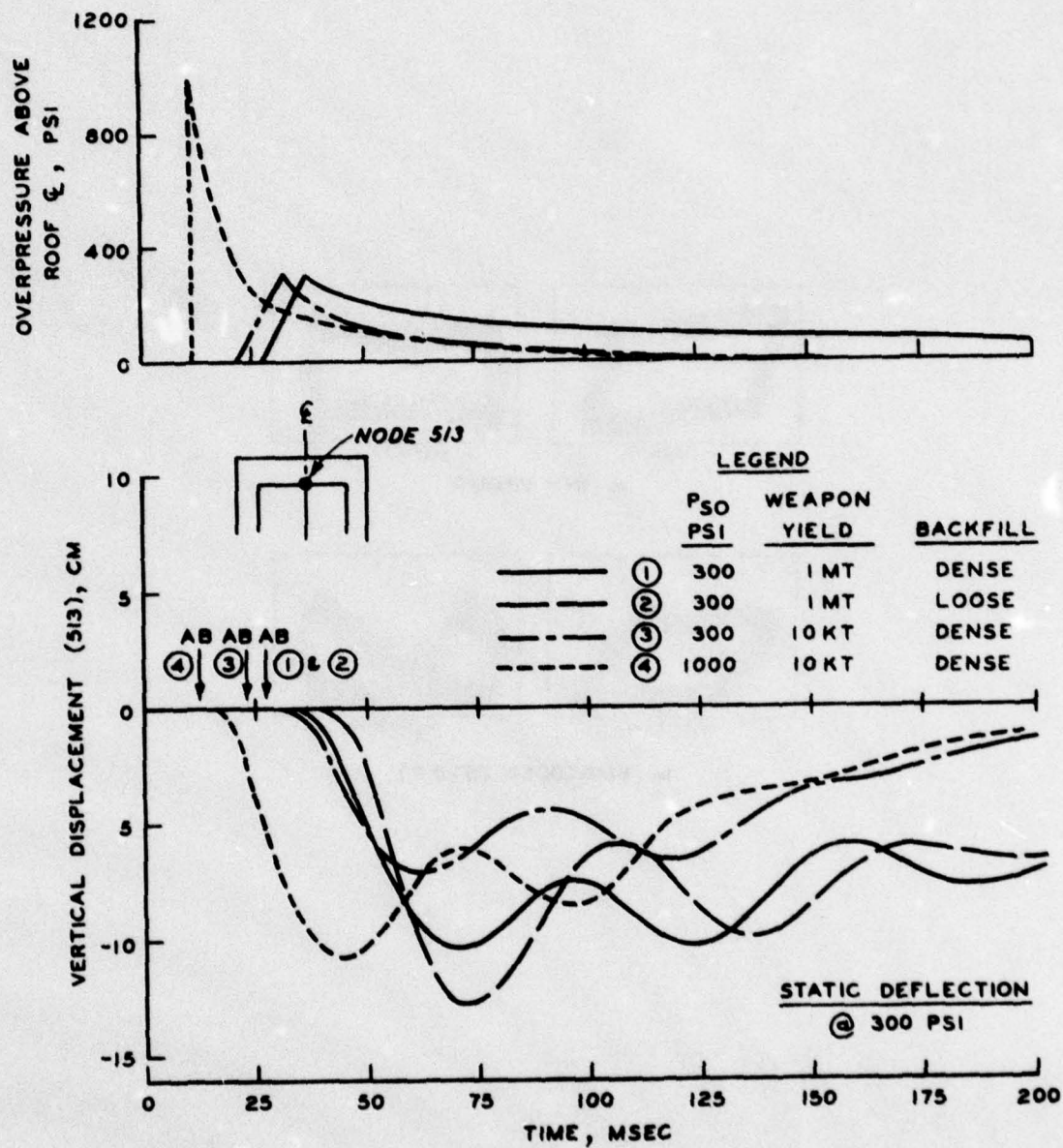


Figure 6.8 Comparison of roof deflections.

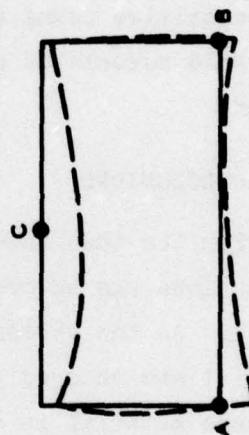
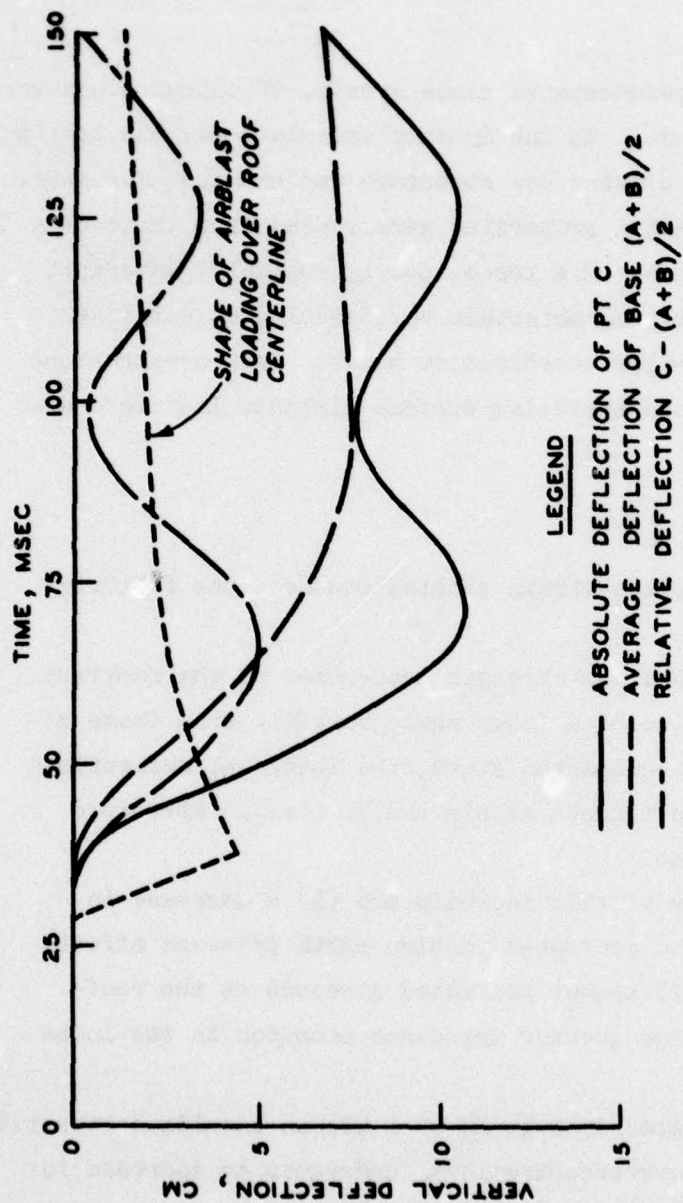


Figure 6.9 Relative roof deflection versus time for 300-psi (20-bar)/1-MT/dense backfill calculation.

## CHAPTER 7

### SUMMARY, CONCLUSIONS, AND RECOMMENDATIONS

#### 7.1 SUMMARY

Five dynamic and one pseudostatic plane strain, FE calculations were performed with the HONDO code. In the dynamic calculations, the response of a shallow-buried linear elastic box structure was examined for several conditions. Nonlinear backfill properties were varied from those of a dense, well-compacted to those of a loose, poorly compacted material. Both the backfill and underlying materials were modeled as nonlinear and repetitive using a cap-type constitutive model. Peak overpressure and yield associated with the traveling surface airblast load were also varied.

#### 7.2 CONCLUSIONS

For the idealized 2D plane-strain problem studied, the following conclusions can be drawn:

1. As the stress-strain and strength properties of the backfill material are changed to those of a loose shale backfill from those of the same material in a well-compacted state, the loads on, deflections of, and shears, moments, and thrusts within the 2D elastic structure increase by 25 to 40 percent.
2. The primary causes of this increase are (1) a decrease in corner fixity resulting from decreased passive earth pressure effects along the sidewalls, and (2) higher reflected stresses at the roof-backfill interface due to the greater impedance mismatch in the loose backfill case.
3. As yield is increased from 10 KT to 1 MT, an idealized structure at the 300-psi (20.7-bar) overpressure level undergoes an increase in peak response (in terms of maximum applied stress, deflections, and internal moments, thrusts, and shears) of approximately 45 to 60 percent.
4. An increase in peak overpressure from 300 to 1000 psi (20.7 to

68.9 bars) at a constant 10-KT yield generally resulted in a 40 to 60 percent increase in structural response.

5. Supporting linear elastic eigenvalue analyses revealed mode shapes and frequencies consistent with those observed in the HONDO calculations. The decrease in backfill stiffness caused a noticeable decrease in frequency associated with the predominant mode of deformation.

6. The linear SDF system that best simulated the response of the 2D linear elastic structure to the locally applied airblasts was one whose natural frequency was the same as that of the predominant mode of deformation and that was damped at 20 to 40 percent of critical damping. The latter appears necessary to account for energy lost to the surrounding media.

### 7.3 RECOMMENDATIONS

In targeting analyses of shallow-buried box structures, it is conventional to use an equivalent SDF model of the facility (References 5 and 9 provide examples of SDF models) and to assume that the roof loading is the surface overpressure produced by a given detonation. The studies performed here suggest that this may result in an underestimation of the hardness of the facility if the airblast has a short effective duration because the radiation damping provided by the surrounding media and its hysteresis both permit energy to be removed from the structure. Apparent damping of more than 20 percent of critical was noted in the cases studied here and was responsible for reduced deformation levels under short-duration transient loading. In view of the potential implications of this on the delivery accuracy-yield trade-off, further studies of apparent damping should be undertaken to determine the class of cases for which it is significant and how best to account for the additional hardness provided by the surrounding media's dispersive and dissipative nature.

## REFERENCES

1. J. E. Windham; "Effect of Backfill Compaction on Design Criteria for Hardened Facilities: Results of Soil Structure Interaction Calculations for Dry Types, I and II Backfill Materials"; Technical Report S-76-4, Jun 1976; U. S. Army Engineer Waterways Experiment Station, CE, Vicksburg, MS.
2. S. W. Key; HONDO--A Finite Element Computer Program for the Large Deformation Dynamic Response of Axisymmetric Soils"; SLA-74-0039, Apr 1974; Sandia Laboratories, Albuquerque, NM.
3. J. O. Curtis; "Modification and Evaluation of HONDO: A Dynamic, Axisymmetric Finite Element Code"; Miscellaneous Paper S-76-3, Apr 1976; U. S. Army Engineer Waterways Experiment Station, CE, Vicksburg, MS.
4. E. L. Wilson, et al; "Computer Programs for Static and Dynamic Analyses of Linear Structural Systems"; EERC Report No. 72-10, Nov 1972; Department of Civil Engineering, University of California, Berkeley, CA.
5. R. E. Crawford, et al; "The Air Force Manual for Design and Analysis of Hardened Structures"; AFWL-TR-74-102, 1974; Air Force Weapons Laboratory, Kirtland Air Force Base, NM.
6. WES (WESSD) letter to U. S. Army SAFEGUARD System Command dated 22 December 1973, subject: Site Defense Ground Motion Criteria Studies; Supplementary Profile and Property Information for Site 1.
7. H. L. Brode; "Height of Burst Effect at High Overpressures"; The Rand Corporation; DASA 2506, Report RM-631-DASA, Jul 1970.
8. R. H. Smith and H. M. Newmark; "Numerical Integration for One-Dimensional Stress Waves"; Structural Research Studies No. 126, Aug 1958; Department of Civil Engineering, University of Illinois, Urbana, IL.
9. F. E. Anderson, Jr., et al; "Design of Structures to Resist Nuclear Weapons"; Manuals of Engineering Practice No. 42, 1961; Prepared by the Committee on Structural Dynamics of the Engineering Mechanics Division through its Manual Subcommittee, Headquarters, American Society of Civil Engineers, New York.
10. P. F. Hadala; "Sidewall Friction in Small Blast Load Generator Tests"; Technical Report S-68-4, Aug 1968; U. S. Army Engineer Waterways Experiment Station, CE, Vicksburg, MS.

11. J. Lysmer; "Vertical Motion of Rigid Footing"; Contract Report No. 3-115, Jun 1965; U. S. Army Engineer Waterways Experiment Station, CE, Vicksburg, MS.

12. R. V. Whitman and F. E. Richart, Jr.; "Design Procedure for Dynamically Loaded Foundations"; Journal of the Soil Mechanics and Foundations Division, ASCE, Vol. 93, No. SM6; Nov 1967.

13. J. Isenberg; "A Review of Current Analytic and Field Testing Programs, Status of Research in Structure-Medium Interaction"; Technical Report No. DNA 3976F, Dec 1975; Weidlinger Associates, Menlo Park, CA.

14. E. L. Wilson, et al; "Incompatible Displacement Models"; Numerical and Computer Methods in Structural Mechanics"; 1973, Academic Press, Inc., New York and London.

## APPENDIX A

### IN VACUO AND EMBEDDED MODAL ANALYSES FOR A HYPOTHETICAL STRUCTURE IN PLANE STRAIN

#### A.1 OBJECTIVE AND SCOPE

Prior to performing FE calculations, a series of in vacuo modal analyses was conducted with the SAP IV elastic FE code<sup>4</sup> to (1) determine the effects on the FE-calculated natural frequencies of the hypothetical structure using constant strain elements (i.e., the type employed by the HONDO code) instead of higher order elements, and (2) aid in determining the minimum number of elements needed across structural sections in order to adequately model the response of the structure. A series of embedded modal analyses was subsequently performed to (1) determine the effect of material property variations on the natural frequencies of the buried structure, and (2) assist in planning the follow-on structure/backfill interaction calculations so as to have a sufficient range of frequency response to permit an adequate assessment of the actual stress and motion patterns under the postulated air-blast environments.

The purpose of this appendix is to present the results of both the in vacuo and the embedded modal analyses and to discuss their implication with regard to the overall study.

#### A.2 IN VACUO ANALYSES

Since SAP IV cannot rigorously handle in vacuo analyses, an approximation was made by placing very soft springs at the corners of the structure in such a way that the rigid body modes (i.e., those that are a function of the boundary springs only) did not interfere with the pure in vacuo or deformation modes of the structure. The structure and the springs attached to it are shown in Figure A.1; the concrete was assumed to have a Young's modulus  $E = 2 \times 10^6$  psi ( $1.38 \times 10^5$  bars) and a Poisson's ratio  $\nu = 0.25$ . Eigenvalue calculations for a two-element-per-section structural idealization were conducted using 10-pounds/inch

(1751.2-Newton/metres) and 100-pounds/inch (17,512-Newton/metres) spring constants. Of course, the three rigid body frequencies were significantly altered by the spring constant variation, but the frequencies computed for the first ten structural or deformation modes were identical to four significant figures. Thus, the spring constants for subsequent in vacuo analyses were all 100 pounds/inch (17,512 Newton/metres).

Additional calculations were then performed for structure idealizations employing four and eight elements per section; these FE descriptions of the structure are shown along with the previously used two-element-thickness description in Figure A.2. The elements used in all of the calculations described thus far were of the higher order type developed by Wilson.<sup>14</sup> These higher order elements are provided in SAP IV by adding incompatible displacement modes to the basic quadrilateral element description in order to improve the bending properties of the element. The frequencies calculated for the first ten structural modes are given in Table A.1; those for the eight-element description are assumed to best approximate the true frequencies for this structure. By examining Table A.1, it was found that the frequencies for the two- and four-element-thickness idealizations differ only slightly from those computed for the more detailed eight-element idealization.

The HONDO code being used for the structure/backfill interaction calculations only employs isoparametric quadrilateral elements and assumes that the strains computed at the center of the element represent average values for the entire element.<sup>1,3</sup> Such elements are hereinafter referred to as constant strain elements and were used in another series of two-, four-, and eight-element-sectional-thickness calculations. The frequencies obtained for the first ten structural modes for the constant strain element in vacuo calculations are given in Table A.2. As with the higher order elements, there is little difference in the two-, four-, and eight-element-thickness frequencies; and the structural mode shapes were similar for all six of these calculations. However, a

comparison of the frequencies in Table A.2 with those in Table A.1 shows that those obtained using the higher order element description are not significantly improved.

The four-element-thickness structural approximation was chosen for both the structure/backfill interaction parameter study and the embedded eigenvalue analyses, because the in vacuo results indicate that the rather large additional costs associated with using eight-element thicknesses are not justifiable. Since the structure/backfill interaction calculations will have to employ constant strain elements, such elements were selected for the embedded eigenvalue analyses. Thus, for purposes of subsequent comparison, the frequencies and deflected structure shapes for the three rigid body modes and the first 10 structural modes obtained from the in vacuo analysis using a constant strain element description and the four-element-thickness approximation are given in Figure A.3.

### A.3 EMBEDDED ANALYSIS

Two embedded eigenvalue analyses were conducted, one using a lower bound approximation to the stiffness of the soils surrounding the structure and the other an upper bound approximation. The FE grid representation for the plane-strain structure/backfill interaction calculation study is shown in Figure A.4 along with the portion of grid included in the embedded modal analyses (i.e., area ABCD). The boundary constraints for the SAP IV modal analyses were similar to those planned for the HONDO study, i.e., boundaries AB, BC, and CD were rollers, boundary AD was free, and points B and C were fixed. The free-field material descriptions as well as those for the loose and dense backfill materials used in the HONDO calculations are all nonlinear and inelastic. For the SAP IV modal analyses, linear elastic property specifications were required.

Elastic properties for the lower bound case were determined by calculating  $E$  and  $\nu$  for the free-field and loose backfill materials based on (1) the loading secant constrained modulus to 300 psi (20.7 bars)

from the UX vertical stress versus vertical strain relations, and (2) the associated secant to the UX loading paths of principal stress difference versus mean normal stress. The values obtained (along with their implied shear modulus  $G$  values) are given in Table A.3. The first 25 natural frequencies calculated for the structure embedded in materials having lower bound elastic properties are listed in Table A.4. The structure mode shapes associated with each of the 25 frequencies are shown in Figure A.5; mode shapes for both the structure and the surrounding soil are shown for the first 12 of these frequencies in Figure A.6.

Elastic properties for the upper bound case were determined by calculating  $E$  and  $\nu$  for the free-field and dense backfill materials based on secant- to 300-psi (20.7-bar) moduli from UX unloading relations. The values obtained are given in Table A.3. The first 25 natural frequencies calculated for the upper bound case are listed in Table A.4; the associated mode shapes for the structure are shown in Figure A.7.

#### A.4 DISCUSSION OF RESULTS

The in vacuo analyses indicated that the frequency responses of the structure based on the use of constant strain elements were not appreciably different from those obtained using higher order elements. They also indicated that use of four-element thicknesses across all sections would provide an adequate idealization of the structure for the structure/backfill interaction calculations. The in vacuo results for constant strain elements and four-element thicknesses gave frequencies for the first 10 structural or deformation modes ranging from 15.08 to 121.7 Hz.

The embedded analyses indicated a significant effect of material property variation on the frequencies of the buried structure, i.e., frequencies obtained for the first 25 modes using lower bound properties ranged from 4.315 to 14.35 Hz, while those for upper bound properties ranged from 11.99 to 54.87 Hz. Embedment in either set of soils obviously lowers the frequencies from those obtained in vacuo, but it is difficult to make mode-for-mode comparisons because the deflected shapes are quite different, e.g.,

compare Figure A.3 with Figures A.5, A.6, and A.7. The embedded eigenvalue analyses do indicate, however, that the structure/backfill interaction calculations have a sufficient range of frequency response to permit an adequate assessment of the structure stresses and motions under the postulated airblast environments. The lowest frequencies that can be fully transmitted in these calculations will be about 5 Hz; the lowest modal frequencies calculated from the embedded analyses were 4.315 Hz with the lower bound properties and 11.99 Hz with the upper bound properties. The upper cutoff frequencies for the planned calculations are assumed to be 25 Hz for the loose backfill case and 50 Hz for the case of dense backfill; the embedded modal analyses using lower bound moduli gave a 25th mode frequency of just 14.35 Hz, and using upper bound moduli, the frequency for the 20th mode was 49.11 Hz.

Table A.1 Calculated Natural Frequencies from In Vacuo Analyses with Higher Order Element Description.

Number of Elements Across Structural Sections	Structural Mode No.									
	1	2	3	4	5	6	7	8	9	10
	<u>Frequency <math>\omega</math>, Hz</u>									
2 (Figure A.2a)	14.74	17.49	33.33	47.91	61.45	72.02	90.30	93.39	101.1	116.6
4 (Figure A.2b)	14.49	17.45	33.01	48.03	60.73	71.98	88.69	93.41	101.4	117.7
8 (Figure A.2c)	14.25	17.38	32.58	42.82	59.59	71.33	86.44	93.40	101.3	117.1

Table A.2 Calculated Natural Frequencies from In Vacuo Analyses with Constant Strain Element Description.

Number of Elements Across Structural Sections	Structural Mode No.									
	1	2	3	4	5	6	7	8	9	10
	Frequency $\omega$ , Hz									
2 (Figure A.2a)	15.48	18.46	34.91	50.17	63.26	75.42	93.39	93.97	103.0	121.6
4 (Figure A.2b)	15.08	18.24	34.26	49.84	62.32	74.67	91.48	93.92	102.9	121.7
8 (Figure A.2c)	14.43	17.58	32.95	48.29	60.11	72.09	87.41	93.56	101.7	118.1

Table A.3 Elastic Properties of Materials Used in Embedded Analyses.

Material Number Figure A.4	Lower Bound Properties				Upper Bound Properties					
	Young's Modulus, E		Poisson's Ratio, $\nu$		Young's Modulus, E		Poisson's Ratio, $\nu$			
	psi	bars	psi	bars	psi	bars	psi	bars		
1	7,214	497	2,754	190	0.31	50,905	3,510	20,526	1,415	0.24
2	24,153	1,665	9,818	677	0.23	697,771	48,110	298,193	20,560	0.17
3	100,728	6,945	41,282	2,846	0.22	1,126,857	77,694	485,714	33,489	0.16
4	267,083	18,415	113,171	7,803	0.18	1,622,512	111,868	711,628	49,065	0.14
5	2,000,000	137,895	800,000	55,158	0.25	2,000,000	137,895	800,000	55,158	0.25
6	1,908	132	739	51	0.29	34,732	2,395	16,383	1,130	0.06

Table A.4 Calculated Natural Frequencies for Embedded Analyses.

Mode No.	Frequencies $\omega$ , Hz	
	Calculated Using Lower Bound Material Properties	Calculated Using Upper Bound Material Properties
1	4.315	11.99
2	4.350	16.68
3	5.054	17.17
4	5.978	17.43
5	6.044	25.28
6	6.825	25.47
7	7.649	27.80
8	8.989	31.07
9	9.032	31.88
10	9.189	34.18
11	9.369	37.92
12	10.27	39.69
13	10.52	40.49
14	10.65	40.95
15	10.87	41.96
16	11.09	42.39
17	11.28	45.80
18	11.37	47.55
19	11.87	47.96
20	12.10	49.11
21	12.35	51.22
22	12.64	51.55
23	12.83	52.50
24	13.39	52.61
25	14.35	54.87

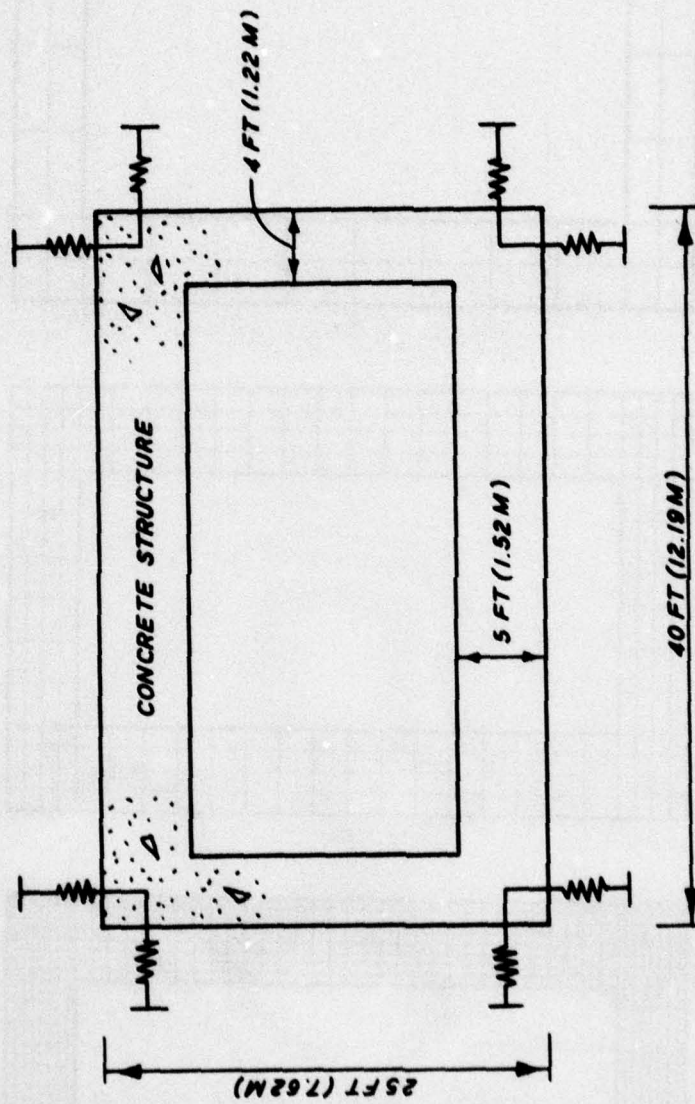
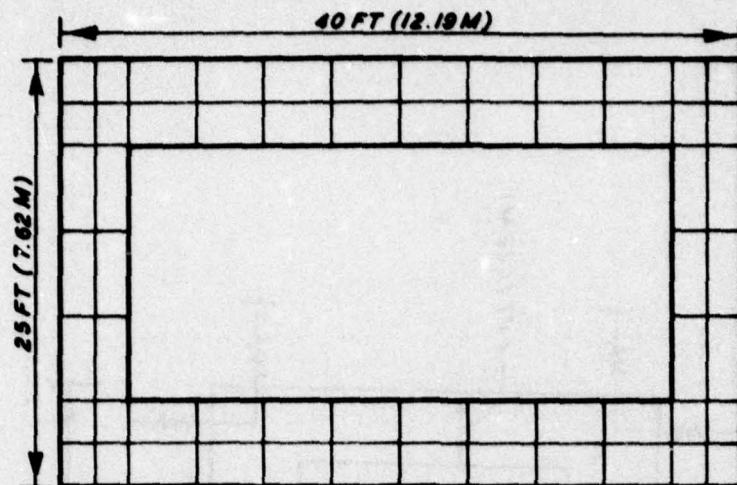
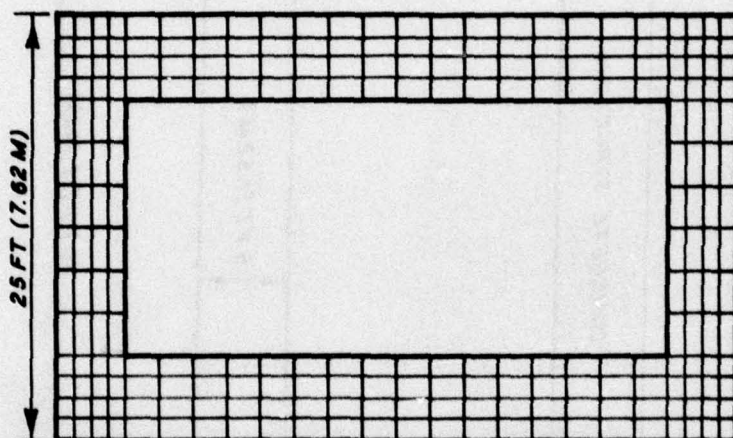


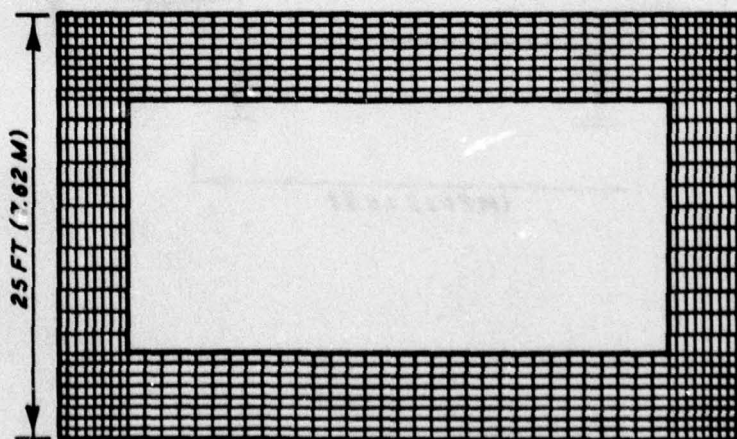
Figure A.1 Idealized structure and springs added to approximate in vacuo condition.



a.



b.



c.

Figure A.2 Finite element descriptions of structure used for in vacuo and embedded eigenvalue calculations.

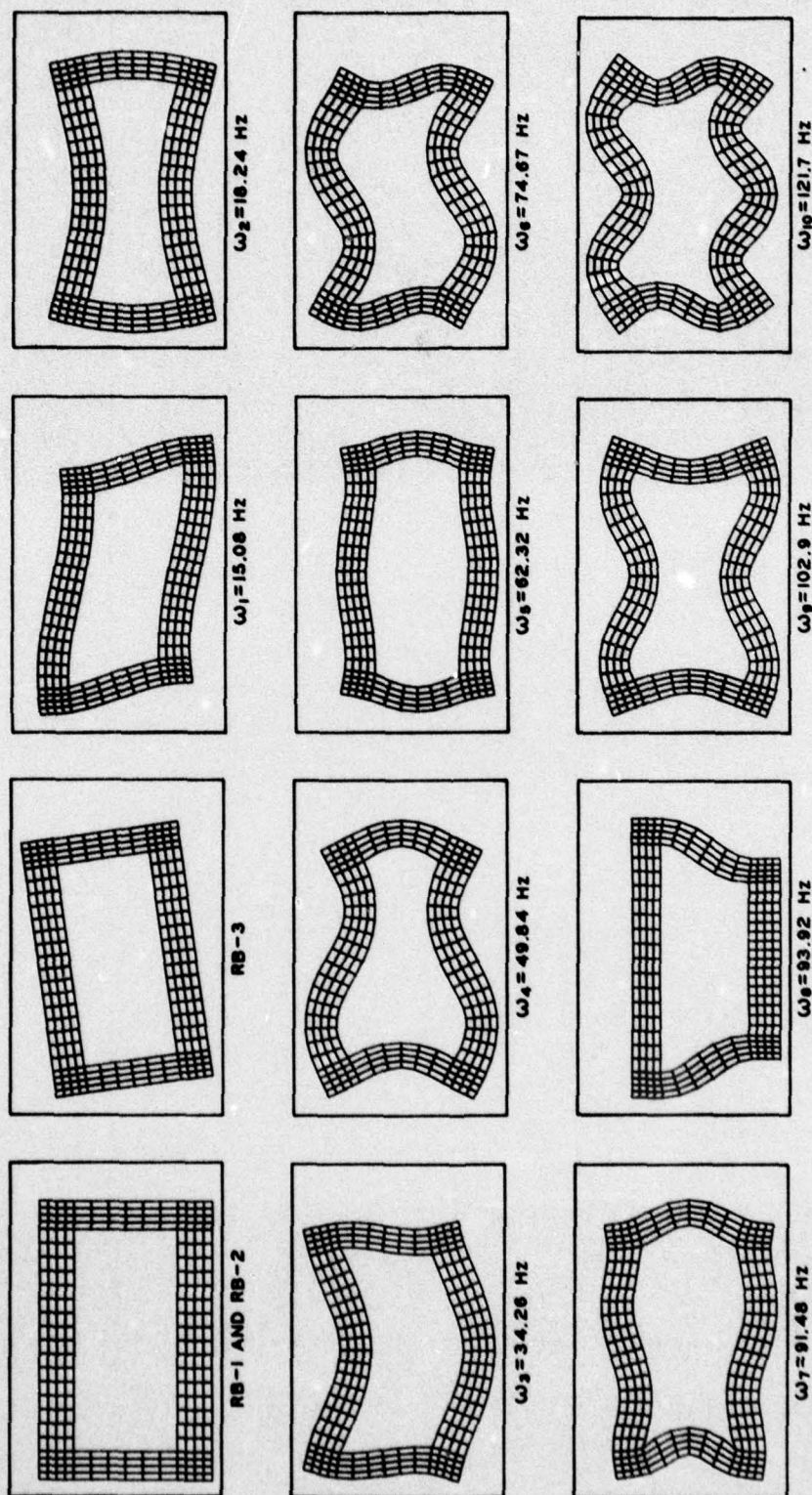


Figure A.3 Frequencies and associated mode shapes from the in vacuo eigenvalue analysis for the four-element-thickness structural approximation using constant strain elements.

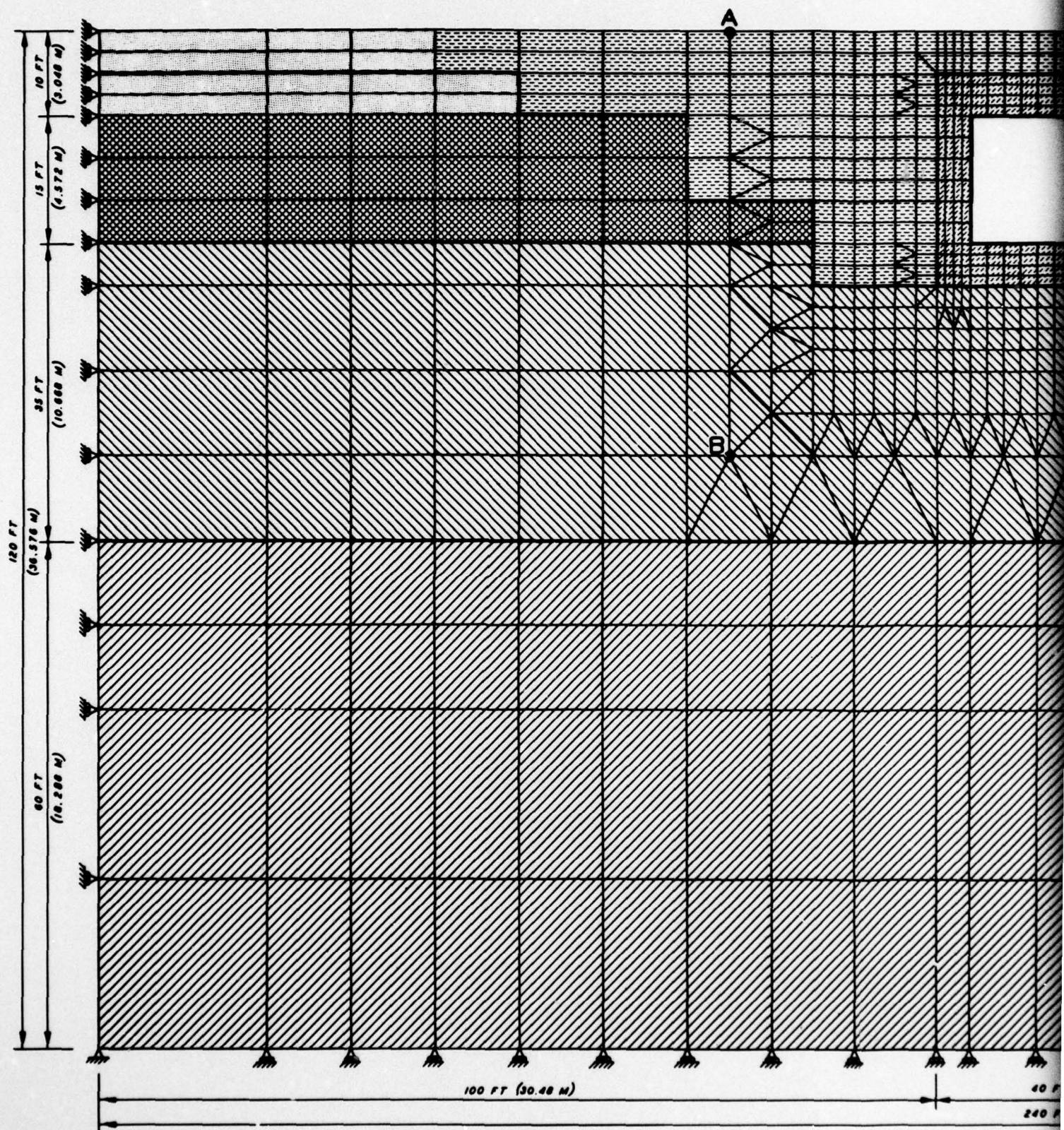
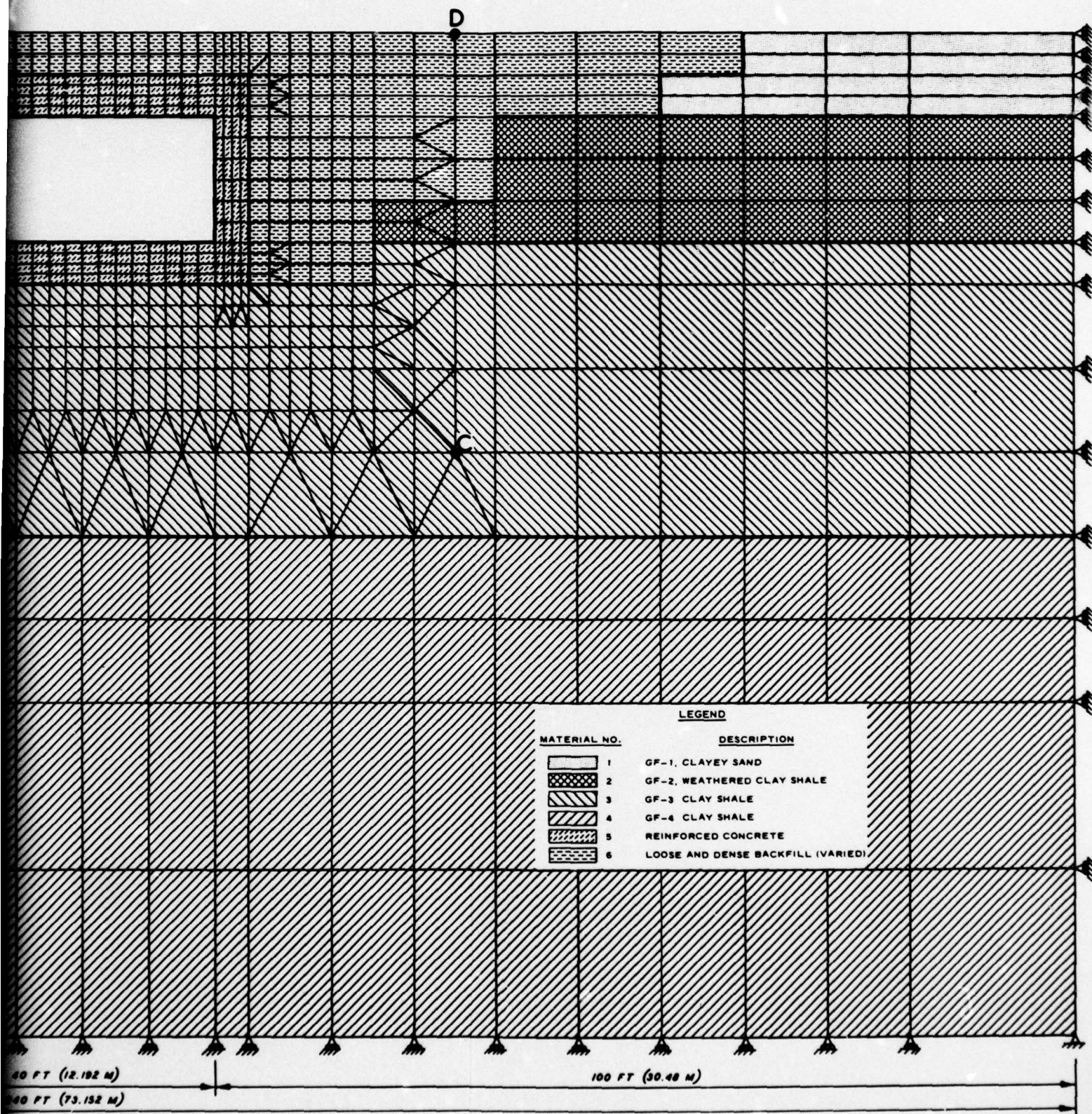


Figure A.4 FE grid representations and SAP IV embedded modal



s for HONDO structure/backfill interaction calculations  
 al analyses.

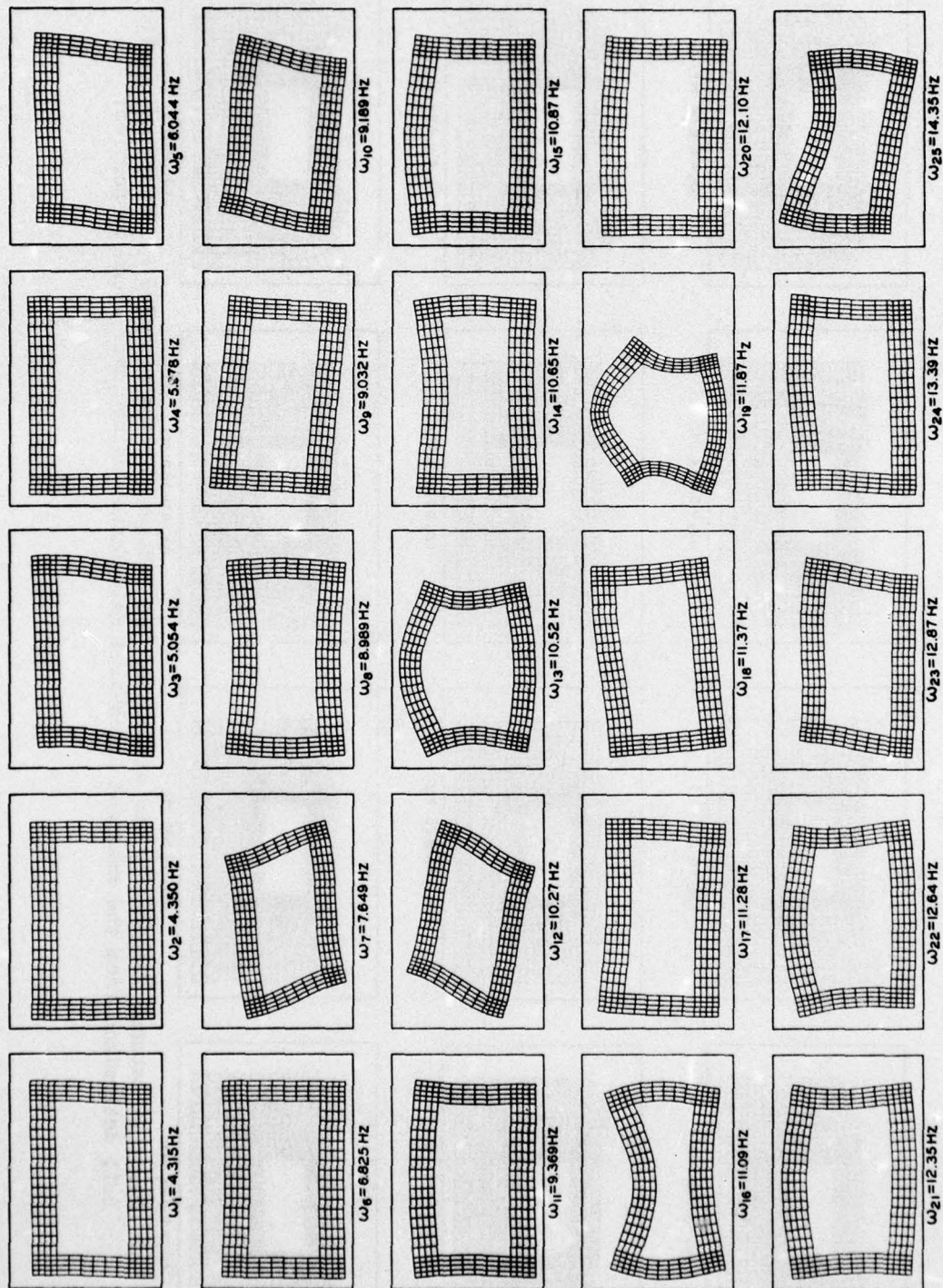


Figure A.5 Frequencies and associated mode shapes of structure from the embedded eigenvalue calculation using lower bound properties.

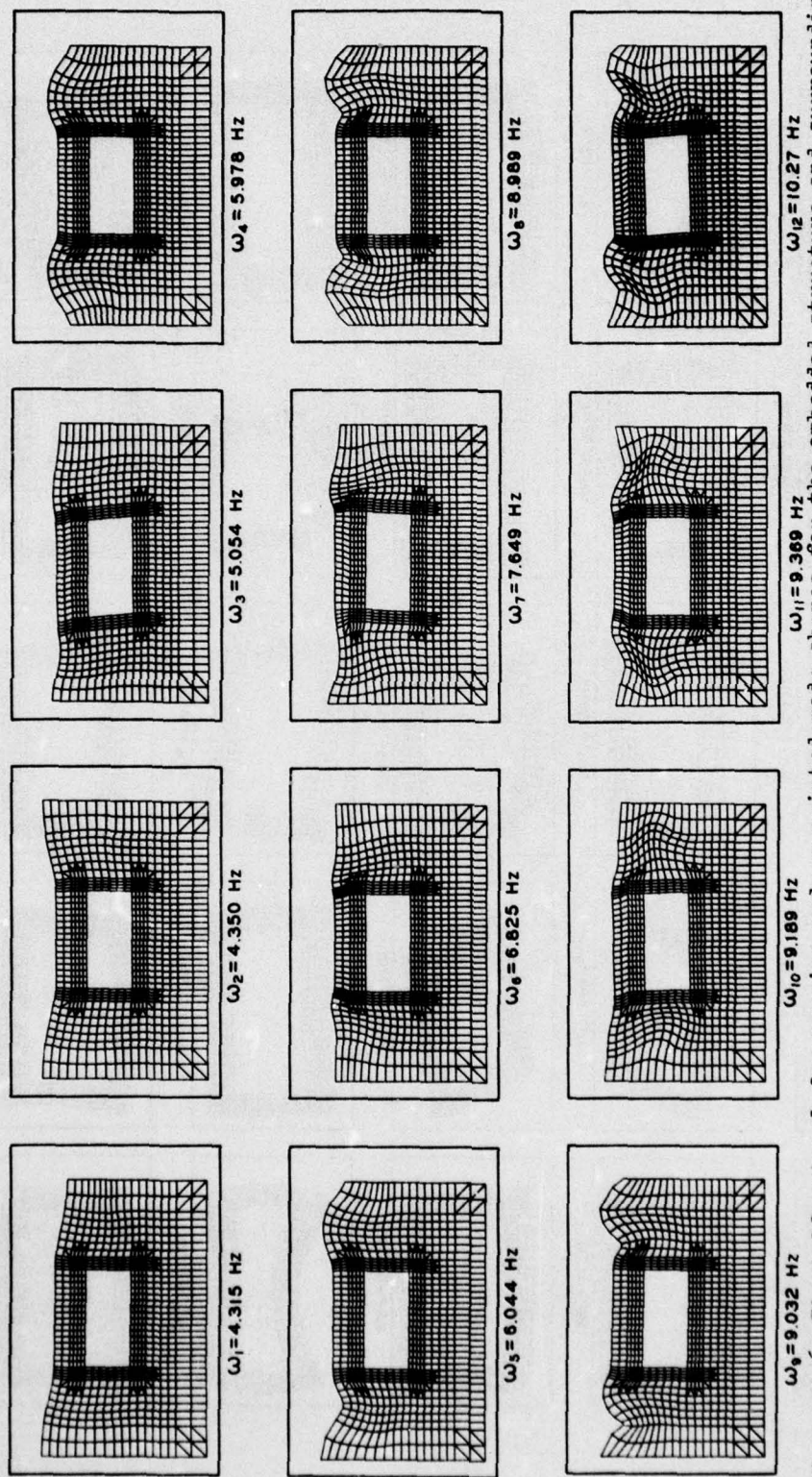


Figure A.6 First 12 natural frequencies and associated mode shapes for the embedded structure and surrounding soil determined from the embedded eigenvalue calculation using lower bound properties.

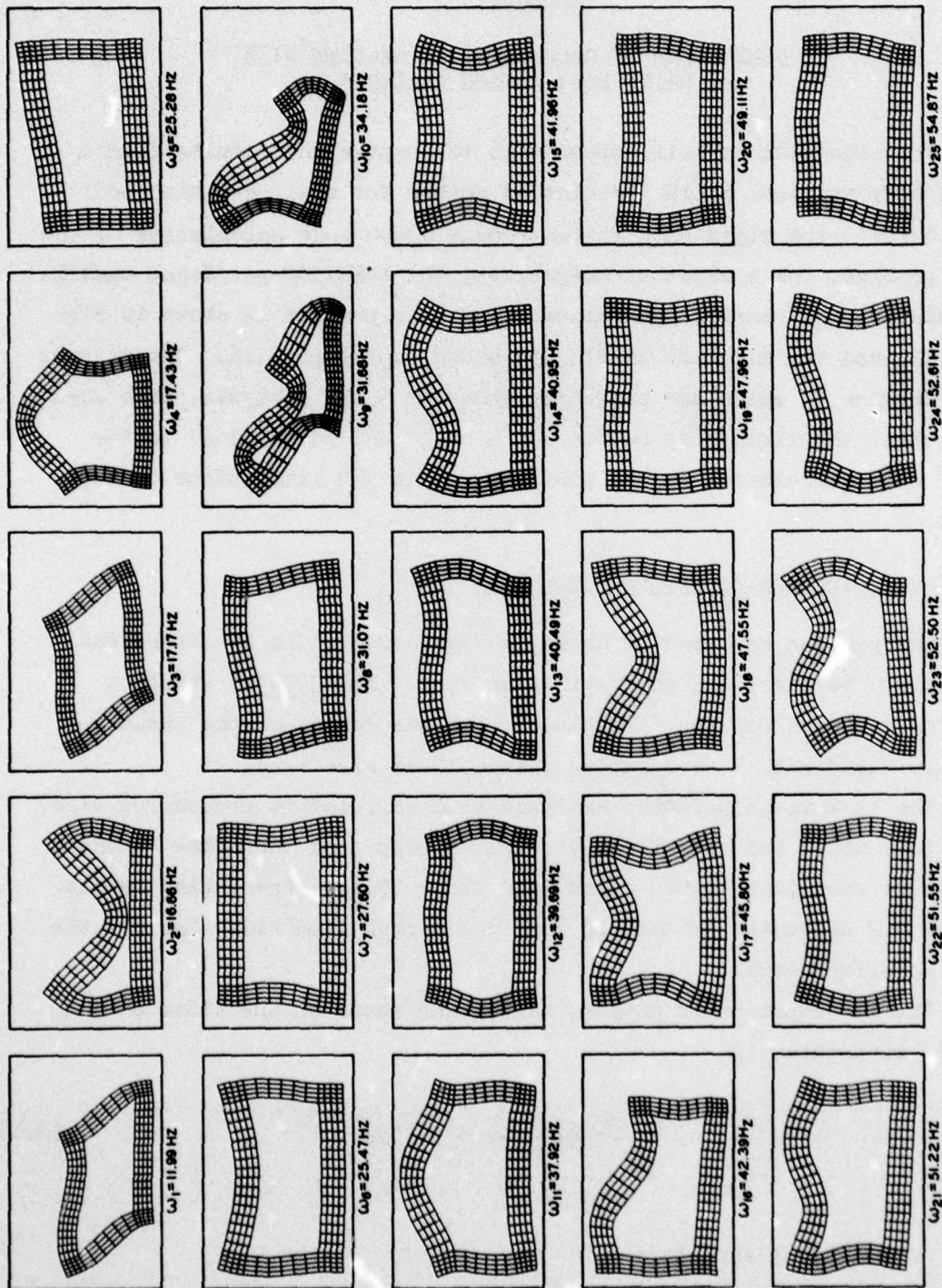


Figure A.7 Frequencies and associated mode shapes of structure from the embedded eigenvalue calculation using upper bound properties.

## APPENDIX B

### COMPARISON OF CALCULATIONAL RESULTS WITH RIGID BODY MOTION ANALYSIS

The objective of this appendix is to compare the results from a rigid body vertical motion prediction method for shallow-buried box structures<sup>5</sup> with rigid body motion from a HONDO code calculation of the same problem. As a basis of comparison, the 1-MT/300-psi/dense backfill calculation was chosen. The geometry of this problem is shown in Figure 2.1, and the airblast loading is shown in Figure 2.16. The methods of Reference 5, which are basically those of a SDF analysis, were used to predict the rigid body motion for a case that is as close to the HONDO code calculation as was possible within the limitations of the model.

#### B.1 SINGLE-DEGREE-OF-FREEDOM ANALYSES

The problem analyzed is shown in Figure B.1. The structure was assumed to be rigid and square in plan view. The 300-psi airblast loading was used for the 1-MT weapon over the center of the structure (Figure 2.16) with a zero rather than a 10-ms rise time.

The 1D wave-propagation-analysis hand calculation procedures were used to compute the free-field vertical stress time histories at the structure roof (1.52-metre depth) and floor (9.14-metre depth) levels. Figure B.2 shows the free-field vertical stress time histories for the roof and floor level.

The SDF equation of motion, neglecting shear on the sides of the buried structure, is

$$M\dot{v}_s = A[\sigma_R(t) - \sigma_F(t)] \quad (B.1)$$

where

$M$  = mass of structure

$\dot{v}_s$  = acceleration of structure

$A$  = vertically projected area of structure

$\sigma_R(t)$  = see Equation B.2

$\sigma_F(t)$  = see Equation B.3

In Reference 10, the vertical stress  $\sigma_R$  acting on the roof of a rectangular rigid structure buried in a half-space of elastic soil is approximated by

$$\sigma_R = 2\sigma_{ff_R} - \rho_1 C_{L_1} v_s \quad (B.2)$$

where

$\sigma_{ff_R}$  = free-field vertical stress at roof level

$\rho_1$  = mass density of soil at roof level

$C_{L_1}$  = wave velocity of soil at roof level

$v_s$  = velocity of structure

In this same reference, the stress acting on the floor is approximated by

$$\sigma_F = \sigma_{ff_F} + \rho_2 C_{L_2} v_s \quad (B.3)$$

where

$\sigma_{ff_F}$  = free-field stress at floor level

$\rho_2$  = mass density of soil at floor level

$C_{L_2}$  = wave velocity of soil at floor level

The result of combining Equations B.1, B.2, and B.3 gives

$$\dot{v}_s = \frac{A}{M} (2\sigma_{ff_R} - \sigma_{ff_F}) - \frac{Av_s}{M} (\rho_1 C_{L_1} + \rho_2 C_{L_2}) \quad (B.4)$$

The stress time history for the net or resultant stress ( $2\sigma_{ff_R} - \sigma_{ff_F}$ ) is given in Figure B.3. Equation B.4 was solved numerically using the values

of  $A$ ,  $M$ ,  $C_{L_1}$ ,  $\rho_2$ ,  $C_{L_2}$  given in Figure B.7, and the stress time history in Figure B.3 to determine the velocity time history of the structure. A time increment of 2 ms was used. The displacement time history of the structure was determined by integrating the velocity time history.

## B.2 COMPARISONS WITH 2D CALCULATION RESULTS

The free-field stress and structure velocity and displacement time histories from the SDF analyses are compared with those from the 2D calculation for the 1-MT/300-psi/dense backfill calculations in Figures B.4 through B.7.

As shown in Figure B.4, the free-field vertical stress at the 1.52-metre depth (structure roof level) from the 1D analysis are compared with free-field vertical stresses from elements 179 and 180, which are located at depths of 1.0 and 1.9 metres, respectively, at a distance of 2.67 metres upstream from the structure. All three time histories were adjusted to be compatible with the arrival time of surface stress of 27.5 ms above the center of the structure. Also, in Figure B.4, the free-field vertical stress time history from the 1D analyses compares very well with those from the 2D calculations with the major discrepancy being the rise time to peak stress. The surface airblast relation for the 1D analyses contained a shock front, i.e., 0-ms rise time, while that for the 2D calculation contained a 10-ms rise time.

In Figure B.5, the free-field vertical stress at the 9.14-metre depth (structure floor level) from the 1D analysis is compared with the free-field vertical stresses from elements 189 and 190, which are located at depths of 8.75 and 9.52 metres, respectively, at a distance of 2.67 metres upstream from the structure. The arrival times for all cases were also adjusted to correspond with an airblast time of arrival at 27.5 ms at the ground surface over the center of the structure. As

AD-A058 669

ARMY ENGINEER WATERWAYS EXPERIMENT STATION VICKSBURG MISS F/G 18/3  
EFFECT OF BACKFILL PROPERTY AND AIRBLAST VARIATIONS ON THE EXTE--ETC(U)  
JUN 78 J E WINDHAM, J O CURTIS

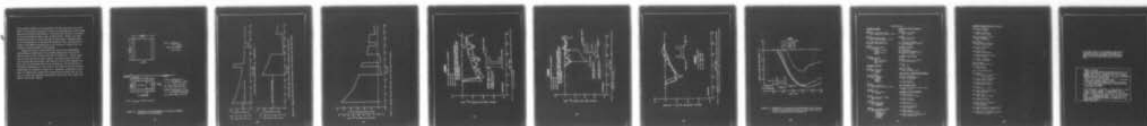
UNCLASSIFIED

WES-TR-S-78-5

NL

3 OF 3

AD  
A058 669



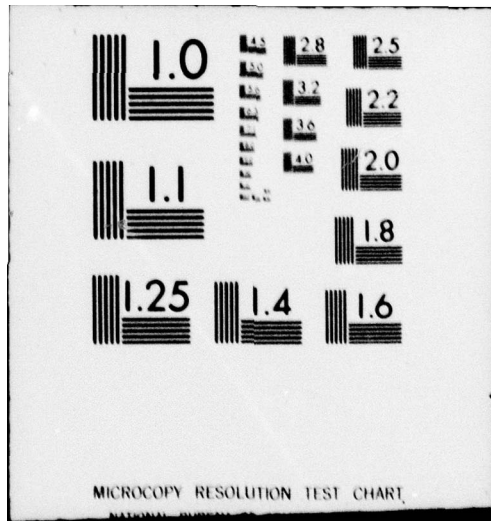
END

DATE

FILMED

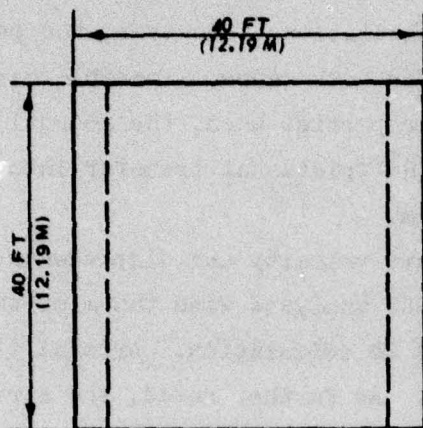
11-78

DDC



can be seen in Figure B.5, the free-field vertical stress near the floor level of the structure determined from the 1D considerations is much higher than that from the 2D calculations. The stress also arrives 15 ms faster in the 2D calculations than in the 1D calculations. However, the peak stress arrival time is nearly the same for both cases. Possible causes of the differences are in the material properties used, the reduction in stress in the HONDO calculation due to the frictional transfer into the concrete, or the 2D nature of the problem.

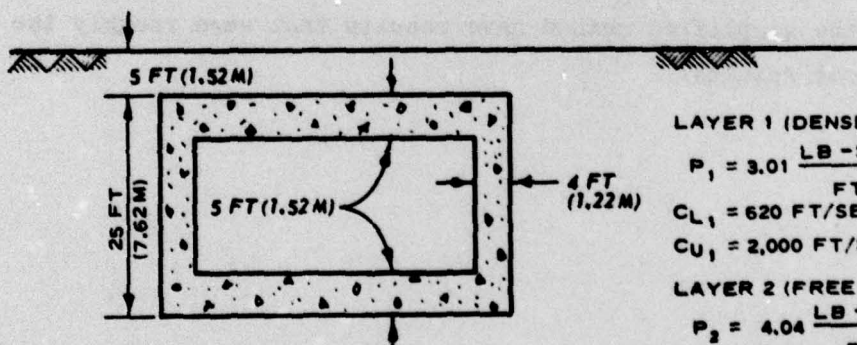
Figures B.6 and B.7 compare structure velocity and displacement time histories, respectively, from the SDF analyses with those of the bottom corners of the structure from the 2D calculation. Arrival times have not been adjusted in these figures. As further noted, the structure velocity and displacement time histories from the SDF analyses compare very well with those from the 2D calculation. The 2D-calculation free-field displacement at floor level is much smaller than the structure displacement as indicated in Figure B.7. Therefore, considerable interaction is taking place between the structure and the media, and for this case, at least, the simplified method gave results that were roughly the same as the 2D-code results.



a. PLAN

$$\text{AREA, } A = 230,400 \text{ IN}^2 \\ = (1.49 \times 10^6 \text{ CM}^2)$$

$$\text{MASS} = 7,800 \frac{\text{LB} \cdot \text{SEC}^2}{\text{IN.}} \\ = (1.37 \times 10^6 \text{ KG})$$



b. ELEVATION

LAYER 1 (DENSE BACKFILL)

$$P_1 = 3.01 \frac{\text{LB} \cdot \text{SEC}^2}{\text{FT}^4} \left( 18,616 \frac{\text{KG}}{\text{M}^3} \right)$$

$$CL_1 = 620 \text{ FT/SEC (189 M/SEC)}$$

$$CU_1 = 2,000 \text{ FT/SEC (610 M/SEC)}$$

LAYER 2 (FREE FIELD LAYER 3)

$$P_2 = 4.04 \frac{\text{LB} \cdot \text{SEC}^2}{\text{FT}^4} \left( 24,986 \frac{\text{KG}}{\text{M}^3} \right)$$

$$CL_2 = 2,025 \text{ FT/SEC (617 M/SEC)}$$

NOTE:  $\gamma_{\text{CONCRETE}} = 145 \text{ PCF (2.32 g/cm}^3\text{)}$

Figure B.1 Dimensions and configuration of buried rectangular structure for SDF analyses.

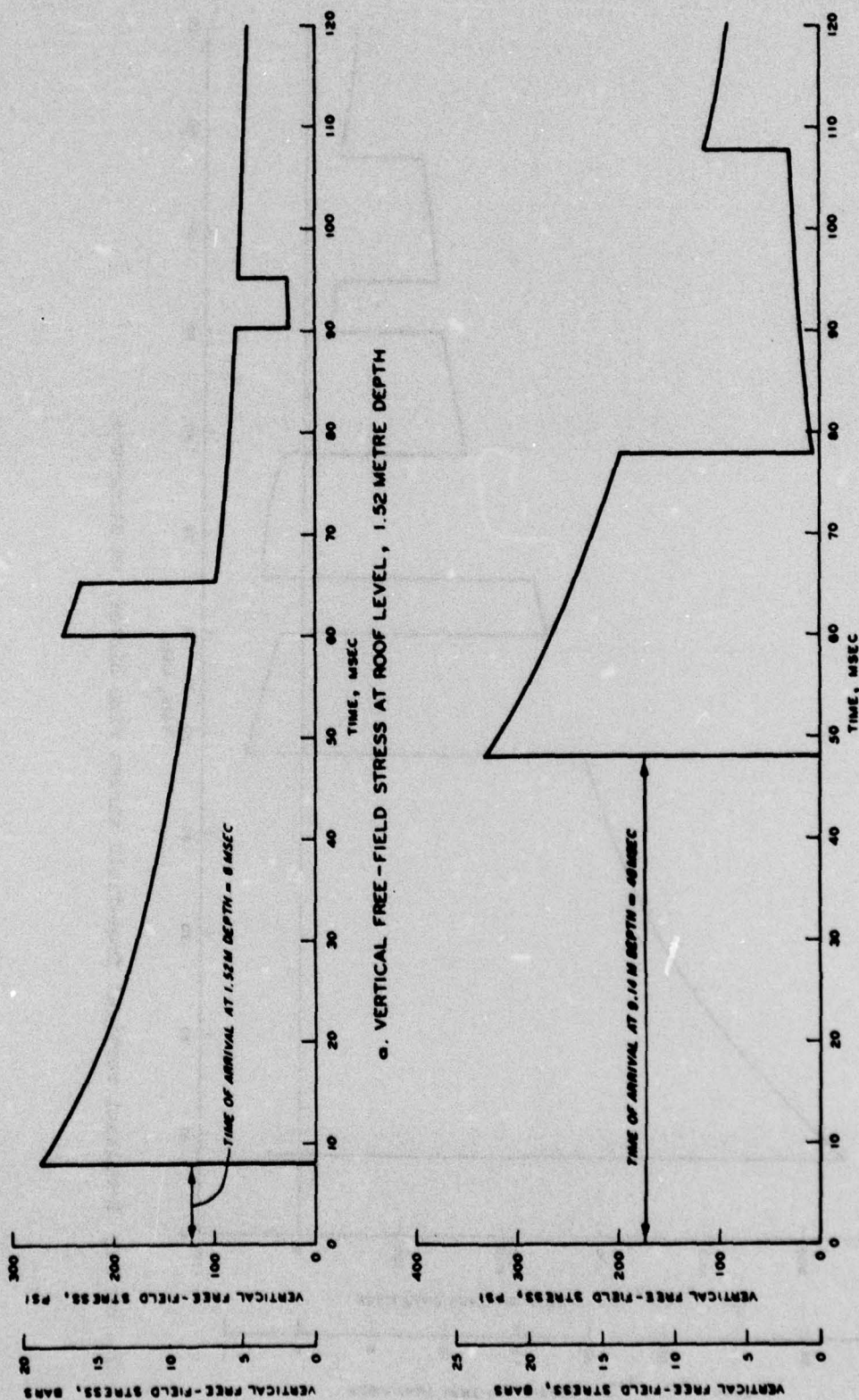


Figure B.2 Vertical free-field stress time history at the structure roof and floor level.

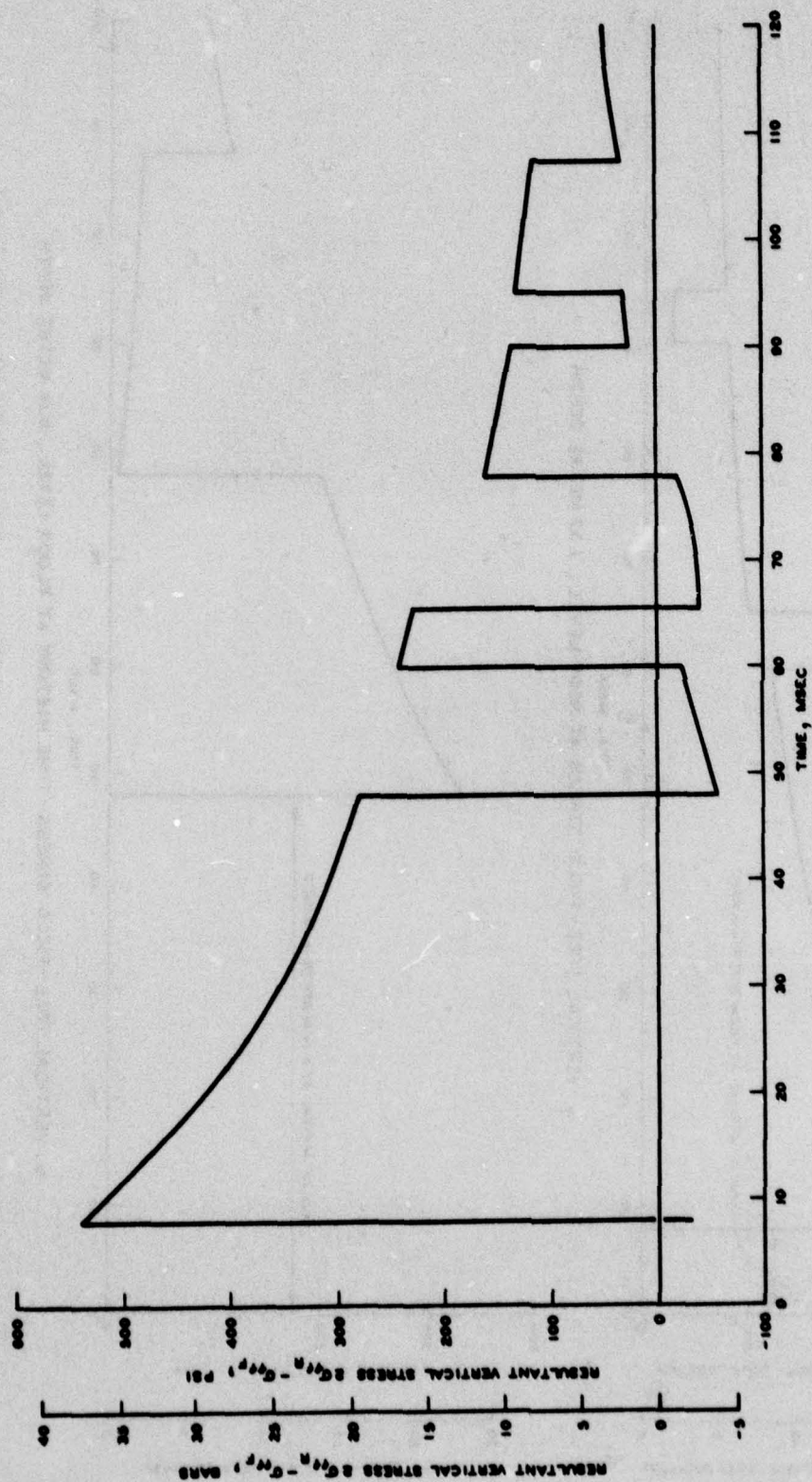


Figure B.3 Resultant vertical free-field stress time history on structure.

# **LEGEND**

- 1-D ANALYSES 5 FT (1.52M) DEPTH
- EL 179
- EL 180

NOTE: ALL TIMES WERE ADJUSTED TO CORRESPOND WITH AN AIRBLAST TIME OF ARRIVAL OF 27.5 MSEC AT THE GROUND SURFACE OVER THE CENTER OF THE STRUCTURE.

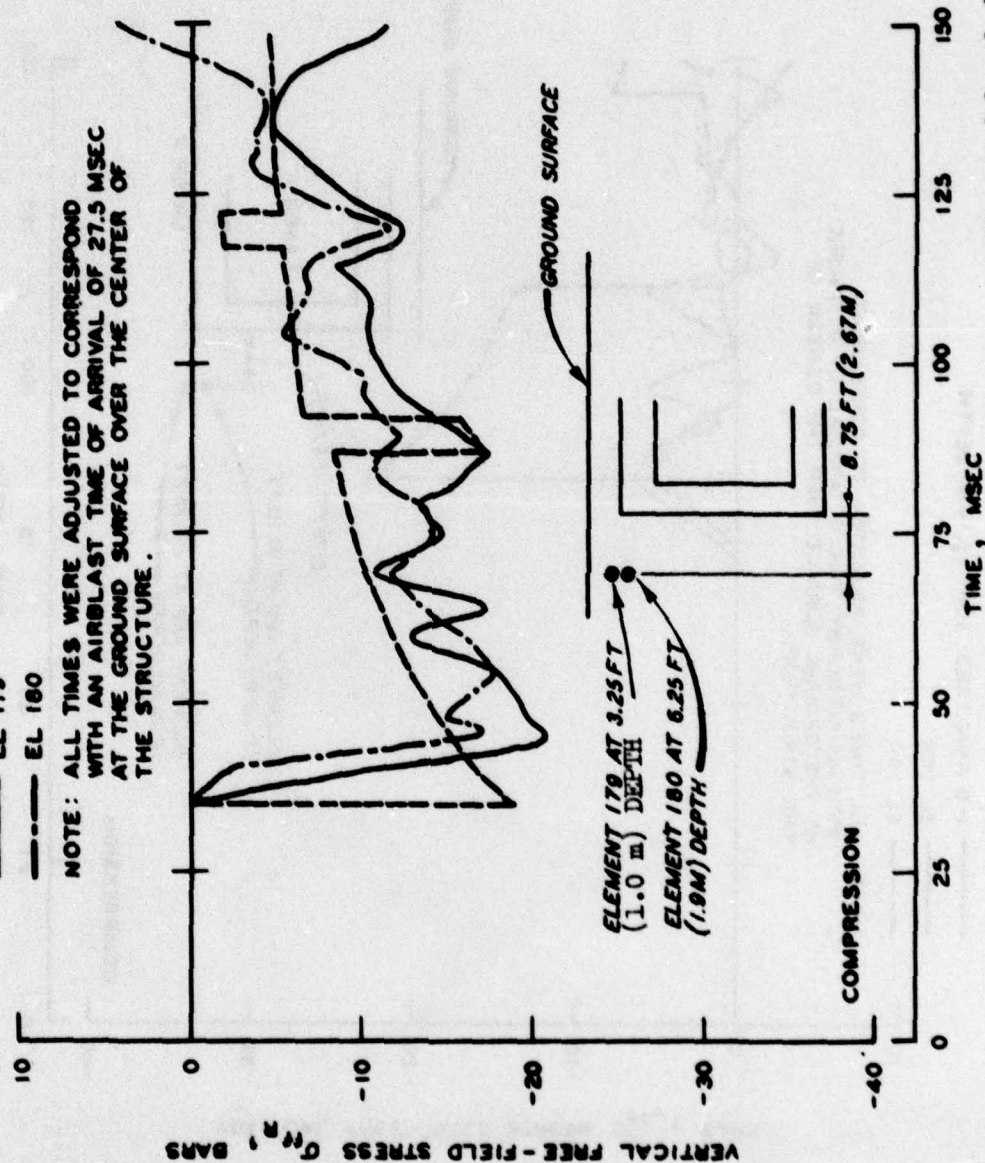


Figure B.4 Comparison of the free-field vertical stress at the roof level from 1D and 2D calculations.

# **LEGEND**

--- 1-D ANALYSES 30FT (9.14M) DEPTH

— EL 189

--- EL 190

NOTE: ALL TIMES WERE ADJUSTED TO CORRESPOND WITH AN AIRBLAST TIME OF ARRIVAL OF 27.5 MSEC AT THE GROUND SURFACE OVER THE CENTER OF THE STRUCTURE.

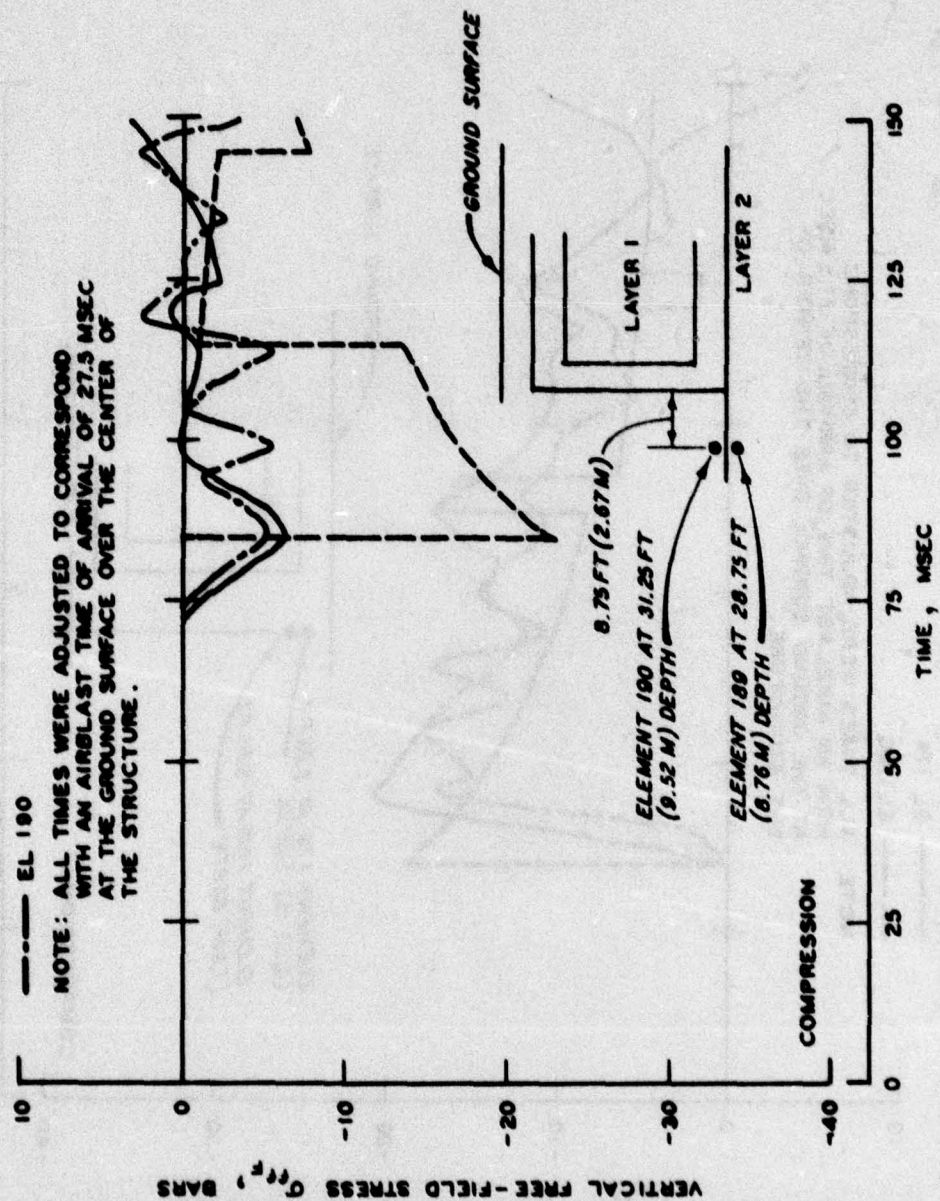


Figure B.5 Comparison of the free-field vertical stress at the floor level from 1D and 2D calculations.

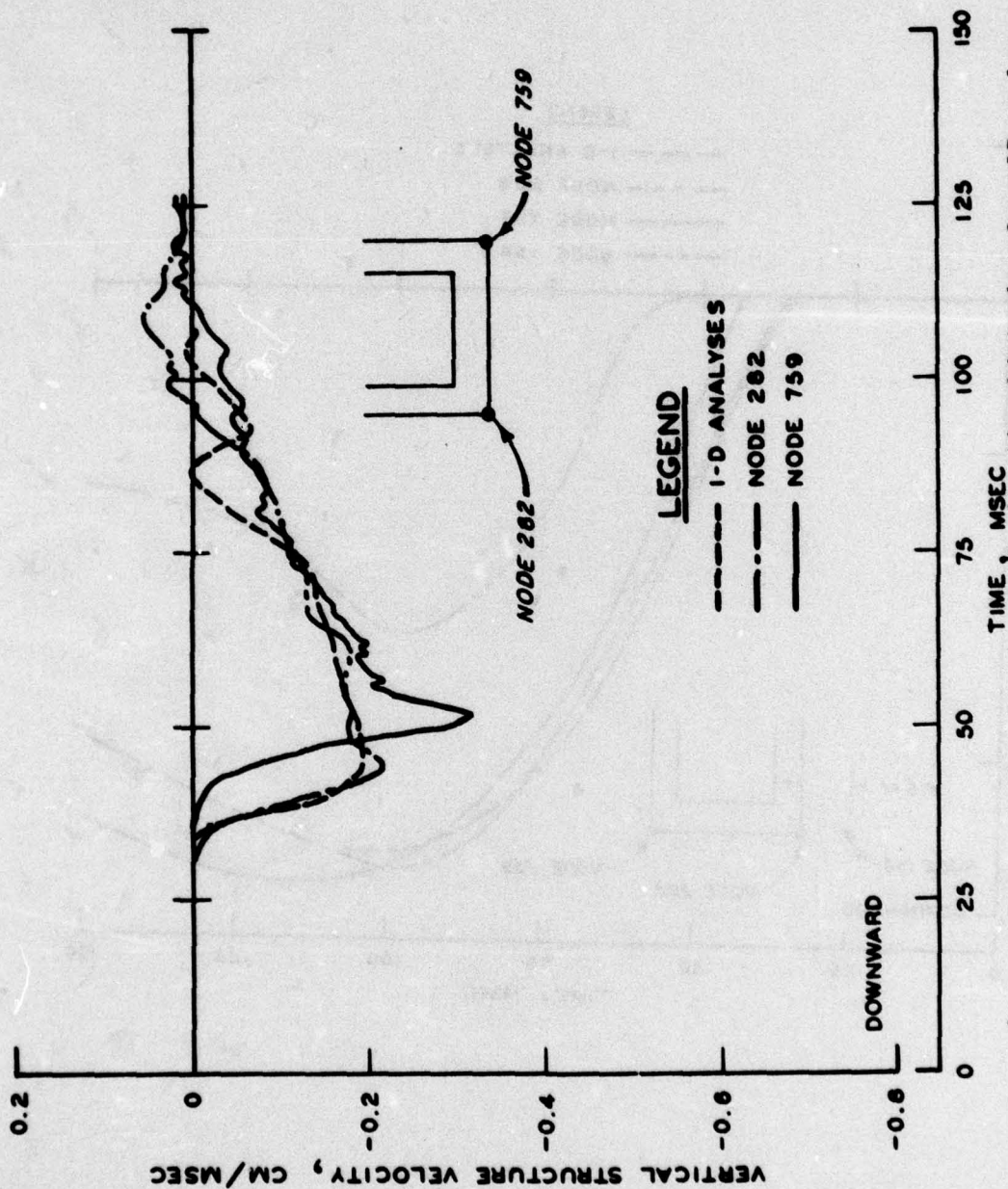


Figure B.6 Comparison of the structure velocity time histories from 1D analyses with those for the bottom corners of the structure from 2D calculations.

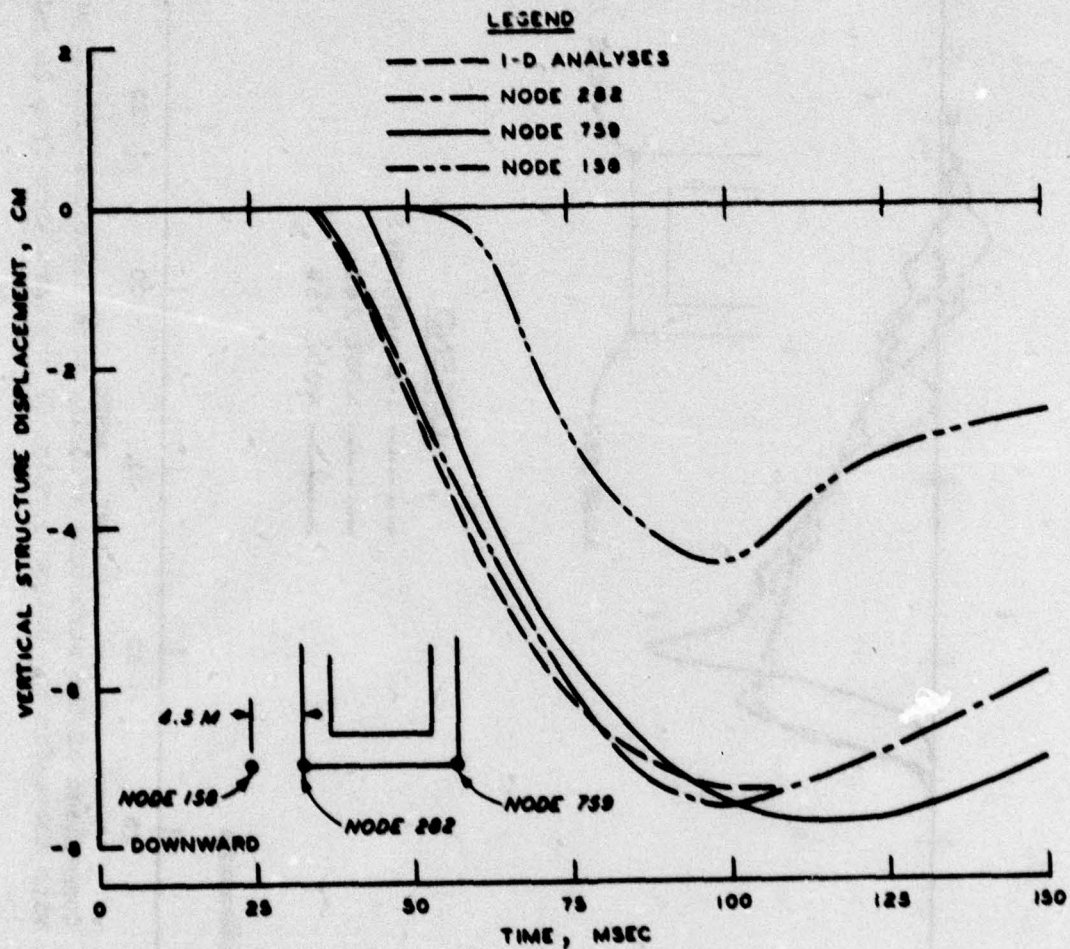


Figure B.7 Comparison of the structure displacement time histories from the 1D analyses with those for the bottom corners of the structure from 2D calculations.

# DISTRIBUTION LIST

## DEPARTMENT OF DEFENSE

Director  
Defense Civil Preparedness Agency  
ATTN: Staff Dir Rear George N. Sisson

Director  
Defense Communications Agency  
ATTN: CCTC/C672 Franklin D. Moore

Defense Documentation Center  
12 cy ATTN: TC/Mr. Myer B. Kahn

Director  
Defense Intelligence Agency  
ATTN: DB-4C2  
DT-2 Wpns & Sys Div  
DB-4C1  
Technical Library  
DB-4C3

Director  
Defense Nuclear Agency  
ATTN: SPSS  
STTL (Tech Library)  
STSI (Archives)  
DDST

## DEPARTMENT OF THE ARMY

Director  
BMD Advanced Tech Center  
ATTN: CRDABH-S  
CRDABH-X

Chief of Engineers  
Department of the Army  
ATTN: DAEN-MCE-D  
DAEN-RDM  
DAEN-RDL  
2 cy DAEN-ASI-L

Commander  
Harry Diamond Laboratories  
ATTN: AMXDO-TI, Technical Library

Commander  
Picatinny Arsenal  
ATTN: Phil Angelotti  
Tech Lib

Commander  
U. S. Army Communications Command  
ATTN: Tech Lib

Commandant  
U. S. Army Engineer School  
ATTN: ATSE-CTD-CS  
ATSE-TEA-AD

Director  
USAR Waterways Experiment Station  
ATTN: James Ballard  
Tech Lib  
William Flathau  
Guy Jackson  
Jim Balsara  
Bob Walker

## DEPARTMENT OF THE ARMY (Continued)

Commander  
U. S. Army Missile Command  
ATTN: J. Hogan

Commander  
U. S. Army Nuclear Agency  
ATTN: Tech Lib

U. S. Army Material Command  
Project Manager for Nuclear Munitions  
ATTN: DRCPM-MUC

## DEPARTMENT OF THE NAVY

Officer-in-Charge  
Civil Engineering Laboratory  
Naval Construction Battalion Center  
ATTN: R. J. Odello

## DEPARTMENT OF THE AIR FORCE

Commander  
Foreign Technology Division, AFSC  
ATTN: TD-BTA Library

SAMSO/DE  
ATTN: DEB

Commander-in-Chief  
Strategic Air Command  
ATTN: NRI-STINFO Library

## ENERGY RESEARCH & DEVELOPMENT ADMINISTRATION

University of California  
Lawrence Livermore Laboratory  
ATTN: M. Fernandez

Sandia Laboratories  
ATTN: John Keisur

## OTHER GOVERNMENT AGENCIES

Department of the Interior, Bureau of Mines  
ATTN: Tech Lib

## DEPARTMENT OF DEFENSE CONTRACTORS

Aerospace Corporation  
ATTN: Tech Info Services

Agabian Associates  
ATTN: M. Agabian

Applied Theory, Inc.  
ATTN: John G. Trullio

Bell Telephone Laboratories  
ATTN: John Foss

The Boeing Company  
ATTN: Aerospace Library

California Research and Technology, Inc.  
ATTN: Sheldon Shuster

DEPARTMENT OF DEFENSE CONTRACTORS (Continued)

University of California  
ATTN: G. Sachman

Civil/Nuclear Systems Corp.  
ATTN: Robert Crawford

University of Illinois at Chicago  
College of Engineering  
ATTN: Ted Belytschko

Kaman Avidyne  
Division of Kaman Sciences Corp  
ATTN: Technical Library

Kaman Sciences Corporation  
ATTN: Library

Karagozian and Case  
ATTN: John Karagozian

Lockheed Missiles and Space Company  
ATTN: Tom Geers

Merritt Cases, Incorporated  
ATTN: J. L. Merritt

Nathan M. Newmark  
Consulting Engineering Services

Pacifica Technology  
ATTN: R. Bjork

Physics International Company

R&D Associates  
ATTN: Dr. H. J. Cooper Jr.  
Technical Library

Science Applications, Incorporated  
ATTN: William M. Layson

Stanford Research Institute  
ATTN: George R. Abramson

Terra Tek, Inc.  
ATTN: Dr. A. H. Jones

TRW Defense and Space Systems Group  
ATTN: Nora Lipner

TRW Systems Group  
ATTN: Gregory D. Hulcher

Universal Analytics, Inc.  
ATTN: F. I. Field

The Eric H. Wang Civil Engineering  
Research Facility  
ATTN: Neal Baum

Weidlinger Associates, Consulting Engineers  
ATTN: Dr. Melvin L. Baron

Weidlinger Associates, Consulting Engineers  
ATTN: Dr. J. Isenberg

In accordance with letter from DAEN-RDC, DAEN-ASI dated 22 July 1977, Subject: Facsimile Catalog Cards for Laboratory Technical Publications, a facsimile catalog card in Library of Congress MARC format is reproduced below.

Windham, Jon Enrique

Effect of backfill property and airblast variations on the external loads delivered to buried box structures / by Jon E. Windham, John O. Curtis. Vicksburg, Miss. : U. S. Waterways Experiment Station ; Springfield, Va. : available from National Technical Information Service, 1978.

202 p. : ill. ; 27 cm. (Technical report - U. S. Army Engineer Waterways Experiment Station ; S-78-5)

Prepared for Director, Defense Nuclear Agency, Washington, D. C., under Subtask SC062, Work Unit 01, "Influence of Backfill on Structural Response."

References: p. 170-171.

1. Air blast waves. 2. Backfills. 3. Blast effects. 4. Blast loads. 5. Dynamic response. 6. Finite element method. 7. HONDO (Computer program). 8. Loads (Forces). 9. Overpressure. 10. Soil-structure interaction. 11. Surface explosions. 12. Underground structures. I. Curtis, John O., joint author. II. Defense Nuclear Agency. III. Series: United States. Waterways Experiment Station, Vicksburg, Miss. Technical report ; S-78-5.  
TA7.W34 no.S-78-5